NANOMATERIALS FOR SOLID OXIDE FUEL CELL ELECTROLYTES AND REFORMING CATALYSTS

Marcin Robert Kosiński

A Thesis Submitted for the Degree of PhD
at the
University of St Andrews

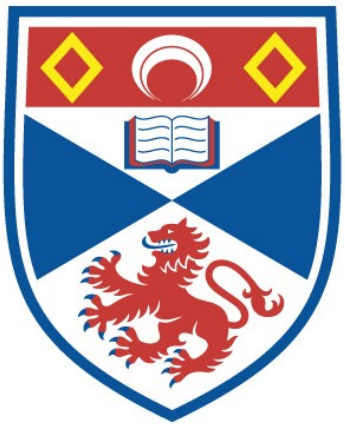

2012

Nanomaterials for Solid Oxide Fuel Cell Electrolytes and Reforming Catalysts

A thesis submitted for the degree of Doctor of Philosophy

by

Marcin Robert Kosiński

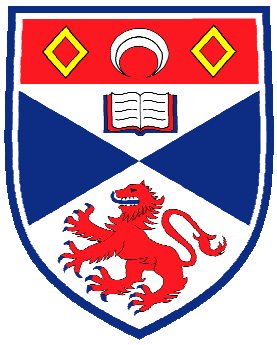

University
of
St Andrews

Supervised by Dr R.T. Baker

Submitted September 2011

DECLARATION

I, Marcin Robert Kosiński, hereby certify that this thesis, which is approximately 52,500 words in length, has been written by me, that it is the record of work carried out by me and that it has not been submitted in any previous application for a higher degree.

I was admitted as a research student in June 2007 and as a candidate for the degree of PhD in June 2007. The higher study for which this is a record was carried out in the University of St Andrews between 2007 and 2011.

Date: 21/9/11 Signature of candidate: ……..

I hereby certify that the candidate has fulfilled the conditions of the Resolution and Regulations appropriate for the degree of PhD in the University of St Andrews and that the candidate is qualified to submit this thesis in application for that degree.

Date: 21/9/11 Signature of supervisor: ……..

In submitting this thesis to the University of St Andrews we understand that we are giving permission for it to be made available for use in accordance with the regulations of the University Library for the time being in force, subject to any copyright vested in the work not being affected thereby. We also understand that the title and the abstract will be published, and that a copy of the work may be made and supplied to any bona fide library or research worker, that the thesis will be electronically accessible for personal or research use unless exempt by award of an embargo as requested below, and that the library has the right to migrate my thesis into new electronic forms as required to ensure continued access to the thesis. We have obtained any third-party copyright permissions that may be required in order to allow such access and migration, or have requested the appropriate embargo below.

The following is an agreed request by candidate and supervisor regarding the electronic publication of this thesis:

Embargo on both the printed copy and electronic copy for the same fixed period of two years on the following ground(s):

publication would be commercially damaging to the researcher, or to the supervisor, or the University;
publication would preclude future publication.

Date: 21/9/11 Signature of candidate: …… Signature of supervisor: …….

for my sons

ACKNOWLEDGEMENTS

There are many people, who deserve to be acknowledged in this part of my thesis. First of all, I would like to thank my supervisor, Dr Richard Baker, for his great support, encouragement and optimism during my PhD studies. Our numerous discussions were of invaluable help to me. I am very appreciative for his performance of TEM. It was a real pleasure to work in his research group.

I am very grateful to the School of Chemistry, University of St Andrews, the EPSRC, Powdermatrix and our industrial partner, MEL Chemicals Ltd, for funding my PhD studies. I would like to thank Colin Norman and Clare Jones at MEL for their help, advice and encouragement in this Project. Thanks to MEL Chemicals Ltd for supplying the materials for the studies described in Chapter 4. Initial dilatometry of YSZ materials was performed by Stephanie Tate.

I would like to express my deep gratitude to Dr Luisa Gomez-Sainero, of the Universidad Autonoma de Madrid, who shared her valuable knowledge on catalysis and XPS with me which I have used in Chapter 6 of this thesis. For this chapter, XPS was performed at the University of Valencia and the catalytic tests were carried out at the University Juan Carlos, Madrid.

I am grateful for all the assistance from the analytical and technical staff of the School of Chemistry, University of St Andrews. Thanks to Ross Blackley (Electron Microscopy, XRD), Sylvia Williamson (TA, BET, ICP-MS), Donna McColl (Microanalysis), Derek Waddell (IT), Jim Bews (IT), Marjory Parker (stores), Artur Czernik (stores), Colin Smith (glass blowing), Brian Walker (electronics), Bob Cathcart and George Anthony (workshop).

I also want to thank Dr Nigel Botting, Dr Finlay Morrison, Dr Christopher Baddeley and Arnot Williamson for their support and help during demonstration.

I would like to thank all the members of the Baker research group, many of whom became good friends; Shidong, Stephanie, Jonathan, Troy, Bo, Juan Carlos and John.

I also wish to thank all the amazing people who I met during my time in St Andrews. Especially, the BMS basketball team: Deng, Guillaume, Matthieu, Natalie, Nelly and Vincent as well as the famous JTSI football team: Christian, Marteen, George, Steven and Nick for great games. Big thanks to Ana, Andrei, Gina, Tomas for bringing Greek, Romanian and Czech culture to my everyday life. I would also like to thank Marzia and Peter for the "Prison Break" and lots of support in family and cat matters.

Finally, I would like to say thank you to my wife Agnieszka and sons Dominic and Jeremy, for their endless love and great support during our time in St Andrews.

Dziękuję wszystkim poznanym w St Andrews polskim przyjaciołom: Ani, Asi, Arturowi, Gosi, Ilonie, Irenie, Izie, Krzyśkowi, Lilce, Łukaszowi, Michałowi, Monice, Oli i Piotrowi za wspólne spotkania i polskie klimaty.

Jestem ogromnie wdzięczny wszystkim moim bliskim znajomym w Polsce: Kasi i Grzesiowi, Adze i Piotrowi, Agacie, Gosi, Elwirze, Magdzie i Rafałowi za duchowe wsparcie oraz wiarę we mnie i moje możliwości.

Bardzo dziękuję moim rodzicom Irenie i Edwardowi, teściom Teresie i Krzysztofowi oraz ciotkom, wujkom i kuzynom za nieocenioną pomoc, wiarę i wsparcie.

Jednak największe podziękowania należą sie mojej żonie Agnieszce oraz synkom Dominikowi i Jeremiemu, za niekończącą się miłość, oddanie i ogromne duchowe wsparcie.

ABBREVIATIONS

AEMFC	Anion Exchange Membrane Fuel Cell
AFC	Alkaline Fuel Cell
BET	Brunauer-Emmett-Teller method
CA	Citric Acid
CHP	Combined Heat and Power
DDP	Digital Diffraction Pattern
DDTA	First Derivative of Differential Thermal Analysis Curve
DMFC	Direct Methanol Fuel Cell
DSC	Differential Scanning Calorimetry
DTA	Differential Thermal Analysis
DTG	First Derivative of Thermogravimetric Curve
EDX	Energy Dispersive X-ray Spectroscopy
FFT	Fast Fourier Transformation
FWHM	Full Width at Half Maximum (Intensity)
GDC	Gadolinium-doped ceria
HR-TEM	High Resolution Transmission Electron Microscopy
ICDD	International Centre for Diffraction Data
ICP-MS	Inductively-Coupled Plasma Mass Spectroscopy
ICSD	International Crystal Structure Database
IS	Impedance Spectroscopy
LGSM	Strontium and Magnesium doped Lanthanum Gallate
LSM	Strontium-doped Lanthanum Manganite
MCFC	Molten Carbonate Fuel Cell
MS	Mass Spectrometry
OSC	Oxygen Storage Capacity
PAFC	Phosphoric Acid Fuel Cell
Pd/SDC	Palladium supported on samarium-doped ceria
PDF	Powder Diffraction File
PEMFC	Proton Exchange Membrane Fuel Cell
QMS	Quadrupole Mass Spectrometer
ScSZ	Scandia-stabilised zirconia
SDC	Samarium-doped ceria

SEM	Scanning Electron Microscopy
SOFC	Solid Oxide Fuel Cell
SRM	Steam Reforming of Methane
SSA	Specific Surface Area
TA	Thermal Analysis
TEM	Transmission Electron Microscopy
TG	Thermogravimetry
TPB	Three Phase Boundary
TWC	Three-Way (Automotive) Catalysts
WGS	Water Gas Shift (Reaction)
XPS	X-ray Photoelectron Spectroscopy
XRD	X-ray Diffraction
YSZ	Yttria-stabilised zirconia

ABSTRACT

In this work, a broad range of analytical methods was applied to the study of the following three materials systems: yttria-stabilised zirconia (YSZ), samarium-doped ceria (SDC) and SDC-supported metal catalysts. YSZ and SDC were studied in the light of their application as solid electrolytes in Solid Oxide Fuel Cells. The SDC-supported metal catalysts were evaluated for application in the reforming of methanol.

The conductive properties of YSZ pellets derived from powders of different Y contents and particle size ranges were investigated using Impedance Spectroscopy (IS). Comparative studies of the crystallography (by X-ray Powder Diffraction (XRD)), morphology (by Scanning and Transmission Electron Microscopy (SEM, TEM)), chemical composition (by Energy Dispersive X-ray Spectroscopy (EDX) and Inductively Coupled Plasma Mass Spectroscopy (ICP-MS)) and sintering behaviour (dilatometry) were employed in the overall assessment of the conductivity results collected.

Detailed studies of three SDC compositions were performed on nanopowders prepared by a low temperature method developed in the Baker group. Modifications led to a simple and reliable method for producing high quality materials with crystallites of ~10 nm diameter. The products were confirmed by XRD and TEM to be single-phase materials. Thermogravimetric analysis, dilatometry, specific surface area determination, elemental analysis and IS were carried out on these SDC powders. The relationships between particle size, chemical composition, sintering conditions and conductivity were studied in detail allowing optimum sintering conditions to be identified and ionic migration and defect association enthalpies to be calculated. This work is now published.

Finally, the interesting results obtained for the SDC nanopowders were a driving force for the preparation of SDC-supported metal catalysts. These were prepared by three different methods and characterised in terms of crystallographic phase, specific surface area and bulk and surface chemical composition. Isothermal catalytic tests showed that all catalysts had some activity for the reforming of methanol and that some compositions showed both very high conversions and high selectivities to hydrogen. These catalysts are of interest for further study and possibly for commercial application.

TABLE OF CONTENTS

CHAPTER I – **INTRODUCTION**

1. Introduction

This chapter describes a relatively new and environmentally clean power generation system, that is fuel cell technology. The issues that relate to worldwide energy demands and possible responses are briefly described. One of these responses concentrates on the implementation of renewable energy sources on a larger scale. The potential of Solid Oxide Fuel Cell technology is also emphasised in the context of the supplied fuel, which in the case of H_2, can be generated using renewables or efficient reforming catalysts.

1.1 Worldwide energy demands

The global demand for energy is expected to grow as mankind has become more technologically driven and world population continuously increases.[1] In relation to this fact, the global energy consumption was predicted to increase by 49% from 2007 to 2035.[2] A significant part of energy consumption is still assigned to developing countries such as China and India. On the other hand, most of the highly developed European countries and the USA seem to be recovering after the consequences of financial and economic crisis in 2009 and a noticeable upturn in their energy demand is anticipated shortly.

As worldwide energy is still mainly produced from fossil fuels (oil, natural gas and coal), recently serious, justifiable concerns have arisen in relation to the stability of supply and the ecological impact of the combustion of fossil fuels. In the near future, existing oil supplies may not be sufficient, even though new resources are constantly discovered. These are connected either to more sophisticated, expensive extraction processes on land or to an infringement of so far inaccessible oil-rich areas such as the Arctic. It is expected that these factors together will quickly result in the "end of cheap oil". In addition, a trend of increasing oil prices is already observed to be well-established, because of the factors already mentioned and to additional geopolitical reasons. Therefore, an appropriate development and investment in novel energy technologies together with more strict environmental policies are required for a more sustainable future power generation infrastructure. In 2007, the UK government set out its vision of developments in new power generation systems up to 2030.[3] The key postulates included the need to maintain a reliability of supply of electricity as well as security of supply of the required fuels for electrical power generation. The requirement to reduce the levels of CO_2 emissions and other greenhouse gases was also taken into consideration. In relation to these issues, the UK energy economy will continue to be based on electricity generation by the combustion of fossil fuels, but the emphasis is expected to move away from

coal towards gas fired power stations. Similar policies were already established in other European countries. In order to reduce harmful emissions, a more aggressive policy including Carbon Capture and Storage technology will be required very quickly. Moreover, the safety of nuclear power plants needs to be carefully verified in the light of the recent disaster in Fukushima, Japan. Growth in renewable energy sources is also projected to increase to 20% of total electricity generation by 2020.[3] Because of the intermittent operating mode of renewables, their combination with fuel cell technology offers a very promising alternative to other power generation systems. Although electrical energy from solar or wind power resources can be used directly, a more efficient power generation process can be designed in which pure H_2 is produced by the electrolysis of H_2O using the electrical output from renewable energy sources and so becomes a clean chemical energy source for a fuel cell system. Such electrolyser-H_2 storage-fuel cell systems offer the opportunity of smoothing the intermittency of renewable energy sources, capturing energy output which would otherwise be lost in times of low demand and storing it as chemical energy for use when demand increases. In addition, fuel cell technology is being developed to utilise all types of fossil fuel at high efficiencies. Apart from hydrogen, hydrocarbon and oxyhydrocarbon fuels can be used directly in the fuel cell or may require efficient reforming catalysts in order to produce hydrogen. Therefore, it seems to be important during the worldwide crisis to finally make fuel cell technology commercially available to the masses. The development of reforming catalysts for efficient hydrogen generation is also of great interest.

1.2 Fuel cell technology

Fuel cells are devices capable of producing electricity directly from a fuel and an oxidant through electrochemical reactions without any combustion. They give much higher conversion efficiencies than conventional thermomechanical systems, as they do not have the multiple steps and the thermodynamic limitations of heat engines. They work in a similar way to batteries and consist of two electrodes separated by an electrolyte. The nature of the electrolyte dictates the nature and direction of the ions transferred in the overall electrochemical reaction. This in turn determines on which side of the cell water is produced. Unlike batteries, fuel cells can generate electricity continuously as long as the oxidant (usually air) and the fuel are supplied to their respective electrodes. Many types of fuels can be employed, such as hydrogen or carbon-based fuels. The most environmentally friendly is hydrogen, because only H_2O and heat are produced. However, because of the inefficiencies in the transportation and storage of H_2, and because the majority of H_2 is presently derived

from fossil fuels, much attention has also been paid to other fuels. It is reported that the amount of air pollutants released from use of carbon-based fuels (methanol, biofuels, natural gas) in fuel cells is below that for combustion technology, because of the higher efficiency of the fuel cell systems.[4]

Fuel cells are generally categorized by the chemical characteristics of the electrolyte or their operating temperature. The most developed fuel cell types are briefly presented in Table 1.1. The flexible choice of different fuel sources enables the usage of fuel cells in many applications. Currently, research concentrates mostly on portable, automotive and stationary usages.[4]

Table 1.1 Types of fuel cells and their selected properties.[4-6]

Fuel Cell Type	*Electrolyte*	*Operating temperature*	*Fuel*	*Limitations*	*Benefits*
SOFC	YSZ GDC SDC perovskites	600-1000°C	H_2 CH_4 natural gas CO	long start-up time	CHP efficiency 70-90%
MCFC	$(Li,Na)_2CO_3$	600-700°C	H_2 CH_4 natural gas CO	corrosive electrolyte	resistance to impurities
PAFC	H_3PO_4	160-210°C	H_2 CH_4 natural gas CH_3OH	expensive electrodes, corrosive electrolyte	CHP efficiency 70-90%
DMFC	polymer	60-200°C	CH_3OH	possible permeation of methanol	methanol, reforming not required
PEMFC	polymer, proton exchange membrane	50-100°C	H_2 CH_3OH	expensive electrodes, sensitive to impurities	low operating temperature
AFC	KOH	50-200°C	H_2 N_2H_4	sensitive to impurities	inexpensive catalysts, good efficiency
AEMFC	alkaline anion exchange membrane	50-80°C	H_2 CH_3OH	poor stability above 80°C	inexpensive catalysts, no CH_3OH crossover

Solid Oxide Fuel Cells (SOFCs) incorporate electrolytes produced from oxide ceramics and operate at temperatures up to 1000°C. The high efficiency and flexibility of the fuels that can be used are among many other benefits they possess. A long start-up time which is a result of their high operating temperature limits slightly their implementation. This type of fuel cells is described in more detail in Section 1.3, in relation to the materials presented in this thesis.

Molten Carbonate Fuel Cells (MCFCs) use molten alkali carbonates as the electrolyte.[4] Dicks pointed out in his review that a mixture of Li_2CO_3 and Na_2CO_3 is a preferred electrolyte material in contrast to the previously used K_2CO_3.[7] The temperature of 600-700ºC must be precisely controlled to ensure stable conditions for cell operation.[8] Similarly to SOFCs, they can run on a wide variety of fuels that makes them useful in stationary power generators. It should be noted that the carbonate ion is responsible for ionic charge transport in MCFCs.

Phosphoric Acid Fuel Cells (PAFCs) currently employ concentrated phosphoric acid as the main constituent, which is a proton conductor. In some previous projects, it had to be diluted to reduce corrosion. So far, it is one of the most successful, commercially available fuel cell technologies, despite its relatively low efficiency if it is not employed in CHP applications. Sammes *et al* demonstrated a net electrical efficiency of 37% and total efficiency of 87% for such systems running on natural gas.[9] PAFCs usually operate on a reformate gas mixture, and a reduced concentration of CO of up to 1-2% is acceptable.[8] The level of other contaminants such as H_2S and NH_3 in the anodic and cathodic gas must also be strictly controlled to avoid a loss in performance of the cell.

Proton Exchange Membrane Fuel Cells (PEMFCs) employ a polymeric cation exchange membrane as the electrolyte. As explained by Lin *et al* in their work, the water management is a critical parameter for the efficient operation of the membrane.[10] Therefore, a thermally and chemically stable ionomeric electrolyte, such as the sulfonated fluorocarbon polymer, Nafion, must be hydrated in order to conduct H^+ and allow the proper functioning of the cell. PEMFCs have the advantage of being easily adapted for portable systems as well as the possibility of operating at low temperatures. De Bruijn reported that cold starting below 0°C is also possible.[8] Pure hydrogen is the most preferable fuel. One of the more developed PEMFC applications is in the replacement the combustion engines in automobiles. However adapting this technology to vehicles presents challenges due to the severe cost, pressures, aggressive environment and operation and the smaller space available to hold such systems.[11] These must include reforming technology if other readily available fuels (e.g. gasoline, natural gas) are to be utilised.

Direct Methanol Fuel Cells (DMFCs) use aqueous CH_3OH solution as the fuel, which is easy to manage and handle. As for PEMFCs, DMFCs are considered to be a good candidate for portable applications if harmful CO levels and methanol crossover between electrodes can be minimised.[12] Micro-DMFCs offer a potential to replace batteries due to the high energy density of methanol. According to Stambouli *et al*, good efficiency levels of 40-55% can be easily achieved.[4] They are very attractive for car applications due to similar costs for CH_3OH and gasoline as well as their low operating temperature.

Alkaline Fuel Cells (AFCs) utilise an alkaline solution of potassium hydroxide (KOH) as the electrolyte. A large number of materials, such as noble and non-noble metals can be used as catalysts. However, due to their sensitivity to impurities present in the air or fuel, practically only pure oxygen and hydrogen can be employed. AFCs are currently used for power generation on spacecraft.

An interesting approach in the development of fuel cell technology which combines the benefits of PEMFCs, DMFCs and AFCs was pointed out by Varcoe and Slade in their review.[6] The authors indicated the application of Alkaline Anion-Exchange Membranes (AAEMs) instead of Proton-Exchange Membranes (PEM), which are considered to be high-maintenance and expensive. The transport of OH^- ions from cathode to anode in Anion Exchange Membrane Fuel Cells (AEMFCs) is the opposite to that observed for PEM-based fuel cells. Because of this, the issues related to water management, as seen in PEMFCs, can be overcome. In addition, methanol crossover (as for traditional DMFCs) and electrode and electrolyte degradation (as for AFCs) were reported to be reduced in DMFCs operated with AAEMs. However, extensive studies in order to improve conductivity and stability of AAEM systems are still required. AEMFCs containing benzyltrimethylammonium moieties prepared by means of radiation-grafting onto PTFE membranes, were recently found to be stable at temperatures up to 80°C.

Although the maximum operating voltage of an individual fuel cell is about 1 V under load conditions, an increase in power density can be achieved by varying the cell size and number of cells thanks to the modular nature of the fuel cell system.[8] Cells can be connected either in series or in parallel (in so-called stacks), thus increasing the power output by increasing the voltage or current. Meeting the challenges for all types of fuel cells, in order to speed up their commercialisation, revolves mostly around the reduction of manufacturing costs. The improvement of reproducibility, consistency of performance and the scaling-up to larger output devices is also of great importance. In the case of SOFCs, the potential solutions include development of new electrolyte and electrode materials, improved powder feedstock

consistency for the manufacture of these components and improved control over their sintering processes, which would allow the decrease of fabrication costs.

1.3 Solid Oxide Fuel Cells

SOFCs are very competitive among other fuel cell technologies, especially in the context of stationary power generation. Their high efficiency, simple design, modularity, quiet operation and fuel adaptability make them very attractive for distributed energy applications even in remote areas.[13] In addition, excess heat energy, which is a by-product, can be used in Combined Heat and Power (CHP) operation mode. This increases significantly the overall efficiency of the fuel cell system (Table 1.1). Due to their considerably lower emissions of CO_2, SO_2 and NO_x, which are heavily released in the combustion of fossil fuels in conventional power plants, they are likely to contribute positively to air quality, the environment and human health. On the whole, they are expected to have a positive effect on the global environment by displacing conventional electricity generation and so preserving natural resources. The operating principles, configurations and components of SOFCs are presented in this Section. A literature review on the electrolyte materials investigated by the author is also included.

1.3.1 Principle and design of a typical SOFC

In general, SOFCs consist of two permeable electrodes separated by a dense, ionically conducting electrolyte. The fourth component – the interconnect – allows the flow of the current between single cells in the fuel cell stack and completes the main structure of the cell. The cathode is the positive terminal of the fuel cell, which mediates the reduction of molecular oxygen (usually from air) to oxygen anions, using electrons from the external circuit. The anode, the negative terminal, is responsible for electrochemical oxidation of the fuel and release of electrons, thanks to oxygen ions conducted through the impermeable electrolyte. As a result, water (with H_2 fuel) and heat are generated as the main products. The electrolyte conducts by oxygen ions moving through it *via* oxygen ion vacancies in its crystal structure and down a concentration gradient caused by the low O_2 partial pressure at the anode.

Figure 1.1 shows a schematic of an SOFC operating either on H_2 or CH_4 as the fuel. If hydrocarbons are employed as the fuel, CO_2 is also released as a final product besides water.

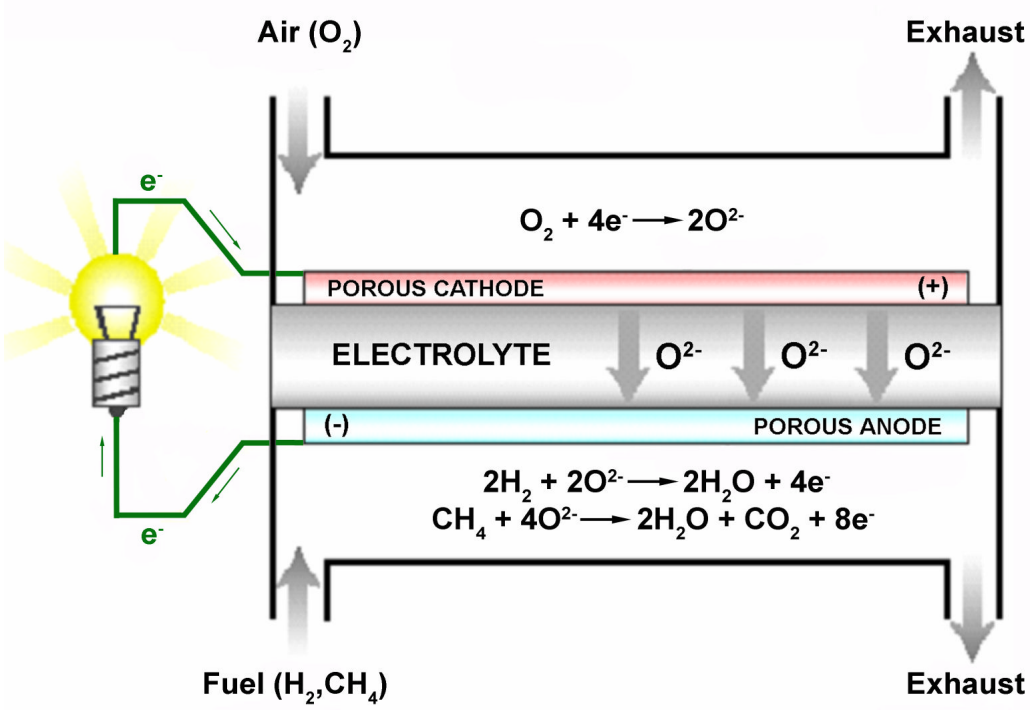

Figure 1.1 Schematic of a SOFC, adapted from Huijsmans.[14]

One very important feature of SOFCs is that all of the components are solids, which means that no restrictions are placed on the cell design by the need to manage liquids. The SOFCs are mainly constructed in two types – tubular or planar. These are presented schematically in Figure 1.2. However, alternative configurations such as monolithic or roll designs have also been considered.[5] The latter has been developed at the University of St Andrews and combines ideas from leading designs of planar and tubular geometry.[15]

In the tubular design, components are assembled in the form of a hollow tube constructed in layers around, for example, a tubular cathode. In this case, air flows through the inside of the tube and fuel flows around the exterior. The inverse geometry, with the anode inside, is also possible. Tubular fuel cells are mechanically durable and their seals can be made outside the hot zone. One of their disadvantages is the relatively long current path around the circumference of the cell to the interconnect, which limits their performance.[16]

An alternative to the tubular SOFCs is a planar configuration. In this case, the components are assembled in flat stacks, with air and fuel flowing through channels built into interconnects of each repeating unit. Such a configuration increases stack performance and gives much higher volumetric power density compared to the tubular design. The high power density is critical to reduce costs, because the amount of required material per kW is minimised. Furthermore, the planar design allows the use of inexpensive fabrication methods

such as screen-printing and tape casting. However, electrical resistance of the relatively thick supporting electrolyte, mechanical strength, thermal robustness and sealant durability are some of the technical issues that still limit development and commercialisation of the planar SOFCs.[17]

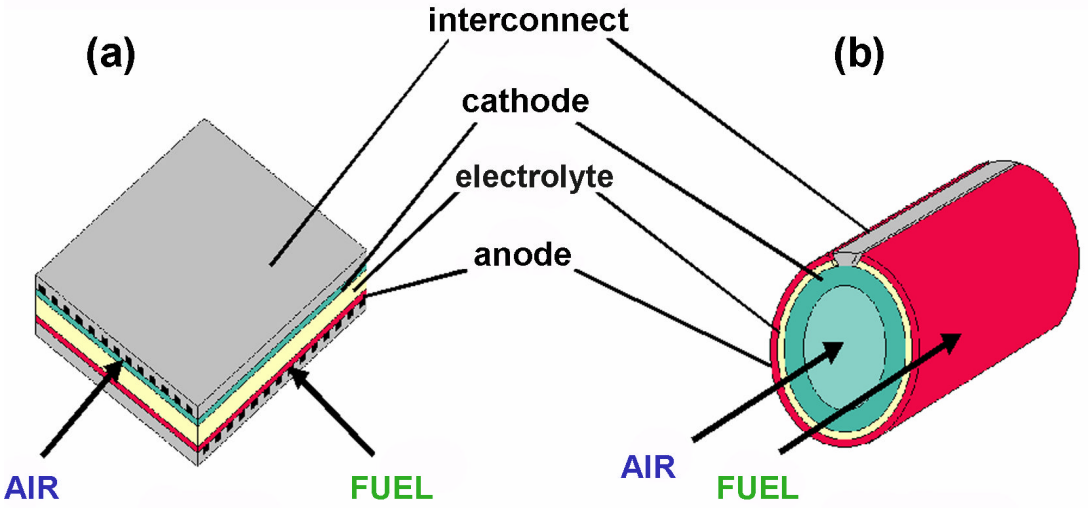

Figure 1.2 (a) Planar and (b) tubular designs of a SOFC, adapted from Yamamoto[5] and Singhal.[17]

1.3.2 Components of the SOFC

The high operating temperature of SOFCs allows for the internal reforming of a wide range of fuels. On the other hand, it contributes to the higher costs of cell components and to the decrease in the cells lifetime, which has been stated to be between 40000 and 80000 h.[4] Therefore, recent worldwide efforts have concentrated on development of materials for SOFCs which could operate efficiently below 600°C. The selection of materials for the individual components of SOFCs seems to be enormously challenging due the strong oxidizing atmosphere at the air side and reducing atmosphere at the fuel side of the cell. Each material must have the electrical properties required to perform its function. It must be also chemically and structurally stable enough to endure fabrication and operation at such high temperatures.[18] The reactivity and interdiffusion between the components of the SOFC should be as low as possible. In addition, the thermal expansion coefficients of the components should be as close to each other as possible in order to minimise thermal stresses, which could lead to cracking and mechanical failure of the cell. These aspects will be described in the following sections with particular reference to the most developed materials used in the SOFC technology.

1.3.2.1 Electrodes

In the fuel cell, the electrochemical reactions occur at the three phase boundary (TPB), a place where electrolyte, electrode and gaseous reactant meet. Therefore, providing as large a TPB length as possible between these three phases is of extreme importance, at both the anode and the cathode. The permeable structure (with porosity of 20-40%) of the electrodes ensures contact between electrolyte and fuel or oxidant (respectively).[4] The electrode material must possess catalytic activity for the relevant half-reaction and good electronic conductivity. Considerable effort must be made to match the electrode materials with the electrolyte in use, in order to avoid thermal stresses or chemical reactions between these components either during fabrication or in long-term operation. Moreover, such a combination of electrode materials, which are both, mixed electronic and ionic conductors, allows the extension of the reaction zone beyond the TPB.

The negative electrode of the fuel cell (the anode) is most often produced from the composite mixture of nickel oxide (NiO) and an ionically conducting material, for example, yttria-stabilised zirconia (YSZ). Prior to operation, the former must be reduced to metallic nickel, simultaneously creating the porous network because of the decrease in its volume. Application of this two-phase mixture inhibits sintering of metal particles and results in a thermal expansion coefficient comparable to those of the other components. Ni/YSZ cermets work most effectively with pure hydrogen and are suitable for applications with YSZ electrolytes. If internal reforming of hydrocarbons (e.g. natural gas) is performed, they may experience carbon or sulphur deposition and the TPB area is minimised. To avoid the problems mentioned above, the use of perovskites (e.g. $CaTiO_3$, $La_{0.33}Sr_{0.66}TiO_3$, $Sr_{0.86}Y_{0.08}TiO_{3-\delta}$ or $(La_{0.75}Sr_{0.25})_{0.95}Cr_{0.5}Mn_{0.5}O_{3-\delta}$) seems to be a promising solution.[19] Other studies also confirmed progress in elimination of these harmful deposits. He *et al* in their work with humidified methane observed a reduction of the carbon deposition effect by applying a physical layer of Zr-doped ceria on Ni/YSZ cermets.[20] This approach was also found to be successful for NiO/SDC and NiO/GDC anode materials, which work efficiently with ceria-based electrolytes.[21] Recent modifications of such anodes were performed by Wang *et al*, who incorporated Cu nanoparticles into a previously prepared Ni/SDC matrix.[22] The reported effect of carbon deposition for a cell operating on dry CH_4 was greatly reduced.

The positive electrode (cathode) of the fuel cell is often made of electronically conducting perovskite-type oxide blended with a relevant electrolyte material. Similarly to the preparation of anodes, the improvement of their performance can be achieved and the TPB length is enlarged by introducing porosity into the cathode layer. The use of noble metals is possible,

but insufficient long term stability and excessive cost has made them impractical so far. A much-used set of cathode materials are the Sr-doped lanthanum manganite family (LSM), which show a very good match with Ni/YSZ/YSZ components.[14] For example, $La_{0.65}Sr_{0.3}MnO_{3-\delta}$ shows good characteristics at operating temperatures above 800°C when it is matched with zirconia electrolytes[4, 23] However, at above 1000°C, the precipitation of $La_2Zr_2O_7$ and $SrZrO_3$ phases (depending on Sr/Zr ratio) was found to have a disadvantageous effect on fuel cell performance.[24, 25] The current efforts to lower the operating temperature of SOFCs may mean that these disadvantageous reactions can be avoided. Moreover, other perovskite family cathode materials such as lanthanum strontium cobaltite (LSC), lanthanum strontium ferrite (LSF), lanthanum strontium cobaltite ferrite (LSCF), samarium strontium cobaltite (SSC) or praseodymium strontium manganite (PSM) are recommended for IT-SOFCs.[4, 26] Bebelis *et al* reported the highest electrocatalytic activity for oxygen reduction for $La_{0.78}Sr_{0.2}Co_{0.2}Fe_{0.8}O_{3-\delta}$ material interfaced to a double layer of CGO and YSZ electrolytes.[23] As for the anode, this approach ensures the reduction of strain during the cell fabrication process due to the excellent thermal expansion compatibility. However, a main benefit consists in the increase of the electrode efficiency due to the improvement of electronic and ionic properties from added electrolyte materials.

1.3.2.2 Electrolyte

The commonly used electrolyte materials in SOFCs are zirconia-based and ceria-based solid solutions.[27-30] Due to the different chemical and physical properties of these compounds, ZrO_2-based electrolytes are successfully applied in high temperature Solid Oxide Fuel Cells (HT-SOFCs), while CeO_2-based materials are considered for intermediate temperature Solid Oxide Fuel Cells (IT-SOFCs). Other alternatives recognised as perovskites are also being intensively investigated and some of these are reported by Haile to have even higher ionic conductivities than ZrO_2 and CeO_2-based electrolytes, for example doped $Ba(Zr,Ce)O_3$.[30] For example, $La_{0.9}Sr_{0.1}Ga_{0.8}Mg_{0.2}O_{3-\delta}$ (LSGM) was found to be a promising electrolyte due to excellent ionic conductivity observed at 600°C.[31] However, the presence of second phases such as $SrLaGa_3O_7$ and $La_4Ga_2O_9$ was detected during the fabrication process. The diffusion of Ni from the anode used in the cell, was reported to cause chemical instability of LSGM electrolyte.[30] These factors limited the application of LSGM as an SOFC electrolyte. Kharton *et al* pointed out the field of other materials such as derivatives of δ-Bi_2O_3, γ-$Bi_4V_2O_{11}$, $La_2Mo_2O_9$ and $Ba_2In_2O_5$, which may possess higher ionic conductivity than zirconia and ceria-based electrolytes.[32] However, these new materials experience thermodynamic instability in

reducing atmospheres, high corrosion activity and low mechanical strength. The volatilisation of bismuth oxide at intermediate temperatures was also observed, thus limiting the application of Bi-containing materials as electrolytes in SOFCs.

The transport of oxygen ions between electrodes in SOFCs is possible due to the introduction of di- or trivalent cations into the crystal structure of the parent electrolyte oxide, for example zirconia or ceria. Usually a number of host cations are replaced, at the same lattice sites, by guest cations of lower charge and different ionic radius in such mixed oxides during their preparation. This leads to structural defects and, very importantly, to oxygen ion vacancies which are generated in order to maintain the charge neutrality of the crystal lattice.[33] These oxygen ion vacancies are essentially responsible for introducing ionic conductivity in to the electrolyte solid. Their number is controlled by the concentration and formal charge of the dopant, as well as the partial pressure of O_2 in contact with the material, where cations of variable oxidation state are present. These aspects are reviewed in more detail in Section 1.3.3.

Homogeneous, dense electrolytes are typically produced by compaction of a mixture of ground powders of the appropriate simple metal oxides into green bodies, followed by a sintering process. Temperatures above 1300°C and an isothermal dwell of at least a few hours are usually employed.[34] This method is known as the ceramic or solid state route. The more uniform the distribution of elements in the starting powder mix achieved during their preparation step, the more efficient will be the sintering process.

Certain further developments in electrolyte manufacture include the introduction of limited amounts of additives, which can promote the sintering process by controlled grain growth at lower sintering temperatures. The most effective sintering aids for ceria-based electrolytes were found to be Co_3O_4 and Ga_2O_3.[35-39] Usually these were added from their corresponding metal nitrates solution and then added to already sintered doped ceria powders. An additional ball milling process was required over 24 h period as well as drying. Yan et al observed enhanced densification rate during their dilatometry studies on SDC doped with up to 5 mol% of cobalt oxide.[39] The authors concluded that reduction of Co_3O_4 to CoO is possible above 900°C as a main contributor to the improved sintering kinetics. The impact on ionic conductivity of $Ce_{0.8}Sm_{0.2}O_{1.9}$ composition (20SDC) by addition of either 1 at% CuO or 2.5 at% CoO was studied by Zhang *et al.*[35] Both transition metal oxides were found to be effective during the sintering process as they allowed for full densification of commercial micron-sized SDC powders at only 1000°C. However, at 600°C, the decrease in ionic conductivity from 0.0210 $S{\cdot}cm^{-1}$ (for 20SDC) to 0.0173 $S{\cdot}cm^{-1}$ (for 20SDC electrolyte with Cu addition) was observed. The addition of Co resulted in a very small increase of electrolyte

conductivity. It increased to the value of only 0.0224 $S \cdot cm^{-1}$, measured at the same temperature. The sintering behaviour of a group of ceria-based oxides with 0.5 at% of gallia additive was investigated by Yoshida *et al.*[36] All Ln-doped ceria (Y, La, Gd, Sm and Nd) solid solutions, when subjected to Ga doping allowed for the decrease of the sintering temperature from 1600 to 1500°C retaining similar densities, but different microstructures were observed than for undoped analogs. The conductivity of Ga-doped YDC slightly decreased, while Ga-doped GDC and Ga-doped SDC were almost unchanged in relation to Ga-undoped ceria samples. Ga-NdDC and Ga-LaDC showed a certain increase of ionic conductivity. The authors concluded that the promotion of the grain growth for Ga co-doped ceria-based solid solution, could be a result of Ln oxide-gallia liquid phase formation during the sintering step. These studies, however, were relevant to electrolytes prepared only by the conventional solid-state method. The use of nanostructured starting materials, which may possess more desirable properties for sintering than the micron-size powders typically used in the ceramic route, seems to be an attractive approach for improving sintering as an alternative to the introduction of additional sintering promoters. Recently, this trend has been widely accepted for the preparation of dense electrolytes.[34, 40, 41]

Sintered SOFC electrolytes are polycrystalline ceramics, characterised by a grain microstructure with grain boundaries between them. An example of typical electrolyte microstructure is presented in Figure 1.3. The bulk material in the grains of a crystal presents a resistance to the movement of ions. The grain boundaries also represent an additional barrier to their movement, acting as a series resistance. In addition, poorly conducting impurities (i.e. SiO_2) or segregating phases may also accumulate at grain boundaries and cause an increase in the grain boundary resistance.[42-44] Badwal *et al* in their studies on YSZ material showed a significant decrease of grain boundary conductivity if only 0.2 wt% of SiO_2 was introduced as contamination.[45] Therefore, it is of great interest to obtain high-purity ionic conductors.

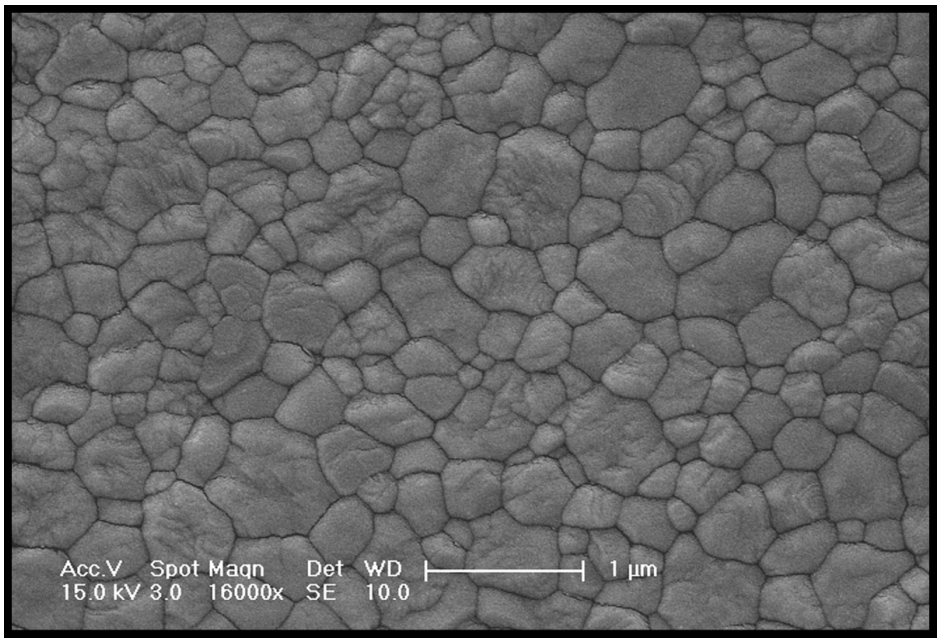

Figure 1.3 An example of YSZ pellet microstructure.

A variety of synthetic methods is used by researchers in order to prepare electrolyte precursor powders. They often lead to different properties in the final product, for example, in terms of morphology and particle size. Such effects are likely to have an influence on the sintering process. As mentioned above, the electrolyte powders are often synthesised by a conventional mixing and grinding of simple starting metal oxide powders.[46, 47] Wet chemical routes such as co-precipitation, sol-gel methods or combustion techniques, among many others, have also been applied.[34, 48-51] Some of these are quite complex and expensive. In addition, each method might introduce a different level of impurities, which hypothetically increases with the number of steps involved in the preparation method. Solid state methods are the simplest to carry out, but the homogeneity and density of the final product may be poor. On the other hand, the solution methods are also recognised as relatively simple to perform. They are inexpensive and effective for producing high surface area powders with ultra-fine particle sizes. Recently, wet chemical techniques have been proposed to have some advantages over conventional mechanical processing, because the precursor generally possesses considerable purity, uniformity in particle size and higher reactivity during sintering step.[52] The Pechini method, which involves the creation of metal-organic acid complexes along with acid-ethylene glycol coordinated compounds, was recognised as one of the most successful variations of the sol-gel method.[53]

More sophisticated, but efficient and time saving synthetic methods, such as the plasma spray technique, are constantly being developed. Wang *et al* considered this process to be

promising for mass production of YSZ nanopowders, so speeding up the commercialisation of SOFCs.[49] A certain modification was reported by Yuan *et al*, who used flame-assisted ultrasonic spray pyrolysis as an effective technique for producing a narrow particle size distribution of YSZ powders in the micron or submicron range.[54] In their studies, the powders were produced directly from an alcohol solution of metal precursors, whose concentration was found to affect their shape and final size.

A decrease of the ohmic resistance of a fuel cell can be achieved by the preparation of thinner electrolytes.[5, 26, 55] An electrolyte thickness of about 150 μm is generally accepted for self-supported planar SOFCs and might be even smaller for supported electrolytes.[14, 56, 57] Lao *et al*, stated that dense YSZ electrolyte films on the order of 100 nm can be successfully fabricated using a radio frequency-sputtering technique.[58] It should be noted, that the reduction of electrolyte thickness also contributes to lower the production costs of fuel cells. Moreover, thin electrolytes can be fabricated using low-cost methods. Zhao *et al* in their work optimised the screen-printing technique and successfully produced 16.5 μm dense SDC films on an NiO-SDC support.[57]

1.3.2.3 Interconnects

Individual cells must be combined in stacks to generate the desired voltage and power by interconnects. They act as the electrical contacts between individual fuel cells. When connecting the cathode of one cell to the anode of the next (series connection), they must protect the cathode from the reducing atmosphere at the anode of the next cell, and *vice versa*. To avoid mixing of fuel and oxygen, interconnects must be non-porous. They must also be inert with respect to other fuel cell components. The basic material of choice is rare earth chromite (e.g. $LaCrO_3$) doped with Mg, Ca or Sr in order to improve its electronic conductivity and overall processing.[5, 26, 59, 60] Calcium doped yttrium chromite has also been investigated as an alternative material to the former. Unfortunately, both types contribute to the high cost of the fuel cell system. Currently, the strong economic motivation to use traditional metals is promoting the development of SOFCs operating at low and intermediate temperatures at which the application of nickel based alloys (at 900°C) or ferritic steels (below 800°C) as well as stainless steel (below 700°C) becomes possible.[8, 61] The last two materials are comparatively inexpensive and readily available.

1.3.3 Review of selected electrolyte materials

According to many studies, Yttria-stabilised zirconia (YSZ) and Samarium-doped ceria (SDC) are considered to be reliable candidates for the electrolytes in SOFCs.[32] These two materials were subjected to detailed analysis in this thesis, with particular reference to the starting particle size of powders used in their preparation step. Both YSZ and SDC electrolytes still experience some problems mostly associated with their long-term stability in fuel cell operating conditions, so their further development continues.[18]

1.3.3.1 Zirconia-based electrolytes

The presence of dopants was found to be necessary to improve the physical properties of pure zirconia. The most important dopants of zirconia for electrolyte applications are yttrium oxide (Y_2O_3), scandium oxide (Sc_2O_3), calcium oxide (CaO) and ytterbium oxide (Yb_2O_3).[62] Doping of pure zirconia stabilises its less thermodynamically stable phase at low temperatures. As a result, a new zirconia-based composition becomes an ionic conductor.

Zirconia (ZrO_2) is a white, crystalline powder. It can also occur as a single crystal, which is an extremely refractory material of a low thermal conductivity, high toughness and density. It exhibits an inertness to corrosion at temperatures up to 2400°C, and is resistant to molten metals. There are three common crystal structures of ZrO_2, which are presented in Figure 1.4.

Figure 1.4 Cubic (a), tetragonal (b) and monoclinic (c) crystalline forms of ZrO_2.[63]

Pure zirconia has a monoclinic crystal structure at low temperatures and it undergoes a transition to tetragonal (at ~1050°C) and then to cubic (at ~2350°C) phases with increasing temperature. A volume expansion of ~3-5% occurs when the temperature decreases and the material experiences return phase transformations. The tetragonal to monoclinic phase change results in cracking of ZrO_2 pellets due to the very large mechanical stresses induced. The phase diagram, which represents transitions in the yttria-zirconia system, is provided in Figure 1.5.

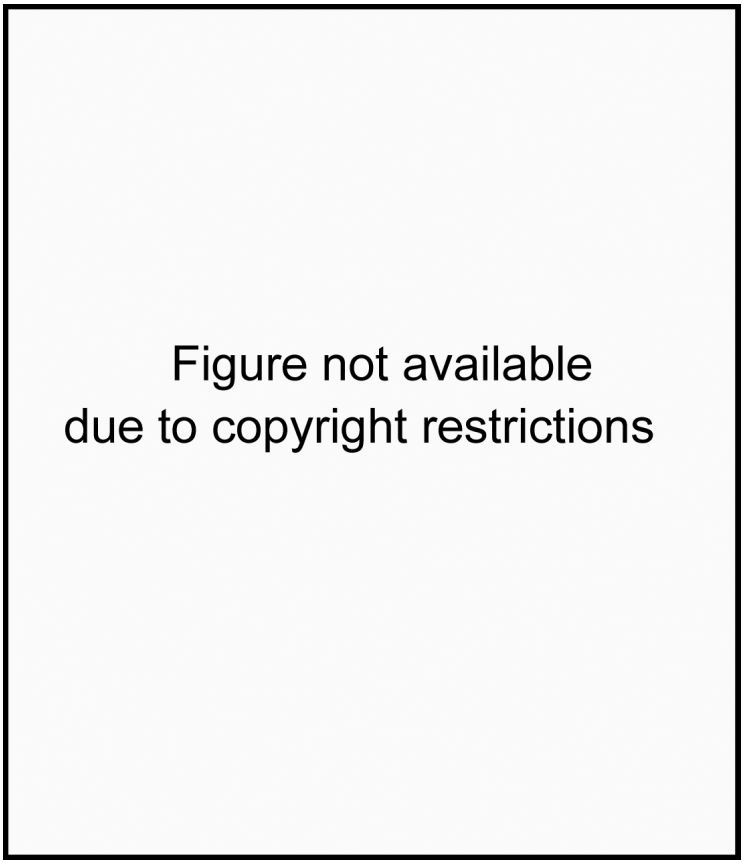

Figure 1.5 Y_2O_3-ZrO_2 phase diagram (M, T, C denote the monoclinic, tetragonal and cubic phases respectively).[64]

ZrO_2 is doped with Y_2O_3 to give YSZ in order to stabilise the crystal phase at lower temperatures. The addition of yttria stabilizes the tetragonal and then the cubic structure, so the harmful processes that occur in ZrO_2 during cooling are avoided.

One of the major advantages of YSZ is its high ionic and negligible electronic conductivity. The substitution of the Zr^{4+} by Y^{3+} results in formation of oxygen ion vacancies, which maintain the charge neutrality of the material. The defect reaction (Eqn. 1.1) is often presented in the Kröger-Vink notation:

$$Y_2O_3 \xrightarrow{ZrO_2} 2Y'_{Zr} + 3O_O^{\times} + V_O^{\bullet\bullet} \quad \textbf{(1.1)}$$

As a result, one oxygen vacancy with double positive charge ($V_O^{\bullet\bullet}$), three oxygen ions on normal O sites with neutral charge ($3O_O^{\times}$) and two yttrium ions with single negative charge ($2Y'_{Zr}$) are created for one mole of Y_2O_3. The defect structure is presented in Figure 1.6.

Figure 1.6 Defect structure of YSZ.[63]

Figure 1.7 shows how the concentration of the selected dopants affects the conductivity of zirconia-based electrolytes. It is clearly seen that the ionic conductivity curves possess characteristic maxima for each doped zirconia electrolyte and no longer increase after reaching a specific value. The highest values were found for scandia-stabilised zirconia (ScSZ) and ytterbia-stabilised zirconia (YbSZ). However, these materials are not widely used due to high costs.[65] In addition, a phase transformation, which results in a decrease in ionic conductivity during long-term operation of ScSZ, was reported by Yamamoto.[66]

In the case of YSZ, the ionic conductivity is related to the yttria content. Generally, the increase of percentage of Y_2O_3 causes an increase in the concentration of oxygen vacancies. It has been reported in the literature, that the ionic conductivity for YSZ electrolytes exhibits a maximum at around 8 mol% Y_2O_3, as it is stabilised in the symmetrical cubic phase [8, 62, 67] It has also been noted that usage of nanocrystalline powders could result in higher ionic conductivity.[68, 69]

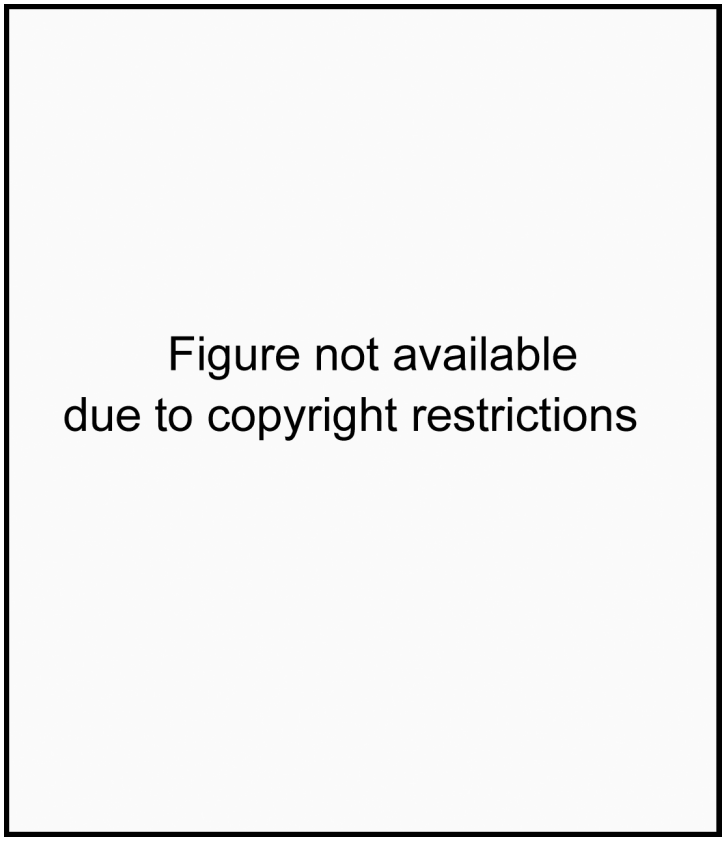

Figure 1.7 Ionic conductivity of zirconia doped with different oxides at 800°C.[70]

Mayo *et al* studied grain and particle size effects on the phase transformations in lightly yttria-stabilised zirconia systems.[71] The authors observed certain shifts in the Y_2O_3-ZrO_2 phase diagram, which correlated with a systematic decrease in tetragonal to monoclinic transformation temperature with decreasing particle size. They also suggested the improvement of the YSZ phase diagram by including crystallite/grain size as a third variable of extreme importance.

Such aliovalent doping not only enables the electrolyte to be stable during thermal cycles to the high temperatures associated with fuel cell operation, but is also responsible for introducing very high levels of oxygen ion conductivity into the material, as mentioned previously in this chapter. It should be remembered that the presence of either the mixture of monoclinic and cubic phases or the mixture of tetragonal and cubic phases is also possible during the thermal treatment of lightly yttria-stabilised (or 'partially-stabilised') zirconia electrolytes.

1.3.3.2 Ceria-based electrolytes

Ceria is the metal oxide of the most abundant rare-earth element, cerium. This fact must favourably contribute to the price of the starting materials based on Ce. CeO_2 exhibits face centered cubic (fcc) crystal structure and no phase transformations occur under atmospheric conditions. Cerium (IV) oxide usually appears as a pale white-yellow, slightly hygroscopic powder. The most stable form under atmospheric conditions is CeO_2, however it easily undergoes reduction to a lower oxidation state under reducing conditions to give Ce_2O_3. This feature makes ceria useful in a number of applications. Apart from the important ceria usages in catalysis and in fuel cell technology, the other common practical applications include gas sensors, UV absorbents, abrasives and glass polishing material. For application in SOFCs electrolytes, the problem of electronic conductivity above 700°C (due to the variable oxidation state of cerium) and stability of Ce^{4+} under reducing atmosphere (at low oxygen partial pressure) must be overcome.[29] This is achieved to a degree by doping ceria with rare-earth aliovalent elements, whose radii are smaller than host Ce^{4+}. The rare earth metal oxides such as samarium oxide (Sm_2O_3), gadolinium oxide (Gd_2O_3) and neodymium oxide (Nd_2O_3) were reported to be effective CeO_2 dopants.[28, 72] Similarly to YSZ, the introduction of aliovalent cations in ceria lattice, i.e. Sm^{3+}, gives rise to oxygen vacancies as charge compensating defects. However, this doping process results in a neutralisation of the electronic conductivity of ceria, which is already a good ionic conductor in its cubic phase. The defect reaction in the case of samarium can be written in Kröger-Vink notation (Eqn. 1.2)

$$Sm_2O_3 \xrightarrow{2CeO_2} 2Sm'_{Ce} + 3O_O^X + V_O^{\bullet\bullet} \qquad \textbf{(1.2)}$$

Ceria-based compounds were found to possess higher ionic conductivity than stabilised zirconia materials, when compared in the same, intermediate-temperature range. They are also reported to be more active for the oxidation of hydrocarbon fuels.[55]

The conductivity enhancement in this fluorite-structured material, as reported by Mogensen *et al*, is attributed to the minimal difference in the ionic radii between the host Ce^{4+} and the dopant cation.[73] Eguchi *et al* found that ionic conductivity measured at 800°C for selected lanthanide-doped cerium oxides (Figure 1.8) at first increased and then decreased across the dopant series from Yb to La, peaking at Sm. Indeed, Sm and Gd-doped ceria solid solutions are reported to possess among the highest values of oxygen ion conductivity.[74] Some scientists report that SDC exhibits the highest ionic conductivity of the rare-earth metal doped ceria solid solutions at the same dopant concentration.[75, 76] For example, Balazs *et al* reported

the highest value of 0.012 $S \cdot cm^{-1}$ at 600°C for $Ce_{0.8}Sm_{0.2}O_{1.9}$ among a series of rare-earth doped cerium oxides prepared by a solid state method.[77] However, some of current research is directed towards application of 10GDC as a state-of-the-art electrolyte material.[34, 78]

Figure 1.8 Dependence of ionic conductivity for $(CeO_2)_{0.8}(LnO_{1.5})_{0.2}$ at 800°C on a radius of dopant cation; adapted from Eguchi *et al.*[79]

The effect of composition and synthetic method on the ionic conductivity of SDC electrolytes was investigated by Shemilt *et al.*[80] 5 and 10 mol% Sm_2O_3-doped ceria powders were prepared by high energy milling. Sintering of the green bodies occurred at 1550°C for 2h in air, resulting in >98% of theoretical density regardless of the composition. Bulk and grain conductivity were found to be higher for $Sm_{0.1}Ce_{0.9}O_{1.95}$.

The sol-gel method was applied by Jung *et al* in preparation of SDC powders in three variants.[81] Starting metal salt solutions were mixed with ammonia and the final precipitate was divided and treated separately with water, ethanol and octanol. The biggest improvement in homogeneity compared to traditional solid state methods, with the highest densities of 98% theoretical, was achieved in the octanol modified synthesis. Jung *et al,* in different early paper, also studied the effect of temperature and Sm concentration on ceria-based solid solutions.[82] They found the highest conductivity of 0.56 $S \cdot cm^{-1}$ at 800°C for the $Sm_{0.2}Ce_{0.8}O_{1.9}$ composition prepared by a sol-gel method and confirmed oxygen vacancy mechanism as a main contribution to the total ionic conductivity.

The glycine-nitrate method was used by Peng *et al* in studies of the sintering and electrical properties of 10 mol% Sm_2O_3-doped CeO_2.[83] Different glycine/metal ratios were employed in

the precursor solution with an optimum reported at 1.7 for the highest density of ~95% and conductivity of 0.011 $S \cdot cm^{-1}$ at 600°C. This technique was reported to prevent selective precipitation of metal cations due to formation of complexes with glycine. However, a high sintering temperature of 1500°C was still required for SDC pellet densification.

The implementation of citric acid as a complexing agent for cations, in comparison to the sol-gel methods, was found to be a successful solution in the preparation of doped ceria powders.[84-86] This method was reported to produce amorphous metal citrates which, if they are subjected to thermal decomposition, lead to ceria-based solid solutions of high chemical homogeneity. Single phase homogenous electrolyte materials of nanosized particles were prepared using the citrate complexation route by various groups.[87, 88] Recent developments include modifications of the sintering process by introducing additional sintering steps,[89] use of sintering additives and the preparation of novel compositions of co-doped ceria.[47, 90, 91] Omar *et al* reported the grain conductivity of $Sm_{0.075}Nd_{0.075}Ce_{0.85}O_{2-\delta}$ to be 30% higher than that of $Gd_{0.1}Gd_{0.9}O_{2-\delta}$ at 550°C.[47] An increase in ionic conductivity of co-doped ceria was observed also by Liu *et al*.[90] The value of 0.012 $S \cdot cm^{-1}$ for $Ce_{0.8}Sm_{0.1}Nd_{0.1}O_{1.9}$ composition was measured at 500°C. The co-doping effect was also studied by Sha *et al* on $Ce_{0.8}Sm_{0.1}Y_{0.1}O_{1.9}$,[92] who revealed oversintering effect in pellets processed above 1400°C, which negatively affected ionic conductivity. However, still better ionic characteristics were noticed for such composition sintered below that temperature, than for (singly) doped SDC pellets. It seems that the increasing trend in the number of dopants is unavoidable and this is likely to lead to an increasing number of publications in this area.

1.4 Catalysis and ceria

Catalysts are any element or chemical compound which increase the rate of a chemical reaction but which are not consumed by it. They might be delivered in the same phase (homogeneous catalysis) or in a different phase (heterogeneous catalysis) from the reactants. The majority of chemical reactions which occur in industry are heterogeneously catalysed. One of the main factors considered in evaluation of a catalyst is its activity. It provides information on the rate of a transformation achieved in a catalytic reaction, usually expressed per gram or per unit surface area of catalyst. High specific surface area and high initial dispersion of the catalytically active phase are therefore important in heterogeneous catalysts, as is resistance to deactivation by loss of surface area or poisoning by accumulated impurities.[93] Another important parameter is the selectivity of a catalytic process to the desired

product. This is usually expressed as the rate of production of the desired product divided by the rate of production of all products.

A close understanding of the constituent processes occurring in heterogeneous catalysis is needed since they play a key role in many chemical reactions. Diffusion of the reactants to the catalytic reaction site and their adsorption on the surface take place at first. Then, the main reaction occurs, after which desorption and diffusion of the products away from the active site occur. These diffusion processes often limit the kinetic rate of reaction. Rate of reaction is also affected by the concentration of the active sites, which is related to the physical and chemical nature of the catalyst. Deactivation of a catalyst is also common and can occur by a number of mechanisms including sintering (loss of specific surface area), fouling by impurities and poisoning by irreversible adsorption of impurities or by-products on the surface of the catalyst.

One industrially important family of catalyst are those based on ceria, because of its excellent oxygen exchange properties.[94, 95] It is well known that the catalytic properties of ceria can be improved by doping with some rare earth metals. However, the best results are reported, if ceria-based oxides with high surface area are employed as a support for catalytically active noble metals such as Au, Pt, Pd, Rh, Ir or Ru.[96-99] If these are also provided at nanoparticulate dimensions, an excellent dispersion of such metals can be achieved. Low loadings of noble metals can be employed, decreasing the total cost of catalyst fabrication. The dispersion of noble metals is usually performed by impregnation methods. The incipient wetness impregnation technique is based on incorporation of a volume of active metal solution into the solid support equal to the pore volume of the support. Due to capillary action, the organic or aqueous precursor solution fills up the pores. Drying and/or a calcination step are required in order to remove the solvent and deposit the active phase on the surface of support.

Three-way catalysts (TWCs) for automobile exhaust gas converters are a good example of the application of ceria-based materials in catalysis.[100] In these, CO, NO_x and unburned hydrocarbon emissions in petrol and diesel engines are largely eliminated. The reduction of nitrogen oxides to nitrogen and oxygen (Eqn. 1.3), the oxidation of carbon monoxide to carbon dioxide (Eqn. 1.4) and the oxidation of hydrocarbons to carbon dioxide and water (Eqn. 1.5) are achieved.

$$2NO_x \rightarrow xO_2 + N_2 \quad \textbf{(1.3)}$$

$$2CO + O_2 \rightarrow 2CO_2 \quad \textbf{(1.4)}$$

$$C_xH_{2x+2} + [(3x+1)/2]O_2 \rightarrow xCO_2 + (x+1)H_2O \quad \textbf{(1.5)}$$

The efficiency and stability of TWCs have been increased by development of noble metal catalysts supported on ceria oxides.[101, 102] A further improvement on red-ox processes in TWCs was found to be possible by use of CeO_2-ZrO_2 solid solutions as the support.[85, 103] Very recent studies are involved in application of noble metals supported on ceria-zirconia nanotubes.[104]

Ilieva *et al* studied reduction of NO_x by CO over Au catalyst supported on CeO_2 and CeO_2-Al_2O_3.[105] The addition of alumina (up to 20 wt%) led to enhanced oxygen vacancy formation in ceria, however a slight increase of Au particle size was observed. Wang *et al* worked on CO oxidation and successfully applied Cu on an SDC-alumina support.[106]

The steam reforming of methane (SRM) and other hydrocarbons has been recognized for many years as the main route to global H_2 production (Eqn. 1.6).[107] The water gas shift reaction (WGS) complements the SRM process, because H_2 is additionally produced in an exothermic reaction of CO and water vapour (Eqn. 1.7).

$$CH_{4(g)} + H_2O_{(g)} \rightarrow CO_{(g)} + 3H_{2(g)} \quad \textbf{(1.6)}$$

$$CO_{(g)} + H_2O_{(g)} \rightarrow CO_{2(g)} + H_{2(g)} \quad \textbf{(1.7)}$$

WGS occurs commercially in two steps, with the help of catalysts such as transition metal oxides, e.g. Fe_3O_4, Cu/ZnO. The first step employs a temperature range of about 350-600°C, while the second is performed at 150-300°C, depending on the catalyst. The interest of many scientific groups all over the world has been attracted to replacing traditional catalysts, which are sensitive to impurities and require some special activation procedures. In addition, the lowering of reaction temperature and/or increase in H_2 productivity could be made possible by application of new catalysts, such as ceria-based solid solutions.[108, 109]

Andreeva *et al* studied the properties of gold catalysts dispersed on ceria doped with a range of rare earth metals (Y, Sm, Gd and Yb) for the WGS reaction.[110] Two preparation methods of the supports were investigated: co-precipitation by K_2CO_3 and mechanochemical UV activation. Sm- and Yb-doped ceria supports prepared by the second method, with 2 wt% Au impregnated from Au^{3+} complexes suspended in water, resulted in the highest catalytic activity for the WGS reaction. The authors reported that single- or double-phase catalysts were formed as a result of the two different preparation methods. TEM results showed an Au particle size of 2-3 nm regardless of the synthetic route.

Saeki *et al* worked with microcrystalline Ru, Rh, Ir, Ni and Pt metals supported on SDC for application in IT-SOFCs.[96] A standard impregnation technique for the metal salt solutions

(2 wt% metal loadings) on SDC powders of more than 100 μm particle size was employed. The best performance was ascribed to Ru and Ir supported on SDC, as observed in CH_4 conversion experiments.

Due to the fact that the SRM reaction is strongly endothermic and occurs at the temperature range of 700-1100°C, some alternative ways of H_2 generation have been investigated. The reforming of methanol seems to be a promising solution and the benefits of such a fuel are widely accepted.[111] One of them includes the ability of methanol production from a variety of carbon-based feedstocks (i.e. natural gas, coal, biomass). The reforming of methanol (Eqn. 1.8) is of particular interest in the light of fuel cell technology, where pure H_2 is often required, for example in PEMFCs.

$$CH_3OH_{(l)} + H_2O_{(v)} \rightarrow CO_{2(g)} + 3H_{2(g)} \quad \textbf{(1.8)}$$

The steam reforming of methanol can be catalysed by ceria-supported noble metals. One of the most catalytically active noble metals for the methanol reforming reaction is palladium.

Gomez-Sainero *et al*, in studies on Pd deposited on three transition metal oxides for reforming of methanol investigated the role of the support.[112] These included commercially available CeO_2, Sm_2O_3 and one composition prepared by solid state reaction of these two oxides, $(CeO_2)_{0.8}(Sm_2O_3)_{0.2}$. H_2PdCl_4 solution was used for impregnation of 2 wt% of Pd on these supports. The catalytic activity results showed the Pd/Sm_2O_3 catalyst was inactive towards CH_3OH decomposition. Moderate activity was noticed for Pd-supported on CeO_2, while methanol conversion up to 72% was obtained for the mixed oxide support. It was concluded that the preparation method, which employed strong acid media could affect a proper deposition of noble metal on the samaria support. The presence of a new mixed phase of highly dispersed Pd and Sm_2O_3 was speculated. The authors also suggested that the Pd deposited on the $(CeO_2)_{0.8}(Sm_2O_3)_{0.2}$ support was mainly associated with the Sm_2O_3 phase in the catalyst prepared in this way.

In relation to this paper, Baker *et al*,[113] performed High Resolution Transmission Electron Microscopy (HRTEM) studies on $Pd/(CeO_2)_{0.8}(Sm_2O_3)_{0.2}$ and observed that a beneficial hierarchical nanostructure had developed. Pd nanoparticles were supported on Sm_2O_3 crystals and then these were dispersed over the surfaces of larger CeO_2 particles. The reprecipitation of a semiamorphous phase containing Pd, Sm and O during the impregnation step, followed by crystallisation of Pd nanoparticles on Sm_2O_3 crystallites, was suggested by the authors to give rise to this structure.

Laosiripojana *et al* studied the effect of specific surface area (SSA) on the activity of nanoparticulate CeO_2 catalysts for CH_3OH decomposition.[93] Prior to the measurements, two commercial cerium oxides were calcined at 1000°C for 6 h, resulting in powders of 8 and 24 $m^2 \cdot g^{-1}$ SSA. Their results showed considerably higher decomposition rates over the higher surface area ceria powders.

In the light of this review, the preparation method of ceria-based supports for noble metals is a key parameter for catalytic methanol conversion to hydrogen. More efficient catalysts are expected to be developed if high purity and high surface area supports can be synthesised. In this connection, Pd-supported on nanoparticulate SDC supports prepared by several impregnation techniques are investigated in Chapter 6 of this thesis.

CHAPTER II – **ANALYTICAL TECHNIQUES**

2. Analytical techniques

This chapter provides an overview of the analytical methods used for characterisation of the materials investigated during these PhD studies. The general principles related to all techniques are outlined. In addition, typical designs of the instruments are described and some of these are presented schematically.

2.1 X-ray Diffraction

X-ray Diffraction (XRD) is one of the most important analytical methods used in solid-state chemistry. A solid can be described either as amorphous with randomly arranged atoms or crystalline with atoms arranged in a regular manner. The latter are built up of repeating elements, the unit cell, which are the smallest volume element that can represent the crystal structure. Both single crystal or polycrystalline materials such as powders can be analysed. About 95% of solid materials are classified as crystalline and XRD is a versatile tool, which allows for their quick, non-destructive and repeatable characterisation. The identification of crystal phases is possible due to the interaction between incident X-rays and the electrons of the matter through which the radiation passes. As each crystalline material has its own atomic structure, and therefore diffracts X-rays in a unique way, a characteristic pattern with peaks of various intensities results. The identification occurs by a comparison of the diffraction pattern obtained with relevant Powder Diffraction Files (PDF) stored in the database of the International Centre for Diffraction Data (ICDD).[114] The phase purity can be easily determined, because mixtures of different materials with different crystal phases in the same material will contribute their own unique set of peaks to the total XRD pattern.

X-rays are short wavelength electromagnetic radiation within the range of 0.00001-100 Å. However, for diffraction studies wavelengths are limited to about 0.1-25 Å as this range corresponds well to the order of magnitude of interatomic distances observed in crystalline materials. A common method for the generation of X-rays is the bombardment of a metal target (e.g. Cu or Mo) by a beam of high-energy electrons. The electron beam ejects an electron from one of the metal core orbitals, so that an electron from a higher energy orbital replaces the ejected one and emits radiation. The X-ray spectrum is specific to the metal target and consists of a continuous background (white radiation) as well as a few intense peaks. The positions of these characteristic peaks are related to the energy difference between the electron shells involved in producing the X-rays. For example, the transition from the L to the K shell is labelled as K_{α}, while the M to K transition is designated as K_{β}. In addition, these transitions

may appear as unfavourable close doublets (usually at high 2θ angles), so especially $K_{\alpha 1}$ and $K_{\alpha 2}$ are distinguished for common anode materials.

An accelerating voltage up to 100 kV is used in a highly evacuated tube for X-ray generation. Interestingly, only about 1% of the electrical power can be converted to X-rays and the rest is released as heat, so an efficient cooling system is required. A single energy X-ray beam is necessary to carry out a diffraction experiment. This is achieved by a system of collimators, which restricts radiation from the source. The use of a relevant filter is also a common technique to obtain a monochromatic beam. Obviously, the intensity of the background must be reduced. The diffracted beam is detected by using an X-ray detector and two methods of data collection were developed. Usually the detector is scanned around the specimen in a circle to collect diffracted X-rays. A schematic of the experimental set-up with the instrument operating in reflection mode is presented in Figure 2.1(a). The incident X-rays reach the sample at various angles and penetrate only its top layer. In the transmission method, the incident beam passes through a thin sample, which is placed in a rotating sample holder (Figure 2.1(b)).

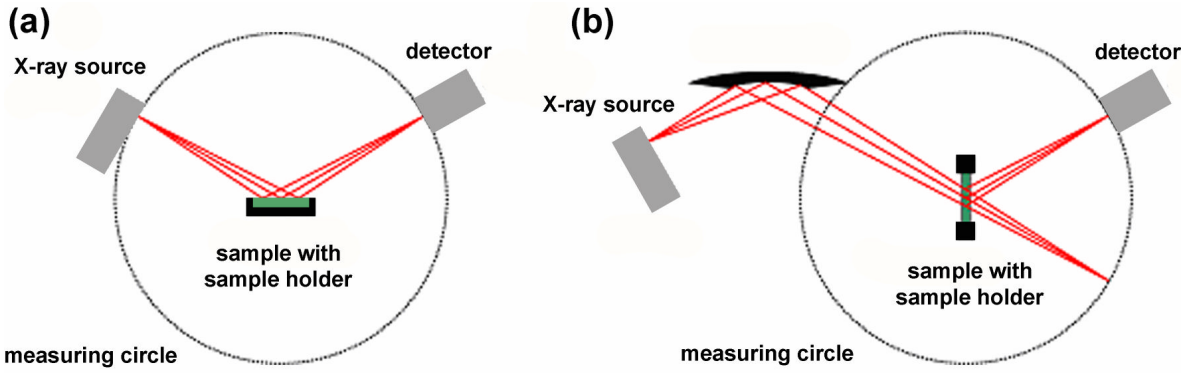

Figure 2.1 Schematic diagram of XRD experiment in (a) reflection and (b) transmission mode.

The scattered rays can be out of phase and cause destructive interference. They can also be in phase with each other, so that they interfere constructively. Diffraction is possible, because the distances between the scattering centres are of the same order of magnitude as the wavelength of the radiation. When an incident beam (always in phase) strikes a crystal surface at some angle θ, a portion is scattered by the layer of the atoms at the surface. The unscattered portion penetrates to the second and third layer of atoms, where the next fractions are scattered. The cumulative effect of this scattering is the diffraction of the beam as presented in Figure 2.2. The beam is diffracted from the parallel lattice planes at an angle, which depends on the spacing of the lattice. As each crystalline material possesses a number of lattice planes,

this results in a number of diffraction peaks, which appear in the pattern at specific diffraction angles. Miller indices are used for referring to lattice planes and allocating them to the corresponding family of crystallographic planes in the crystal system. Each family of symmetrically equivalent lattice planes, which have equal interplanar distances, are labelled with identical Miller indices using the reciprocal space lattice vectors (hkl).

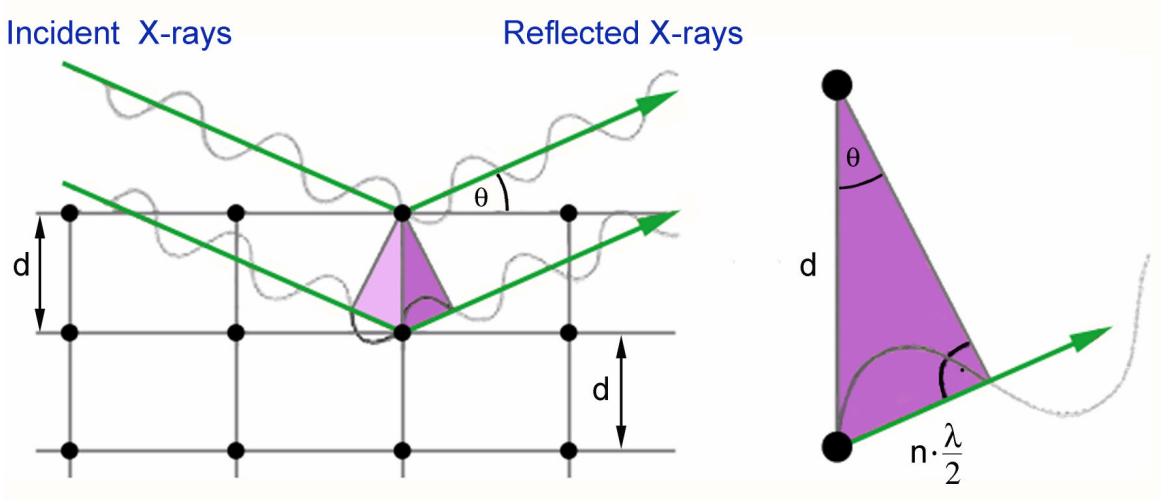

Figure 2.2 Schematic of incident and reflected X-ray beam.

The condition for constructive interference of the beam at angle θ can be expressed as Bragg's law (Eqn. 2.1).

$$n \cdot \lambda = 2 \cdot d \cdot \sin\theta \qquad \textbf{(2.1)}$$

n – an integer,
λ – the wavelength of the X-rays,
d – the distance between planes (d-spacing),
θ – the diffraction angle.

The diffraction peaks are usually represented on a plot of their intensity against 2θ diffraction angle. From Equation 2.1, the peak position and the X-ray wavelength can be used to determine the d-spacing. The latter can be expressed in terms of the unit cell dimensions for the crystal system under study. In the case of the cubic system considered in this work, the characteristic unit cell parameter (a) was obtained using Equation 2.2.

$$d = \sqrt{\frac{a^2}{h^2 + k^2 + l^2}} \qquad \textbf{(2.2)}$$

This equation was simplified to $a = d \cdot \sqrt{3}$ in order to calculate the lattice parameter using the main (111) peak.

2.2 Thermal methods

Thermal analysis is represented by a group of techniques, which uses a controlled temperature program during measurement of a physical or chemical change of a sample and its reaction products. These changes are mainly related to the mass, enthalpy and thermal expansion coefficient. This section covers the basics of four major techniques used in assessment of materials presented in this thesis – Thermogravimetry (TG), Differential Thermal Analysis (DTA), Differential Scanning Calorimetry (DSC) and dilatometry measurements.

2.2.1 Thermogravimetry

In thermogravimetric analysis (TG) the weight of a sample in a controlled gas environment is recorded continuously as a function of increasing temperature or time. If a plot of mass or mass percent as a function of time is prepared, a thermal decomposition curve can be constructed. In general, a typical instrument consists of a sensitive balance, furnace, purge gas system and microcomputer-based controller. The most important application of TG is related to the decomposition studies of many compounds with connection to such physical processes as desorption, sublimation or vaporisation. Therefore, the TG instrument is often coupled with a mass spectrometer to allow analysis of gaseous products.

2.2.2 Differential Thermal Analysis

Differential Thermal Analysis (DTA) is a technique, which measures the difference in temperature between a sample and a reference material, while both are subjected to a controlled heating programme. The temperature of the sample is usually increased linearly with time. The difference in temperature between the sample and the reference can be precisely recorded during the experiment as both possess separate thermocouples. The differential thermogram gives information on endothermic and exothermic processes which take place during the thermal treatment of a sample. In this way, it may provide information about dehydration, oxidation, reduction or change in crystal structure for many chemical compounds such as oxides, ceramics or catalysts.

2.2.3 Differential Scanning Calorimetry

The methodology of Differential Scanning Calorimetry (DSC) is similar to DTA. This technique allows however for direct measurement of enthalpy change since a different design

of the cell holding the sample and inert reference material is used. The difference in the rate of heat flow that is required to keep the sample and the reference at the same temperature is measured.

2.2.4 Dilatometry

Dilatometry is based on the measurement of the dimensional change of a sample as a function of temperature or time under negligible mechanical load. Information on the sintering behaviour of a sample such as sintering rate, sintering temperature, sintering duration or thermal expansion coefficient can be obtained. It is necessary to perform a correction run prior to sample measurement. In dilatometry, this is done by running the temperature programme with an alumina correction pellet of the same size as the sample. The results obtained from running an actual sample are then determined relative to the data from the correction run. The green pellet is positioned between two alumina spacers and placed in the sample holder tube. The thermocouple is attached as close as possible to the sample to measure the applied temperature during the experiment.

2.3 Brunauer-Emmett-Teller method

The specific surface area (SSA) is an important parameter in characterization of powders and can be defined as the accessible area of solid surface per unit mass or volume. The determination of SSA is possible by adsorption of a controlled amount of N_2 onto the surface of the specimen at a range of applied pressures. Usually, a sample must be preheated at ~120°C, and then degassed of foreign molecules prior to analysis. Near liquid nitrogen temperature is required for measurement. A physisorption isotherm is generated by plotting gas uptake against pressure (P/P_o).

In this thesis, measurements of SSA are based on the Brunauer-Emmett-Teller (BET) method. It applies to the linear section of the isotherm, which was very often limited to the pressure range 0.05-0.30. If a straight line plot is produced over that range, the amount of gas adsorbed for all the surface to be covered with a monolayer (V_m) can be derived, according to the BET equation:

$$\frac{P}{V_a \cdot (P_o - P)} = \frac{1}{V_m \cdot C} + \frac{C-1}{V_m \cdot C} \cdot \left(\frac{P}{P_o}\right) \qquad \textbf{(2.3)}$$

where: $y = \frac{P}{V_a \cdot (P_o - P)}$, $c = \frac{1}{V_m \cdot C}$, $m = \frac{C-1}{V_m \cdot C}$ and $x = \left(\frac{P}{P_o}\right)$

V_a – amount of adsorbed gas for infinite number of layers,
P/P_0 – relative pressure,
C – BET constant.

In the next step, SSA can be calculated using equation:

$$SSA = \frac{N_A \cdot A_M \cdot V_m}{m \cdot M} \quad \textbf{(2.4)}$$

N_A – Avogadro number,
A_M – area occupied by adsorbed molecule (16.2 Å for N_2),
m – mass of the specimen,
M – molar mass of the adsorbate.

2.4 Inductively Coupled Plasma Mass Spectroscopy

Inductively Coupled Plasma Mass Spectroscopy (ICP-MS) is a very powerful tool for trace elemental analysis with detection limits of parts per billion. It allows for simultaneous determination of elements with atomic mass ranges from lithium to uranium. It is based on combining a method of ionising the elements in the sample by means of plasma and a method of separating and detecting the ions using a mass spectrometer. Firstly, the plasma – a gas consisting of ions, electrons and neutral particles - is formed using argon. The energy required for this reaction is obtained by pulsing an electrical current in the wires that surround the Ar gas. Secondly, the sample must be introduced into the plasma containing a sufficient concentration of previously formed ions. For solid state materials, laser ablation is used. In this method, a laser is focused on the sample and creates a plume of ablated material, which can be swept into the plasma. The sample material is ionised in the plasma and the resulting ions are passed through a series of cones into the high vacuum mass analyser. The ions are separated and collected according to their mass to charge ratios. The intensity of a specific peak in the mass spectrum is related to the concentration of the element in the original sample.

2.5 Electron microscopy

Electron microscopy was developed due to the limitations of light microscopes and provides structural information of a sample over a wide range of magnifications. Much higher resolutions can be obtained by Scanning Electron Microscopy (SEM) and Transmission Electron Microscopy (TEM) than in optical microscopy because of the specific interactions between a high-energy electron beam and the electrons in the sample under study. The principles of the SEM and TEM techniques, which were used in this thesis, are presented in this section.

2.5.1 Scanning Electron Microscopy

Scanning Electron Microscopy (SEM) is a common technique, which allows surface characterisation of solid materials, for example fuel cell components. It provides topographic, morphological and compositional information of the specimen. Samples have a three dimensional appearance in SEM images as a result of the large depth of field possible with these microscopes. Therefore surface features, shape, size and the arrangement of the constituents of a sample can be determined. The data relevant to chemical composition (quantitative and qualitative analysis) can be obtained if the microscope is equipped with an X-ray detector.

The typical set-up of the SEM instrument is shown in Figure 2.3. The electron gun is responsible for thermionic generation of electrons, which are accelerated towards the sample by an anode held at a high voltage. The magnetic condenser and objective lens system serves to reduce the image to a final spot diameter on the specimen of 5 to 200 nm. Firstly, the beam passes through the condenser lens system, which is responsible for achieving the correct electron beam characteristics. Next, the electrons pass through a set of scan coils where, by varying the electrical signal, the electron beam can be moved across the sample. Finally, the magnetic objective lens focuses the scanning beam onto the area of interest in the sample. Large-capacity vacuum pumps and efficient cooling systems are necessary to run SEM instruments.

One limitation of SEM is the fact that the sample must be electrically conductive to avoid accumulation of electrical charge in the sample, which results in undesirable artefacts in the images. Therefore, it is common to apply a thin metallic or carbon film to the surface of poor conductors. Sputtering is usually used to deposit carbon or a metal – e.g. Au, Ag, Cr, Pt or Pd – from a target giving a uniform conductive surface coating of a few nm in thickness.

A number of different types of interaction between the beam electrons and the sample electrons can occur. Incident beam electrons can be absorbed into the sample losing their energy and causing another electron to be ejected (secondary electrons) as illustrated in Figure 2.4. Other electrons can be repelled from the surface by electrostatic forces losing only a small part of their energy (backscattered electrons). Additionally, Auger electrons, X-rays and cathodoluminescence phenomena may result from the influence of the incident beam electrons on the sample. The Auger electrons and emitted X-rays are characteristic of atoms in the specimen.

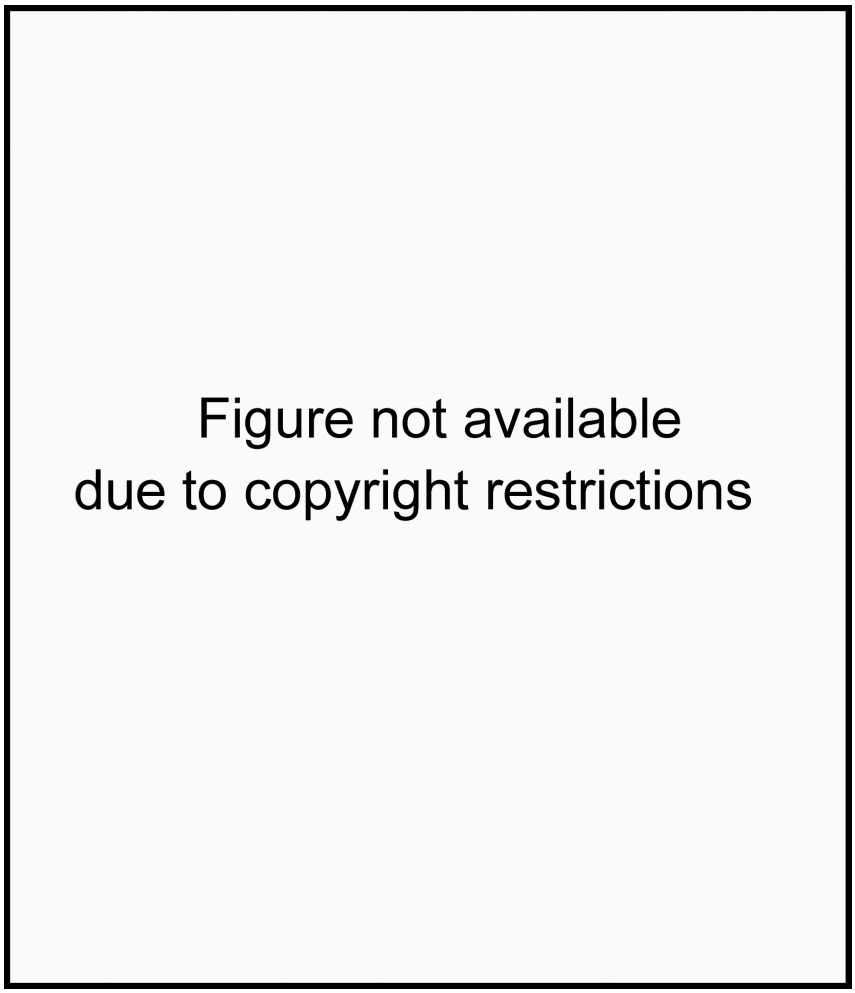

Figure 2.3 Schematic of a scanning electron microscope.[115]

Each of the previously mentioned effects can be utilised in surface studies, but the use of secondary electrons is the most common imaging method in the SEM. These electrons can be attracted to a positively charged detector. The signal is then amplified and converted to an image, which shows the three dimensional structure of the surface of the specimen.

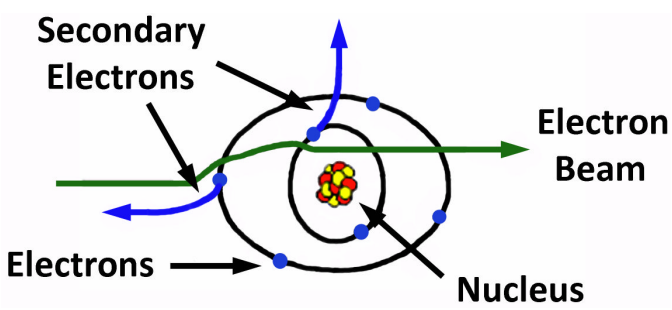

Figure 2.4 Schematic of the formation of secondary electrons.

2.5.2 Transmission Electron Microscopy

Transmission Electron Microscopy (TEM) is a powerful tool, which in contrast to SEM, provides more detailed information about the microstructure of thin specimens. The typical set-up of the TEM instrument with listed main components is presented in Figure 2.5.

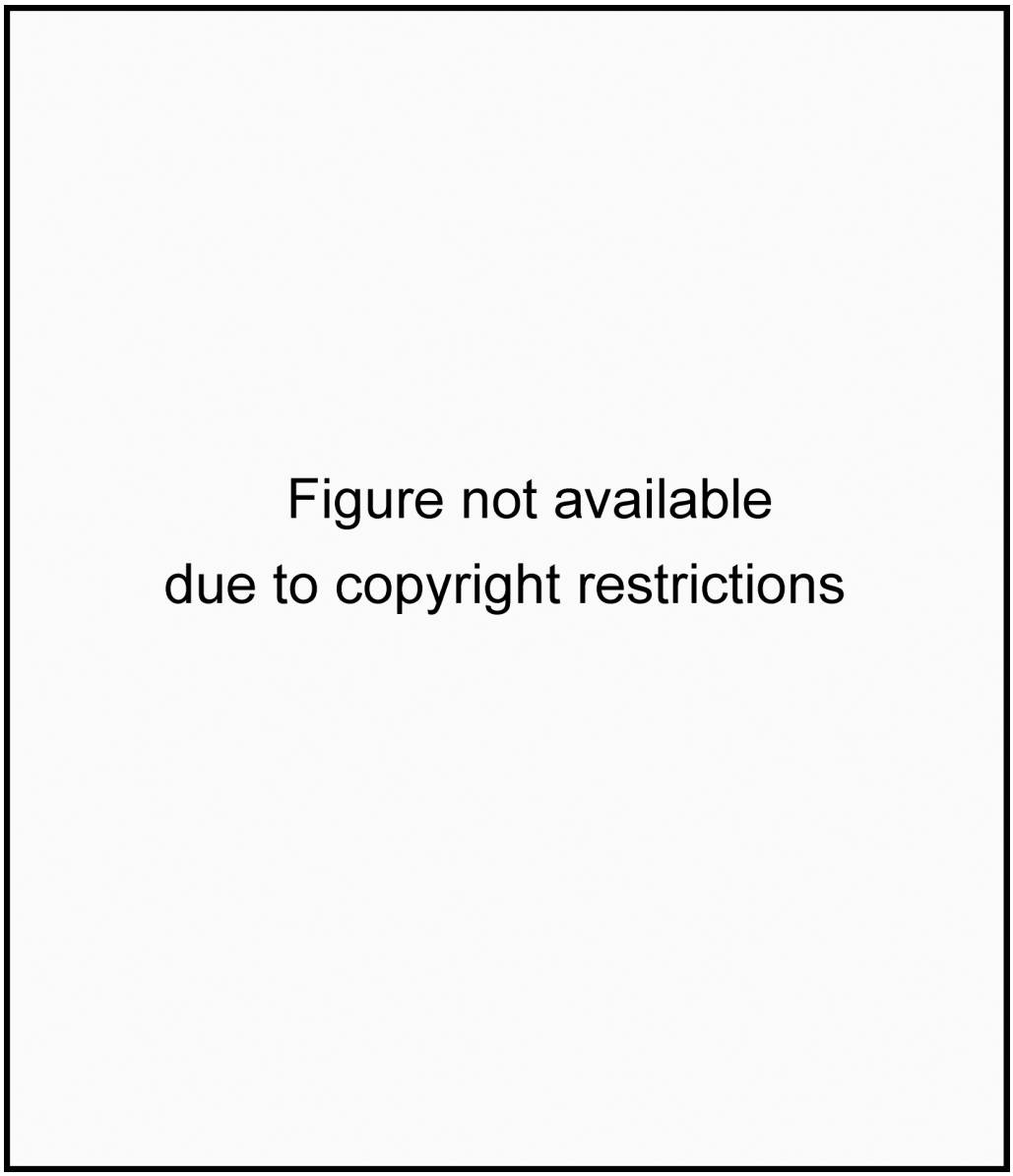

Figure 2.5 Schematic outlining the internal components of a typical TEM system, adapted from[116].

The emission of electrons occurs by a thermionic process from a cathodic filament, typically made of W or of LaB_6. The emitted electrons are converged by a negatively charged Wehnelt cylinder, forming a focused beam of electrons, which is accelerated towards the anode. Due to the high potential applied (typically 200 kV); the resulting high energy electron beam possesses a much shorter wavelength than visible light, according to Equation 2.5. Therefore, much higher imaging resolution can be obtained in the TEM instrument than in optical microscopy.

$$\lambda = \frac{h}{\sqrt{2 \cdot m \cdot E_k}} \tag{2.5}$$

λ – the wavelength (nm),
h – the Planck constant ($6.626 \cdot 10^{34}$ J·s),
m – the rest mass of the electron (g),
E_k – the kinetic energy (J).

A proper alignment of the beam is of extreme importance in order to obtain reliable data in the TEM experiment. The condenser lenses are used for additional alignment of the beam. The objective lenses concentrate the beam on the sample. All sets of electromagnetic lenses must be symmetrical and set correctly to provide a focused beam of electrons and minimise spherical and chromic aberrations as well as astigmatism phenomena. At lower magnifications, the image can be thought as being simply a magnified shadow of the sample, electrons being absorbed by the thick parts of the sample and allowed to pass through the thin parts and the areas where there is no sample. At higher magnifications, the interaction between the incident electron wave and the periodic crystal structure must be considered. An electron beam with a uniform current density irradiates a layer of atoms in the specimen. The atoms scatter the electrons, which cause the non-uniformity of the electron current density (above and below the atomic plane) and pass through the specimen. Two conditions may occur. If the objective current is increased (overfocus condition), the TEM will image a plane below the specimen causing the atoms to appear bright in the image. On the contrary, if the objective lens is weakened in order to image a plane just above the specimen (underfocus condition), the image will show the atoms appearing dark. This is the more desired imaging condition since there is a more direct relationship between the sample and the image. The interaction between the incident beam of electrons and the specimen depends on the sample thickness, its chemical composition and the accelerating voltage. The final beam, which leaves the sample, is then transformed by intermediate and projector lenses to form a phase contrast image on a viewing screen or in a camera.

2.5.3 Energy Dispersive X-ray Spectroscopy

The Energy Dispersive X-ray Spectroscopy (EDX or EDS) technique is a common technique in both SEM and TEM. It utilises X-rays generated by the interaction of the incident electron beam with the specimen. The energies of these emitted X-rays are characteristic of specific electron transitions in the atoms of the sample and therefore of the chemical elements present in the sample. These are collected by an additional detector and compositional information can be obtained within a specific selected area of the sample. In addition, compositional variations along a line – linescans and over an area – elemental maps can be recorded using the EDX technique.

2.6 Impedance Spectroscopy

Impedance Spectroscopy (IS) is a typical method used to study electrochemical systems such as electroceramics. One of the main advantages of IS is that an electrochemical cell can be represented as a purely electronic equivalent circuit model. The electrical properties of a material are analysed through a wide range of frequencies in order to find various conduction contributions, which are usually related to different structural parts of a sample. Therefore, in contrast to direct current (DC) theory, where the frequency equals 0 Hz, the alternating current (AC) theory must be applied. The impedance (Z) is the AC equivalent of resistance (R) and represents total opposition to the flow of electrons in the circuit.

In DC theory, the resistor is the only element which impedes the current. According to Ohm's Law, the resistance is defined by the simple equation:

$$R = \frac{E}{I} \tag{2.6}$$

E – the potential (V),
I – the current in (A),
R – the resistance (Ω).

In AC theory, capacitors and inductors also resist the flow of electrons. Equation 2.7 includes then impedance measured in ohms and is expressed below:

$$Z = \frac{E}{I} \tag{2.7}$$

Z – the impedance (Ω).

The total impedance in a circuit is the combined opposition of all elements. The inductors and capacitors contribute to the reactance of a system (X), which symbolises the sum of inductive (X_L) and capacitive (X_C) reactance (Eqn. 2.8).

$$X = X_L + X_C \tag{2.8}$$

The reactance varies with the frequency of the electrical signal and causes a phase shift between the current and voltage. Therefore, the resistance and reactance cannot be simply added to determine the impedance but they must be added as vectors as shown in Figure 2.6.

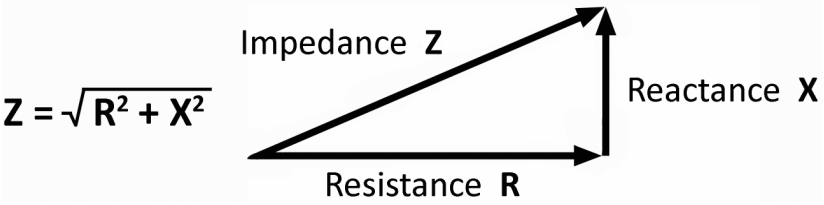

Figure 2.6 Schematic of the impedance vector.

In IS measurements, a small AC potential (E_t) is applied to the sample and can be represented as a function of time.

$$E_t = E_o \cdot \sin(\omega t) \tag{2.9}$$

E_t – the potential at time t,
E_o – the amplitude of the signal,
ω – the angular radial frequency ($\omega = 2\pi f$)

The applied signal causes the response of the current (I_t) shifted by the phase angle (φ).

$$I_t = I_o \cdot \sin(\omega t + \varphi) \tag{2.10}$$

According to Ohm's law, the impedance can be represented in terms of a magnitude (Z_o) and a phase angle (φ) as shown below:

$$Z = \frac{E_t}{I_t} = \frac{E_o \cdot \sin(\omega t)}{I_o \cdot \sin(\omega t + \varphi)} = Z_o \frac{\sin(\omega t)}{\sin(\omega t + \varphi)} \tag{2.11}$$

With Euler's relationship (Eqn. 2.12), the impedance can be represented as a complex function with resistance as the real part and reactance as the imaginary part.

$$\exp(j\varphi) = \cos\varphi + j\sin\varphi \tag{2.12}$$

$$E_t = E_o \exp(j\omega t) \tag{2.13}$$

$$I_t = I_o \cdot \exp(j\omega t - \varphi) \tag{2.14}$$

therefore,

$$Z(\omega) = \frac{E}{I} = Z_o \exp(j\varphi) = Z_o(\cos\varphi + j\sin\varphi) \qquad \textbf{(2.15)}$$

A typical representation of the impedance spectrum with the impedance vector |Z| is shown in Figure 2.7. The Nyquist plot represents real values on the x axis, while imaginary data is placed on the y axis.

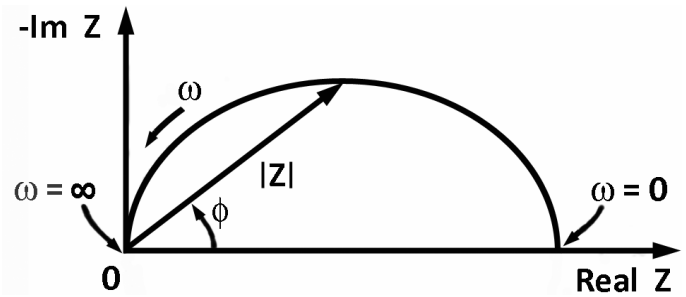

Figure 2.7 Nyquist plot for a simple electrochemical system.

The semicircle corresponds to one or more physical processes, which typically take place in specific regions of the sample. In many cases, Nyquist plots contain several semicircles which contribute to the total impedance of the sample. They are related to different areas of the electrochemical cell and can be analysed separately due to their different frequencies. Therefore, in a solid ionic conductor, for example, electrochemical processes within the grains, across the grain boundaries, charge transfer processes between the electrode and electrolyte and processes within the electrodes are often represented by different arcs in the same Nyquist plot. An example of such an impedance spectrum and its equivalent circuit model is presented in Figure 2.8.

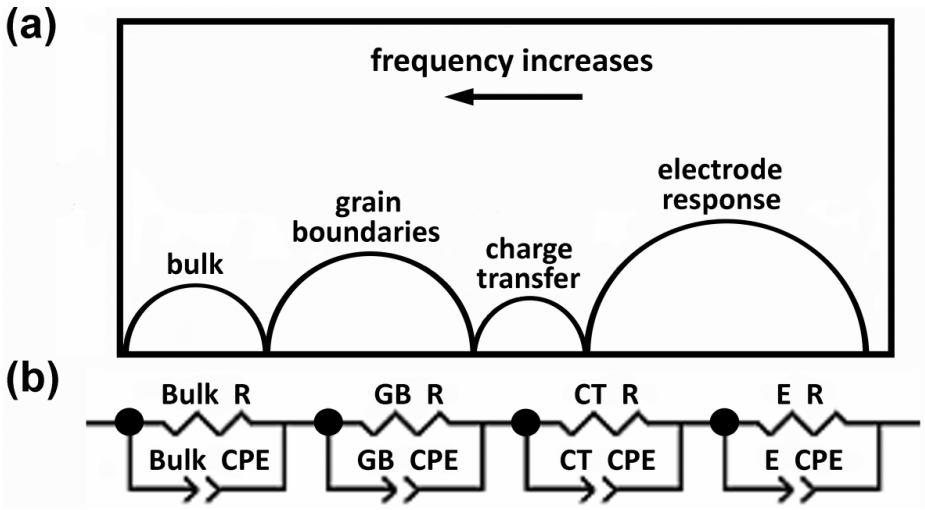

Figure 2.8 Complex impedance spectrum (a) and its equivalent circuit model (b).

The experimental data from the Nyquist plot can be processed using computer software, employing an appropriate model of the equivalent circuit, which possesses resistors, capacitors and inductors which form subcircuits which relate to the semicircles, and other features, in the IS spectrum. Since perfect capacitors do not exist, the use of constant phase elements (CPEs) in the equivalent circuit usually gives a more accurate fit. The impedance of a CPE is defined in Equation 2.16.

$$Z = \frac{1}{Z_0}(j\omega)^{-\alpha} \tag{2.16}$$

$1/Z_0$ – the admittance of the element,
α – an exponent (equal to 1 for a perfect capacitor).

Once all values of resistance related to each process in the cell are calculated, the conductivity can be found using following equation:

$$\sigma = \frac{L}{R \cdot S} \tag{2.17}$$

σ – the conductivity (S/cm),
R – the resistance (Ω),
L – the thickness (cm),
S – the area of electrode (cm^2).

In the case of solid electrolyte materials, the resistances of the bulk (grain) and grain boundary contribute to the total ionic conductivity. Arrhenius plots are often used to express the conductivities of total electrolyte or individual components in relation to temperature. The following expression is used for determination of their activation energies, usually with the rate constant, k, replaced by ionic conductivity, σ:

$$\ln k = \ln A - \frac{E_a}{RT} \tag{2.18}$$

k – rate constant,
A – pre-exponential factor,
E_a – the activation energy,
R – ideal gas constant (8.314 $J \cdot K^{-1} \cdot mol^{-1}$),
T – the absolute temperature.

The activation energy of bulk or grain boundary conductivity can be related to the activation energies required for oxygen ions to jump from one lattice site to another within a grain and from one grain to another, respectively.

2.7 X-ray Photoelectron Spectroscopy

X-ray Photoelectron Spectroscopy (XPS) is an analytical method used for characterisation of the surfaces of solids. It typically gives data from only the uppermost few atomic layers (0 to 50 Å) of a surface. It is an analysis technique of fundamental importance for many applications, for example in heterogeneous catalysis. In this field, as the surface of a catalyst is in contact with a liquid or gaseous phase, it may differ significantly from the bulk. XPS provides information on chemical composition and physical properties (e.g. oxidation state) while a surface is irradiated with monochromatic X-radiation. X-ray photons form a primary beam and its impact on the surface generates emission of a secondary beam, which is made up of electrons. The kinetic energy (E_k) of the emitted electrons is recorded by a spectrometer. E_k data is used to calculate the binding energy (E_b) of the electron according to Equation 2.19, where $h\nu$ represents the energy of the X-ray photon and w is a correction factor (work function) associated with the spectrometer.

$$E_b = h\nu - E_k - w \tag{2.19}$$

The XPS spectrum consists of a plot of electron counts as a function of binding energy (E_b). E_b is characteristic of the atom and orbital from which the electron is emitted. Therefore, the elements contained in a sample surface can be identified and quantified. The energy resolution of XPS is also often good enough to allow identification of different oxidation states, or coordination environments of a particular element. This allows information on the chemical environment of these atoms to be extracted from the XPS spectra.

CHAPTER III – **EXPERIMENTAL PROCEDURES**

3. Experimental procedures

Information on the preparation of the materials studied in this work is presented in the corresponding results chapter. Details of the preparation and investigation of materials based on YSZ micro- and nanoscale powders is given in Chapter 4, on SDC nanopowders in Chapter 5 and on Pd/SDC catalyst powders in Chapter 6.

3.1 X-ray Diffraction

In this work, the crystal structure of all samples was determined by room temperature X-ray powder diffraction. A Philips (PW 1710) instrument operated in reflection mode at 40 kV and 40 mA with CuK_α radiation was employed. A plate-type Aluminium sample holder containing a sample powder layer of uniform thickness was used. No Al phase-related peaks were detected in any pattern. High-grade silicon powder was used as an external standard to allow correction for instrumental broadening.

In an XRD experiment typical for all materials, data acquisition in standard runs was performed by scanning 2θ between 10° and 100° with a step length of 0.02° and at a rate of $1°\cdot min^{-1}$. In addition, more detailed information in the specific range of 2θ = 70–77° was obtained only for YSZ samples by employing the same step, but a lower speed of 0.1°/min. STOE WinXPOW software (v.1.04) was used to determine lattice parameters and crystal structure of the samples investigated. Additionally, some XRD patterns were fitted using Rietveld procedures using the FullProf programme.[117]

The determination of crystallite size from analysis of peak broadening was performed for SDC electrolyte powders using the Scherrer equation (Eqn. 3.1). The main (most intense) diffraction peak was used to calculate the average crystallite size.

$$D_{XRD} = \frac{0.9 \cdot \lambda}{\beta \cdot \cos\theta} \qquad \textbf{(3.1)}$$

λ – the wavelength of the X-rays (nm),
θ – the diffraction angle,
β – the corrected full width at half maximum (FWHM) intensity, where:

$$\beta = \left(\beta_m{}^2 - \beta_s{}^2\right)^{1/2} \qquad \textbf{(3.2)}$$

β_m – the measured FWHM intensity of the main reflection,
β_s – the measured FHWM intensity of the standard silicon sample (0.15º)

Full width at half maximum intensity calculations were performed using Origin software.

3.2 Thermal methods

3.2.1 TG, DTA/DSC experiments

The thermal behaviour of all precursor gels was investigated by TG and DTA/DSC using a Netzsch STA 449C Jupiter instrument, which is schematically presented in Figure 3.1. The heat flow and weight change of samples placed in crucibles were measured in air (50 ml·min^{-1}) from 25ºC to 800ºC at a heating rate of 5ºC·min^{-1}. In addition, these experiments were repeated in flowing oxygen to allow simultaneous analysis of off-gases by mass spectrometry (MS). A correction run with empty crucibles was performed before analysis of a sample. All data was analysed using Netzsch Proteus-Thermal Analysis software package, version 4.8.5.

Figure 3.1 (a) Cross-section of the Netzsch STA 449C Jupiter, (b) TG and DTA crucibles.[118]

3.2.2 Dilatometry

The sintering properties of compacted samples were studied using a Netzsch DIL 402C push-rod dilatometer, which is presented in Figure 3.2. Due to the different characteristics of the materials tested – YSZ and SDC – different temperature programs were applied, the details of which are provided in Sections 4.3.3 and 5.3.7, respectively. Air (50 ml/min) was employed as the purge gas in all experiments.

Figure 3.2 Schematic of the DIL 402C dilatometer: (a) cross section and (b) sample holder.[119]

3.3 Brunauer-Emmett-Teller method

Brunauer-Emmett-Teller analysis (BET) by nitrogen adsorption-desorption were performed on powders using a Micrometrics ASAP 2020 instrument in order to obtain values of specific surface area (SSA). All samples were pre-treated at 120°C for 6 h. The Micrometrics TriStar software V1.01 was used to obtain automatically results of specific surface area.

3.4 Inductively Coupled Plasma Mass Spectroscopy

Elemental analysis was performed for all materials investigated in this thesis using an AGILENT 7500 Series ICP-MS instrument (New Wave Research Products), equipped with a UP-213 Laser Ablation System. The powder samples were blended with a Teflon standard in order to form a pellet prior to analysis supported by laser ablation. All sintered pellets were analysed using this method without any additional preparation procedures.

3.5 Electron microscopy

3.5.1 Scanning Electron Microscopy

SEM images, which are presented in this thesis, were obtained with two microscopes. A Philips XL30 ESEM instrument with a field emission gun was employed for microstructure studies of YSZ pellets and SDC nanopowders. The details of these analyses, including sputter coating and thermal etching aspects of surface preparation of the samples, are specified in the relevant results chapters. The other micrographs were obtained using a JEOL JSM-5600 instrument and this was intensively used for ceria samples. Conductive carbon sticky pads were used to attach all specimens to the sample holder in both microscopes. Grain size analyses were performed using either the Scion Image (version Alpha 4.0.3.2) or ImageJ (v. 1.42d) software packages and further details are given in the respective results sections.

3.5.2 Transmission Electron Microscopy

All materials investigated in this work were analysed in a JEOL JEM-2011 HRTEM instrument operated at 200 kV. Elemental analysis was performed using an Oxford Instruments X-ray analysis detector (ISIS 300 EDS) in order to obtain the chemical composition of each sample and assess for potential impurities. The DigitalMicrograph v.3.3.4 (Gatan Software Team, USA) and the ImageJ v.1.42d (National Institutes of Health, USA) software packages were used for analysis of images and for Fast Fourier Transform (FFT) procedures. Grain size analyses were performed using the ImageJ (v.1.42d) software package.

An increased dispersion of particles of each specimen was of interest in order to obtain reliable TEM results. This was usually obtained by placing a small amount of each powder in vials with n-hexane, which were subjected to 5 min ultrasonication. Differences in preparation procedure were applied only for YSZ nanopowders and these details are provided in Chapter 4. All samples were deposited on 3 mm Cu TEM grids coated with holey carbon film by repeatedly dipping the grid into an ultrasonicated dispersion of the relevant sample powder. The grids with deposited sample were dried overnight using a lamp as a heat source before being loaded into the TEM instrument for study.

3.6 Impedance Spectroscopy

All electrolyte materials in the form of sintered discs were analysed by two-electrode IS conductivity measurements using a Solartron 1260 Frequency Response Analyser (FRA). The main physical differences between the pellets were associated with the pellet thickness and the area of the electrodes for each sample. These parameters were taken into account in conductivity calculations, according to Equation 2.17. In addition, two different techniques of electrodes preparation were employed in this experiment.

In order to prepare cells for impedance measurements, electrodes were deposited on both sides of the YSZ pellets by sputtering from a platinum target onto the sample surface in areas defined by aluminium foil templates. These were prepared with significantly smaller diameters than the sintered pellets themselves in order to avoid transfer of electrons between the two electrodes by surface conduction. The templates were also helpful to avoid displacing the electrodes on the two opposing surfaces of the pellet with respect to each other. Each exposed area on either side of the pellet was covered with a 120 nm layer using 0.1 mm Pt targets mounted in a Cressington 208 HR Sputter Coater. A current of 80 mA and gas pressure of 0.01 mbar were necessary to carry out this deposition process.

The surface of each SDC pellet was polished with a diamond paste prior to IS measurements. An inorganic-free Pt ink (Engelhardt) was used to deposit electrodes on both sides of the pellet using a screen printer. Special care was taken to apply a similar amount of the Pt paint. It was thought that this technique would allow symmetrical electrodes of 12 mm diameter with approximately the same thickness to be obtained. The position of a pellet in the screen printer was fixed by a template, so that deposited electrodes were placed in the same positions on both sides of each pellet.

Platinum wires (Alfa Aesar, 0.25 mm dia, 99.9%) in a spiral shape were attached to the electrodes using the Engelhardt Pt ink. The paint was lightly dabbed onto the spiral, which rested on the top of sputtered or screen-printed electrode. Due to the surface tension from the paint, the wires were permanently bonded, when the whole assembly was exposed to thermal treatment. In the first step, samples were heated at 2°C/min rate to 200°C and kept for 2 h at this temperature. In the second step, the temperature was increased to 1000°C at 4°C/min and maintained at this temperature for 1 h. An example of an SDC sample used in the IS measurements is presented in Figure 3.3.

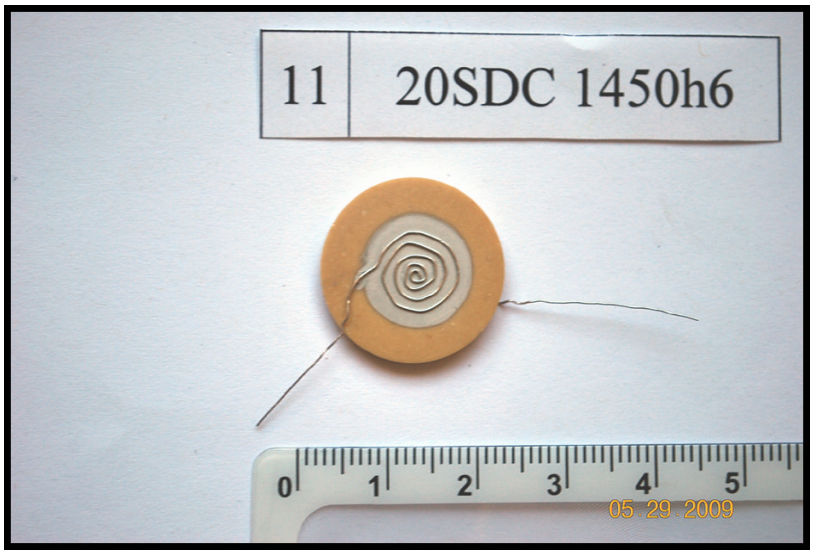

Figure 3.3 SDC pellet Pt electrodes with attached wires on representative.

The resulting pellets were placed onto the sample support inside the quartz reactor, which is presented in Figure 3.4. Electrical connections between the Pt wires attached to the electrodes and the Pt wires connected to the leads of the FRA were made by welding. The resistance of the Pt wires (R_w), which varied in the range 2-5 Ω, was measured using a multimeter (Metrix MX 56C) before each set of impedance measurements and was subtracted from the impedance data.

All complex impedance measurements were carried out under an atmosphere of flowing pre-dried, synthetic air (50 ml/min) at a number of temperatures over the range 150 – 800°C. The rig including moisture trap, control valves and flow meter was built to ensure identical conditions across all of the samples tested. The temperature of the furnace was controlled by a chromel-alumel (Type K) thermocouple connected to a computer programme *via* a PICO 8 channel Thermocouple Data Logger. An a.c. voltage of 0.1 V amplitude was applied and the frequency was swept from 20 MHz to 1 Hz. At each test temperature, spectra were recorded repeatedly until no change was noted between them. Once the final spectrum was taken, the temperature of the furnace was increased to the next test temperature. Before starting measurements at each temperature, the system was left for a period of at least 1 h in order to allow the system to attain chemical and thermal equilibrium. All impedance spectra recorded in order of increasing temperature were repeated over the same range of temperature in decreasing order.

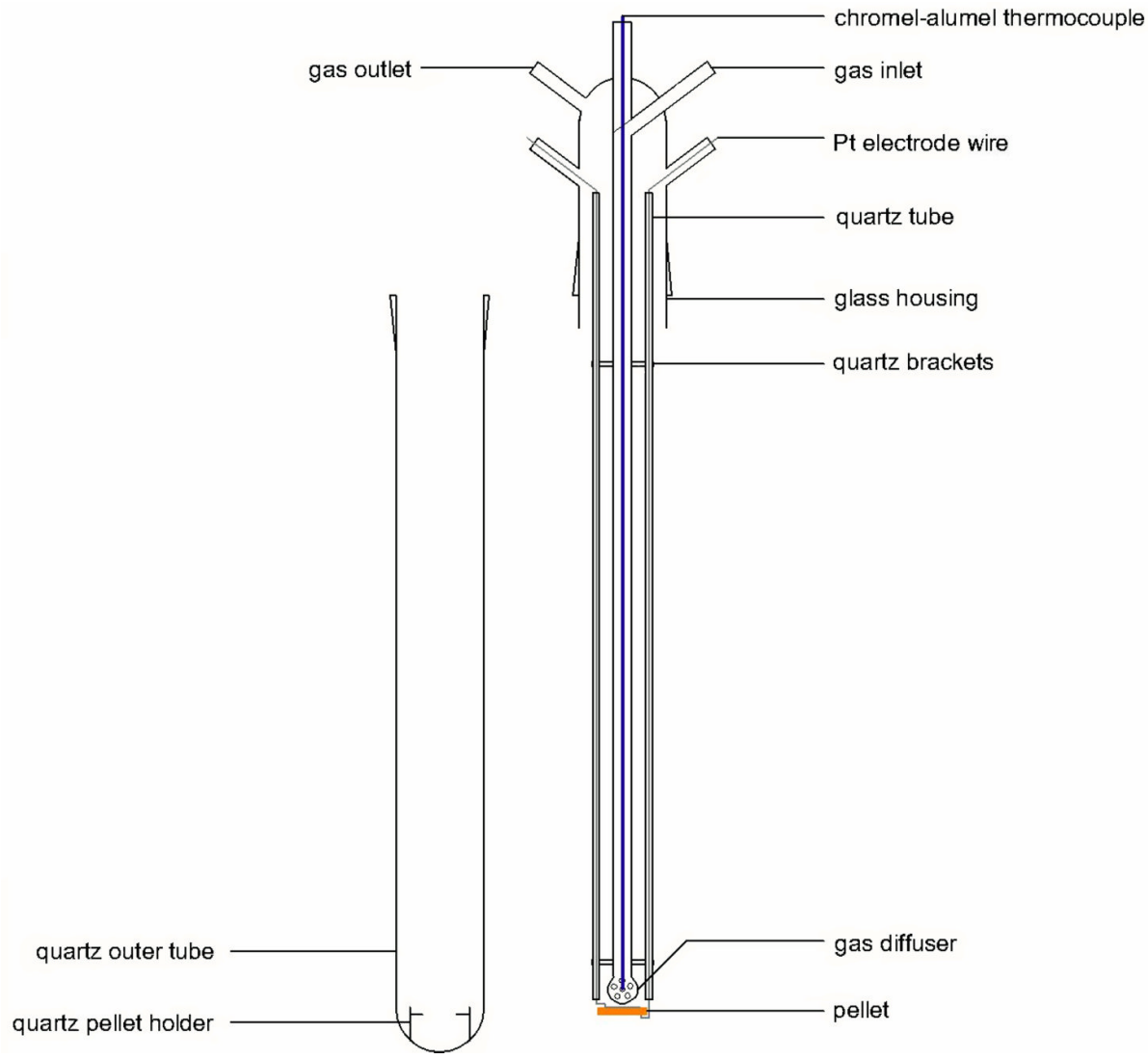

Figure 3.4 Schematic of a quartz reactor used in IS measurements.

The resistance, capacitance and inductance values were extracted from each spectrum using ZView software (Scribner Associates, Inc). Each Nyquist plot was first examined with reference to the number of processes occurring within the sample. Usually arcs were easy to identify. Bulk and grain boundary contribution arcs were of interest in the studies of both electrolyte materials. In some impedance plots, two small arcs were represented as one elongated feature in the lower frequency range, therefore additional precautions had to be taken to ensure that numerous minor processes were not overlooked. Inductive effects as a result of the current and its magnetic field were taken into account by including a corresponding inductance element in the equivalent electronic circuit. For example, the proposed model at low temperatures included: R_w as the resistance of the wires, L as the inductance, R_1 and CPE_1 for the bulk response, and R_2 and CPE_2 for the grain boundary

contribution. Single out-lying points at 50 Hz were occasionally seen on some spectra. These corresponded to interference from the mains power and were deleted as otherwise they would affect the fitting procedure.

Care was taken to select appropriate points on the Nyquist plot in order to obtain preliminary data values for each arc by using the 'fit circle' option. When the circle was fitted, the program provided visual representation of the fitted circle and gave the estimated values of the resistance (R) and (where possible) the capacitance (C). Next, these rough values were entered into the equivalent circuit tool and a least squares fitting method was run to optimise the results. The different circuit values were manipulated ensuring that the resistance and capacitance data were realistic until the best fit model for the arcs of interest was obtained. Additionally, it was ensured that the circuit values were only being fitted over the relevant frequency range. This produced much more reliable values for the equivalent circuit than if all the points were fitted simultaneously. Figure 3.5 demonstrates the final fitted impedance data (green line) of the Nyquist plot for a representative YSZ sample.

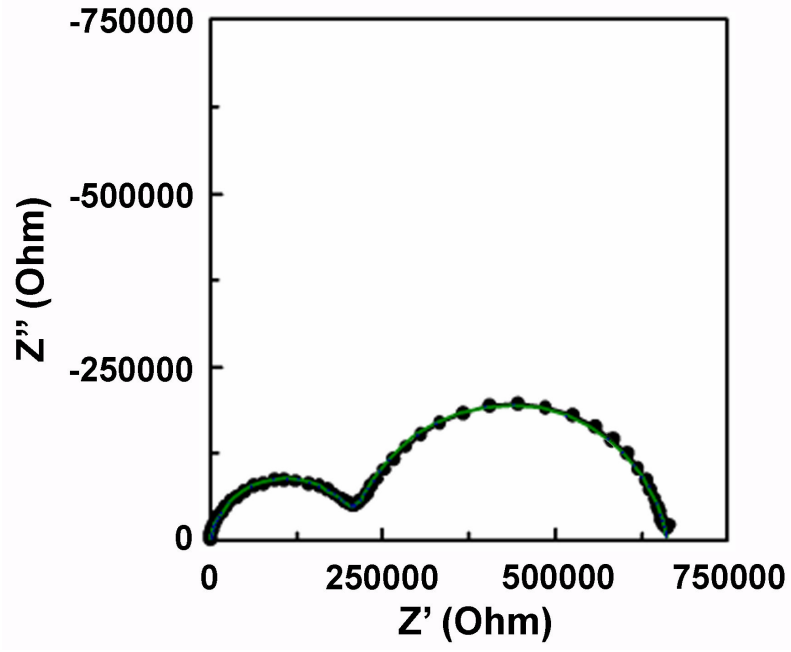

Figure 3.5 Final fitting and experimental data in Nyquist plot for YSZ pellet recorded at 250°C depicting bulk and grain boundary contributions.

3.7 X-ray Photoelectron Spectroscopy

XPS measurements were carried out on SDC and Pd/SDC samples at the University of Málaga (Spain) using a Physical Electronics 5700C Multitechnique spectrometer, which operated with Mg K_α radiation ($h\nu$ = 1253.6 eV). In order to determine all the elements present on the catalyst surface, general spectra were recorded for the samples by scanning up to a binding energy (E_b) of 1200 eV. The E_b of the Pd 3d, Sm 3d, Ce 3d and O 1s core level and full width at half maximum (FWHM) values were used to determine the chemical state of the elements. Correction for binding energies due to sample charging was done by taking the C 1s peak (284.6 eV) as an internal standard. The accuracy of the E_b scale was ±0.1 eV. The data analysis procedure involved smoothing, a Shirley background subtraction and curve fitting using mixed Gaussian-Lorentzian functions by a least-squares method. The atomic ratios of the elements were calculated from the relative peak areas of the respective core level lines using Wagner sensitivity factors.

3.8 Catalytic activity studies

Methanol steam reforming tests were carried out on SDC and Pd/SDC materials at the University Rey Juan Carlos in Madrid (Spain) using a Microactivity-Pro unit (PID Eng&Tech. S.L.). The equipment consisted of a stainless steel tubular reactor (9.2 mm i.d., length 300 mm) located inside an electric oven. The temperature in the catalytic bed was measured by means of a thermocouple. A six-port VICI valve allowed the gas flow to be directed into the reactor or to bypass it. These components were located inside a stainless steel hot box, equipped with an air convector, to vaporise liquid reactants, preheat the carrier gas, and prevent condensation of volatile products in the ducts. The mixture of liquid reactants (methanol and water) was fed by means of a GILSON 307 piston pump. At the reactor outlet, a thermoelectric unit was used to separate condensable vapors. The gaseous product stream from the reactor was analysed online using a Varian CP-3380 gas chromatograph equipped with a heated sampling valve, two columns (6 m Hayesep Q and 1 m Molecular Sieve 13X), and a thermal conductivity detector. Helium was used as both the carrier gas and the reference gas.

Catalyst (100 mg) was placed on a quartz wool plug inside the tube reactor and reduced under a flow of 20 vol% H_2/N_2 (50 $cm^3 \cdot min^{-1}$, STP) at 500°C for 1 h. The heating rate was 3°C/min. After this catalyst activation step, the reaction temperature was set to 400°C, and

the catalytic test was performed isothermally at atmospheric pressure. The liquid water/methanol mixture (1.2 molar ratio) was fed at 2 $cm^3 \cdot h^{-1}$, vaporized at 160°C, and further diluted by a flow of N_2 (50 $cm^3 \cdot min^{-1}$, STP).

Catalytic performance of synthesised Pd/SDC catalysts and SDC solid solutions was assessed in terms of the methanol conversion (Eqn. 3.3), the yield to hydrogen (Eqn. 3.4) and selectivities to product on carbon or hydrogen basis (Eqn. 3.5).

$$X_{CH_3OH} = \frac{F_{CH_3OH,in} - F_{CH_3OH,out}}{F_{CH_3OH,in}} \cdot 100\% \qquad \textbf{(3.3)}$$

X_{CH_3OH} – the methanol conversion (mol %),
$F_{CH_3OH,\,in}$ – the methanol molar flow rate at the inlet of the reactor,
$F_{CH_3OH,\,out}$ – the methanol molar flow rate at the outlet of the reactor.

$$R_{H_2} = \frac{F_{H_2,out}}{F_{CH_3OH,in}} \cdot 100\% \qquad \textbf{(3.4)}$$

R_{H_2} – the hydrogen yield (%),
$F_{H_2,\,out}$ – the hydrogen molar flow rate at the outlet of the reactor.

$$S_i = \frac{R_i / \upsilon_i}{X_{CH_3OH}} \cdot 100\ \% \qquad \textbf{(3.5)}$$

S_i – the selectivity to the product *i* (%),
R_i – the yield to the product *i*,
υ_i – the stoichiometric coefficient related to the transformation of CH_3OH into the product *i*.

Results and Discussion

CHAPTER IV – **YTTRIA-STABILISED ZIRCONIA**

4. Yttria-stabilised zirconia

4.1 Introduction

The main focus of this part of the work described in this thesis was to investigate the relationship between the ionic conductivity of yttria-stabilised zirconia (YSZ) as an electrolyte material and its yttria (Y_2O_3) content and microstructure, with particular reference to the particle size of the starting powders. This investigation was supported by X-ray powder diffraction (XRD), electron microscopy (SEM, TEM/EDX), dilatometry, inductively coupled plasma mass spectroscopy (ICP-MS) and impedance spectroscopy (IS) studies. All of the analytical methods were applied for micro-scale and nano-scale powders with varying mol% of yttria.

4.2 Sample information

The samples were analysed in five variants, i.e. 0, 3, 5, 8 and 10 mol% Y_2O_3, and were labelled as presented in Table 4.1, to indicate composition, micro- or nano-scale starting material and whether the sample was studied in the powder or the pellet form.

Table 4.1 The range of samples for YSZ studies.

mol% Y_2O_3	*Micro-scale samples*		*Nano-scale samples*	
	Powder	*Pellet*	*Powder*	*Pellet*
0	m0YSZ	M0YSZ	n0YSZ	N0YSZ
3	m3YSZ	M3YSZ	n3YSZ	N3YSZ
5	m5YSZ	M5YSZ	n5YSZ	N5YSZ
8	m8YSZ	M8YSZ	n8YSZ	N8YSZ
10	m10YSZ	M10YSZ	n10YSZ	N10YSZ

All powders used in the project were produced by MEL Chemicals Ltd, UK and no detailed information about their synthesis was provided. The micro-scale batch of samples was supplied in the form of dry, commercial powders and these are named as micropowders in this thesis. The nano-scale samples were delivered in aqueous suspensions. Therefore, the nanopowders (as they will be named herein) had to be extracted *via* oven drying at 125°C over a 24 h period. They were then milled for 1 h in 20 min intervals at 200 rpm in order to remove agglomerates before their compaction to obtain dense green bodies. The micropowders were synthesised by a solid state ceramic method, while a solution method was applied to prepare the nanopowders. The properties of the resulting pellets for both

batches are presented in Section 4.4. The sintered dense bodies were consequently named as micropellets and nanopellets, respectively, after the powder batches they were descended from. Two sets of sintered micropellets were also supplied by MEL Chemicals Ltd, but all nanopellets were prepared at the University of St Andrews.

4.3 Powder characterisation

Micro-scale powders used as starting materials for SOFC electrolytes are of interest in industry, because these might be produced in relatively quick, cheap and cost-effective processes. However, it is common to believe that by using nanoparticles, improved grain structure and grain size distribution might be obtained in the resulting dense bodies. Additionally, the application of nanopowders may also have a positive impact on the reduction of sintering time and temperature. If these parameters can be reduced, with the final electrolyte still showing similar or improved conductivity, this would result in a significant reduction of cost associated with the production of SOFCs.

In relation to these findings XRD, electron microscopy and dilatometry results for both sets of powders are presented in the following sections.

4.3.1 X-ray Diffraction

Figures 4.1 and 4.2 show diffractograms obtained from the micropowders. In the case of unstabilised zirconia (m0YSZ), the material exhibited the monoclinic phase. Peaks corresponding to this phase (marked with a purple letter "m") are indicated in these figures. As mol% of Y_2O_3 increased, the phase of the material changed from monoclinic (m) - for pure zirconia, towards a mixture of monoclinic and tetragonal (t) - at low percentages - and finally cubic (c) - at higher values. The intensity of the peaks corresponding to the monoclinic phase (in the angular region of $2\theta = 28\text{-}33^{o}$) decreased as the percentage of the dopant increased and were not present above 5% yttria doping.

More detailed examination of the m3YSZ diffraction pattern in the range of $2\Theta = 70\text{-}77°$ (Figure 4.2), clearly showed that the peaks corresponding to the (004) and (400) reflections of the tetragonal phase occur at different angles – i.e. they are split. This splitting is characteristic of the tetragonal phase since the two corresponding reflections are equivalent in the cubic structure. Analysis of the same region for the m5YSZ pattern showed a wide, uneven peak with less separation, but also with two distinct peaks of the tetragonal phase.

These findings are consistent with a study by Chen *et al*, who observed similar peak separation for 7.6 mol% YSZ.[120] Their studies on 7.6YSZ coatings revealed that this effect was

determined to be caused by the non-equilibrium tetragonal phase, identified as t'-ZrO_2. They suggested that destabilisation of this phase is more effective when an excess of yttria is used or in the presence of an additional dopant such as Ca^{2+}. They found that when the 7.6YSZ sample was additionally stabilised with a smaller cation, the splitting between (004) and (400) characteristic of the tetragonal phase was preserved even after long-term high temperature treatment. In fact, their studies may suggest the presence of some impurities and will be discussed in Section 4.4.4 with connection to ICP-MS results.

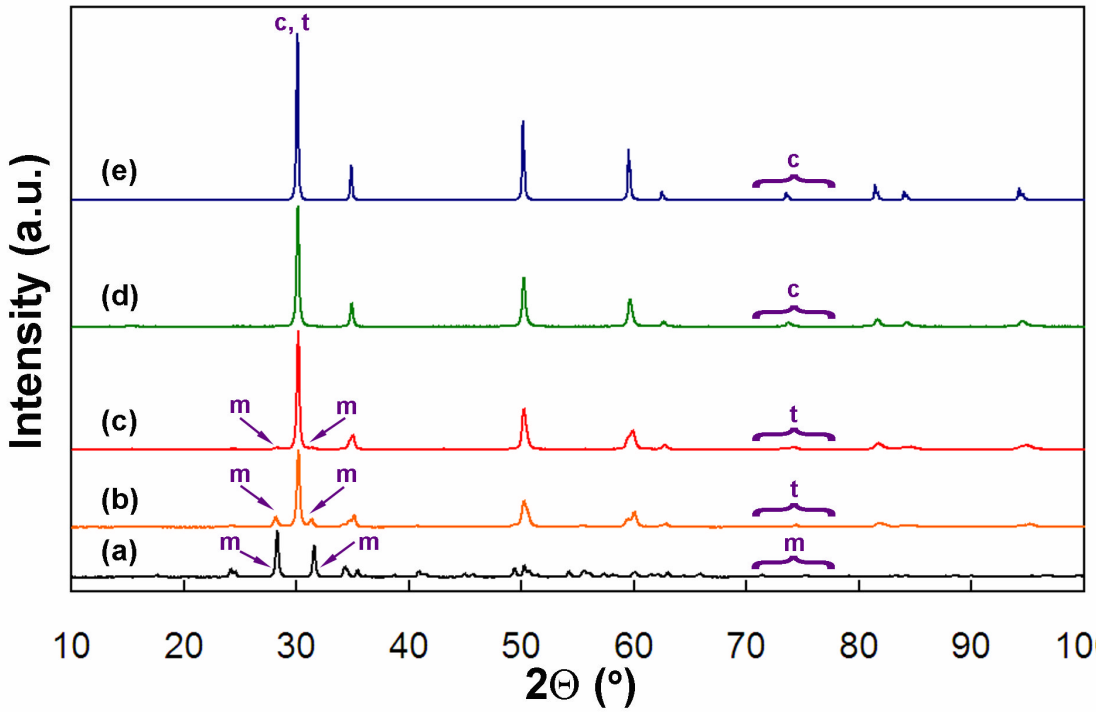

Figure 4.1 Effect of yttria content on the phase of (a) m0YSZ, (b) m3YSZ, (c) m5YSZ, (d) m8YSZ and (e) m10YSZ in 2Θ = 10-100° region.

The XRD patterns observed for m8YSZ and m10YSZ were characteristic of the cubic phase. There was no evidence of the monoclinic phase. However, a closer examination of the region 2Θ = 70-77° was required in order to preclude the presence of the tetragonal phase. Lamas *et al* in their work on nanocrystalline YSZ, observed a symmetrical single peak (above 9% Y_2O_3) at the (400) reflection which was consistent with the cubic phase.[121] This peak was present here in both the m8YSZ and m10YSZ patterns as an unsymmetric peak and a split sharp peak, respectively. However, this splitting effect was an instrumental artefact caused by the existence of two close CuK_α radiation lines. As outlined by Weller, these two components of the CuK_α X-ray source may appear in the diffraction pattern especially when the experimental peaks are narrow.[122]

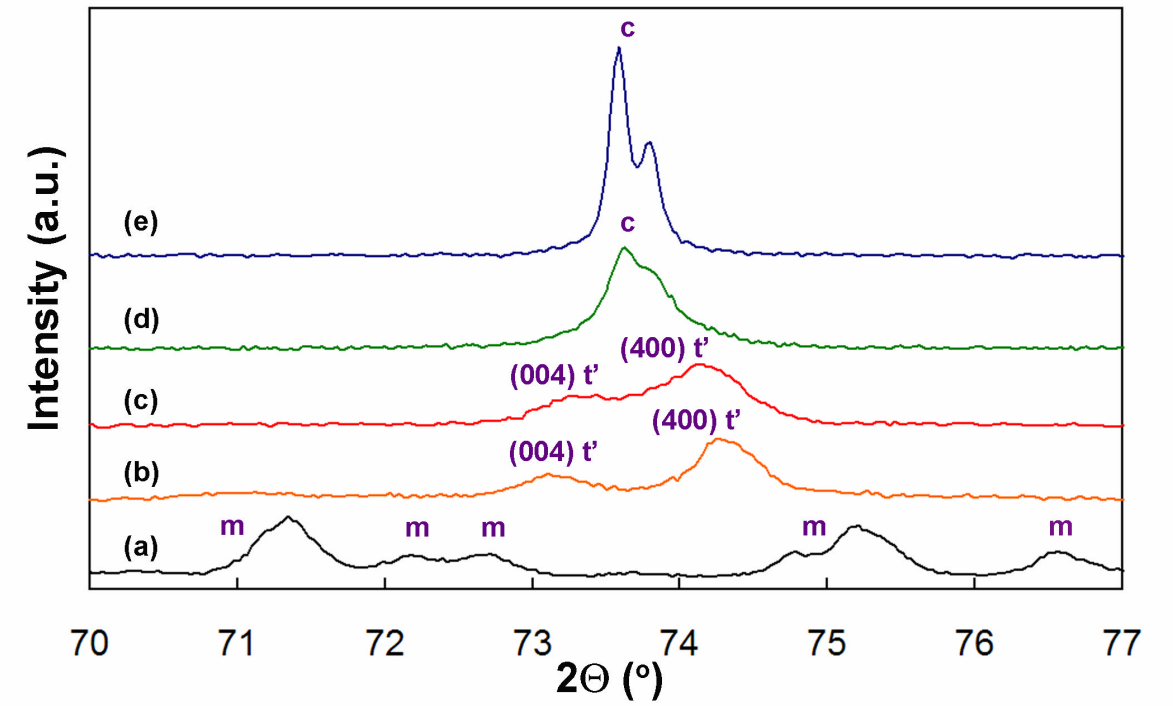

Figure 4.2 Diffraction patterns of (a) m0YSZ, (b) m3YSZ, (c) m5YSZ, (d) m8YSZ and (e) m10YSZ in 2Θ = 70-77° region.

The XRD patterns of the nanopowders exhibited some significant differences from the micropowder results. These are presented in Figures 4.3 and 4.4.

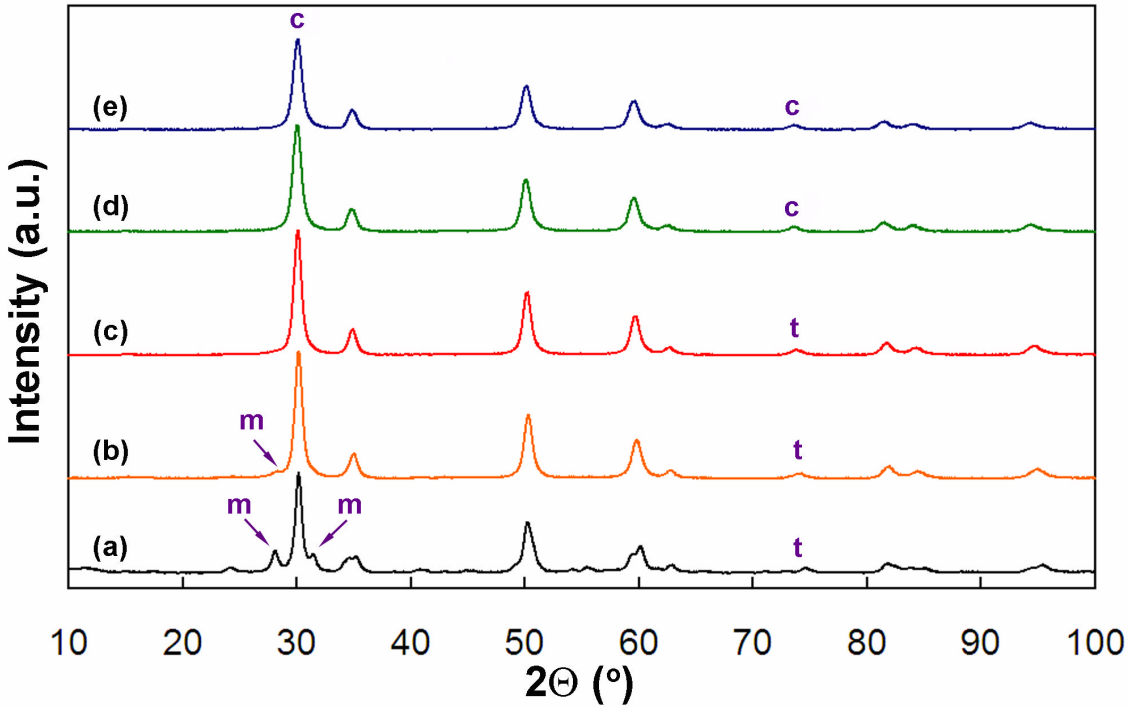

Figure 4.3 Effect of yttria content on the phase of (a) n0YSZ, (b) n3YSZ, (c) n5YSZ, (d) n8YSZ and (e) n10YSZ in 2Θ = 10-100° region.

The direct comparison between micropowder and nanopowder batches showed that all peaks were significantly broader (and less intense) because of the much smaller particles in the nanopowder material. In the n0YSZ and n3YSZ samples, the peaks corresponding to the tetragonal phase were seen together with reflections of the monoclinic phase in the range of 2Θ = 28-33°. The tetragonal phase is clearly the majority phase in both these samples. This shows a marked size effect when compared with the m0YSZ, which appeared to be purely monoclinic. As the dopant level increased to 5 mol%, the peaks related to the monoclinic phase disappeared and intense peaks, which could be assigned to either the stabilised tetragonal or cubic phases, were observed. For example, the main (111) peak, normally associated with tetragonal and cubic phases, was observed in all patterns.

To distinguish the cubic and tetragonal phases, the range of 2Θ = 70-77° was scanned in more detail (Figure 4.4). The presence of separate peaks which could be assigned to the (004) and (400) reflections of the tetragonal phase were observed in the undoped and lightly doped YSZ nanopowders (n0YSZ and n3YSZ).

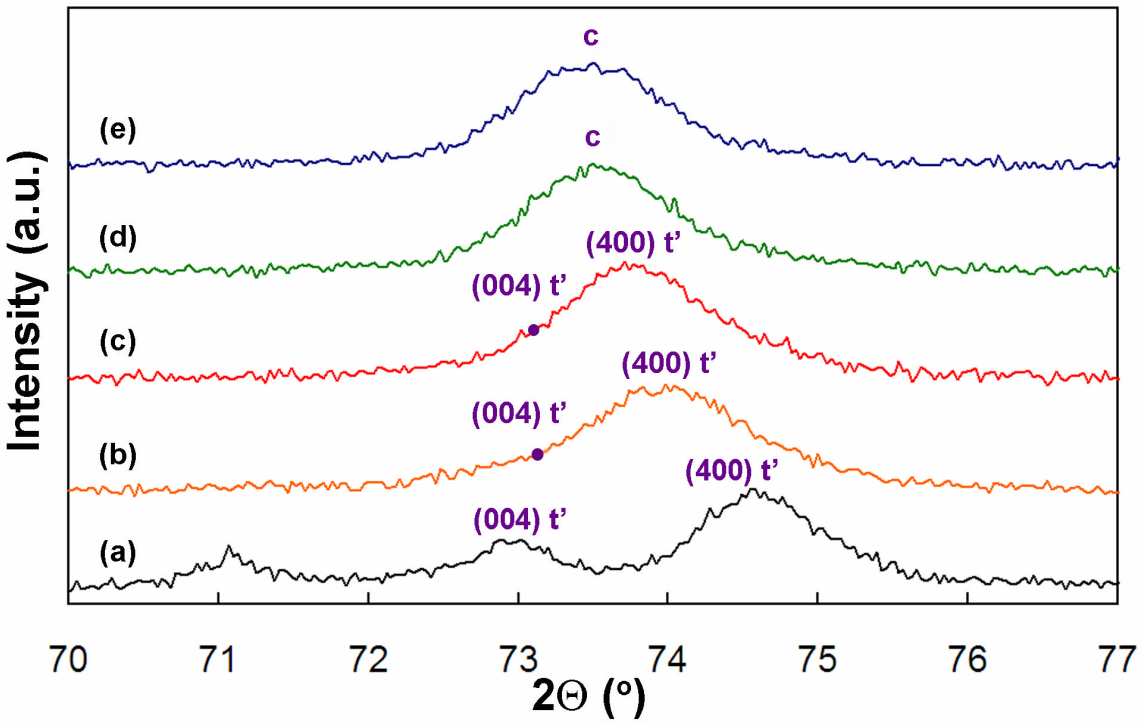

Figure 4.4 Diffraction patterns of (a) n0YSZ, (b) n3YSZ, (c) n5YSZ, (d) n8YSZ and (e) n10YSZ in 2Θ = 70-77° region.

In Figure 4.4, the presence of peaks associated with the tetragonal phase was difficult to distinguish in the cases of n3YSZ and especially n5YSZ samples. However, as the peak appeared uneven and shifted towards the (400) reflection for n3YSZ, it is suggested that the

two separate tetragonal peaks were present. The purple dot shows where the (004) peak of the tetragonal phase could be located for both n3YSZ and n5YSZ samples. These compositions therefore showed evidence of both cubic and tetragonal phases. In addition, a small contribution from the monoclinic phase was noticed for n3YSZ as confirmed on the diffraction pattern at the main (111) reflection in Figure 4.3. Closer inspection of the 2Θ = 70-77° region for n8YSZ and n10YSZ powders brought confirmation of these being of purely cubic phase.

As reported by Lamas *et al*, the retention of the tetragonal phase is possible at room temperature when pure and doped ZrO_2 nanosamples are used and it was clearly seen in these studies.[123] The analysis of the diffraction patterns is also consistent with a study by Mayo *et al*, who reported unusual phases when materials were fabricated in the nanocrystalline form.[71] The authors reported that (pure) zirconia powders have been observed to possess peaks of the tetragonal phase in the absence of stabilising dopants if the particles were refined to the nanometre scale. In the current study, the diffractogram for the zirconia nanopowder showed the same effect with the presence of the tetragonal reflections (111), (004) and (400) whereas the micropowder pattern consisted solely of monoclinic peaks.

4.3.2 Electron microscopy

Five samples containing 0, 3, 5, 8 and 10 mol% Y_2O_3 in ZrO_2 of both batches (micropowders and nanopowders) were investigated by electron microscopy. Data on the particle morphology, particle size distribution, chemical composition and crystal structure of individual crystals were obtained and are presented here.

4.3.2.1 Scanning Electron Microscopy

A small amount of each of the micro- and nanopowders were separately deposited on sticky carbon pads, which were mounted on a sample holder in a JEOL JSM-5600 instrument. No conductive layer was applied to the powder surface. However, a general insight into the morphology of the YSZ samples was easily obtained. Figures 4.5 and 4.6 present micrographs of the five YSZ compositions of the micro- and nanopowders, respectively. Identical images, at low (x1000) and higher (x4000) magnification were recorded for quick and direct comparison between sets of samples.

A tendency to form agglomerates was observed in both Figures 4.5 and 4.6 and slightly bigger clusters of particles were found for the nanopowders. A significant difference in morphology was observed for the m0YSZ as its particles formed individual clusters of more than 5 μm, the biggest among these samples.

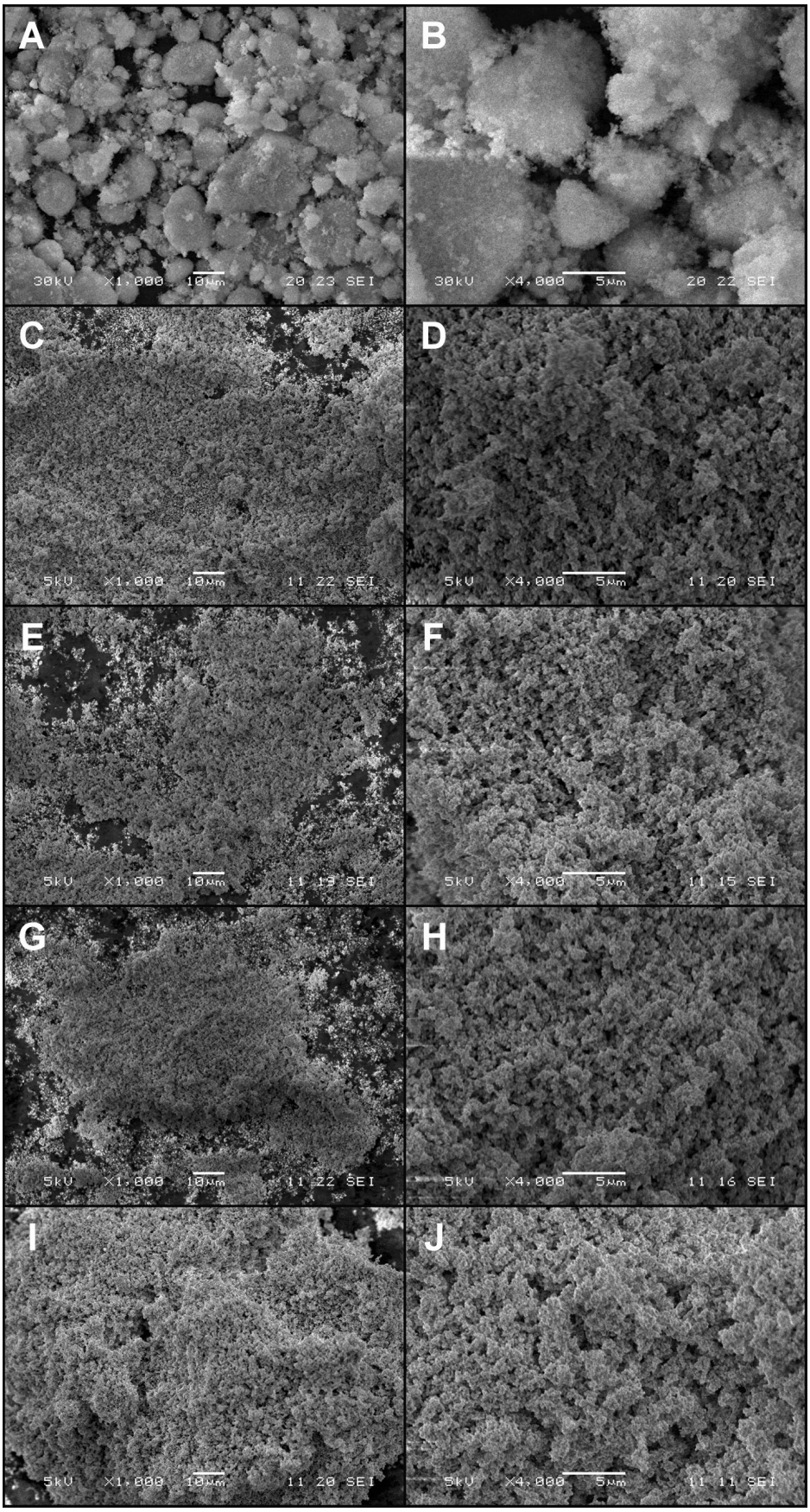

Figure 4.5 SEM images of (A,B) m0YSZ, (C,D) m3YSZ, (E,F) m5YSZ, (G,H) m8YSZ and (I,J) m10YSZ at low and higher magnification, respectively.

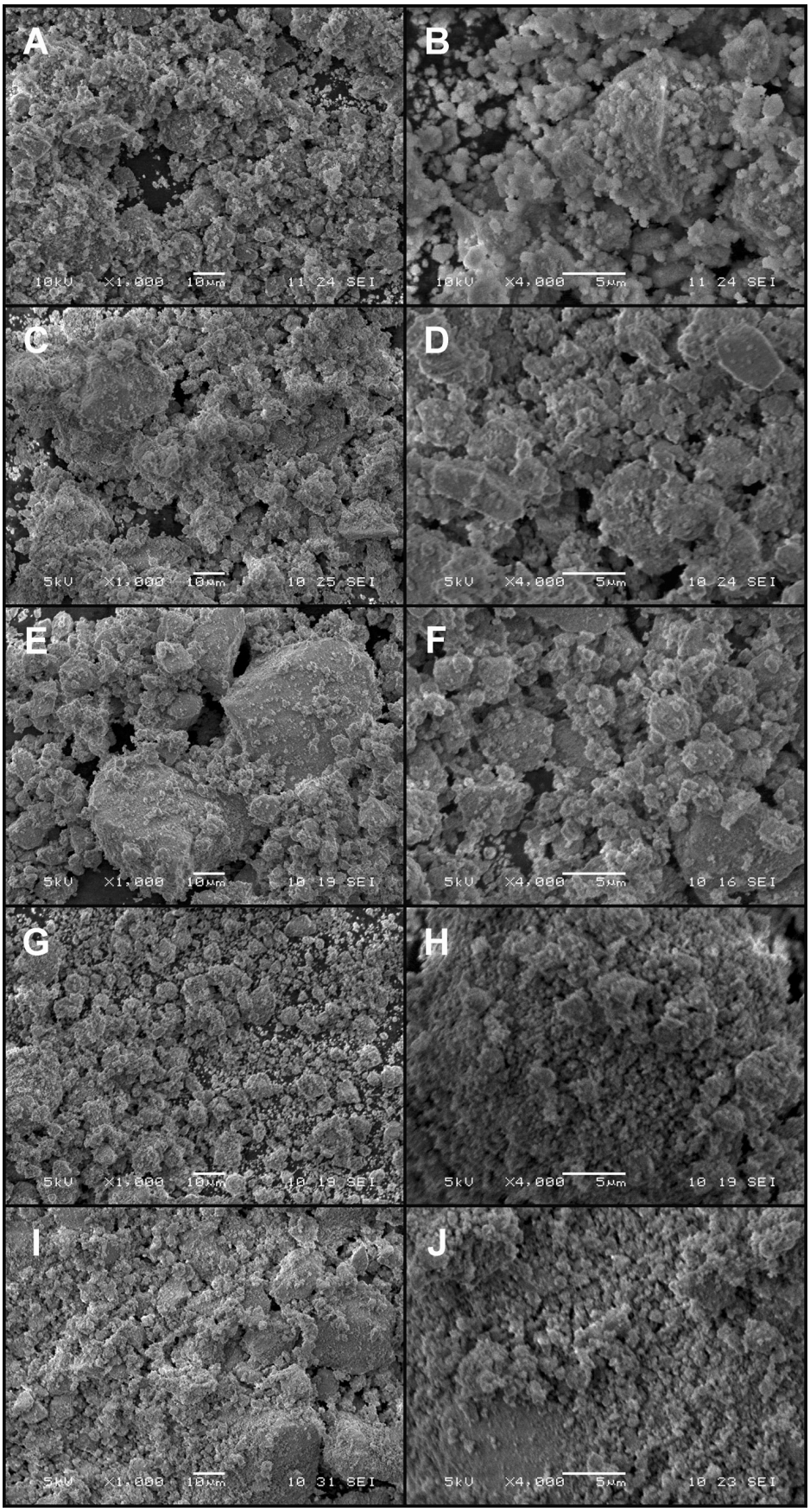

Figure 4.6 SEM images of (A,B) n0YSZ, (C,D) n3YSZ, (E,F) n5YSZ, (G,H) n8YSZ and (I,J) n10YSZ at low and higher magnification, respectively.

Except for the pure zirconia, the micropowders possessed rather uniform microstructure, independent of their chemical composition. Only a very slight trend in increase in cluster size was observed from m3YSZ to m10YSZ. The more detailed inspection represented in images B, D and F in Figure 4.6 showed also the variation in the size and shape of the clusters, which appeared to be in a random arrangement. It might be suggested from Figures 4.5 and 4.6 that two different synthetic methods were applied to prepare the micro and nanopowders, because different forms of agglomerates were observed. It should be noted that immediately before preparation of each specimen for SEM study, samples were additionally ground using a planetary mill and zirconia balls as the grinding medium. This would form "soft" agglomerates, which are loosely held together and should be easily separated. Efforts were concentrated on retaining repeatability and uniformity of each sample during the preparation method. However, the formation of agglomerates was unavoidable.

4.3.2.2 Transmission Electron Microscopy

About 50 mg of each micropowder was dispersed separately in n-hexane in order to prepare sample for TEM studies. Nanoparticles were already supplied in the form of aqueous suspensions and these had only to be diluted by a factor of approximately 100. YSZ samples of both batches were separately placed in vials and were subjected to 5 min ultrasonication to increase the dispersion of particles in the corresponding suspensions. The preparation procedure then followed that described in Section 3.5.2 in the *Experimental procedures* chapter. TEM images of relatively low, intermediate and high magnification were taken to provide clear images of a sufficient number of particles to obtain representative information on both their morphology and their particle size. These are presented in Figures 4.7 and 4.8 for micro- and nanopowders, respectively. The micrographs show that a minority of the mass of each micropowder and nanopowder sample was present in the form of agglomerates of primary particles. The left column in Figure 4.7 presents low magnification images of microparticle clusters. These observations were consistent with findings from SEM studies and confirmed the presence of agglomerates smaller than 1 μm. Images B, E, H, K and N in Figure 4.7 clearly showed the morphologies of individual particles. These were found to be from oval (m0YSZ) to spherical shapes (m3YSZ) and even sharp edged hexagonal particles (m8YSZ). The interplanar spacings observed in some images were consistent with ZrO_2 and YSZ crystal structures.

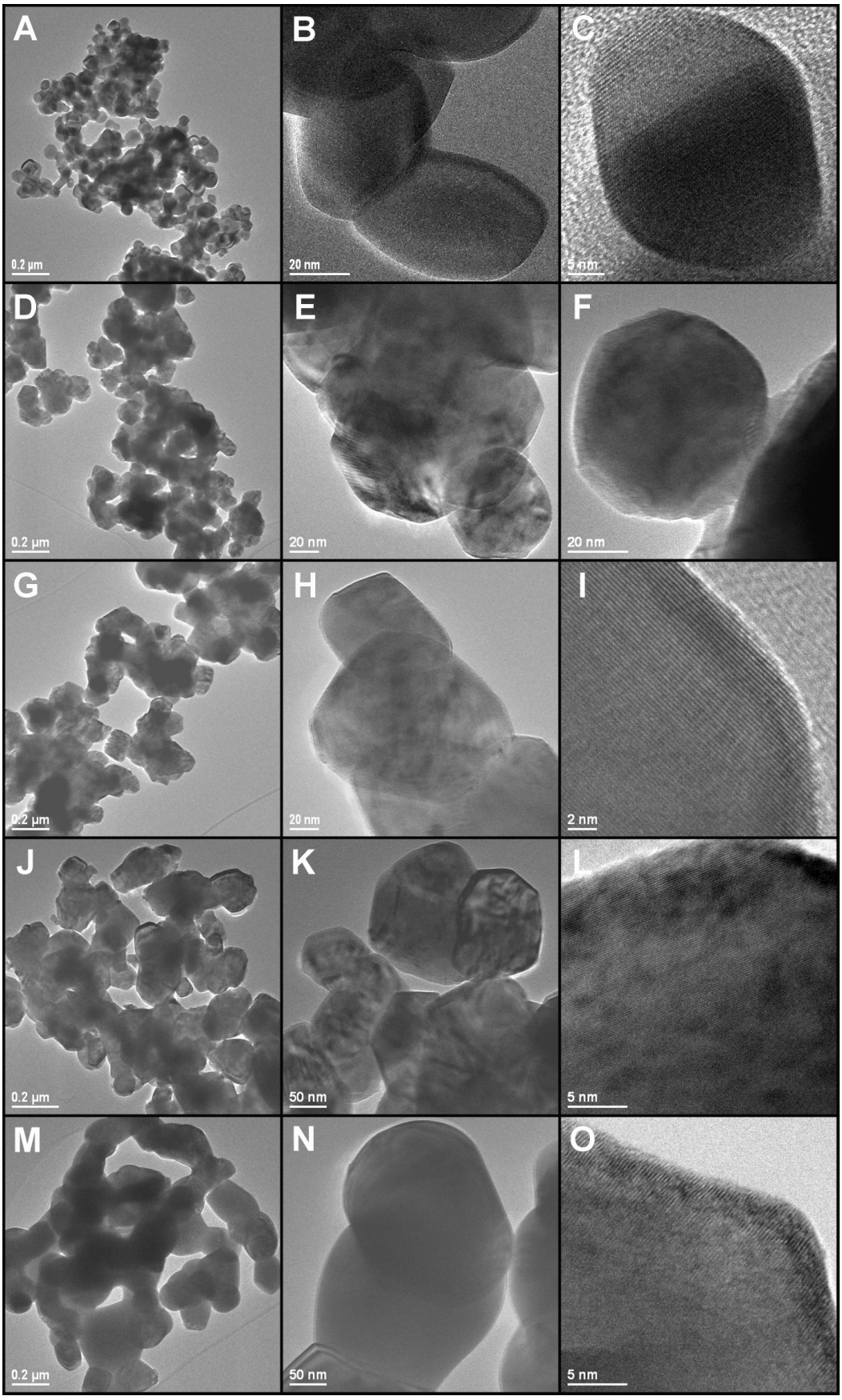

Figure 4.7 TEM images of (A,B,C) m0YSZ, (D,E,F) m3YSZ, (G,H,I) m5YSZ, (J,K,L) m8YSZ and (M,N,O) m10YSZ at low, medium and high magnification, respectively.

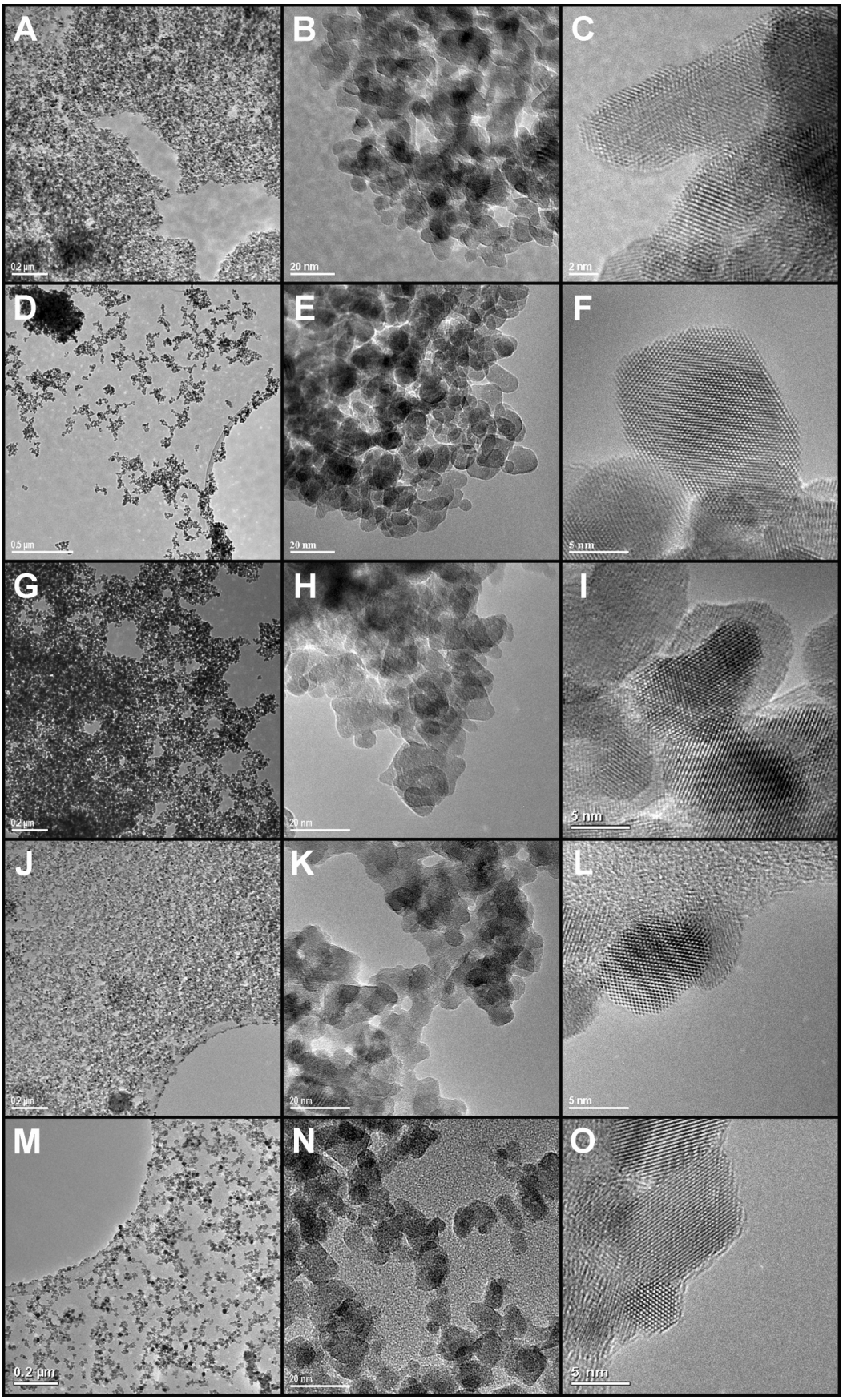

Figure 4.8 TEM images of (A,B,C) n0YSZ, (D,E,F) n3YSZ, (G,H,I) n5YSZ, (J,K,L) n8YSZ and (M,N,O) n10YSZ at low, medium and high magnification, respectively.

The micrographs of nanoparticles at the lowest magnification (Figure 4.8 A, D, G, J, M) showed relatively even distribution of the material across the grids. Large dark spots in these images (i.e. Figure 4.8D) indicated relatively large agglomerates. Their size often exceeded 200 nm. The intermediate magnification images revealed primary particle sizes, which were similar for all five compositions of YSZ nanopowders. At higher magnification, the particles appeared to be very largely well-ordered single crystals. Their form was quite rounded, especially for the lower yttrium contents. On the other hand, some crystals exhibited some rather unusual concave surfaces, e.g. n5YSZ. This could be a consequence of the low temperature preparation method, in that no thermal sintering was undertaken and therefore some high energy particle morphologies were seen. The particles of m5YSZ, m8YSZ and m10YSZ samples appeared to be slightly more angular than those of lower yttrium content.

For more precise assessment of the YSZ samples, particle size distribution histograms were prepared. These are presented in Figure 4.9. ImageJ software was used to obtain the size information from the images. A particle counting technique was established, which gives number-weighted distributions. For micropowders, only about 30-50 individual particles could be distinguished from micrographs of each composition. It was believed that this number was sufficient to obtain useful mean particle size data. In addition, nanoparticles were found to overlap each other. However, it was possible to measure a representative number of particles (~140-230) for this analysis.

A full set of data of number of particles measured (n_p), mean particle size (m_p) and standard deviation (*S.D.*) are given in Table 4.2. In the case of the micropowders, the narrowest particle size distribution was found for pure zirconia. This sample also gave the lowest value of average particle size of 81 nm. An increasing trend in m_p and in the breadth of the size distribution, were observed with increasing yttrium content for the micropowders.

There was a monotonic decrease in mean particle size for nanoparticles as mol% Y_2O_3 increased. However the differences between m_p values were relatively small. This indicates that changes in the concentration of Y in these samples had no major impact on final particle size in the nanopowder preparation method. The particle size distributions of the nanopowder samples were quite narrow; indicating that particle size could be quite well controlled using this preparation method.

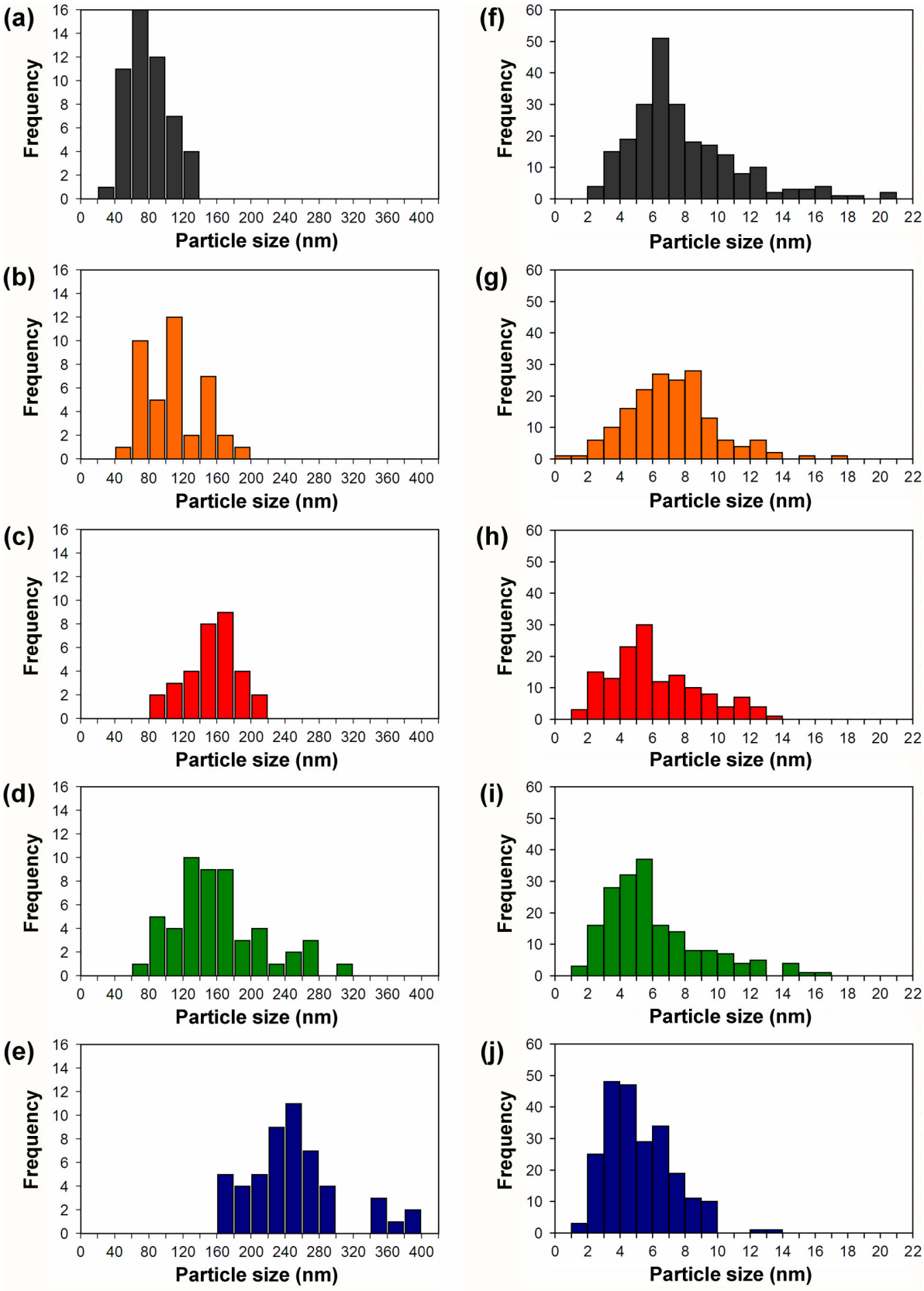

Figure 4.9 Particle size distribution histograms for micropowders (a) m0YSZ, (b) m3YSZ, (c) m5YSZ, (d) m8YSZ (e) m10YSZ and nanopowders (f) n0YSZ, (g) n3YSZ, (h) n5YSZ, (i) n8YSZ (j) n10YSZ.

Table 4.2 Particle size analyses for both sets of YSZ powders.

Sample	n_p	m_p /nm	***S.D.*** /nm
m0YSZ	51	81.0	23.3
m3YSZ	40	110	34.1
m5YSZ	32	155	31.1
m8YSZ	52	162	52.8
m10YSZ	51	251	54.1
n0YSZ	232	7.80	3.27
n3YSZ	169	7.21	2.67
n5YSZ	144	6.13	2.71
n8YSZ	184	6.04	3.02
n10YSZ	228	5.21	2.03

EDX spectra in the energy range 0-20 keV were obtained for all YSZ powder samples and these are presented in Figure 4.10. Characteristic peaks of relevant elements (Y, Zr and O) were identified for both sets of YSZ powders. Elements relating to the composition of the TEM sample grids (Cu, C) were also evident in each spectrum. In the case of the nanopowders, peaks of interest were marked in dark red (spectra f-j). The ratio between the main peaks corresponding to Y (at 14.93 keV) and Zr (at 15.75 keV) increased with the expected increase in the dopant concentration for both the micropowders (spectra a-e) and the nanopowders (spectra f-j). In addition, quantitative data were retrieved from each spectrum and results in molar ratios are summarized in Table 4.3. These indicate that the samples had approximately the expected chemical compositions. The spectra of the micropowders (a-e), which were obtained much later than those for the nanopowders, showed some extra peaks in the 6-7 keV region. These were found to be caused by contamination of the TEM instrument by Co compounds introduced by other users and should be ignored. These Co peaks were confirmed to occur in several areas of the grid without sample, in a new TEM grid and even when EDX measurements were performed without a grid in the microscope. These blank experiments confirmed the presence of Co as instrument contamination.

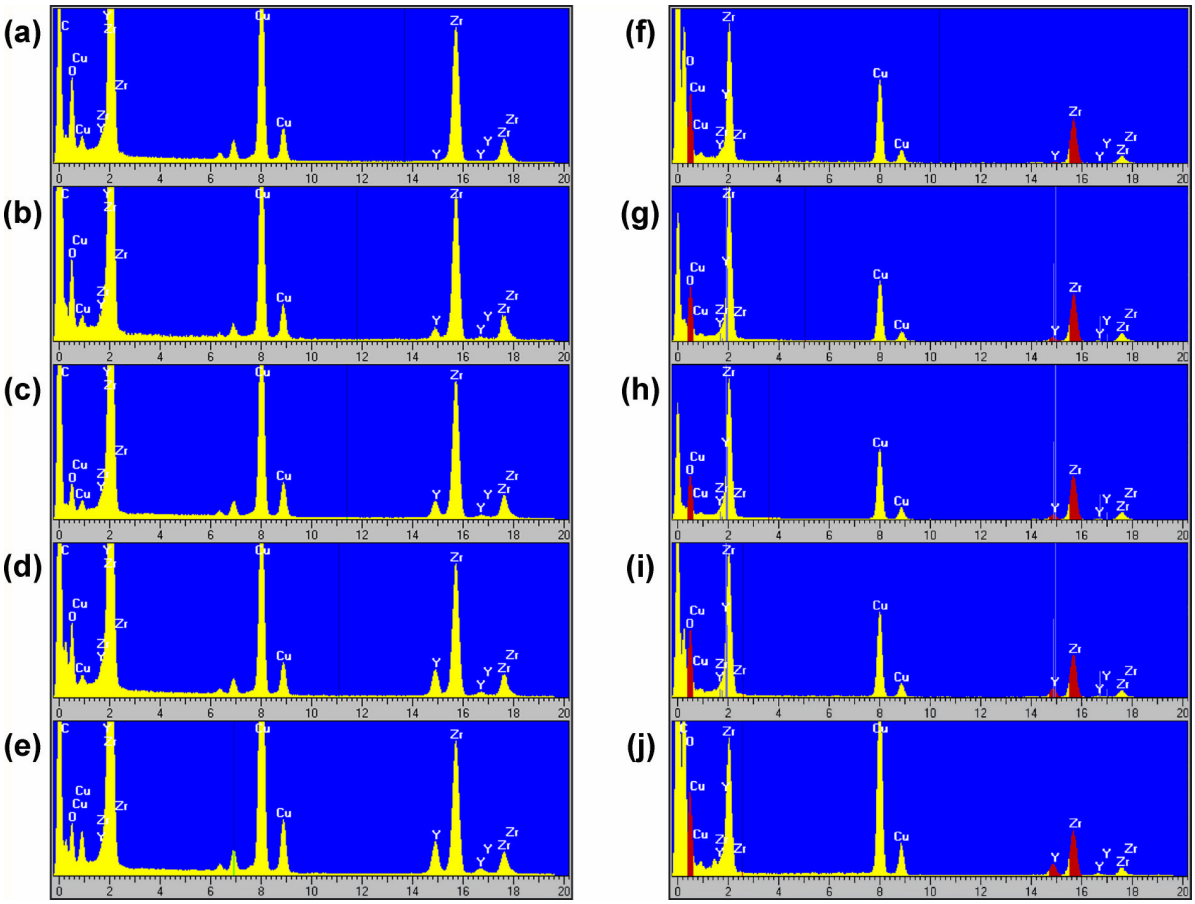

Figure 4.10 EDX spectra of (a) m0YSZ, (b) m3YSZ, (c) m5YSZ, (d) m8YSZ, (e) m10YSZ and (f) n0YSZ, (g) n3YSZ, (h) n5YSZ, (i) n8YSZ (j) n10YSZ.

Table 4.3 gives values for the nominal compositions of the samples and the values obtained by EDX. It should be noted that, since standards for Y and Zr were not employed, these values are more indicative than absolute. Nevertheless, there is reasonable agreement between the target compositions and those measured by EDX. Relatively large areas (several 100 nm in diameter) of the samples were analysed. Background noise in the Y region appeared to cause addition of 0.01-0.02 to the Y/Zr ratios in Table 4.3.

Table 4.3 EDX results for both sets of YSZ powders.

mol% Y_2O_3	***mol% Y***	***Y/Zr*** (molar)	***Y/Zr*** (EDX)	
			Micropowders	***Nanopowders***
0	0	0	0.018	0.013
3	5.8	0.062	0.070	0.085
5	9.5	0.105	0.116	0.102
8	14.8	0.174	0.193	0.190
10	18.2	0.222	0.238	0.233

High Resolution Transmission Electron Microscopy (HR-TEM) images of the five nanopowder compositions were recorded and examples of these are presented in Figures 4.11-4.15. The crystal structures of the five nanoparticulate samples were indexed by obtaining digital diffraction patterns (DDPs) from the images and comparing these to diffraction patterns generated using crystallographic data from the Inorganic Crystal Structure Database (ICSD)[124] for cubic, tetragonal and monoclinic ZrO_2 using the on-line EMS software.[125]

In certain orientations, the DDPs for more than one crystal phase are difficult to distinguish. However, certain patterns are characteristic of either the tetragonal or the monoclinic phase only, and these were important in this work. The pure ZrO_2 (Figure 4.11) appears to be a mixture of monoclinic and tetragonal phases. The assignment of a cubic phase in Figure 4.11C is possible but unlikely. In the n3YSZ and n5YSZ samples (Figures 4.12 and 4.13, respectively), there is also unequivocal evidence for both tetragonal and monoclinic phases, again with symptoms of a cubic phase. At higher Y contents (Figures 4.14 and 4.15) no DDPs were obtained which could be indexed uniquely to the tetragonal or monoclinic phases. It seems therefore, that these samples are largely cubic in structure, this phase being stabilised by the presence of the significant quantities of Y. In many of the high resolution images, the border of the crystal was seen clearly. The steps were often resolved at the different crystal surfaces as well as the shapes of the particles, including concave surfaces in some cases (e.g. Figure 4.12C).

Comparable studies on micropowder samples could not be performed due to the larger size of the individual particles.

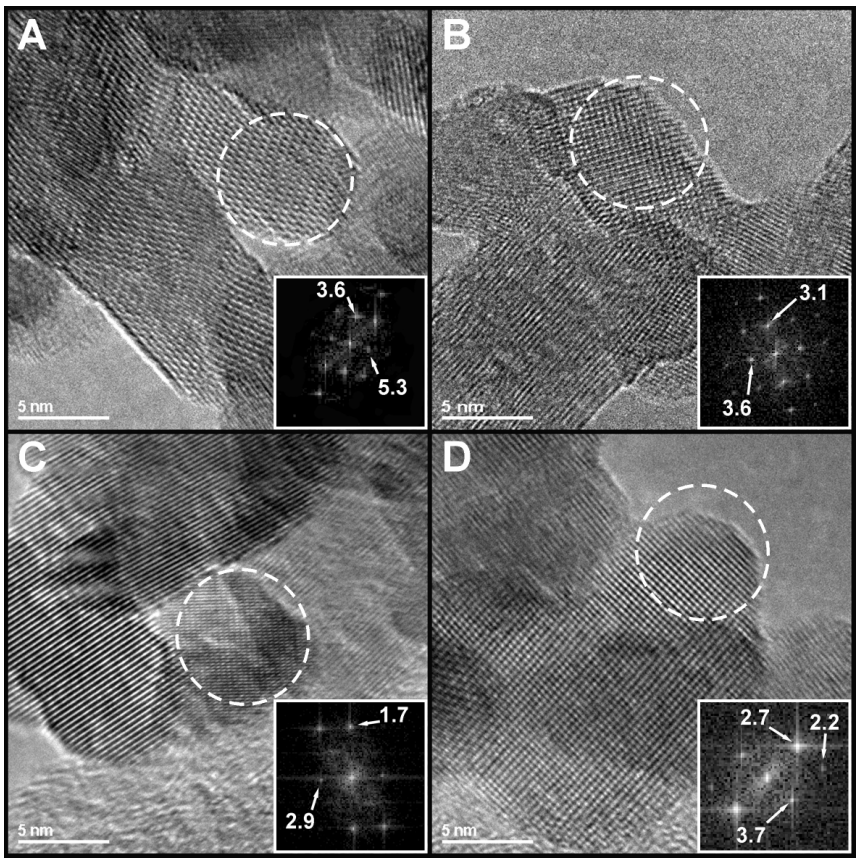

Figure 4.11 HRTEM images with DDPs inset for n0YSZ sample. Crystalline particles indexed to (A) tetragonal ZrO_2 viewed in [100] zone axis, (B) monoclinic ZrO_2 viewed in [112] zone axis (C) either cubic ZrO_2 viewed down [211] zone axis or tetragonal ZrO_2 viewed along either [311] or [131] zone axis, (D) monoclinic ZrO_2 viewed along the [211] zone axis.

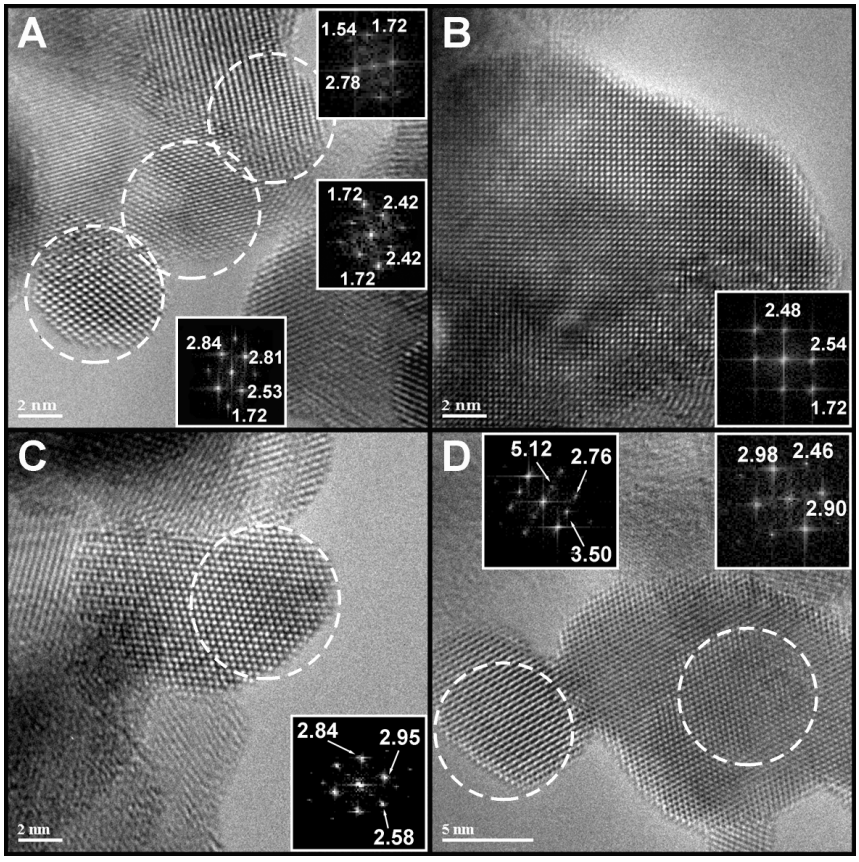

Figure 4.12 HRTEM images with DDPs inset for n3YSZ sample. Crystalline particles indexed to (A) cubic or tetragonal ZrO_2 viewed in three different orientations with DDPs adjacent (B) cubic ZrO_2 viewed in [100] or tetragonal ZrO_2 along either [001] or [110] zone axis, respectively (C) tetragonal ZrO_2 viewed along either [100] or [010] zone axis (D) monoclinic ZrO_2 (at left) along [011].

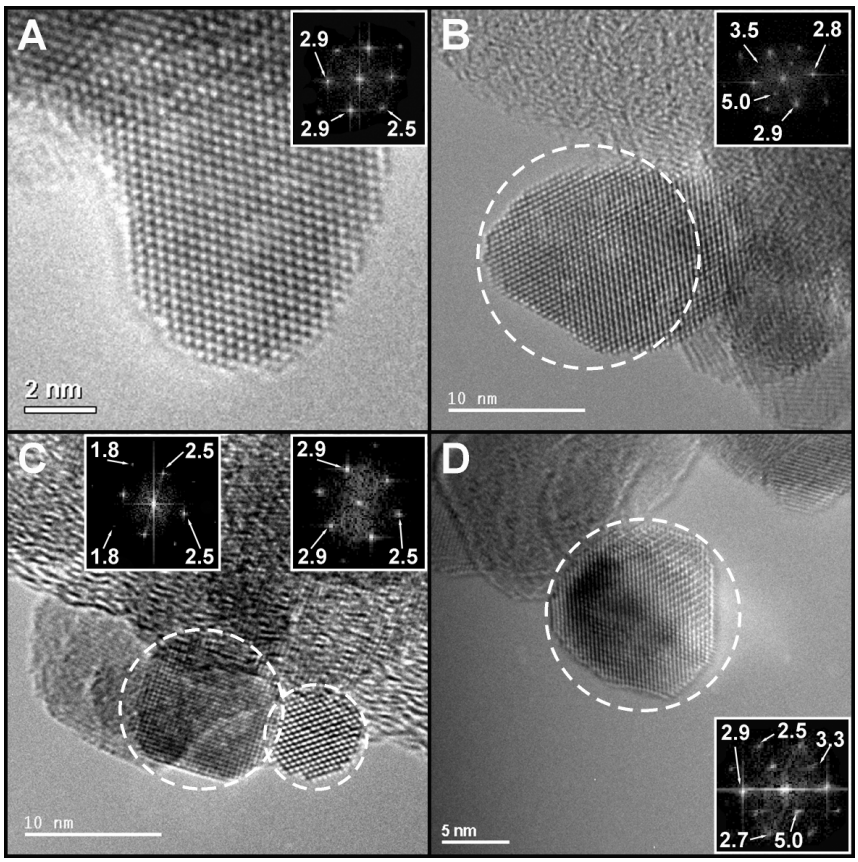

Figure 4.13 HRTEM images with DDPs inset for n5YSZ sample. Crystalline particles indexed to (A) cubic ZrO_2 viewed in [110] or tetragonal ZrO_2 viewed in [111] (B) tetragonal ZrO_2 viewed in [010] (C) two crystals in [100] and [110] (L & R, respectively) orientations if cubic ZrO_2 in [001] or [110], and [111] (L & R) if tetragonal ZrO_2 (D) monoclinic ZrO_2 viewed in [011].

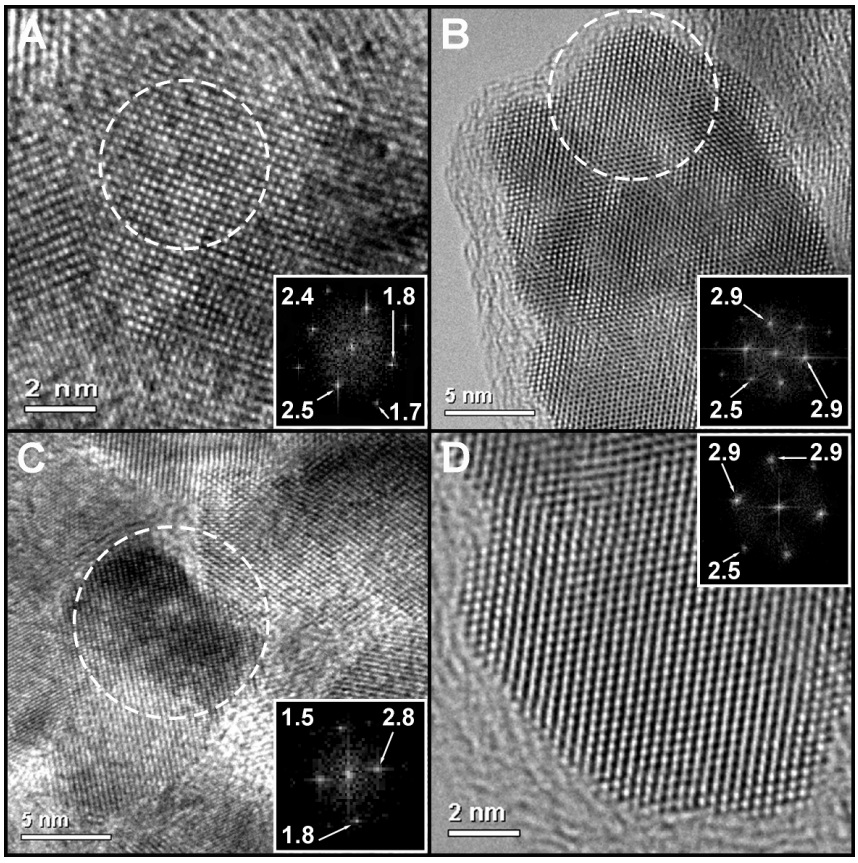

Figure 4.14 HRTEM images with DDPs inset for n8YSZ sample. Crystalline particles indexed to (A) and (B) cubic ZrO_2 viewed in [110] or tetragonal ZrO_2 viewed in [111] (C) cubic ZrO_2 viewed in [211] or tetragonal ZrO_2 viewed in [131]or [311] (D) cubic ZrO_2 viewed in [100] or tetragonal ZrO_2 viewed in [110] or [001].

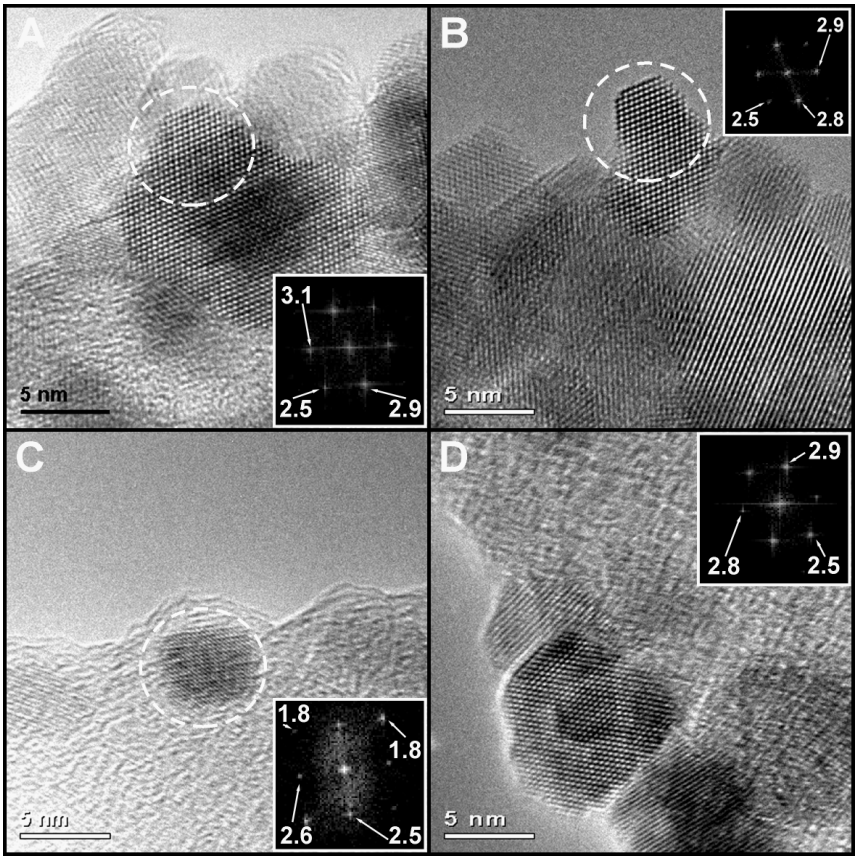

Figure 4.15 HRTEM images with DDPs inset for n10YSZ sample. Crystalline particles (A)&(B) cubic ZrO_2 viewed in [110] or tetragonal ZrO_2 viewed in [111] (C) cubic ZrO_2 viewed in [100] or tetragonal ZrO_2 viewed in [110] or [001] (D) cubic ZrO_2 viewed in [110] or tetragonal ZrO_2 viewed in [111].

4.3.3 Dilatometry

The sintering properties of compacted YSZ micro- and nanopowders in the five compositional variants of each were investigated using dilatometry. In addition, two pressing techniques – uniaxial and isostatic – were applied to all samples. Approximately 0.627 g of each YSZ composition was weighed out and pressed using a 10 mm die. The pressures used for the uniaxial and isostatic presses were 42 MPa and 207 MPa, respectively. After a correction run with an alumina standard, each YSZ pellet was subjected to a standard temperature programme. Synthetic air (50 ml/min) was used as the purge gas. A push-rod type dilatometer (Netzsch DIL 402C) was employed and the temperature was ramped from 25°C to 1500°C and back to 25°C. Heating and cooling rates were both 3°C/min and the duration of the isothermal part of the temperature programme at 1500°C was 4 h.

Figures 4.16 and 4.17 show heating and cooling curves obtained from the micropowder samples, while figures 4.18 and 4.19 represent their equivalents for nanopowders. In each, the two plots, (a) and (b), relate to the two different pressing techniques. Table 4.4 includes

quantitative data on total length change as well as the length changes during the heating, isothermal and cooling phase of the temperature programme.

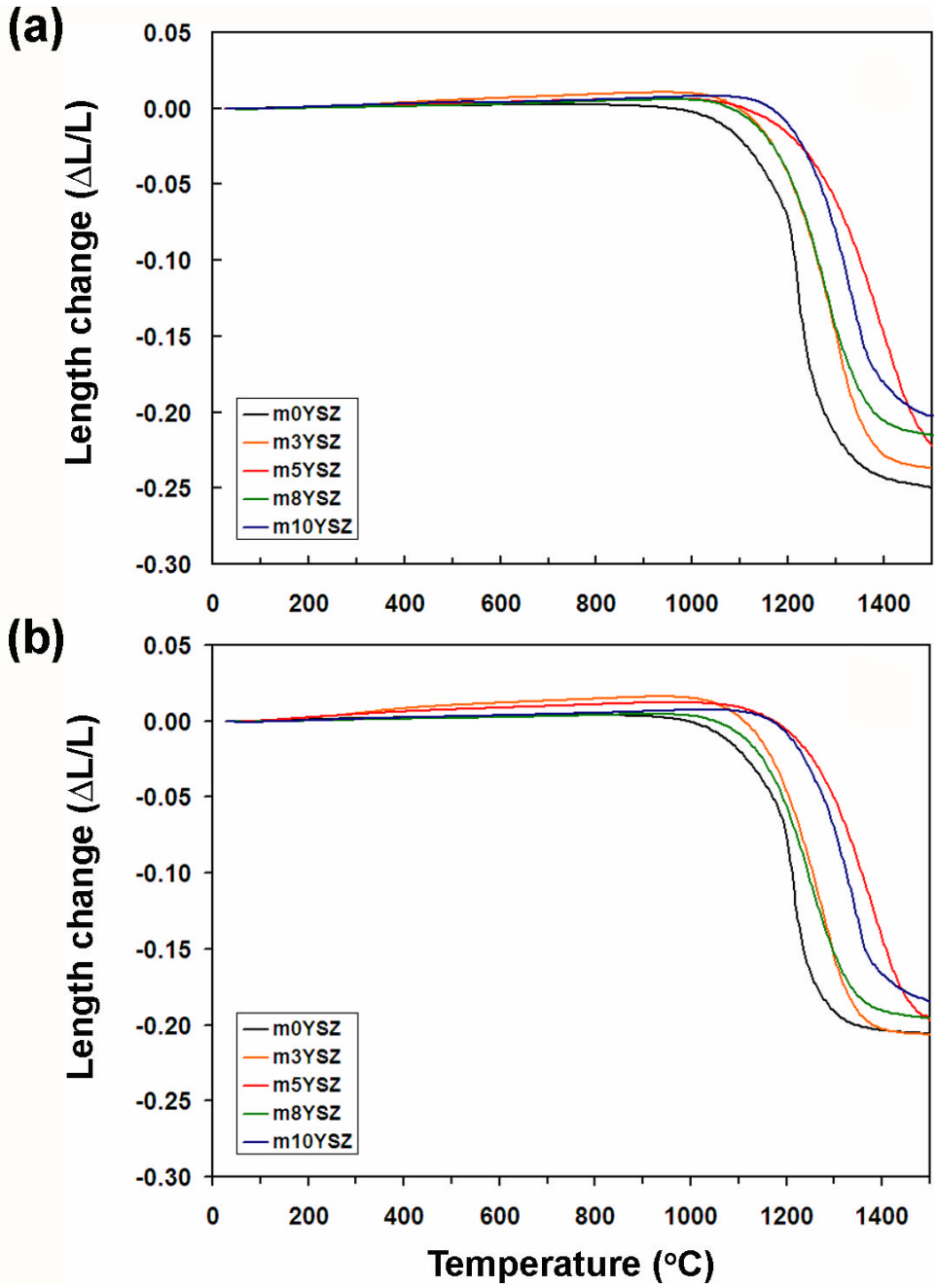

Figure 4.16 Heating phase curves for (a) uniaxially and (b) isostatically pressed micropowders.

In Figure 4.16, a certain thermal expansion was observed for all micropowder heating curves, which progressed up to 850-1000°C, depending on sample composition. This is likely to be caused by thermal expansion of individual microparticles before coalescence starts. It was noticed that unstabilised zirconia (regardless of pressing technique) started to shrink a little earlier, at ~950°C, than the substituted samples. According to the sintering information presented in Table 4.5, the temperature of onset of sintering (T_i) for the uniaxially pressed

micropowders followed the order: m0 < m3 < m5 < m8 < m10YSZ. That is, it corresponded with increasing yttria content. It is relevant that, from the TEM results, average particle size of the micropowders increased with increasing Y content. As particle size increases, surface energy decreases so sintering becomes less favoured. In addition, compositions of lower Y concentration could rearrange their smaller particles for contact growth stages much earlier, so that the sintering process would start earlier for them. This initial order was not maintained till the end of the sintering process, however, and resulted in the following order for the temperature at which the main stage of the sintering process was completed: m0 < m5 < m3 < m10 < m8YSZ. In addition, the total duration of sintering were found to vary slightly among compositions. The order - from the longest to the shortest time - was: m0 > m3 > m8 > m5 > m10YSZ, indicating an unusual behaviour for the m5YSZ sample.

The order of the temperature of onset of sintering for the isostatically pressed pellets was m0 < m8 < m3 < m5 < m10YSZ. Interestingly, the lower initial sintering temperature for the isostatically pressed m8YSZ did not match the order observed for the uniaxially pressed samples. Again, quite unusual behaviour was also observed for the 5 mol% YSZ pellet, in which sintering progressed at the lowest rates of any of these compositions. The temperature of completion of the sintering process (according to Table 4.5) increased in the order m0 < m3 < m8 < m5 < m10YSZ. The full sintering durations were found to decrease in the order m0 > m8 > m3 > m5 > m10YSZ and were found to be slightly different to the results from the uniaxially pressed micropowders.

In general, smaller length changes (shrinkage of up to ~20%) were observed for the isostatically pressed samples than for the uniaxially pressed micropowders (shrinkage of up to ~25%). The quantitative shrinkage data for all YSZ samples is summarised in Table 4.4 and shrinkage during the heating phase of the dilatometry measurements is represented by $\Delta L_h/L$. Overall, a decreasing trend in $\Delta L_h/L$ was observed with increasing Y content (except for 8 mol% YSZ samples), both for uniaxially and isostatically pressed YSZ micropellets. The lowest value of $\Delta L_h/L$ was observed for m10YSZ in the case of both compacting techniques.

Figure 4.17 shows the continuation of the decrease in volume (along with time) for the doped zirconia pellets on cooling from 1500°C to room temperature. Length change on cooling decreased with increasing yttria content, independently of pressing technique. As expected, a discontinuity in the curve for unstabilised zirconia pellets took place at ~1050°C because of the fracture of the pellet, which is related to a phase transformation in this material and is discussed in Section 1.3.3.1. In addition, curves of uniaxially pressed m3 and m5YSZ samples, exhibited less smooth shapes than the more heavily doped samples. For example, the

uniaxially pressed m5YSZ sample even showed a certain expansion on cooling starting at ~600°C. After the dilatometry experiments were completed, these pellets showed evidence of some cracking. It is suggested that this could be due to the fact that these samples with low dopant values are only partially phase-stabilised. The overall length change for the isostatically pressed samples was smaller than for those pressed uniaxially. The largest final shrinkage was observed for both m3YSZ pellets and gradually decreased with increasing Y content for the doped zirconia oxides. The curves for the isostatically pressed samples were more self-consistent than those for the uniaxially pressed samples.

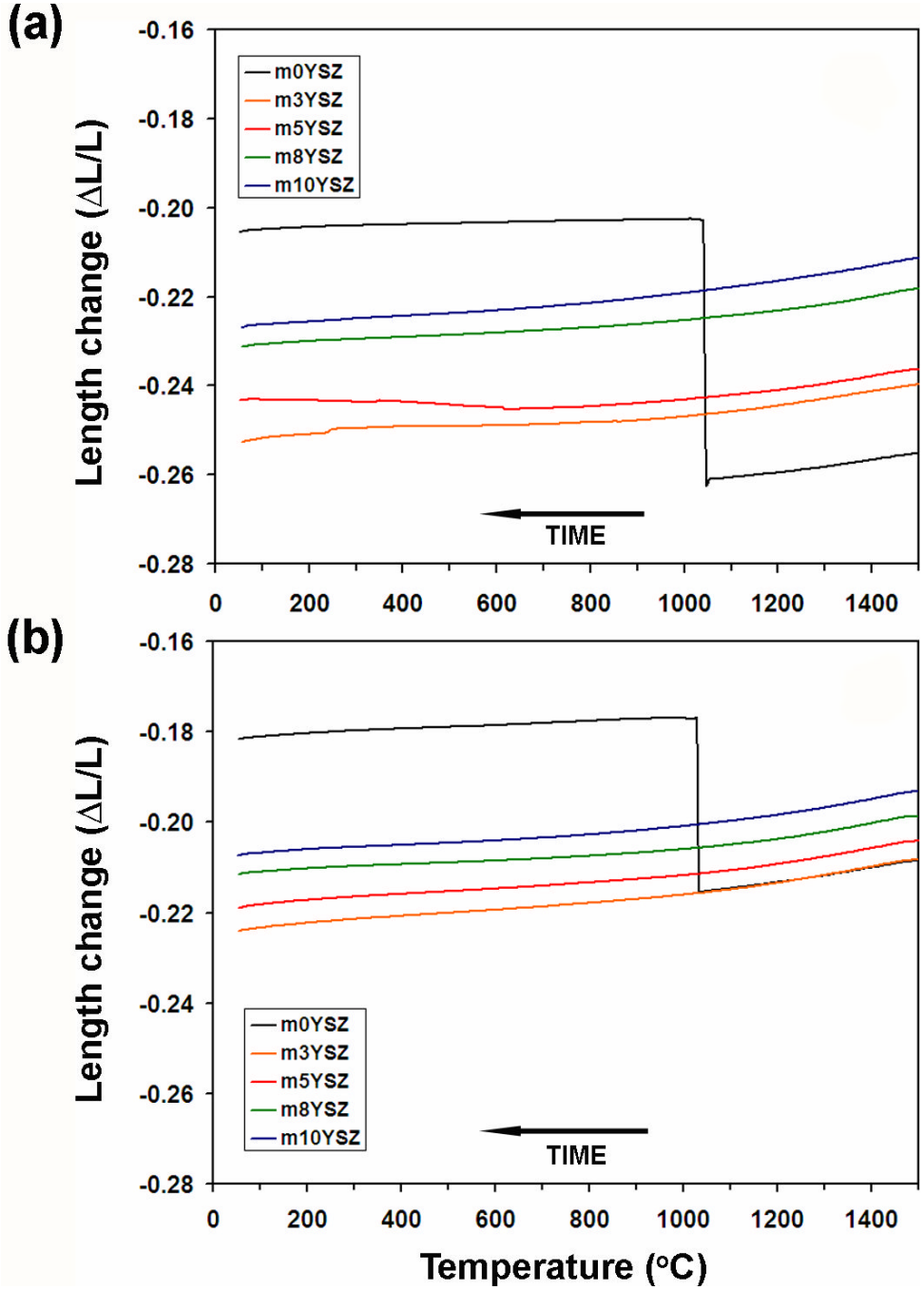

Figure 4.17 Cooling phase curves for (a) uniaxially and (b) isostatically pressed micropowders.

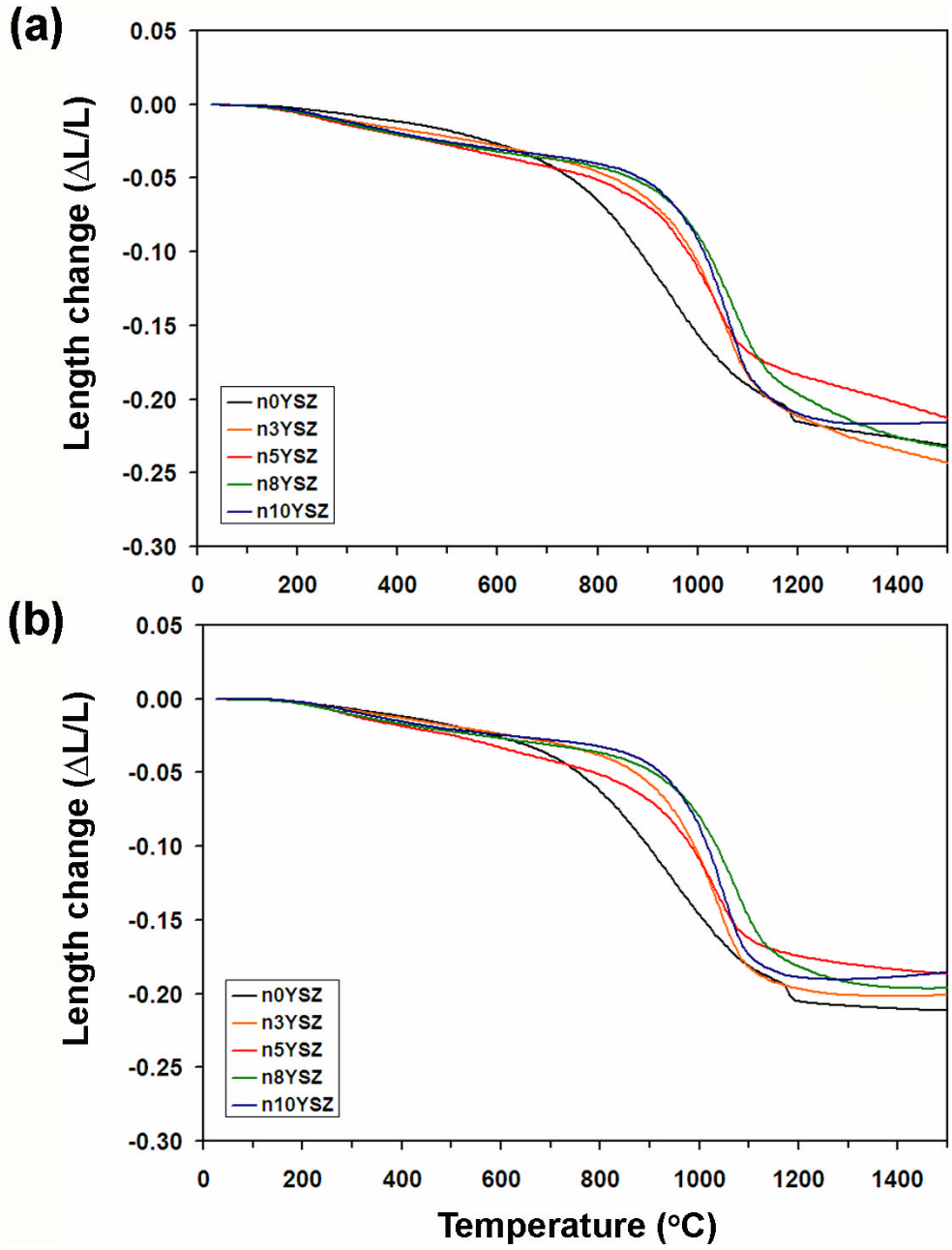

Figure 4.18 Heating phase curves for (a) uniaxially and (b) isostatically pressed nanopowders.

Figure 4.18 shows heating phase curves for uniaxially (plot (a)) and isostatically (plot (b)) pressed nanopowders. All pellets exhibited significantly different curve shapes from those of the micropowder samples. A gradual decrease in length was already observed at around 100°C. Isostatically pressed samples exhibited shorter sintering durations, as was also seen in the case of the micropowder samples. The total dimensional change during the heating phase was again larger than for the uniaxially pressed YSZ pellets and the highest shrinkage value of 24.2% was seen for the n3YSZ pellet (plot (a)). On the other hand, the isostatically pressed n3YSZ pellet showed a contraction of only 20.1% (plot (b)). T_i increased in the order

n0 < n3 < n8 < n10 < n5YSZ for uniaxially pressed nanopowders. The temperature at which the main sintering process was completed (T_f) increased in the order n10 > n0 > n5 > n8 > n3YSZ, as presented in Table 4.5. The undoped zirconia sample was also characterised by an additional abrupt shrinkage step at ~1200°C, which was not observed for the corresponding pressed micropowders in Figure 4.16. Unusually, both n10YSZ pellets exhibited a small degree of expansion in the high temperature region, which might be explained as thermal expansion of the pellet, assuming sintering was essentially complete. The sintering process ended slightly earlier than for the micropellets, at 1317°C and 1251°C for uniaxially and isostatically pressed 10 mol% YSZ nanopellets, respectively.

All of these findings suggest that nanopowders sintered more easily than micropowders and that the actual sintering process for doped samples could start earlier because of the presence of much smaller particles. These observations were consistent with a study by Zhu *et al*, who noticed a similar sintering behaviour for nanostructured 8 mol% YSZ prepared by a hydrothermal route, although they employed a higher heating rate of 5°C/min.[126] The authors pointed out that the early shrinkage could be related to a condensation of surface hydroxyl groups as specific production techniques of nanopowders, which sometimes result in a high quantity of hydroxyl groups being attached on the surface of the sample. As they condense during heating they drag adjacent particles closer, causing early shrinkage of the sample. By comparing the sintering information of samples with and without hydroxyl groups, the authors partially confirmed this theory as such rapid densification did not occur in the samples without surface hydroxyl groups.

Cooling phase results for nanopowders are presented in Figure 4.19. They also showed that smaller total dimensional change values were obtained for the isostatically pressed samples than for those prepared uniaxially. The largest final length change (26.5%) was found for n3YSZ, while the smallest value of 22.8% among uniaxially pressed pellets was for n10YSZ. The results for the isostatically and uniaxially pressed samples during the cooling phase were generally qualitatively similar. The only small difference was observed at ~500°C, when the traces for isostatically pressed n3YSZ and n8YSZ pellets crossed over. Both pure zirconia nanopowder samples exhibited the expected cracking on cooling at above 1000°C and further assessment of the final length change was not performed. Isostatically pressed n10YSZ samples shrunk by 19.8% during the whole dilatometry experiment. The n5YSZ sample decreased in length by 20.5%. Finally, both n3YSZ and n8YSZ ended contraction with a 21.2% dimensional change.

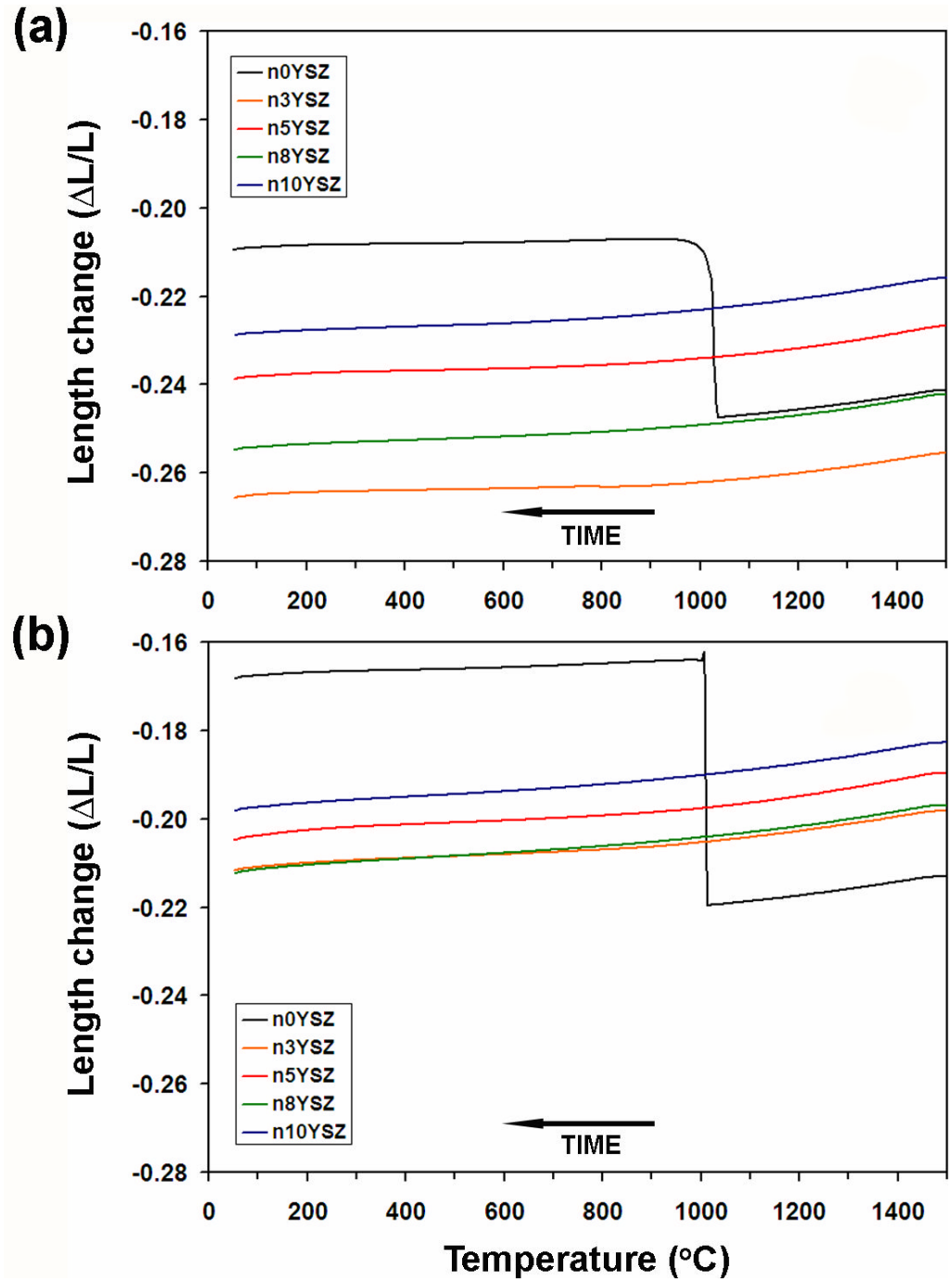

Figure 4.19 Cooling phase curves for (a) uniaxially and (b) isostatically pressed nanopowders.

Data of the total length change ($\Delta L_T/L$) for all YSZ pellets are given in Table 4.4. In addition, length changes during the heating ($\Delta L_h/L$), isothermal ($\Delta L_i/L$) and cooling ($\Delta L_c/L$) phases were extracted and included in this table. Data for the zirconia pellets are marked with an asterisk for $\Delta L_T/L$ and $\Delta L_c/L$ as these values are indicative of being affected by mechanical failure of the sample and are therefore not reliable. Each of the pure zirconia samples increased suddenly in length during the cooling phase, while all of the other samples shrank

during this period. It was confirmed after the measurements that the ZrO_2 samples had cracked. The isostatically pressed nanopowders exhibited the most consistent and the smallest length change among the doped zirconia pellets for the isothermal and cooling phases of the temperature programme for all compositions, shrinking by 1.0-1.5%.

Table 4.4 Information on length change for all YSZ samples.

Pressing method	*Sample*	$\Delta L_T / L$	$\Delta L_h / L$	$\Delta L_i / L$	$\Delta L_c / L$
uniaxial	m0YSZ	-0.205*	-0.249	-0.006	0.050*
	m3YSZ	-0.253	-0.236	-0.003	-0.014
	m5YSZ	-0.243	-0.216	-0.020	-0.007
	m8YSZ	-0.231	-0.217	-0.001	-0.013
	m10YSZ	-0.227	-0.203	-0.008	-0.016
isostatic	m0YSZ	-0.182*	-0.206	-0.003	0.027*
	m3YSZ	-0.224	-0.206	-0.002	-0.016
	m5YSZ	-0.219	-0.194	-0.010	-0.015
	m8YSZ	-0.212	-0.196	-0.003	-0.013
	m10YSZ	-0.207	-0.184	-0.009	-0.014
uniaxial	n0YSZ	-0.209*	-0.231	-0.010	0.032*
	n3YSZ	-0.266	-0.242	-0.013	-0.011
	n5YSZ	-0.239	-0.211	-0.016	-0.012
	n8YSZ	-0.255	-0.233	-0.009	-0.013
	n10YSZ	-0.229	-0.215	-0.001	-0.013
isostatic	n0YSZ	-0.168*	-0.211	-0.001	0.045*
	n3YSZ	-0.212	-0.201	-0.001	-0.010
	n5YSZ	-0.205	-0.186	-0.004	-0.015
	n8YSZ	-0.212	-0.196	-0.001	-0.015
	n10YSZ	-0.198	-0.186	-0.001	-0.011

$\Delta L_T/L$ – total length change during the whole temperature programme,
$\Delta L_h/L$ – length change during the heating phase,
$\Delta L_i/L$ – length change during the isothermal phase,
$\Delta L_c/L$ – length change during the cooling phase,
* – data affected by mechanical failure of the sample.

The sintering information from the heating phase of the temperature programme for all YSZ samples is summarized in Table 4.5. The initial (T_i) and final (T_f) temperatures were identified from each curve. Part of this range was selected and was used to determine values for the maximum sintering rate (SR_{max}) by fitting the near-linear section of each curve to a straight line in order to obtain the gradient.

Table 4.5 Sintering information for all YSZ samples.

Pressing method	*Sample*	T_i/°C	T_f/°C	ΔT/°C	$SR_{max} \times 10^{-4}$/K^{-1}
uniaxial	m0YSZ	939	1484	545	20.4
	m3YSZ	989	1494	505	12.8
	m5YSZ	1030	1485	455	9.71
	m8YSZ	1036	1500	464	11.9
	m10YSZ	1082	1497	415	12.1
isostatic	m0YSZ	966	1456	490	19.6
	m3YSZ	1002	1472	470	12.2
	m5YSZ	1047	1487	440	9.78
	m8YSZ	993	1478	485	9.98
	m10YSZ	1078	1488	410	12.9
uniaxial	n0YSZ	652	1477	825	4.84
	n3YSZ	773	1488	715	8.18
	n5YSZ	809	1479	670	6.60
	n8YSZ	790	1480	690	7.56
	n10YSZ	792	1317	525	10.1
isostatic	n0YSZ	660	1210	550	4.51
	n3YSZ	789	1294	505	8.63
	n5YSZ	770	1480	710	6.51
	n8YSZ	837	1392	555	7.31
	n10YSZ	821	1251	430	10.2

The SR_{max} values showed a significant difference in sintering kinetics between the two sets of YSZ samples. SR_{max} values were much greater for the micropowders. This may be because the micropowders showed much broader particle size distributions across the whole compositional range, which in turn might be expected to affect their sintering behaviour.

Figure 4.20 illustrates variations in the maximum sintering rates among all YSZ compositions. The pressing technique was found to possess a negligible impact on SR_{max} values, except for the 8 and 10 mol% YSZ samples. The highest values of SR_{max} were calculated for both pure zirconia micropellets and this may be explained by its phase

transformation from monoclinic to tetragonal as the temperature increased. The lowest SR_{max} values were observed for m5YSZ. In contrast, both pure zirconia compositions exhibited the smallest SR_{max} values among the nanopellet samples. This corresponds to the XRD results (Figure 4.4), which showed that nanozirconia powder is already (partly) stabilised in tetragonal form. As a result, such a sample showed much slower sintering kinetics than the micropowder equivalents. A smooth increase in SR_{max} values was observed from 5 to 10 mol% YSZ, for both sets of pellets, regardless of the pressing technique.

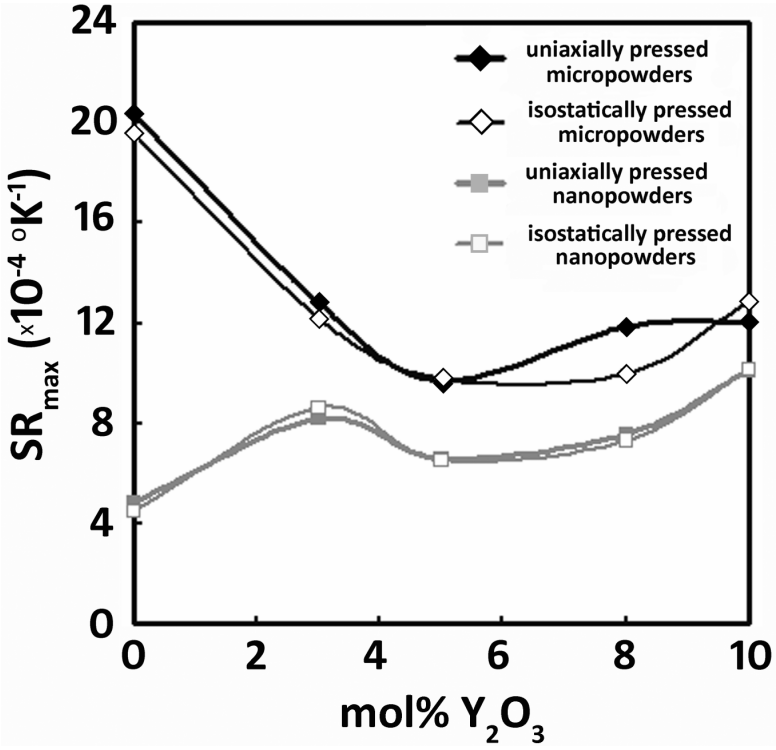

Figure 4.20 Maximum sintering rates for all YSZ pellets.

The fact that nanopowders started sintering at much lower temperatures than the micropowders is in agreement with a study by Han *et al*, who observed that the start of sintering is related to the grain diameter.[127] They stated that the smaller the grain size, the lower the temperature of onset of sintering. The information provided by these authors on the final sintering temperatures and rates is consistent with results obtained in the current work. However, since they applied more complex sintering regimes, the results can not be compared directly.

The data from the cooling curve of each YSZ sample was also used to obtain an approximation of the thermal expansion coefficient (α) - one of the most important thermodynamic properties. These were calculated for three different temperature ranges and are summarised in Table 4.6. The thermal expansion coefficient (α) was calculated from the ratio of length change difference (ΔL/L) to temperature difference (ΔT). α_1 refers to the total temperature range (temperature difference, ΔT_1) during the cooling phase for each pellet. The thermal expansion coefficient for the pure zirconia samples (marked with an asterisk) was taken from the data in the high temperature range, before the sample cracked, (α_2 and ΔT_2) and corresponding values of α_2 were calculated for the other compositions, to allow direct comparison with the pure zirconia samples. Values of α_2 are the most reliable for comparing across the samples. All α_2 values fell in the range of $13.8 – 17.1 \times 10^{-6}$ °C^{-1} and were generally higher for the isostatically than the uniaxially pressed samples. The temperature difference, ΔT_3, related to the low temperature range, thus after the tetragonal to monoclinic phase transformation of pure zirconia. According to Figure 4.19a this change took place over a longer time period for uniaxially pressed nanozirconia than for the other samples. Due to this uncertainty, the temperature interval, ΔT_3, was set at slightly lower temperatures for the nanopellets. The expected discrepancies were found for α_3 for the lightly doped micropellets and were found to be similar to the α_1 results. In the case of the nanopellets, a smooth increasing trend for α_3 was observed with increasing Y content.

The thermal expansion coefficients were found to be in the same range as for YSZ samples reported in the literature.[57, 128, 129] The isostatically pressed nanopowders possessed larger thermal expansion coefficients than the uniaxially pressed nanopowders. The nanopowders exhibited a clear trend in which α increased as mol% Y_2O_3 increased. No such monotonic trend was seen for the micropowders. The trend in α for the nanopowder samples might be attributed to the weakening of the dopant-oxide binding energy resulting from the increase in oxygen vacancy concentration. Arachi *et al* suggested that the difference in the lattice binding energy in ZrO_2-Ln_2O_3 systems is related to the difference in thermal expansion coefficients among samples.[62] Hayashi *et al* reported a gentle decrease in α with increasing Y_2O_3 content.[129] This is partly preserved here for the 3, 5 and 8 mol% YSZ isostatically pressed micropowder samples. It should be noted that differences among α values for different YSZ compositions are relatively small, both in reported α results and those obtained in this work. However, the unusual behaviour of some samples will be further examined with reference to elemental analysis results.

Table 4.6 Thermal expansion coefficients for all YSZ samples.

Pressing method	*Sample*	ΔT_1 /°C	$\alpha_1 \times 10^{-6}$ / °C $^{-1}$	ΔT_2 /°C	$\alpha_2 \times 10^{-6}$ / °C $^{-1}$	ΔT_3 /°C	$\alpha_3 \times 10^{-6}$ / °C $^{-1}$
uniaxial	m0YSZ	-1440	4.79*	-438	15.4	-980	2.71
	m3YSZ	-1445	8.94	-448	14.6	-977	6.21
	m5YSZ	-1435	4.75	-433	14.3	-981	0.43
	m8YSZ	-1444	9.05	-447	14.5	-976	6.50
	m10YSZ	-1445	10.7	-446	16.0	-978	8.30
isostatic	m0YSZ	-1435	4.77*	-434	15.3	-968	4.70
	m3YSZ	-1430	11.0	-429	16.4	-968	8.58
	m5YSZ	-1434	10.3	-435	16.1	-964	7.66
	m8YSZ	-1430	8.96	-429	15.8	-968	5.93
	m10YSZ	-1434	9.85	-433	16.3	-969	6.80
uniaxial	n0YSZ	-1439	4.31*	-437	13.8	-890	2.46
	n3YSZ	-1434	7.00	-434	14.2	-889	3.29
	n5YSZ	-1430	8.35	-429	15.7	-893	4.71
	n8YSZ	-1429	8.68	-429	14.8	-892	5.69
	n10YSZ	-1434	8.98	-443	15.1	-891	5.77
isostatic	n0YSZ	-1430	4.57*	-429	14.2	-893	4.44
	n3YSZ	-1430	9.34	-428	15.1	-894	6.41
	n5YSZ	-1430	10.5	-428	17.1	-894	7.34
	n8YSZ	-1428	10.7	-429	15.5	-891	8.26
	n10YSZ	-1430	10.8	-428	15.7	-894	8.25

ΔT_1 – total temperature difference during the whole cooling phase,
ΔT_2 – the temperature difference between the start of the cooling phase and up to 1050°C (due to ZrO_2 cracking, so that verified consequently for all remaining samples),
ΔT_3 – the temperature difference between the end of ZrO_2 cracking and room temperature.

4.4 Pellet characterisation

As seen in the dilatometry results, further studies of the dense, pure zirconia samples had to be limited to XRD studies because of the pellets cracking under sintering. Initially, four compositions of YSZ pellets derived from the micropowders were provided in duplicate by MEL. For consistency, nanopellets were prepared following the same pressing and sintering regime. Approximately 4.7 g of each nanopowder was pressed uniaxially into 25 mm pellets under 41 MPa. These green bodies were placed in a tube furnace and fired in static air at 1450°C for 4 h to allow sintering to occur. More details of the two-step sintering process are presented in Figure 4.21. The resulting discs were ground flat and polished to a 1 μm finish in order to obtain a smooth surface using diamond paste. The resulting nanopellets, and the micropellets supplied by MEL, were prepared for SEM and IS studies separately because each technique required different procedures of surface preparation. Detailed information is provided in the corresponding sections.

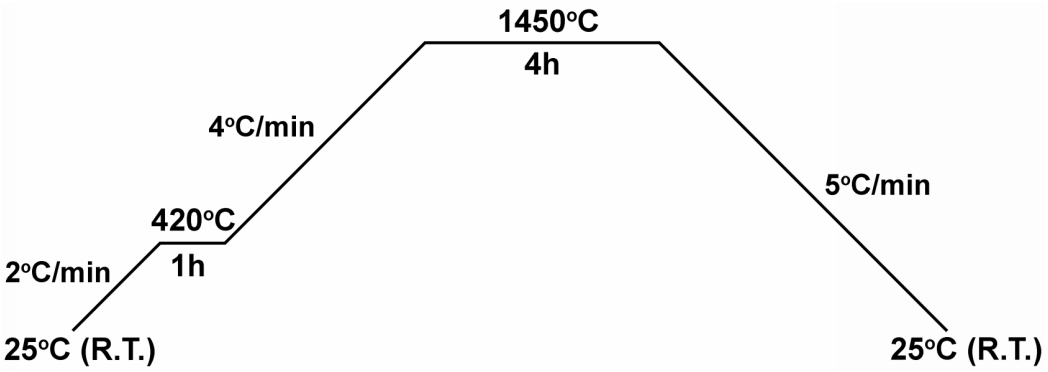

Figure 4.21 Thermal cycle for sintering of YSZ pellets.

4.4.1 X-ray Diffraction

XRD studies were performed in order to compare crystallographic data before and after the sintering process, according to the procedures described in Section 4.3.1. Figure 4.22 shows diffractograms of the micropellets, while Figure 4.23 presents data for the nanopellets. Individual compositions of both sets of YSZ pellets resulted in similar XRD patterns. All micropellet peaks occurred in the same 2θ region as for nanopellets. Peaks corresponding to monoclinic, tetragonal and cubic phases are indicated with m, t and c letters, respectively. Intensities of the peaks obtained were clearly much higher than those for either of the powder sets, and all diffraction peaks were much narrower, because of the bigger crystallite sizes expected after sintering at the high temperature used.

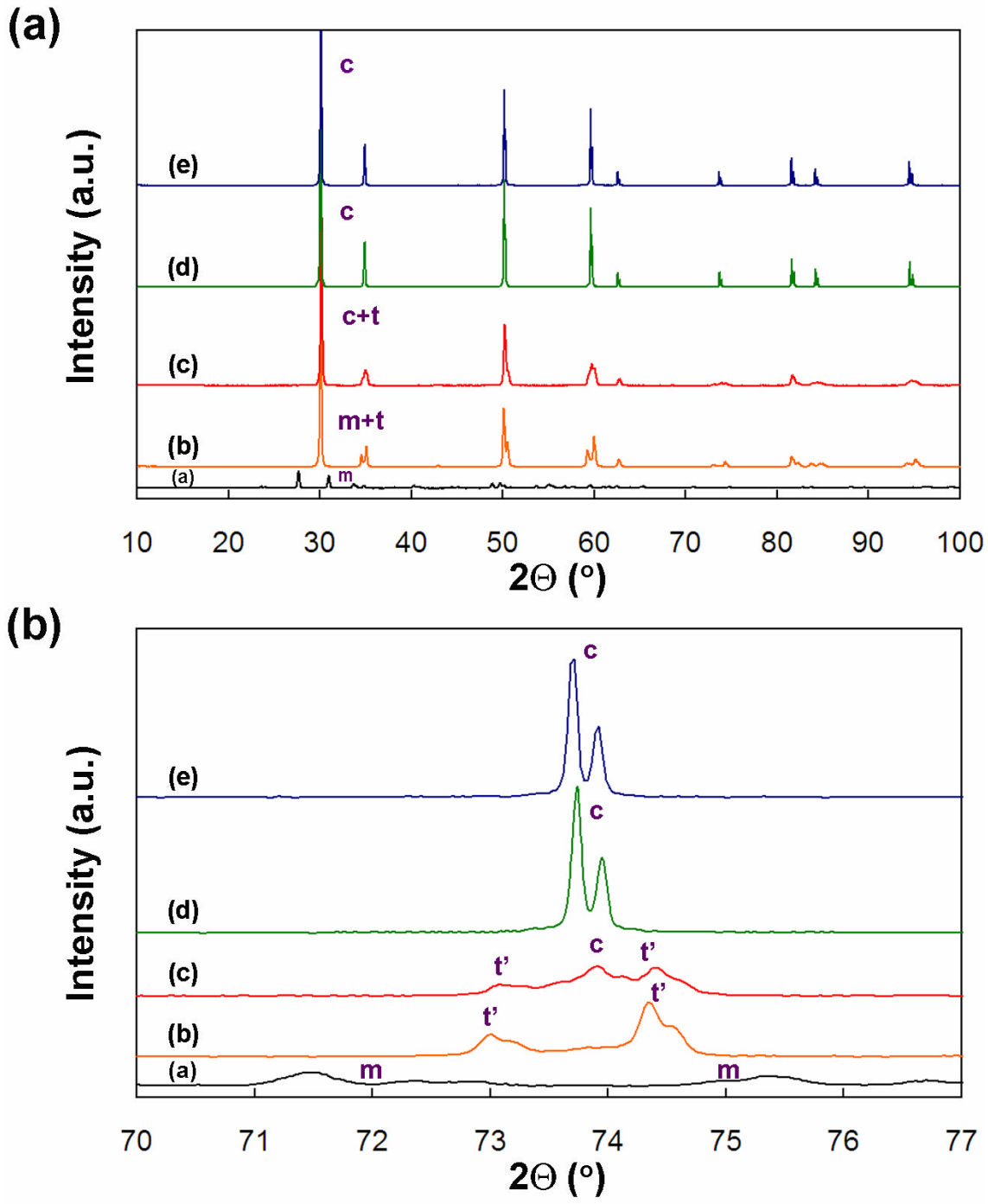

Figure 4.22 (A) Full diffraction patterns (A) and detailed of 2Θ = 70–77° region (B) for (a) M0YSZ, (b) M3YSZ, (c) M5YSZ, (d) M8YSZ and (e) M10YSZ.

All pellet samples exhibited the phases already observed for the micro- and nanopowders. However, in this study these could be confirmed more precisely. Figures 4.22b and 4.23b show a triplet of peaks for the 5 mol% YSZ pellets in the range of 2θ = 70–77°, indicating a mixture of the tetragonal and cubic phases. The peaks corresponding to the tetragonal phase appear to be smaller relative to those of the cubic phase than in the corresponding diffractograms of the 3 mol% YSZ. Doublets characteristic of the two very close X-ray source

frequencies are seen clearly in Figures 4.22b and 4.23b for 8 mol% YSZ, while in the nanopowder material only one broad peak was seen and the splitting effect was deduced by comparison with the relevant micropowder sample (see Figures 4.2 and 4.4). The peaks corresponding to the monoclinic phase for the pure zirconia pellets, when compared in detail in Figures 4.22b and 4.23b, and with those of the nanopowders, show that sintering the nanopowder causes a phase change from largely tetragonal to monoclinic.

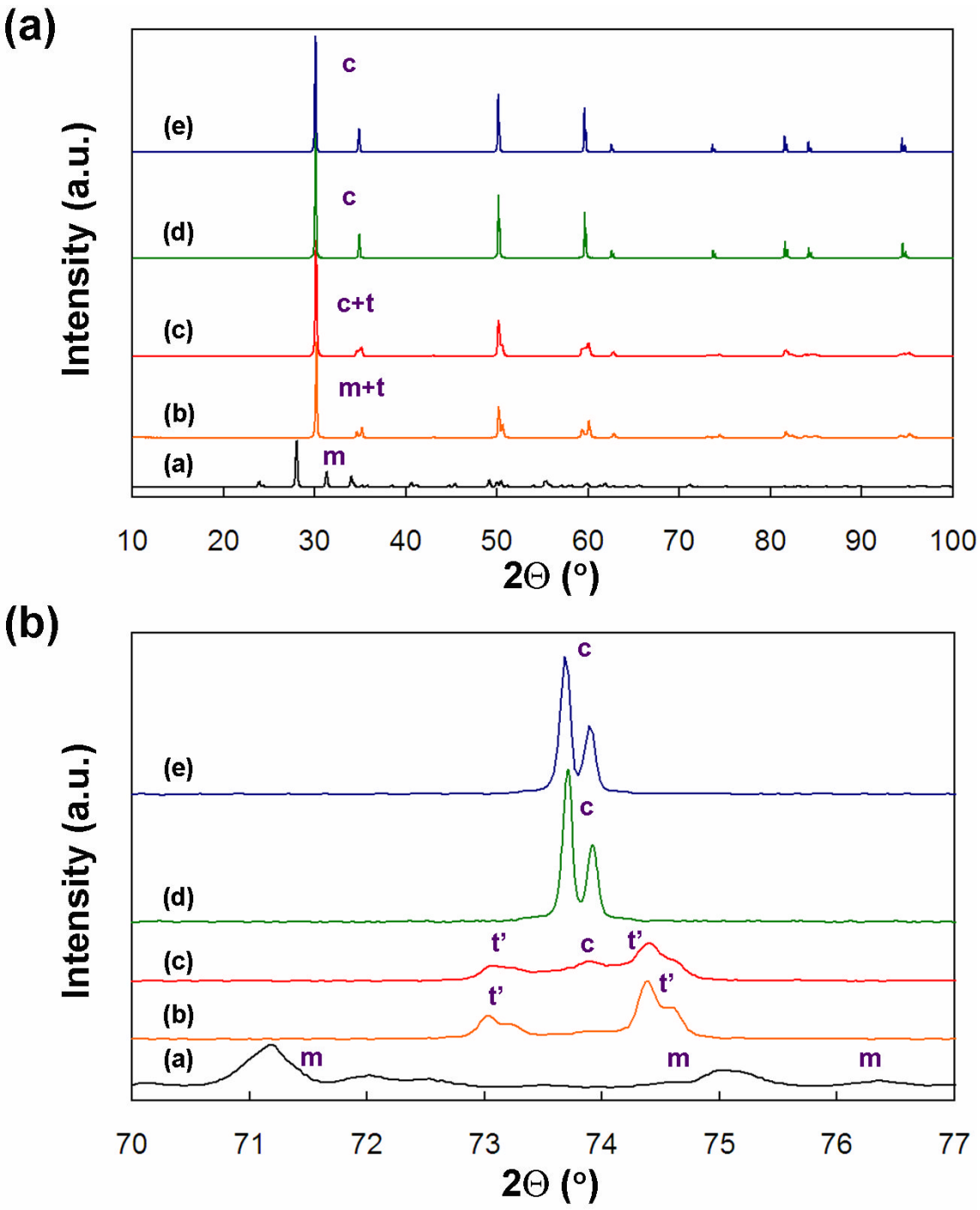

Figure 4.23 Full diffraction patterns (A) and detail of 2Θ = 70–77° region (B) for (a) N0YSZ, (b) N3YSZ, (c) N5YSZ, (d) N8YSZ and (e) N10YSZ.

The results obtained from XRD experiments on the sintered YSZ pellets clearly confirmed that the sintering process led to retention of the phases observed in the powder forms of both batches of raw materials. This thermal treatment revealed, however, the notable exception that the metastable tetragonal phase was stabilised in the nanopowder (Figure 4.4), but it reverted to the thermodynamically preferred monoclinic phase on sintering (Figure 4.23).

4.4.2 Scanning Electron Microscopy

All pellets analysed in SEM experiments were wet ground with SiC paper and then polished using a polishing wheel with diamond paste. In order to obtain high quality images of pellet microstructure, two additional steps were required. First, all pellets were thermally etched by an additional sintering process. This step was performed by employing the same conditions as presented in Figure 4.21, but in which the final isothermal treatment was performed at 1400°C and for only 1 min. The purpose of this step was to cause slight swelling of the grains from the polished surface so as to allow their imaging in the SEM. Since these conditions were less severe than those used to sinter the pellets, the previously established microstructure should essentially be retained. In the second surface preparation step, a 30 nm conducting layer of Au/Pd was deposited by sputtering using a Sputter Coater (Cressington 208 HR). All pellets for SEM studies were mounted using sticky carbon pads as usual. All images were obtained using a Philips XL30 ESEM (Environmental SEM) equipped with a field emission gun. Approximately 20 images were collected for each sample and grain sizes were measured using Scion Image freeware (version Alpha 4.0.3.2).

Figure 4.24 and 4.25 present micrographs of pellets derived from the micropowder and the nanopowder, respectively, and with the four YSZ compositions, at low and high magnifications and accompanied by their corresponding grain size distributions. A dense microstructure was confirmed for all YSZ pellets. Pores were only observed for the 10 mol% YSZ pellets for both sets of samples. All SEM images clearly show how strongly a microstructure is affected by doping of ZrO_2 with different amounts of yttria. Values of average grain size calculated from a representative number of approximately 130 grains for each pellet are presented in Table 4.7. An exponential increase in the grain size with increasing mol% of yttria was observed for both sets of pellets. A significant growth was observed when yttria content increased from 5 to 8 mol%, and then to 10 mol% in both sets of pellets. Mean grain size values for N8YSZ and N10YSZ were significantly lower than for the micropellets of the same compositions. Only a very negligible difference was noticed in mean grain size between the micropellets and the nanopellets for the 3 mol% and for the 5 mol% YSZ

samples. Moreover, only the N3YSZ sample possessed a higher average grain size value than the corresponding M3YSZ sample.

Table 4.7 Mean grain size data for micro- and nanopellets.

mol% Y_2O_3	*Mean grain size/nm*	
	Micropellets	*Nanopellets*
3	380.0	384.0
5	447.0	442.0
8	1422	1188
10	4438	3379

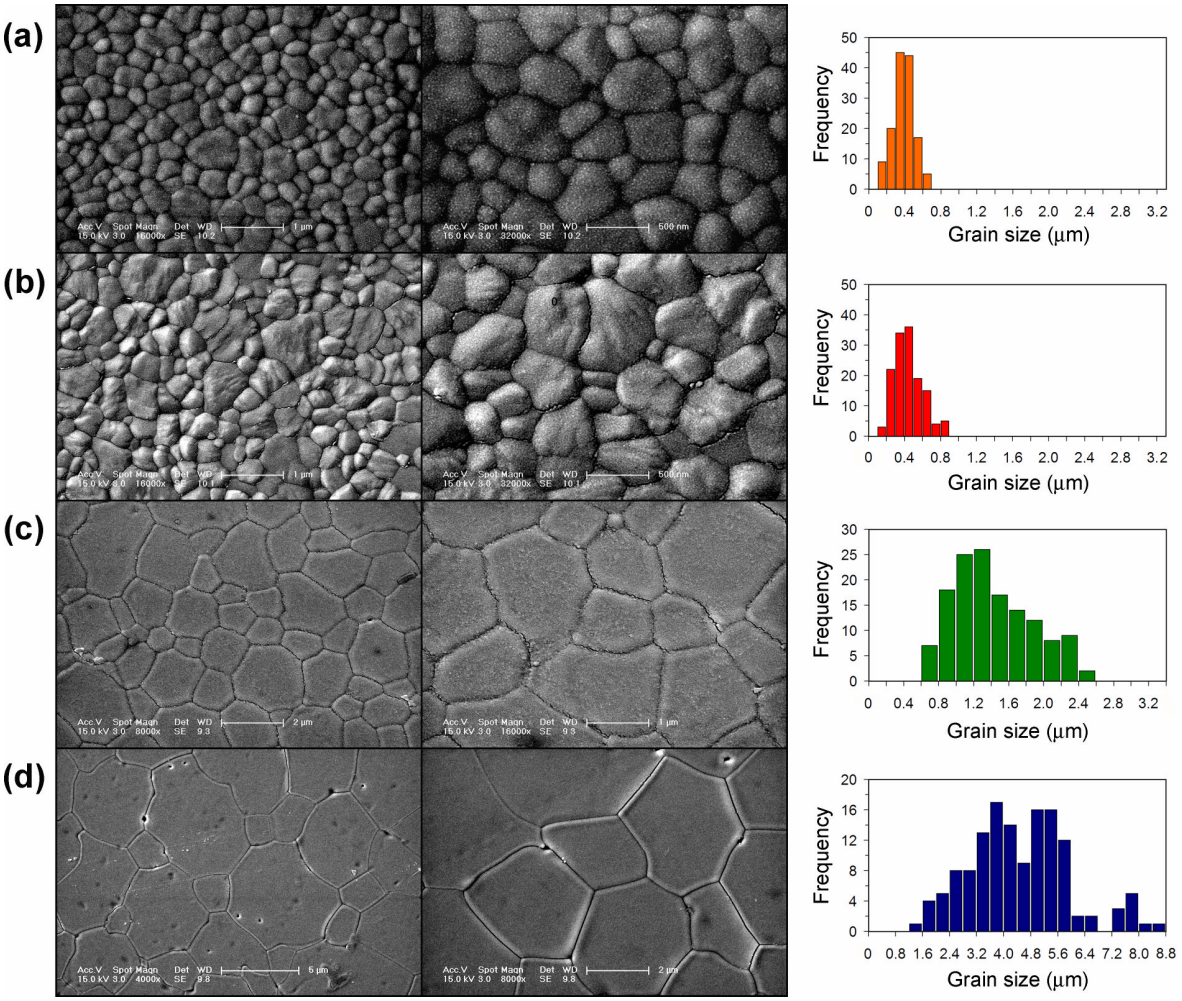

Figure 4.24 SEM images of micropellets and their corresponding grain size distributions for (a) M3YSZ, (b) M5YSZ, (c) M8YSZ and (d) M10YSZ.

The grain size distributions presented in Figure 4.24 and Figure 4.25 confirmed that smaller grains were observed for the nanopellets than for the micropellets for samples with

the higher yttria contents. It was rather unusual, because better sintering characteristics were noticed for nanosamples in the dilatometry results and so larger grains were expected. In general, the increasing trend in the grain size was observed with increasing Y content in both figures. A narrow grain size distribution was observed for 3 and 5 mol% YSZ samples, for both the micro- and nanopellets. A bimodal grain size distribution is suggested for the 10 mol% micropellet, but this is probably an artefact caused by the broad distribution and relatively small number of particles counted.

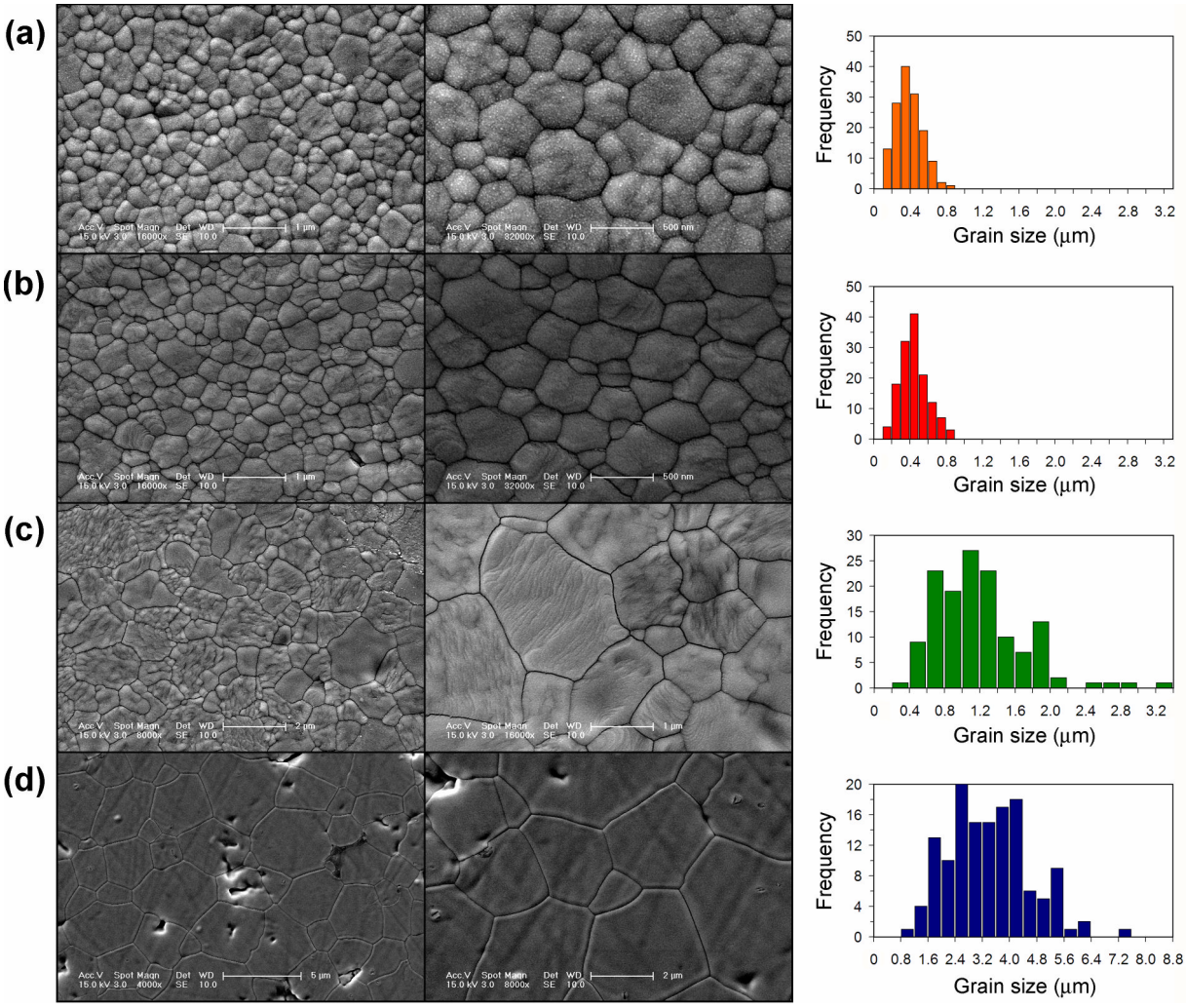

Figure 4.25 SEM images of nanopellets and their corresponding grain size distributions for (a) N3YSZ, (b) N5YSZ, (c) N8YSZ and (d) N10YSZ.

4.4.3 Impedance Spectroscopy

The sintered pellets derived from micro- and nanopowder sets were analysed by IS according to the procedures and experimental set-up described in Section 3.6. Beside the varying percentage of yttria and the variations in microstructure, the main differences between the two batches of YSZ were associated with the thickness of each sample and its electrode surface area. These parameters were taken into account in conductivity calculations, according to Equation 2.17. Figures 4.26 and 4.27 show Nyquist plots of all compositions obtained at selected temperatures of 250, 300, 400, 500, 600 and 800°C. Data collected at other temperatures were included in Arrhenius plots presented in Figures 4.28-4.30 and these are discussed below.

The complex impedance spectra of micro- and nanopellets recorded at 250°C (Fig. 26a and Fig. 27a) exhibited an increase in the relative size of bulk arc and a decrease in the relative size of the grain boundary arc with increasing yttria percentage. The ionic conductivity associated with the grain boundary arc therefore became dominant (as its resistance decreased) compared to the conductivity of the bulk process.

Similar observations on the relative size of the bulk and grain boundary arcs as for 250°C were noticed at 300°C (Fig. 26b and Fig. 27b). Electrode contributions were also observed at low frequencies. These were included during a fitting procedure in equivalent circuit model as a parallel arrangement of a resistor and a constant phase element. The bulk arc was lost from the spectra at 500°C due to the inductive effects between electromagnetic field and wires, which occurred at high frequencies. The complete full arcs due to diffusion processes at electrodes were observed at high frequencies above 500°C.

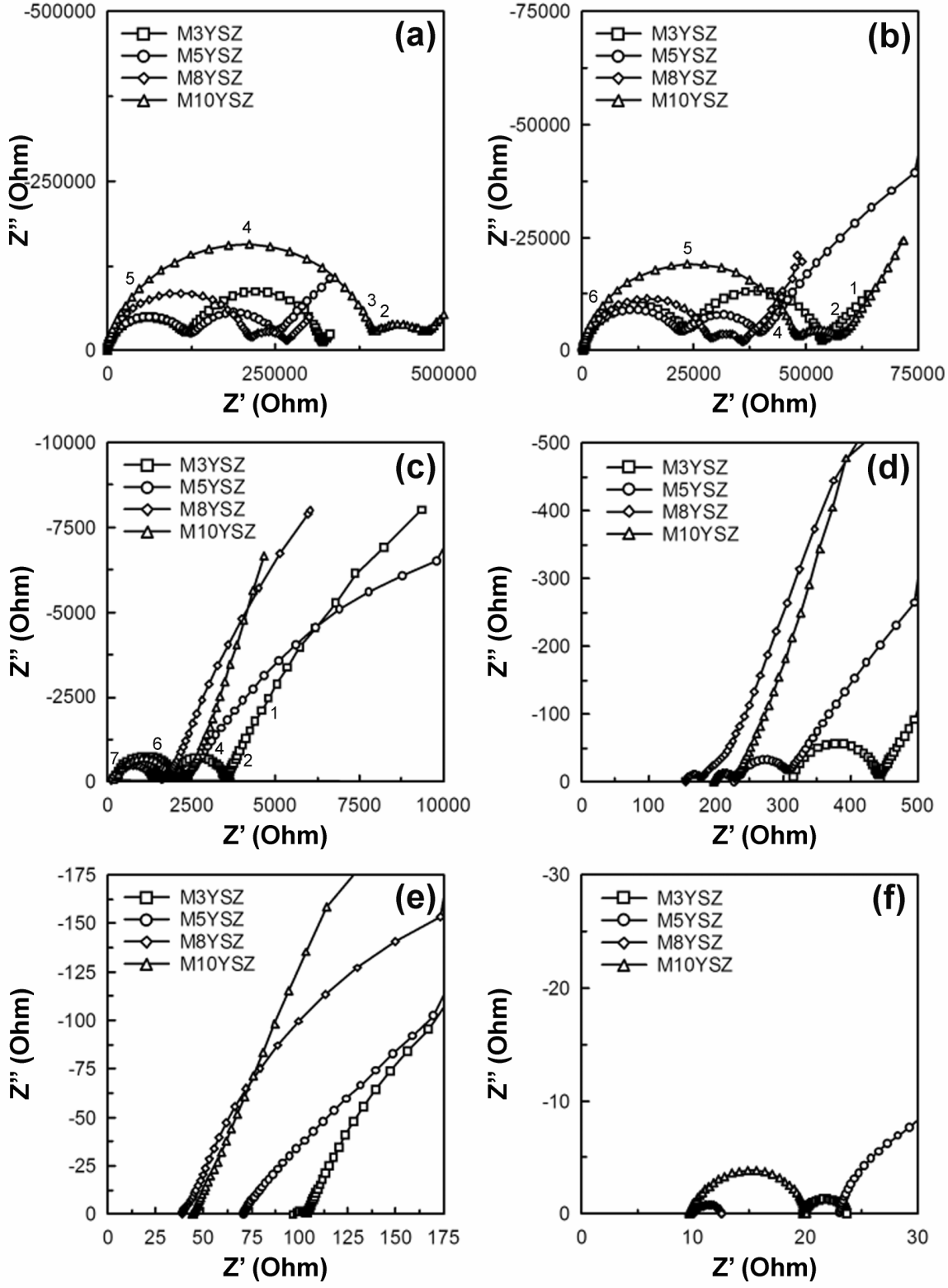

Figure 4.26 Nyquist plots for micropellets obtained in synthetic air at: (a) 250°C, (b) 300°C, (c) 400°C, (d) 500°C, (e) 600°C and (f) 800°C.

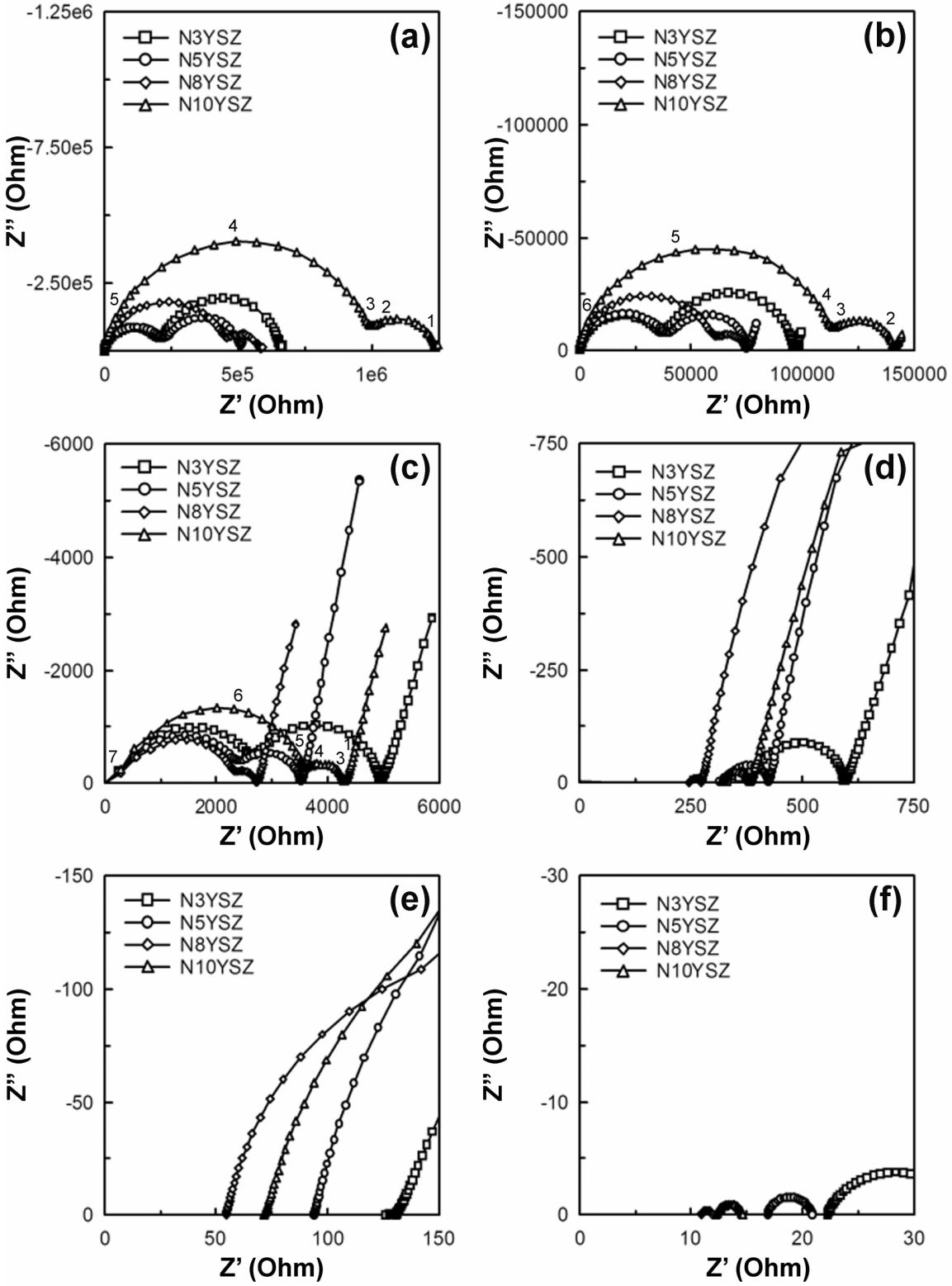

Figure 4.27 Nyquist plots for nanopellets obtained in synthetic air at: (a) 250°C, (b) 300°C, (c) 400°C, (d) 500°C, (e) 600°C and (f) 800°C.

Arrhenius plots were found to be useful for comparing the conductivity data as they include sample geometry. In addition, these were used to understand better the conductivity data in relation to the temperature. The bulk and grain boundary contributions as well as total ionic conductivity for each doped zirconia pellet are presented separately in Figures 4.28-4.30 by plotting data for micro- and nanopellets in the same figure (plot a and b, respectively).

As presented in Figure 4.28a, the bulk conductivity at temperatures up to 400°C decreased with increasing yttria content in the micropellets. The highest values were found for the least doped zirconia, while the lowest conductivities data were for M10YSZ. This order changed to M8YSZ > M10YSZ > M5YSZ > M3YSZ at about 400°C, which was identified as a key temperature in the interpretation of a conduction mechanism on the basis of the Nyquist plots. Conductivity data were also collected at 350°C for both M8YSZ and M10YSZ in order to confirm this significant change. Figure 4.28b shows that the bulk conductivity of the nanopellets decreased in the order: N3YSZ > N5YSZ > N8YSZ > N10YSZ at temperatures up to about 350°C, a slightly lower temperature than for the micropellets. At higher temperatures, the trend changed to N8YSZ > N5YSZ > N3YSZ > N10YSZ and finally to N8YSZ > N10YSZ > N5YSZ > N3YSZ at 500°C.

The grain boundary contribution is compared in Figure 4.29 for micropellets in plot (a) and nanopellets in plot (b). The highest grain boundary conductivity values were confirmed for M8YSZ and the order M8YSZ > M10YSZ > M5YSZ > M3YSZ was maintained throughout the temperature range. In the case of nanopellets, the grain boundary conductivity order of N8YSZ > N10YSZ > N5YSZ > N3YSZ was maintained in the 200-500°C temperature range. For spectra recorded at 150°C and 200°C it was difficult to obtain accurate values for the grain boundary arc, especially for heavily doped zirconia nanopellets. This experimental limitation may explain why the order changed to N8YSZ > N5YSZ > N10YSZ > N3YSZ at these low temperatures.

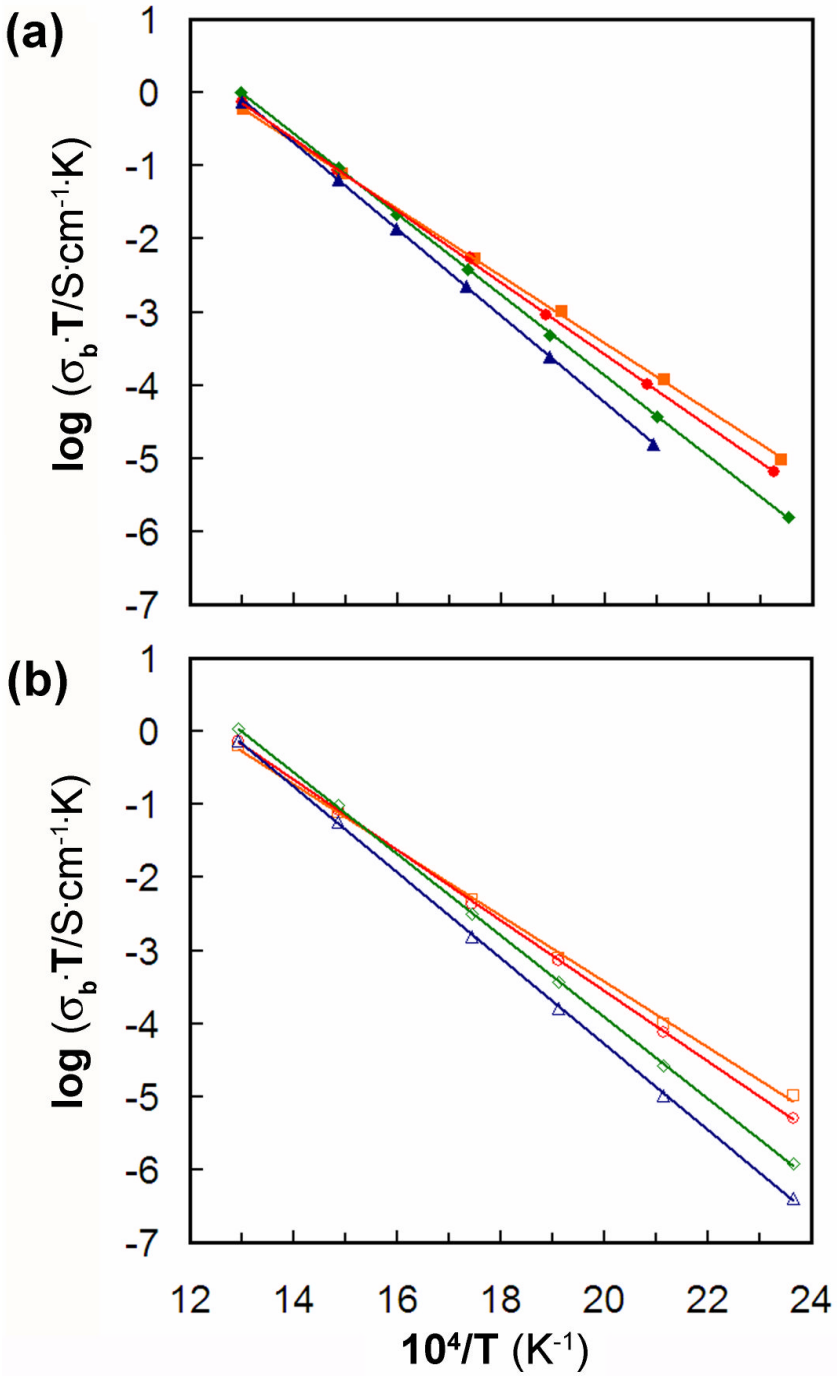

Figure 4.28 Arrhenius-type plots of bulk conductivity of (a) micropellets – M3YSZ(■), M5YSZ(●), M8YSZ(♦), M10YSZ(▲) and (b) nanopellets – N3YSZ(□), N5YSZ(○), N8YSZ(◊), N10YSZ(Δ).

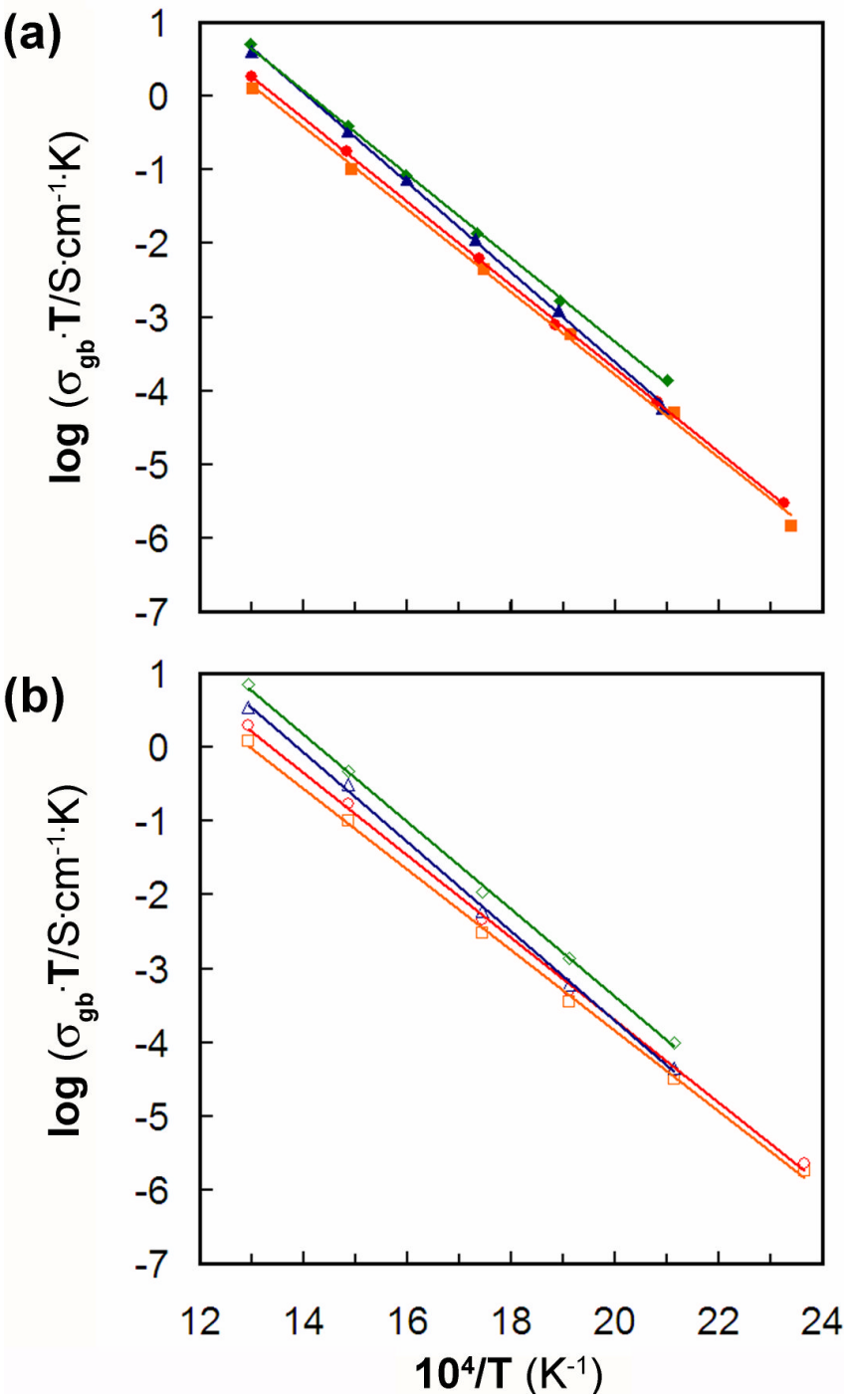

Figure 4.29 Arrhenius-type plots of grain boundary conductivity of (a) micropellets – M3YSZ(■), M5YSZ(●), M8YSZ(♦), M10YSZ(▲) and (b) nanopellets – N3YSZ(□), N5YSZ(○), N8YSZ(◊), N10YSZ(Δ).

Finally, the total electrolyte conductivity data were plotted for the experimental temperature range of 150-800°C as presented in Figure 4.30 for both sets of pellets. It was observed that up to about 250°C, the order of increasing conductivity was M5YSZ > M3YSZ > M8YSZ > M10YSZ. Several changes occurred at around 500°C and the

final order of M10YSZ ≈ M8YSZ > M3YSZ > M5YSZ was established. Figure 4.30b shows that the order of increasing conductivity was N5YSZ > N3YSZ > N8YSZ > N10YSZ until around 450°C. Above this temperature, the order became well-defined and was N8YSZ > N10YSZ > N5YSZ > N3YSZ.

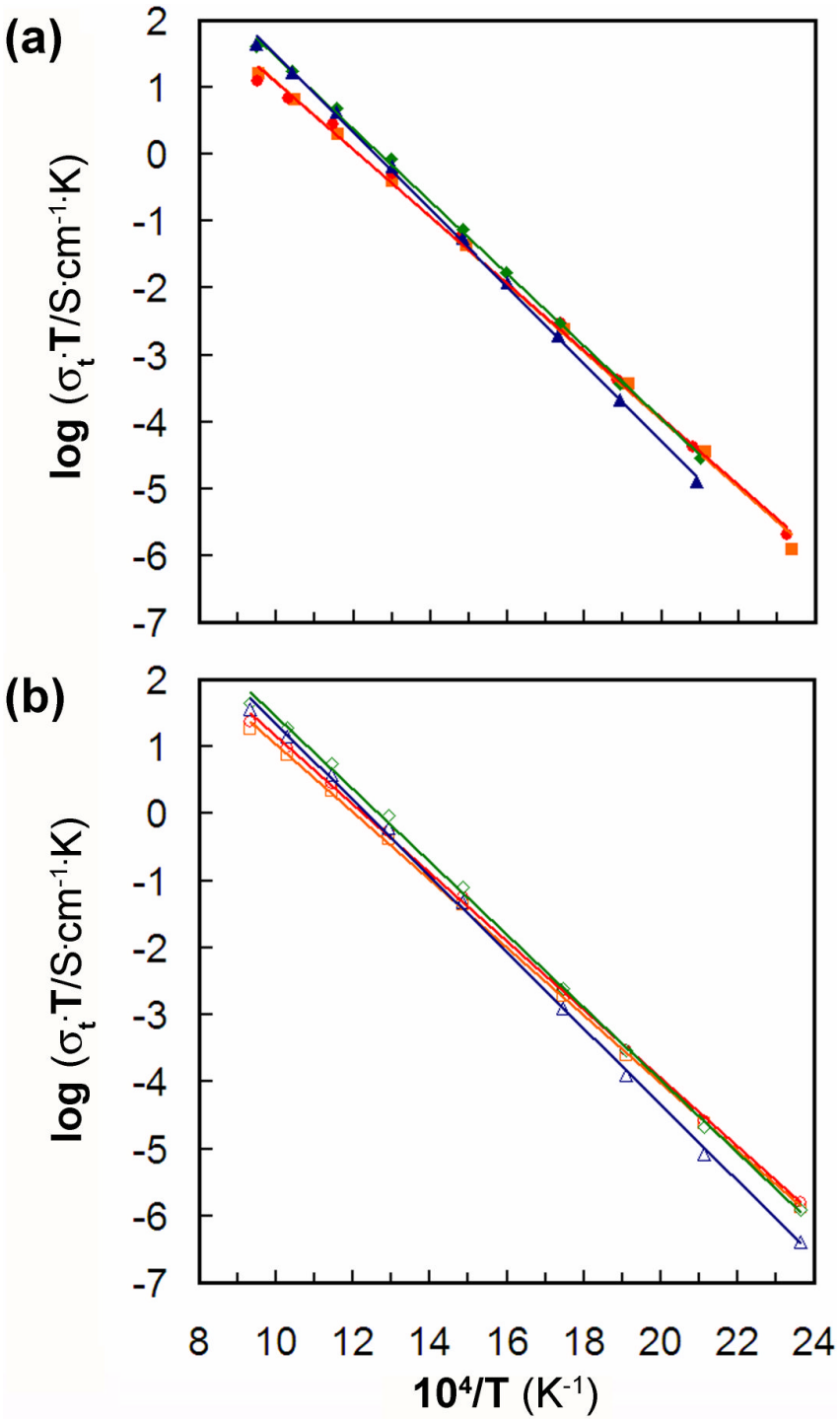

Figure 4.30 Arrhenius-type plots of total electrolyte conductivity of (a) micropellets – M3YSZ(■), M5YSZ(●), M8YSZ(♦), M10YSZ(▲) and (b) nanopellets – N3YSZ(□), N5YSZ(○), N8YSZ(◊), N10YSZ(Δ).

The impedance spectroscopy results are in agreement with the study of Badwal *et al*, who observed a peak in ionic conductivity for 8 mol% YSZ when they studied the compositional range of 2-16 mol% yttria.[130] According to their work, the bulk conductivity was approximately constant over the range 2-8 mol% Y_2O_3 and fell for higher yttria levels. This agrees again with the results for both sets of samples in this work at 400°C as presented in Figure 4.31, where the bulk conductivity for 10 mol% Y_2O_3 is lower than the other, quite closely grouped compositions of both micro- and nanopellets. A similar trend was seen for grain boundary and total electrolyte conductivities at 400°C. Badwal *et al*, did not present results taken at temperatures below 400°C.[130]

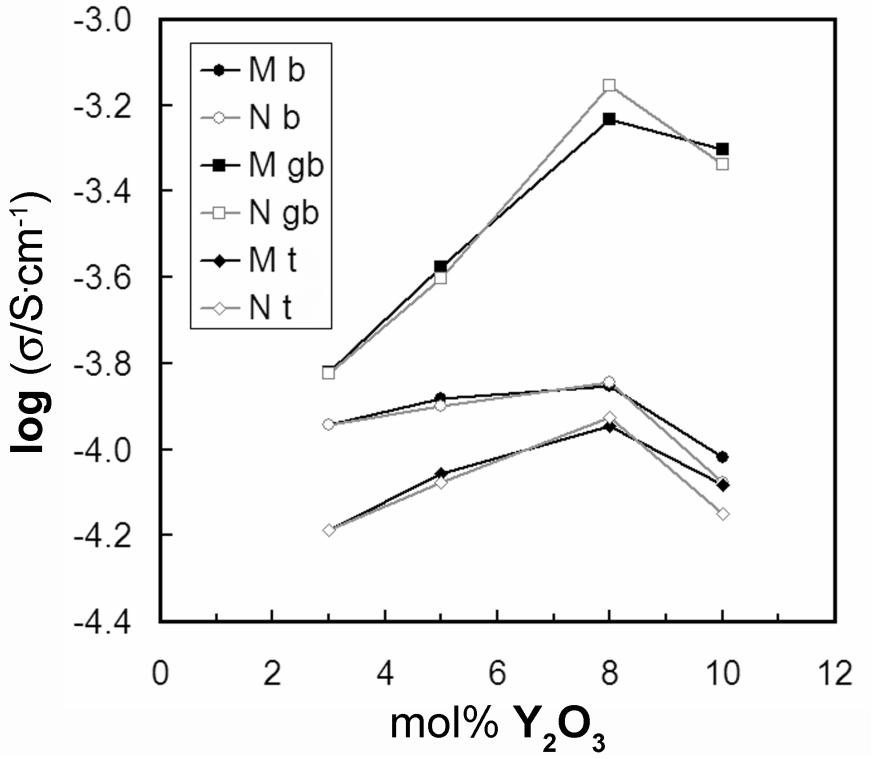

Figure 4.31 Conductivity data measured at 400°C as a function of dopant concentration in microsamples (M closed symbols) and nanosamples (N open symbols) for bulk (b), grain boundary (gb) and total electrolyte (t) contributions, respectively.

The conductivity data measured at 600 and 700°C for both sets of YSZ pellets is presented in Figure 4.32 on plots (a) and (b), respectively. Slightly higher conductivity values were clearly seen for nanopellets (grey line) than for micropellets (black) at both temperatures for all YSZ compositions. The highest conductivity was found for 8 mol% YSZ nanopellets. The differences in conductivity data between the two sets of sintered YSZ material were relatively small, with the largest observed for 5 mol% YSZ pellets measured at 600°C.

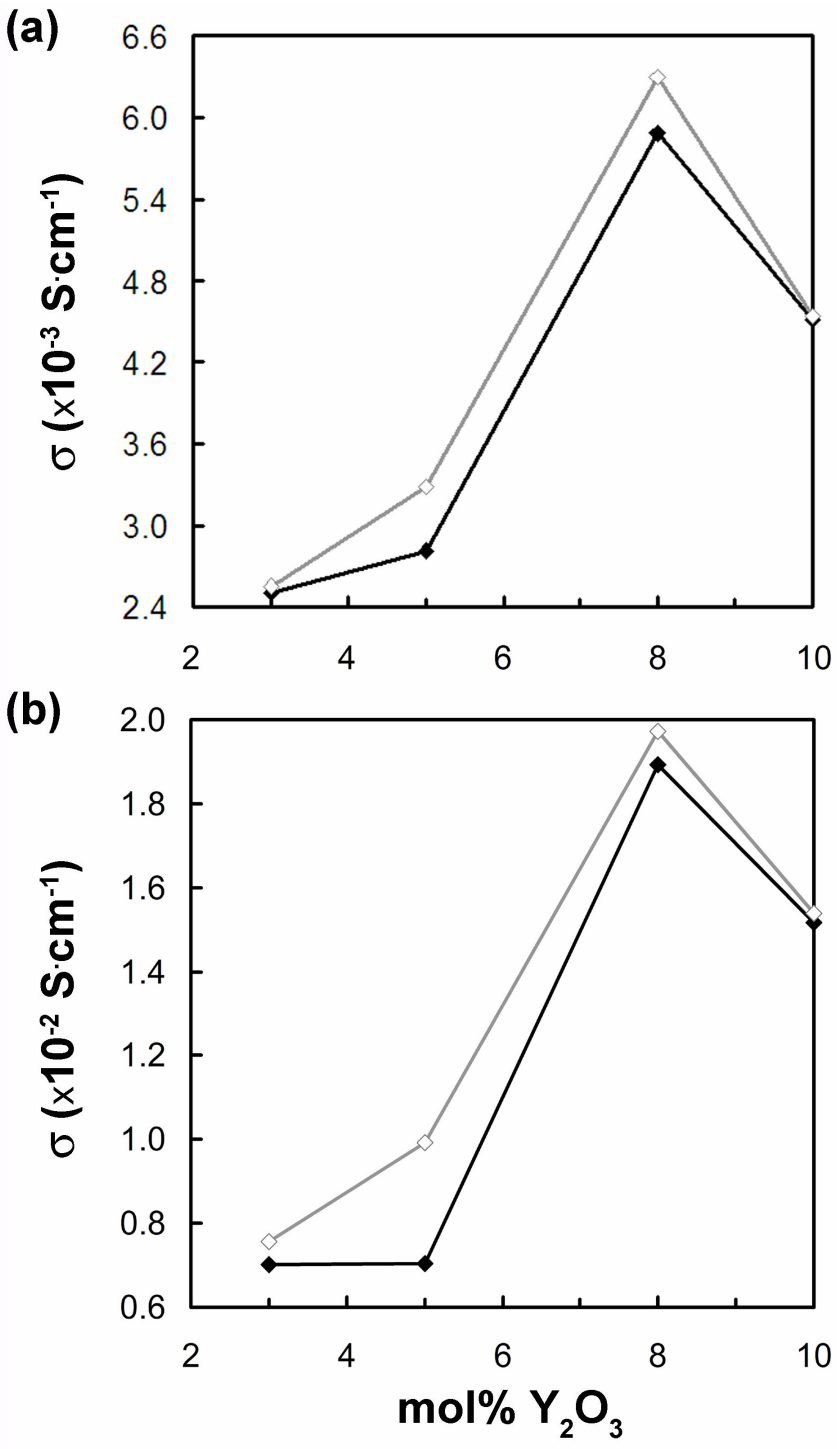

Figure 4.32 Conductivity data measured at (a) 600°C and (b) 700°C as a function of dopant concentration in microsamples (closed symbols) and nanosamples (open symbols) for total electrolyte contribution.

The conductivity results are also compared directly between two compositions of the same yttria content, but derived from different starting materials. These are presented in Arrhenius plots in Figure 4.33. The data for 3 mol% and 5 mol% yttria are plotted in the left column (A,C,E), while 8 mol% and 10 mol% yttria were plotted in the right column (B,D,F).

The following summary can be made for the conductivity of the micropellets and nanopellets. Bulk conductivities were slightly higher for M3 and M10YSZ compositions in comparison to the corresponding nanopellets. However, the N5YSZ sample exhibited a higher bulk conductivity than its equivalent micropellet at lower temperatures. The N8YSZ possessed the highest value of bulk conductivity only at 500°C, it being lower than for M8YSZ below that temperature. Grain boundary conductivities were lower in the case of N3 and N10YSZ than for corresponding micropellets. The N5YSZ possessed higher grain boundary conductivity than its equivalent micropellet below 300°C, but lower values above this temperature. However, the N8YSZ sample exhibited lower grain boundary conductivity than M8YSZ below 300°C, and higher values above this temperature. Slightly lower values of total electrolyte conductivities were obtained for N3 and N10YSZ samples than for the micropellet equivalents when trendlines were plotted. Very similar results were obtained for N5YSZ and M5YSZ as the trendlines overlapped at 500°C. However, the value of the slope for N5YSZ was higher than that for M5YSZ. All conductivity data was in a good agreement with the literature values.

Activation energies for the bulk, grain boundary and total electrolyte of both YSZ batches were calculated from the slope of the corresponding Arrhenius plots. The results are presented in Table 4.8. These were found to correspond to literature data.[131]

Table 4.8 Activation energies of bulk (E_b), grain boundary (E_{gb}) and total electrolyte (E_t) for micro- and nanopellets.

mol% Y_2O_3	***Micropellets***			***Nanopellets***		
	E_b/kJ·mol^{-1}	E_{gb}/kJ·mol^{-1}	E_t/kJ·mol^{-1}	E_b/kJ·mol^{-1}	E_{gb}/kJ·mol^{-1}	E_t/kJ·mol^{-1}
3	86	107	97	89	108	95
5	94	108	96	93	107	96
8	106	109	104	107	113	102
10	113	117	110	114	116	107

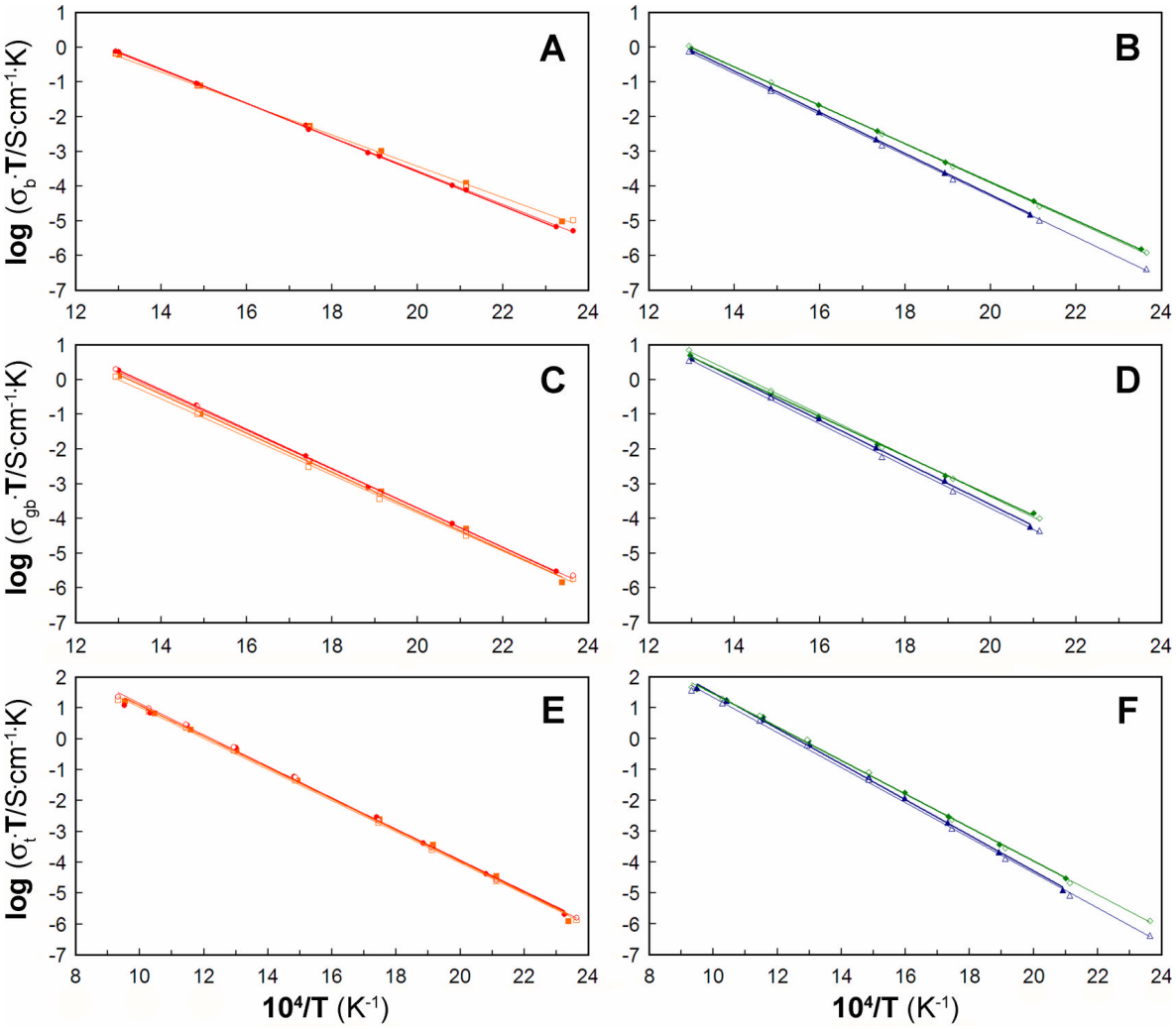

Figure 4.33 Arrhenius-type plots of bulk (A,B), grain boundary (C,D) and total electrolyte conductivity (E,F) for micropellets – M3YSZ(■), M5YSZ(●), M8YSZ(♦), M10YSZ(▲) and nanopellets – N3YSZ(□), N5YSZ(○), N8YSZ(◊), N10YSZ(Δ).

The values of activation energies for the bulk and grain boundary electrolyte conductivities generally increase in the order 3 > 5 > 8 > 10 mol% Y_2O_3. This fact suggests that the energy barrier to the bulk conduction process increases as mol% of Y_2O_3 increases. This is in agreement with a study done by Gibson *et al*, in which the authors stated that bulk and grain boundary activation energies increased with increasing mol% Y_2O_3.[131]

The evolution of grain boundary conductivity with composition for the nano- and micropellets can be related to the SEM results. In both sets of materials grain size increased with %Y, causing the number of grain boundaries impeding the ionic current to decrease. Grain boundary conductivity would therefore be expected to rise with increasing %Y, and this is largely the case. However, grain boundary conductivity was seen to fall from the 8 to the 10 mol% YSZ sample. This may be explained by the association of defects, including

oxygen ion vacancies – which is more marked as dopant concentration increases, and causes ionic conductivity to fall. Defect association is reported to have a major impact on the bulk conduction mechanism and is responsible for the maximum in bulk conductivity in Figures 3.31 and 4.31. Bulk conductivity increases at first with increasing %Y because aliovalent substitution of Zr by Y introduces oxygen ion vacancies, which provide a mechanism for oxygen ionic conductivity. However, at high Y contents, association of these oxygen ion vacancies with the Y species becomes significant and these complexes hinder the ionic conductivity by increasing the energy barrier to occupation of an associated oxygen vacancy by an oxygen ion. Dissociation of such complexes, releasing the oxygen ions for use in the conduction mechanism, is thermally activated. Released oxygen vacancies may thus contribute to the ionic conductivity at high temperatures. The activation energy values in Table 4.8 are consistent with these processes: E_b increases monotonically with increasing %Y for both sets of pellets whilst E_{gb} is initially roughly constant but increases at the high Y contents, perhaps when defect association begins to have a significant deleterious effect on grain boundary conductivity.

In the present study, the activation energy values were found to be higher for the grain boundary processes than for the bulk processes, both for the micro- and the nanopellets. The values for grain boundary activation energies were almost the same for the micro and nanopellets of each composition. However, a small difference from 109 kJ/mol (M8YSZ) to 113 kJ/mol (N8YSZ) was observed. The direct comparison of the results for both sets of samples indicated that nanopellets exhibited slightly lower activation energies for total electrolyte conductivity.

The data presented in Figure 4.34 show the values of the capacitance for the bulk contribution. These were found to be very similar and grouped together for each set of pellets. They were generally slightly lower for nanopellets, but all values fell within the same order of magnitude as the micropellets. This data also indicates that no significant change in the bulk conduction process of nanopellets occurred as the yttria content increased. However, slightly higher values of capacitance can be distinguished for M8YSZ and M10YSZ from the group of micropellets. In addition, a tiny decreasing trend of capacitance was observed for the micropellet set with increase in temperature.

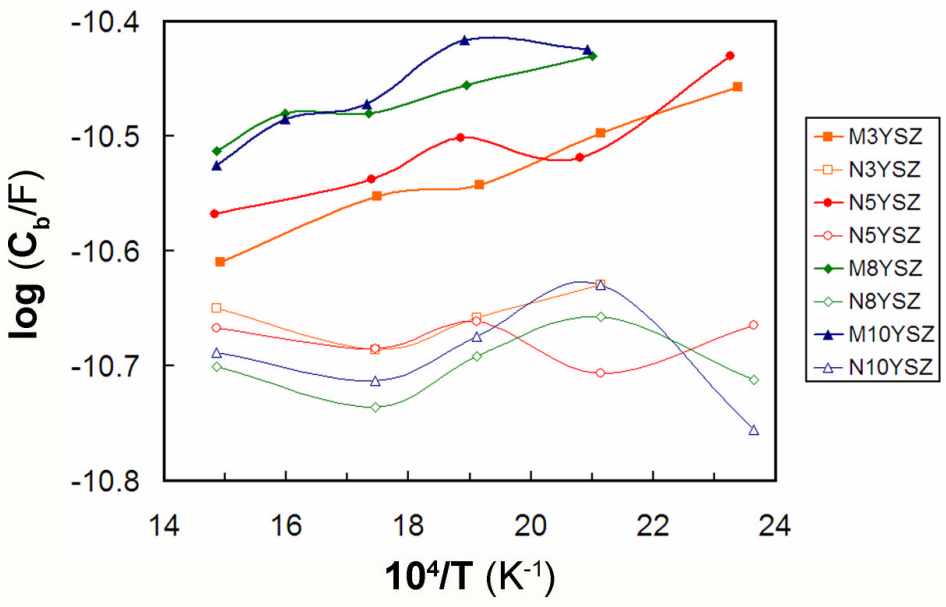

Figure 4.34 Capacitance data of bulk contribution for micropellets (closed symbols) and nanopellets (open symbols).

The results of the grain boundary contribution are presented in Figure 4.35. The capacitance decreases in the order 10 > 8 > 5 > 3 mol% Y_2O_3, for both micro- and nanopellets. This is likely to be due to the increasing grain size with increasing mol% of Y.

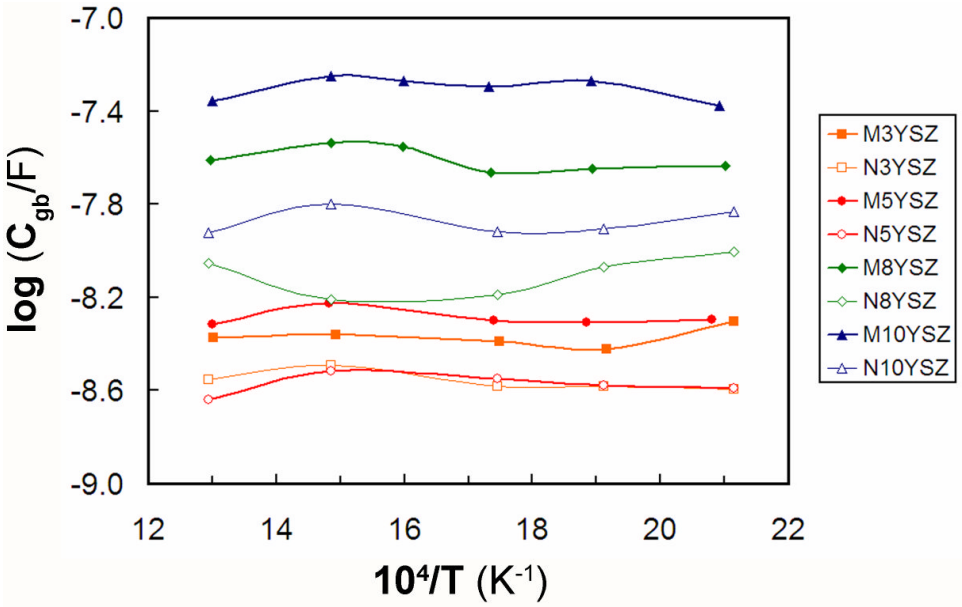

Figure 4.35 Capacitance data of grain boundary contribution for micropellets (closed symbols) and nanopellets (open symbols).

As the effect of having larger grains logically results in less grain boundaries within the sample, the capacitance of a number of grain boundaries can be represented by a number of capacitors in series. If it is assumed that all the grain boundaries within the sample are equivalent, then total capacitance is inversely proportional to the total number of grain boundaries across a sample. This theory is consistent with current capacitance studies on YSZ samples. More grain boundaries were revealed for samples with low mol% Y_2O_3 in the microstructure studies. Therefore, the capacitance was at its lowest value for such compositions. As mol% Y_2O_3 increased, the number of grain boundaries decreased as a result of the presence of larger grains, as observed in SEM. The capacitance related to the grain boundary contribution was found to be the highest for the M10YSZ pellet. Surprisingly, the lowest capacitance data of grain boundary contribution was noticed for N5YSZ pellets.

The inductance data was also presented in Figure 4.36. These results varied slightly among YSZ compositions. Inductive effects were likely to be caused by the changing effect of the electromagnetic field experienced by the conducting components of the impedance spectroscopy rig on going from experiment to experiment. At the highest experimental temperature, the inductance points were quite closely grouped among all compositions. This indicates that the inductive effect was rather consistent and confirmed it to be likely caused by the experimental set-up.

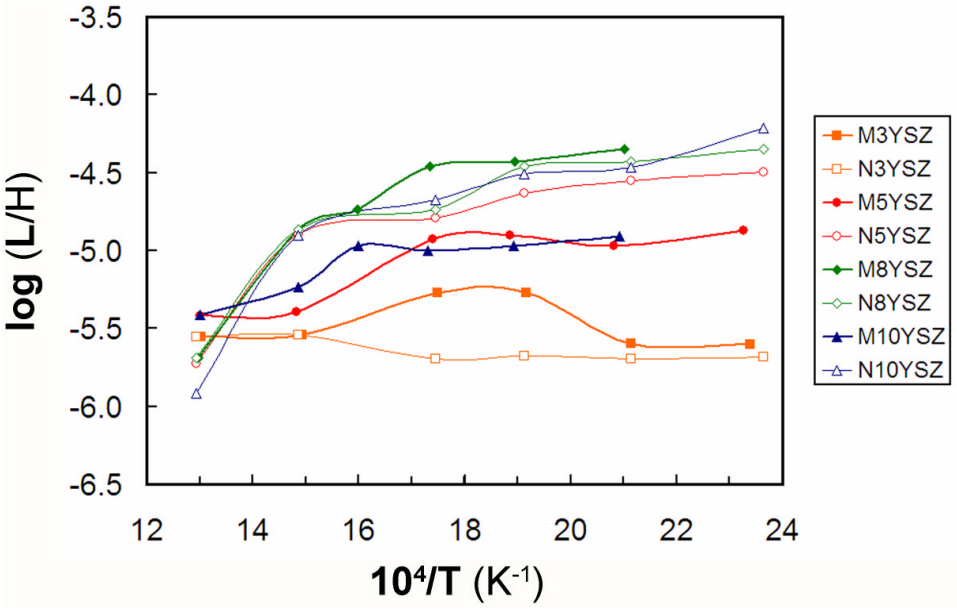

Figure 4.36 Inductance data for micropellets (closed symbols) and nanopellets (open symbols).

4.4.4 Inductively Coupled Plasma Mass Spectroscopy

ICP-MS analysis on both batches of YSZ pellets was performed in order to confirm the expected chemical composition of the samples provided by the industrial partner, MEL Chemicals, as well as to assess levels of impurities and to enable interpretation of results collected by other methods. Average concentrations of relevant elements were calculated in terms of the Y/Zr molar ratio and compared with the expected nominal values. ICP-MS data for the main two elements, Zr and Y, is presented in Table 4.9 for all YSZ pellets. Measurements from 3 to 5 points on the pellet surface were made.

Table 4.9 ICP-MS results on molar basis for all stabilized zirconia pellets.

mol% Y_2O_3	*Y/Zr (theor.)*	*Y/Zr (ICP-MS)*	
		Micropellets	*Nanopellets*
0	0	0.000100	0.00100
3	0.062	0.0720	0.0700
5	0.105	0.117	0.105
8	0.174	0.198	0.192
10	0.222	0.253	0.261

The amounts of Y and Zr expected from their nominal stoichiometries were calculated for all YSZ samples and these corresponded well with the EDX data presented in Table 4.3. Small discrepancies only were observed for pellets with the higher Y concentrations. It should be remembered that the ICP-MS method, when it is performed on solid samples, is often treated as a semi-quantitative analysis.

The concentration of Al and especially Si are of particular interest for electrolyte materials because they may adversely affect the conductivity. Hearing *et al* reported a decrease in oxygen ion conductivity of ScSZ with the increase in concentration of dopant, such as Al_2O_3 and TiO_2, from 1 to 5.5 mol%.[132] However, they found this degradation effect to be negligible at the smallest concentration of Al. Choi *et al* observed an increase in density and grain growth of sintered 1 mol% Al_2O_3-doped 20SDC. However, this effect was found to decrease when 2 mol% of dopant concentration was employed.[133] Similar disadvantageous results were obtained by Lee *et al* for 20GDC co-doped with alumina, when 2 mol% doping was reached.[134] Colomer *et al,* in their studies on 10 mol% TiO_2 doped YSZ (as a potential anode

material), observed a significant electronic conductivity contribution at high temperatures as a result of Ti enrichment at grain boundaries.[135]

All these three elements were detected by ICP-MS in the present studies. Although their concentrations were much smaller than those reported above, it is possible that they could have had an effect on the IS results.

Only 0.003 wt% of Si was found in M0YSZ among samples of this batch. All nanopellets showed a significant concentration of Si, however the smallest value of 0.0014 wt% among both sets of pellets was found for N3YSZ. N5YSZ possessed 0.50 wt% of Si, while N8YSZ had 0.16 wt% and N10YSZ 0.12 wt%. This could have caused slightly lower than expected ionic conductivities for this batch of YSZ samples. As shown in Table 4.10, Al contamination was seen in all pellets. The N0YSZ pellet exhibited the lowest concentration of Al. Aluminium concentrations for the remaining compositions varied from 0.04 to 0.40 wt%. Surprisingly, certain amounts of Sc, Ti and Hf were detected in the ICP-MS measurements. The roughly constant Sc concentration of 0.06 wt% was found throughout the set of micropellets. Sc was also found in all nanopellets to be slightly higher at ~0.10 wt%. In addition, a constant Ti concentration of 0.30 wt% was detected in the microsamples, with slightly higher values of up to 0.6 wt% observed for the nanopellets. A significant level of Hf in the range of 2.0-2.4 wt% was only found in the micropellets.

Table 4.10 ICP-MS results in wt% for the most abundant elements, except for Y and Zr.

Sample	*Al*	*Si*	*Sc*	*Ti*	*Hf*
M0YSZ	0.40	0.0031	0.055	0.27	2.1
M3YSZ	0.38	0	0.058	0.32	2.4
M5YSZ	0.027	0.030	0.056	0.27	2.2
M8YSZ	0.35	0	0.055	0.26	2.4
M10YSZ	0.24	0	0.054	0.27	2.0
N0YSZ	0.0086	0.13	0.10	0.48	0
N3YSZ	0.40	0.0014	0.11	0.53	0
N5YSZ	0.037	0.50	0.12	0.65	0
N8YSZ	0.065	0.16	0.082	0.31	0
N10YSZ	0.32	0.12	0.076	0.29	0

It is speculated how these 5 additional elements could be introduced into the YSZ pellets. As the two sets of YSZ starting materials were prepared by two different methods, some impurities were probably present in the starting materials and could have reached different

levels in the micro- and nanopellets. Good examples are Hf and Si. As Sc, Ti and Hf are located within the same groups of the Periodic Table as Y and Zr, respectively, they could have been introduced as impurities in the yttria or zirconia starting materials in the solid state synthetic preparation method used to prepare the YSZ micropellets. Hf is likely to have been introduced in the solid state synthesis of the micropowders since it was not found in the nanopellets. On the other hand, the fact that relatively constant quantities of Sc and Ti were measured for both sets of YSZ samples suggests a different source of contamination. One possibility is cross-contamination in the ICP-MS column from the samples of other users. This is more likely than their being introduced during materials processing since Sc and Ti compounds were never used in the Baker laboratory during the author's research project. One other possibility, however, is that doubly charged Zr ions were detected as Ti and Sc in the ICP-MS instrument. $^{90}Zr^{2+}$ (isotopic abundance, 51%) could appear as $^{45}Sc^{+}$ (isotopic abundance, 100%) while $^{94}Zr^{2+}$ (isotopic abundance, 17%) could appear as $^{47}Ti^{+}$ (isotopic abundance, 7%, and the mass used to measure Ti in these experiments). The latter explanation seems the more likely. The potential sources of Al and Si could be assigned also to cross-contamination in the ICP-MS or to processing of the YSZ materials by the author. The high temperature furnaces were equipped with alumina tubes and boats. Therefore contamination is a possibility here through high temperature diffusion processes. A similar explanation can be given for the Si content since some glassware was used in the muffle furnace up to 120°C in long-term drying processing of the nanopowders. It should also be mentioned that Si is difficult to exclude from the ICP-MS experiment. The effect of Hf on ionic conductivity of YSZ was reported by Zhuiykov, who compared hafnia-based and zirconia-based systems doped with 10 mol% Y_2O_3.[136] He found the HfO_2-ZrO_2-Y_2O_3 system had the advantages of higher thermal shock stability and chemical resistivity at above 1300°C than the ZrO_2-Y_2O_3 electrolytes. Therefore a certain improvement in these respects may be expected in the micropellets due to their Hf content.

4.5 Summary

The effect of yttria content and powder particle size on phase, microstructure and ionic conductivity of YSZ samples was investigated using a range of analytical methods. Two sets of delivered materials were analysed, both in five variants, i.e. 0, 3, 5, 8 and 10 mol% Y_2O_3. These were named and categorised due to the starting particle size as micro- and nanopowders.

The dense pellets of these powders were either supplied by MEL Chemicals Ltd or prepared by the author, strictly with the same pressing and sintering conditions.

XRD experiments revealed a significant difference between the powder forms of pure and stabilised zirconia with respect to the starting particle size. The diffraction patterns of nanopowders possessed much broader and lower intensity peaks due to smaller crystallites. The peaks associated with monoclinic, tetragonal and cubic phase of all zirconia samples corresponded favourably with the data reported in the literature. Importantly, there was a clear particle size effect in the nanopowders whereby the tetragonal phase was stabilised in pure ZrO_2 when the monoclinic phase is thermodynamically expected. The monoclinic, tetragonal and cubic phases were also observed for sintered, dense YSZ bodies obtained from corresponding YSZ powders. Due to a bigger crystallite size in pellets of both batches, the diffraction patterns were characterised by higher intensity, sharper peaks. Therefore, for example 5 mol% YSZ samples could be assessed as a mixture of tetragonal and cubic phase with more precision. On sintering, the nanopellets of pure ZrO_2 reverted to the monoclinic phase. No additional impurity phases were detected in the XRD patterns.

Electron microscopy studies confirmed that the two synthetic methods used to obtain the starting YSZ materials gave rise to different forms of soft agglomerates in the loosely bound powders. TEM images showed a variety in the shapes and sizes of individual YSZ particles. Hard agglomerates were observed for both the micropowders and the nanopowders. The mean particle size increased from 81 to 251 nm for the micropowders, while a subtle decrease from 7.8 to 5.2 nm was observed for nanopowders, with increasing yttria content. The crystal structure was indexed only for nanopowders by reference to DDPs using crystallographic database. These findings were consistent with the XRD results and confirmed the evidence of three zirconia polymorphs in corresponding YSZ compositions. In addition, EDX results showed Y/Zr molar ratios to be close to the expected nominal values for all samples. The presence of any impurities in significant concentrations in the raw YSZ materials was also excluded in these studies.

The dilatometry data showed nanoparticles to be more active during the sintering process. They exhibited a lower temperature initial shrinkage than the micropowders. This could be explained largely by the higher surface energy of the smaller nanoparticles as well as the fact that, after pressing, the nanosized particles were more closely packed and the resulting green bodies were less porous. Therefore, the orientation of particles and contact growth stages

would have started at much lower temperature.[127] As a result, the nanopowders began to sinter much earlier than the micropowders. Another possible explanation is that thermal removal of surface hydroxyl groups occurred at low temperatures.[137] However, this is unlikely in this case, because of the extended drying procedure used. More varied sintering rates were noticed for the micropowders, which is consistent with their quite broad particle size range. The sintering rates of all nanopowders exhibited much less variation. Thermal expansion coefficients of all YSZ samples were analysed in three different temperature regions using the cooling phase of the temperature programme. These were found to be in a good agreement with reported data. A very small dimensional change was observed during the 4-hour isothermal part of the dilatometry programme for all YSZ samples. However, pure zirconia samples cracked during the cooling step as the result of a tetragonal to monoclinic phase transformation. Although YSZ micropellets were provided by the supplier together with the pressing and sintering conditions, the dilatometry results were useful for further assessment of the YSZ dense bodies. In addition, the results were divided into two sets – made by isostatic or uniaxial pressing. As expected, the uniaxially pressed pellets shrank more than the isostatically pressed pellets. This can be explained by the much lower pressure used in the compacting process in the former. These pressing parameters were set by the supplier and the delivered materials already possessed these characteristics. The isostatically pressed pellets showed slightly better sintering characteristics.

SEM studies confirmed a dense microstructure for all YSZ samples with well-established grains and grain boundaries. A representative number of about 130 grains was used to calculate an average grain size for each composition. Grain size increased with increasing yttria content. While micro- and nanopellets had similar grain size for the 3 and 5 mol% YSZ compositions, smaller grains were observed for heavily doped nanopowders than for the corresponding micropowders.

The IS results were found to be in agreement with literature data, ionic conductivity values peaking for 8 mol% YSZ samples. A small improvement in ionic conductivity values was found for the nanopellets over the micropellets. The grain boundary contribution was found to dominate the overall conductivity of these materials because it was generally significantly higher than bulk conductivity. The total conductivity was a little higher for the nanopellets and the application of nanopowders as starting materials, especially using lower sintering temperatures, should be the priority for further research on such electrolyte-related materials.

The ICP-MS results confirmed the presence of the elements Al and Si in all YSZ samples. The presence of Si and Al may result in a decrease of the ionic conductivity of the materials. Nanopellets appeared to have higher Si and Al concentrations than the micropellets. Small amounts of Ti and Sc were detected by ICP-MS but are explained as instrumental artifacts due to doubly charged Zr^{2+} ions. Hf was detected in relatively high amounts of 2.0-2.4 wt%, but only in the micropellets. The incorporation of small amounts of Hf have been reported to improve thermal and chemical stability.[136]

To summarise, a more significant improvement was expected to be achieved on the ionic conductivity and microstructure of YSZ electrolyte material by application of nanoparticles instead of coarser-sized equivalents as the starting powder. As some of the properties of the delivered materials were controlled by the industrial partner, it was of interest to maintain consistency in the systematic studies of both sets of YSZ powders and resulting pellets by keeping them unchanged. These included pressing and sintering conditions of the delivered YSZ pellets, which were replicated in the group lab. It is thought that these complementary, comparative studies on different sets of YSZ materials have given some insight into the assessment of crystallographic phases, microstructure, sintering process and ionic conductivity of yttria-stabilised zirconia, even though this is a well-known system.

Results and Discussion

CHAPTER V – **SAMARIUM-DOPED CERIA**

5. Samarium-doped ceria

5.1 Introduction

A systematic study of SDC solid solutions of three compositions is presented in this chapter. Mixed oxides were obtained using a low temperature, citrate complexation method, which yields high purity nanoparticulate powders. These are of interest for obtaining good electrolyte densities at relatively low sintering temperatures without any sintering promoters. In this contribution, the results are presented and divided into powder and pellet sections. The major part of these results was published elsewhere.[138]

5.2 Synthetic method

Three compositions of $Sm_xCe_{1-x}O_{2-x/2}$ were prepared with x = 0.1, 0.2 and 0.3 and these were named 10SDC, 20SDC and 30SDC, respectively as presented in detail in Table 5.1. Similar procedures were used in the group to those developed for the preparation and study of GDC.[34, 86] In this project, more complex studies with a larger number of SDC compositions and some modifications to their synthesis were applied.

Table 5.1 Compositions of prepared SDC powders.

mol% Sm_2O_3	*mol% Sm*	*Formula*	*Notation*
5	10	$Sm_{0.1}Ce_{0.9}O_{1.95}$	10SDC
10	20	$Sm_{0.2}Ce_{0.8}O_{1.90}$	20SDC
15	30	$Sm_{0.3}Ce_{0.7}O_{1.85}$	30SDC

Stoichiometric amounts of metal nitrate hexahydrates, $Ce(NO_3)_3{\cdot}6H_2O$ and $Sm(NO_3)_3{\cdot}6H_2O$ (Acros Organics, 99.5%), were dissolved in deionized water separately to make 0.1 M solutions. These were stirred to homogenise and combined. Anhydrous citric acid (Alfa Aesar, 99.5%) was dissolved in water (0.2 M) and this solution was added to the cation solution in the ratio of two moles citrate per mole of total metal cations. After homogenisation of the solution, the temperature was increased to 80ºC and maintained under stirring for 12 h. Simultaneous elimination of water and gas caused an increase in the viscosity of the mixture. The resulting gel became transparent, then increasingly viscous with formation of yellow foam and dark brown bubbles. The initial thermal decomposition of the gel was carried out in a muffle furnace at 250ºC for 2 h. The resulting, ash-like materials were calcined

in static air in a tube furnace at 500ºC for 2 h. In both steps, heating and cooling rates were 2.5ºC·min^{-1} and 5ºC·min^{-1}, respectively.

Figure 5.1 illustrates the procedure of the citrate complexation method employed in this work. After calcination, each powder was placed in 50 cm^3 Nylon jars and dry ground for 1 h using a planetary ball mill (Fritsch Pulverisette 7) operated at 400 rpm. Zirconia balls of 10 mm diameter were used as the grinding medium with a ball to powder weight ratio of 10:1. The milling process was interrupted every 15 min to dislodge the powder from the walls of the container. The three resulting nanopowder compositions were characterised in detail and were used to make the sintered electrolyte pellets.

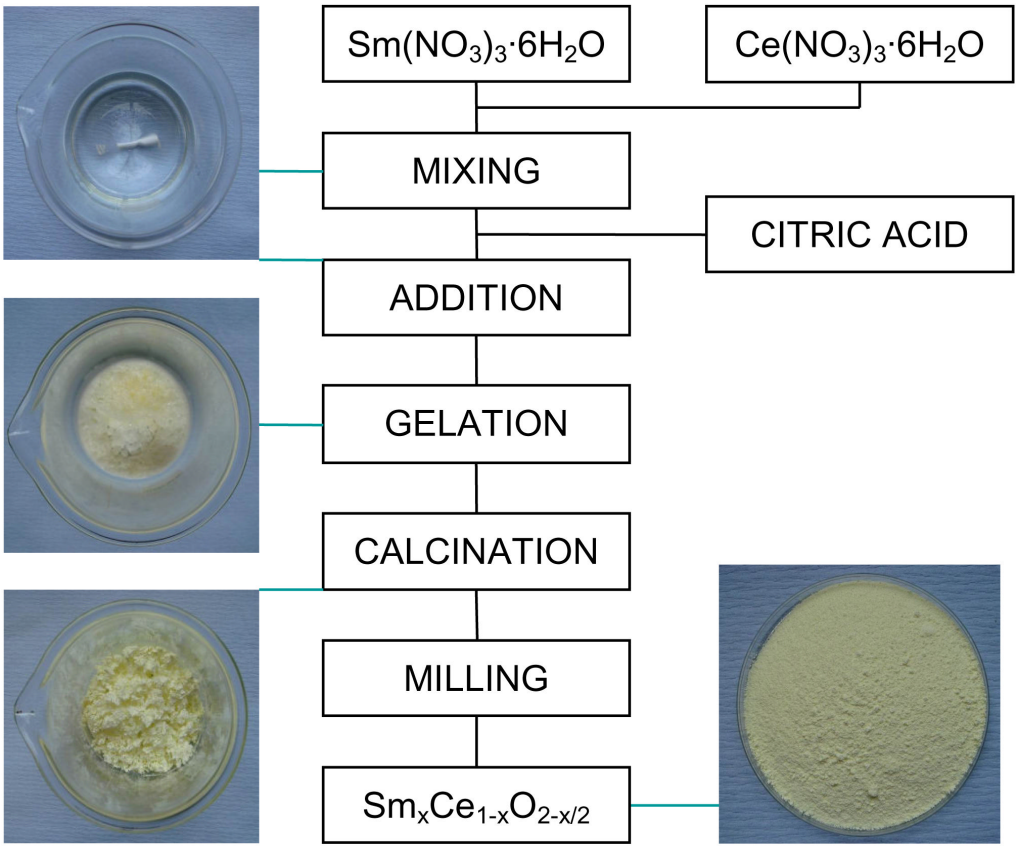

Figure 5.1 Experimental flow chart for the synthesis of SDC powders.

5.3 Powder characterisation

The initial synthesis of the SDC powders was studied using thermal analysis and X-ray diffraction. The resulting powders were further characterised structurally and chemically by elemental analysis, BET, electron microscopy and dilatometry. These data are presented in the following sections.

5.3.1 Thermal analysis methods

Plots of TG/DTA experiments, performed on gel precursors either in air or oxygen environment for all three SDC compositions are presented in Figure 5.2.

In each case, total weight loss was about 67% and occurred in three main steps in the approximate mass ratio 3:1:2 with increasing temperature. Each of these steps corresponded to a peak representing an exothermic process in the DTA trace. At temperatures higher than 500ºC, the TG curve showed no change, implying that no further mass loss occurred.

The peak positions (p_n) and associated enthalpy changes (ΔH_n) of the three exothermic peaks (n = 1-3) are presented in Table 5.2. ΔH values were calculated by integrating the associated peak in the DTA graph, calibrating for the final sample mass and expressing the result per mole of final product. Some care is necessary in the interpretation of these values but they are of some use, in conjunction with the other thermochemical results, in assigning chemical processes to the three exothermic peaks. The DTA traces of all three precursor gels exhibited two large (p_1 and p_3) and one small exothermic peak (p_2). These were shifted towards higher temperatures with increasing Sm content. In addition, one small endothermic peak (p_0) was seen at ~107ºC for all samples and can be assigned to the evaporation of physically adsorbed water. Apparent changes in heat flow in the form of a drift and some sharp fluctuations were observed in all samples at temperatures from 400ºC to 800ºC. It is believed that these were instrumental artefacts. First derivative curves of the TG and DTA (DTG and DDTA, respectively) data are presented in Figure 5.3 for a representative 10SDC sample. These represent the rate of mass loss vs. temperature.[139] DTG and DDTA curves showed no change in the high temperature range.

Table 5.2 Summary of DTA plots for SDC gel precursors run in air.

Sample	p_0 / ºC	p_1 / ºC	ΔH_1 / kJ·mol^{-1}	p_2 / ºC	ΔH_2 / kJ·mol^{-1}	p_3 / ºC	ΔH_3 / kJ·mol^{-1}
10SDC	107	125	-137	203	-11.7	284	-920
20SDC	109	126	-132	212	-8.63	288	-772
30SDC	107	127	-95.3	225	-18.0	297	-836

ΔH_n values expressed per mole of final product

The TG/DTA experiments were repeated for all three precursor gels in a flow of pure oxygen. A representative example (for 30SDC) is presented in Figure 5.2(d), while plots of other compositions are attached in Figure 5.4. Analysis of off-gases was carried out using a quadruple mass spectrometer. Pure O_2 was used to avoid masking CO and N_2 (both mass/charge ratio, m/q=28) released by the sample with the large concentration of N_2 in air.

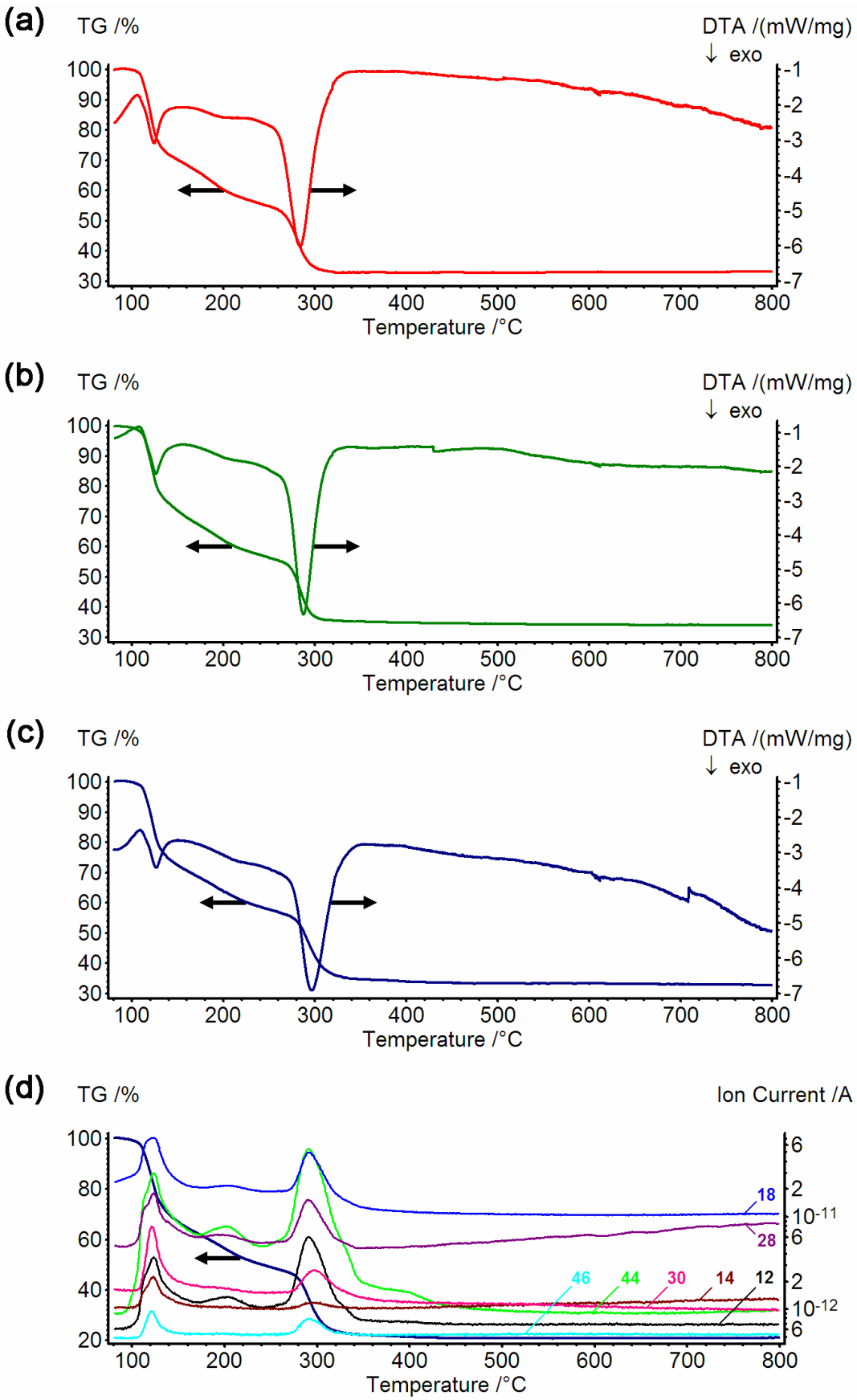

Figure 5.2 Plots of TG and DTA experiments run in air on precursor gels of (a) 10SDC, (b) 20SDC and (c) 30SDC. (d) TG plot run in O_2 for 30SDC including mass spectrometry data. Mass to charge (m/q) ratios are indicated. Note the log scale for ion current.

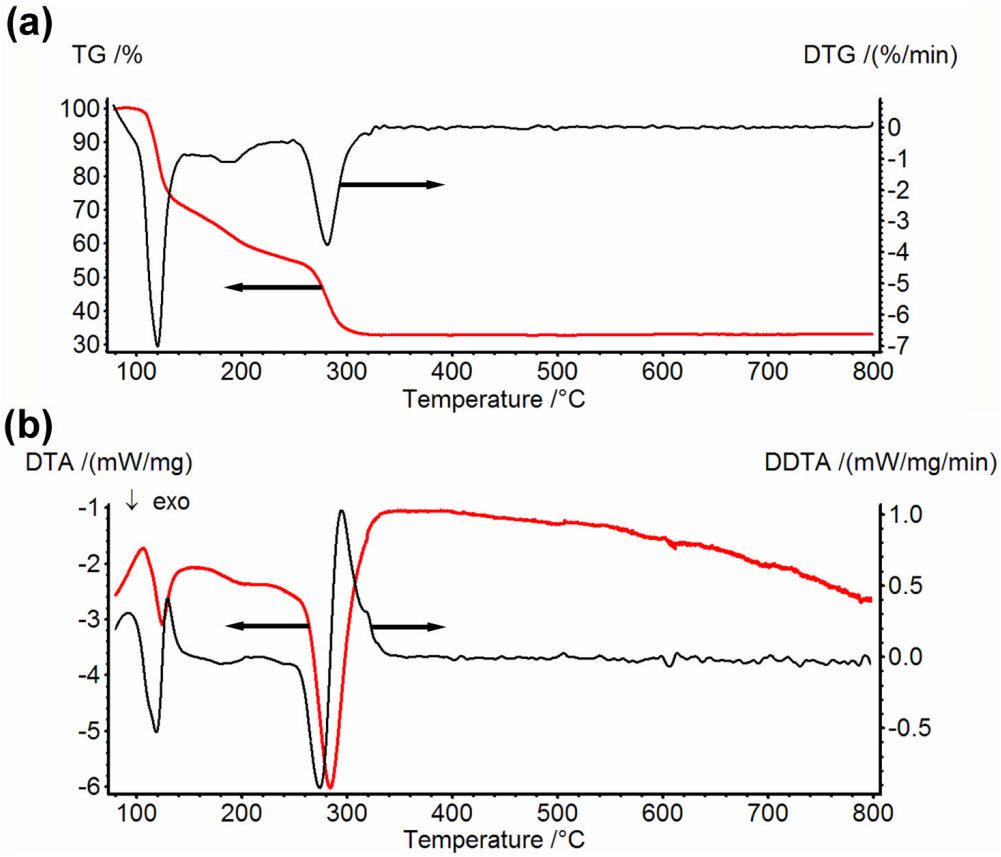

Figure 5.3 TG (a) and DTA (b) plots with their corresponding first derivatives curves (black lines) run in air for representative 10SDC sample.

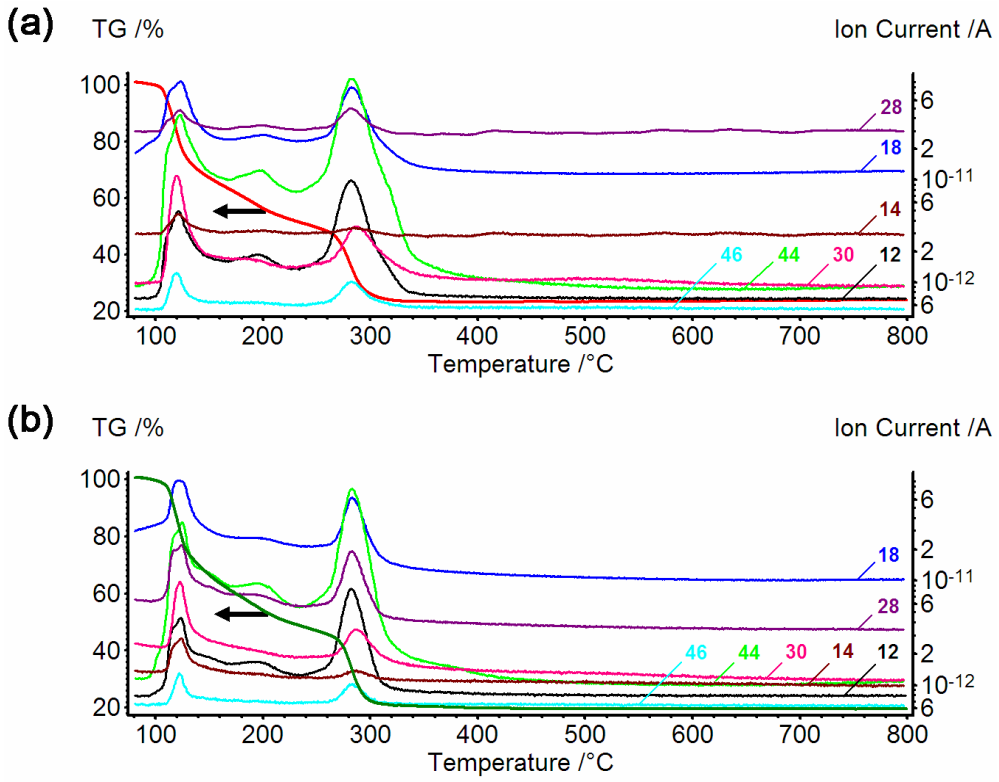

Figure 5.4 TG plots run in O_2 for (a) 10SDC and (b) 20SDC including mass spectrometry data. Mass to charge (m/q) ratios are indicated. Note the log scale for ion current.

It was found that H_2O (m/q=18) was the main product liberated in the first peak - starting at ~110°C with its maximum at 126°C - together with large amounts of CO and CO_2 (28, 44) and small amounts of NO and NO_2 (30, 46). The associated ΔH_1 value was around -100 kJ·mol^{-1}, depending on sample composition. This peak is thought to relate to the polymerisation reactions accompanying the completion of gel formation. The presence of the second exothermic peak, at 175-230°C, was also reflected in the MS data. Here, small peaks could be assigned to release of CO, CO_2 and H_2O with a small amount of NO and negligible NO_2. The matching peaks in the C trace (m/q=12) confirmed the CO_2 and CO peaks. This peak can be assigned to breakdown of the citrate species by dehydration and loss of carboxylate groups as CO_2. The temperature at which this peak occurs matches well with the initial decomposition temperature of citric acid (~175°C), bearing in mind that this is a transient experiment and so processes will be shifted to slightly higher temperatures than would pertain at steady state.[140] The small value of ΔH_2 supports the assignment of this peak as a decomposition rather than a combustion, which would be more exothermic. The third peak starting at 265°C corresponded to the final release of large amounts of CO_2, CO and H_2O with only very small amounts of NO_x. This was attributed to the final complete burn out of the remaining organic matter to leave only oxide material. This assignment is supported by the large value of ΔH_3 – around -800 kJ·mol^{-1} – which is consistent with an energetic combustion reaction. The NO_x peaks were generally small and decreased in size, relative to those for water and carbon oxides, as temperature increased in the TG/DTA experiment. This indicates that most of the nitrogen was liberated during the gel formation step at 80°C. This is confirmed by the observation of the evolution of large amounts of brown gas during the preparation step.

It should be noted that due to the availability and specification of the TA instrument, slightly different experimental conditions were applied in contrast to those in the synthesis. The higher heating rate of 5°C/min and flowing gas of 50 ml/min had to be employed. It was thought that it would still allow for reasonable interpretation of physical and chemical changes of SDC precursors during their thermal treatment. The influence of various heating rates during decomposition of anhydrous citric acid was studied by Barbooti *et al*, who performed their thermal measurements in flowing N_2 at the rate of 25 ml/min.[140] The drop of initial decomposition temperature from 168 to 165°C was observed with the increase of the heating rate from 5 to 10°C/min, while the maximum of the decomposition peak was shifted from 208 to 225°C. According to their studies, the changes in heat flow were not affected and resulted only in the shifting in position of the peaks towards higher temperature.

A multi-step decomposition behaviour of SDC precursor synthesised *via* citrate route was reported by Chung *et al*, which is in good agreement with these studies.[141] The authors observed two exothermic peaks at ~204 and 272°C. They also stated the presence of endothermic peak below ~170°C as the loss of initial moisture and additional dehydration process. However, an oxidant to fuel ratio of unity was employed. This could have affected the initial decomposition process of SDC compounds in comparison to the results presented in this thesis.

5.3.2 X-ray Diffraction

Figure 5.5 presents XRD patterns of the three SDC compositions calcined at 500ºC for 2 h. All peaks were assigned to the cubic fluorite crystal structure, typical of ceria powders. There was no evidence of any other phases. Small shifts of the diffraction peaks to lower 2θ were noticed as Sm content increased. This corresponded to a smooth expansion of the ceria unit cell dimension from 5.4229 to 5.4431 Å on going from 10SDC to 30SDC. The lattice parameters and the average crystallite size of the three SDC compositions are summarised in Table 5.3. The values presented are means from patterns obtained for six different batches of each composition for SDC samples calcined at 500°C for 2 h. These results are consistent with crystallographic data from ICDD for these compositions.[114, 142-144]

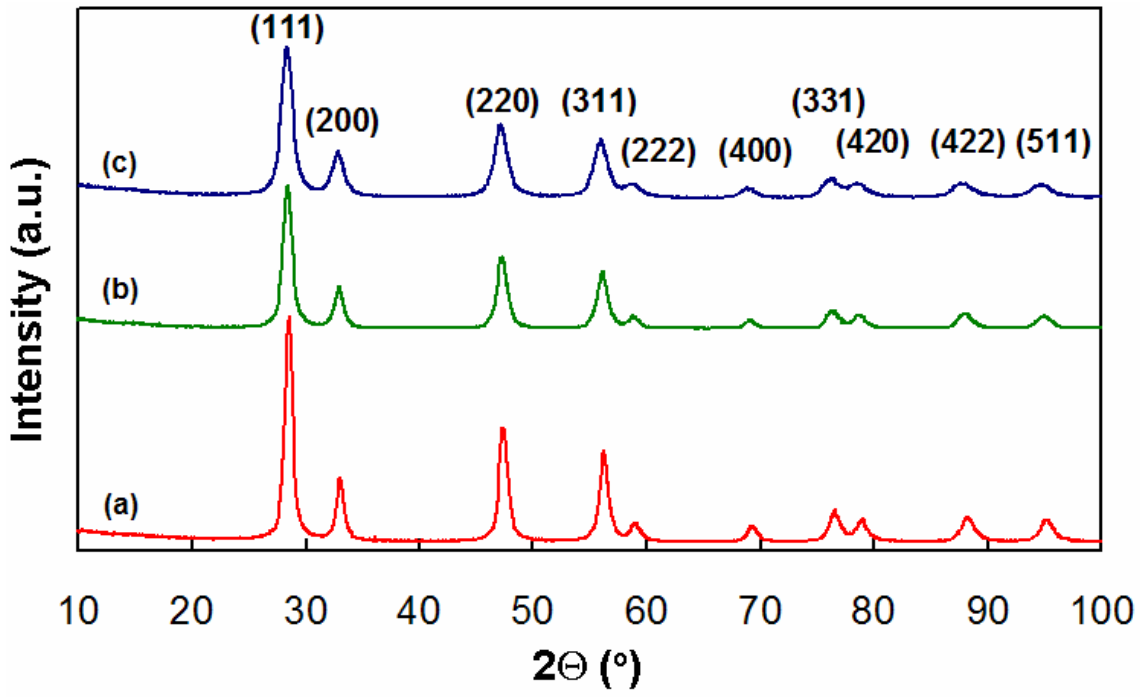

Figure 5.5 XRD patterns of (a) 10SDC, (b) 20SDC and (c) 30SDC powders calcined at 500ºC for 2 h.

Average crystallite size (D_{XRD}) was calculated from the degree of line broadening in the main (111) diffraction peak using the Scherrer equation (Eqn. 3.1).

Table 5.3 Lattice parameters and average crystallite size for SDC powders calcined at 500ºC for 2 h.

Sample	***ICDD***	a_{th} /Å	a /Å	V /Å^3	D_{XRD} /nm
10SDC	01-075-1757	5.4230	5.4229(4)	159.48(3)	11.3(4)
20SDC	01-075-1758	5.4330	5.4332(2)	160.38(1)	9.1(3)
30SDC	01-075-1759	5.4430	5.4431(4)	161.26(4)	7.8(5)

Average crystallite size decreased as Sm content increased, the smallest value being 7.8 nm for 30SDC. Therefore, the XRD data confirmed that SDC nanopowders of ~10 nm mean crystallite size had been successfully prepared *via* the citrate complexation route followed by calcination at 500ºC for 2 h.

More detailed XRD studies were presented in Figure 5.6 for a representative 10SDC sample after calcination at different temperatures for 2 h, starting with the precursor gel. As seen, diffraction patterns taken after treatment at 100 and 200ºC showed that the material was amorphous to the X-rays. After treatment at 300ºC, however, the expected diffraction pattern is clear, even though the peaks are very broad. Therefore, initial crystallisation of the product must have taken place between 200ºC and 300ºC. This is consistent with thermal analysis data in which the final burn out of organics, which would leave only inorganic oxide material, peaked just below 300ºC. As treatment temperature increased further, the peaks became gradually narrower, indicating increasing mean crystallite size with increasing temperature.

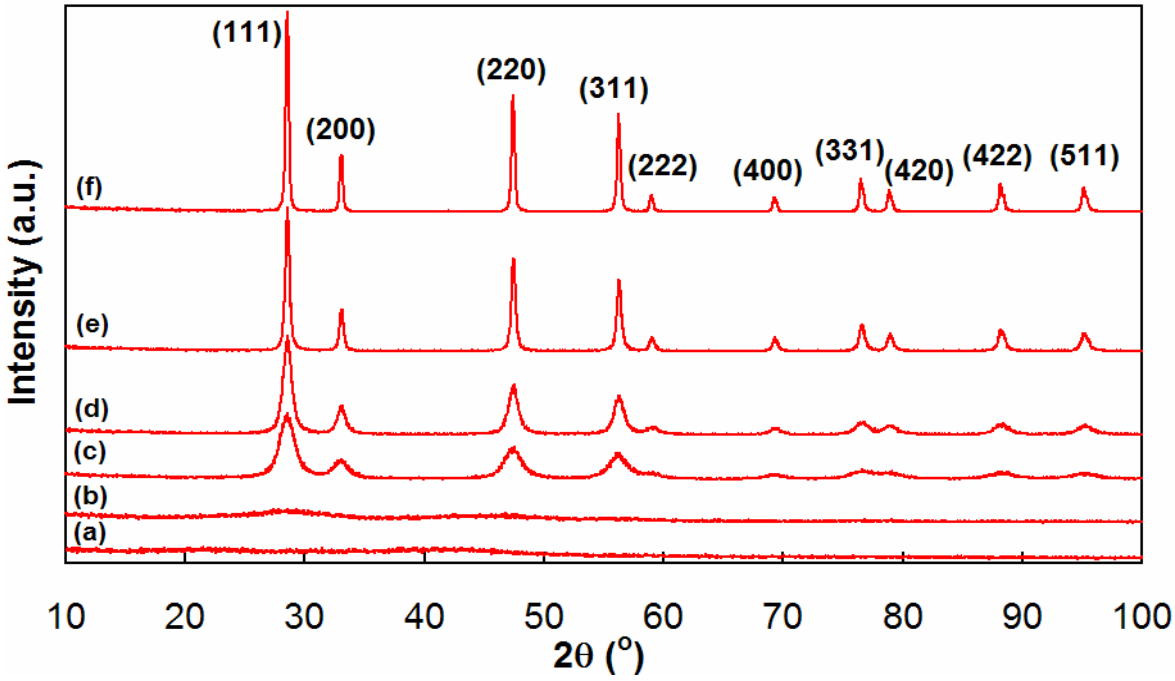

Figure 5.6 XRD patterns of the 10SDC samples calcined for 2 h at (a) 100ºC, (b) 200ºC, (c) 300ºC, (d) 500ºC, (e) 700ºC and (f) 900ºC.

Qualitative analysis of all XRD patterns for 10SDC indicated only reflections relevant to the cubic phase of samarium-doped ceria.[142] Identical thermal evolution studies were performed for the two remaining SDC compositions and results are summarised in Table 5.4. The Scherrer equation (Eqn. 3.1) was again used to obtain values for mean crystallite size, while lattice parameters and resulting volume of the unit cell were obtained using crystallographic software.

Table 5.4 Lattice parameters, volume of the unit cell and crystallite size of SDC powders calcined at different temperatures.

T/°C	***10SDC***			***20SDC***			***30SDC***		
	a/ Å	***V***/ Å^3	D_{XRD}/nm	***a***/ Å	***V***/ Å^3	D_{XRD}/nm	***a***/ Å	***V***/ Å^3	D_{XRD}/nm
250	5.4228	159.47	5.54	5.4329	160.36	4.83	5.4428	161.24	4.34
300	5.4229	159.48	5.87	5.4330	160.37	5.10	5.4434	161.29	4.77
500	5.4228	159.47	10.95	5.4328	160.35	9.23	5.4438	161.33	8.22
700	5.4229	159.48	25.15	5.4332	160.39	21.98	5.4435	161.30	19.51
900	5.4230	159.48	44.32	5.4335	160.41	40.92	5.4426	161.22	32.19

The increasing trend of average crystallite size was retained for 20SDC and 30SDC with the increase of calcination temperature. In addition, a decrease in D_{XRD} values was observed with the increase of Sm content for all thermal treatments.

5.3.3 Elemental analysis

Elemental analysis was performed to obtain values of residual carbon content in the three SDC compositions calcined for 2 h at temperatures from 250 to 900ºC using a Carlo Erba 1110 CHNS analyser. The data are presented in Table 5.5 and show that carbon content was low even after calcination at just 250ºC and that it fell to very low values after calcination at 500ºC. The amount of residual carbon at 500ºC was considered to have negligible impact on processing of these materials. This calcination treatment was employed for further studies on the SDC solid solutions. Carbon content increased slightly with increasing Sm content.

Table 5.5 Carbon content (wt%) in SDC powders calcined at different conditions.

T / ºC	***t*** / h	***10SDC***	***20SDC***	***30SDC***
250	2	0.85	0.96	1.51
300	2	0.45	0.62	1.01
500	2	0.19	0.23	0.44
700	2	0.07	0.08	0.19
900	2	0.03	0.04	0.09

5.3.4 Brunauer-Emmett-Teller method

BET studies by nitrogen adsorption were performed on SDC nanopowders using a Micrometrics ASAP 2020 instrument in order to obtain values of specific surface area (SSA). All samples were pre-treated at 120°C for 6 h.

As reported in the literature by Fuentes *et al*, the SSAs for doped ceria powders prepared by the citrate method could be significantly increased by subjecting them to a dry milling step.[86] Table 5.6 shows the values of SSA of SDC powders calcined at different temperatures for 2 h and then milled using a planetary ball mill with zirconia balls at 400 rpm for 1 h. Values of SSA were converted to equivalent particle diameters (D_{BET}) using Eqn. 5.1, assuming spherical particle shape. In Table 5.6, values of D_{BET} are compared with values of average crystallite size calculated from the XRD patterns (D_{XRD}) using the Scherrer equation (Eqn. 3.1).

$$D_{BET} = \frac{6 \cdot 10^3}{\rho_{XRD} \cdot SSA} \quad \textbf{(5.1)}$$

A – the specific surface area ($m^2 \cdot g^{-1}$),
ϱ_{XRD} – the theoretical density calculated from crystallographic data ($g \cdot cm^{-3}$) according to Equation 5.2.

Table 5.6 Specific surface area (SSA), and average particle size (D_{BET}) of SDC powders after different treatments.

T/°C	***Sample***	***SSA***/$m^2 \cdot g^{-1}$	D_{BET}/nm	D_{XRD}/nm	D_{BET}/D_{XRD}
250	10SDC	58.8	14.2	5.5	2.6
	20SDC	57.6	14.6	4.8	3.0
	30SDC	45.4	18.6	4.3	4.3
300	10SDC	52.6	15.9	5.9	2.7
	20SDC	49.2	17.1	5.1	3.3
	30SDC	37.9	22.3	4.8	4.6
500	10SDC	30.2	27.7	10.9	2.5
	20SDC	32.7	25.7	9.2	2.8
	30SDC	21.8	38.7	8.2	4.7
700	10SDC	12.9	64.8	25.2	2.6
	20SDC	15.5	54.2	22.0	2.5
	30SDC	10.2	82.7	19.5	4.2
900	10SDC	7.0	119.4	44.3	2.7
	20SDC	7.0	120.0	40.9	2.9
	30SDC	6.3	133.8	32.2	4.2

The SSA of the SDC powders significantly decreased, and particle size (D_{BET}) correspondingly increased as the calcination temperature increased, for all compositions. The highest values of SSA were found for 10SDC up to 500ºC. Above that temperature, 20SDC had the highest SSA until 900ºC, when the values for 10SDC and 20SDC were equal. The average particle size (D_{BET}) also showed a general tendency to increase with increasing Sm content at a particular calcination temperature, although there were exceptions to this at 500ºC and 700ºC. For any particular sample, the values of average particle size (D_{BET}) and average crystallite size (D_{XRD}) were not in agreement, even at low temperatures. This disagreement could be caused by the occurrence of crystalline nanodomains within individual nanocrystals. These nanodomains would register in XRD as individual crystals while the BET technique would measure the surface area of the parent nanocrystal only. Highly defective crystals may also give rise to line-broadening in XRD. However, another explanation is that the nanocrystals clustered together to form agglomerates of crystalline nanoparticles. If this is the explanation, the D_{BET}/D_{XRD} ratio is an index of extent of agglomeration. Curiously, these ratios appeared to be independent of temperature, even though the SSA and particle sizes were changing considerably. For each calcination temperature, therefore, the relationship between these ratios for the three compositions is essentially the same. Values for 10SDC and 20SDC are very similar while that for 30SDC is clearly higher.

5.3.5 Electron microscopy

The SDC nanopowders were analyzed by means of electron microscopy to study the morphology of the SDC nanopowders. Scanning Electron Microscopy (SEM) and Transmission Electron Microscopy (TEM) equipped with EDX detector were used as a very powerful tool for these observations.

5.3.5.1 Scanning Electron Microscopy

SEM images were obtained using a Philips XL30 ESEM instrument equipped with a field emission gun and EDX detector. Samples were coated with 30 nm of Au/Pd to reduce charging and allow better surface conductivity. In addition, a JEOL JSM-5600 was employed for elemental analysis experiments as well as to observe elemental distribution *via* the EDX mapping technique.

Figure 5.7 shows the microstructure of as-calcined powders before milling. Sponge-like, shell-like and branched structures were observed for all compositions after calcination at 500ºC for 2 h. The highly porous morphology of this as-prepared material is very likely to be caused by the large volumes of gas produced in the preparation methods, which have been discussed above in connection with the thermochemical analysis of the synthesis step. Equally, the presence of very small pores and their wide distribution is likely to relate to the intimate mixing of reactants achieved in the citrate complexation method. On the macroscale, these powders consisted of papery, fragile structures and were very voluminous. To break down the material, release the nanoparticles and increase the SSA, the materials were milled at 400 rpm for 1 h.

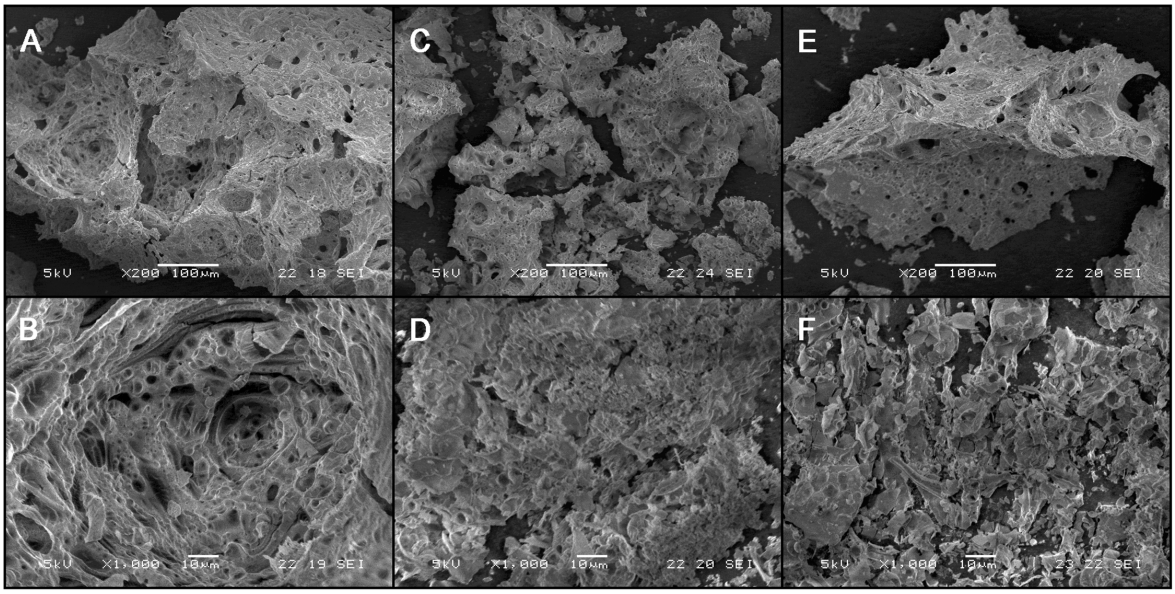

Figure 5.7 Low and high magnification SEM images of unmilled SDC powders calcined at 500ºC for 2 h. (A, B) 10SDC; (C, D) 20SDC; (E, F) 30SDC.

Figure 5.8 presents SEM images of the resulting milled SDC nanopowders in the left column. All three compositions appeared to consist of open structures of roughly spherical clusters made up of a relatively small number of clearly distinguishable primary particles. The spherical shape of these clusters may be advantageous in the preparation of dense pellets in the sintering step. The observation of clustering of the primary particles would tend to support the assignment of the D_{BET}/D_{XRD} ratio as an index of agglomeration.

The column on the right side contains EDX spectra of corresponding areas of SDC samples. Au and Pd peaks were indicated and should be ignored as all specimens were previously coated with these metals. However, no major impurities were noticed from any of these spectra. Elemental analysis data from EDX results are summarised in Table 5.7 to confirm Sm content in each sample. These were calculated as averages with errors quoted to two standard deviations.

Table 5.7 Results of elemental analysis for SDC powders calcined at 500ºC for 2 h.

Sample	$Sm_xCe_{1-x}O_{2-x/2}$	*x*
10SDC	$Sm_{0.1}Ce_{0.9}O_{1.95}$	0.098 ± 0.015
20SDC	$Sm_{0.2}Ce_{0.8}O_{1.90}$	0.195 ± 0.005
30SDC	$Sm_{0.3}Ce_{0.7}O_{1.85}$	0.307 ± 0.014

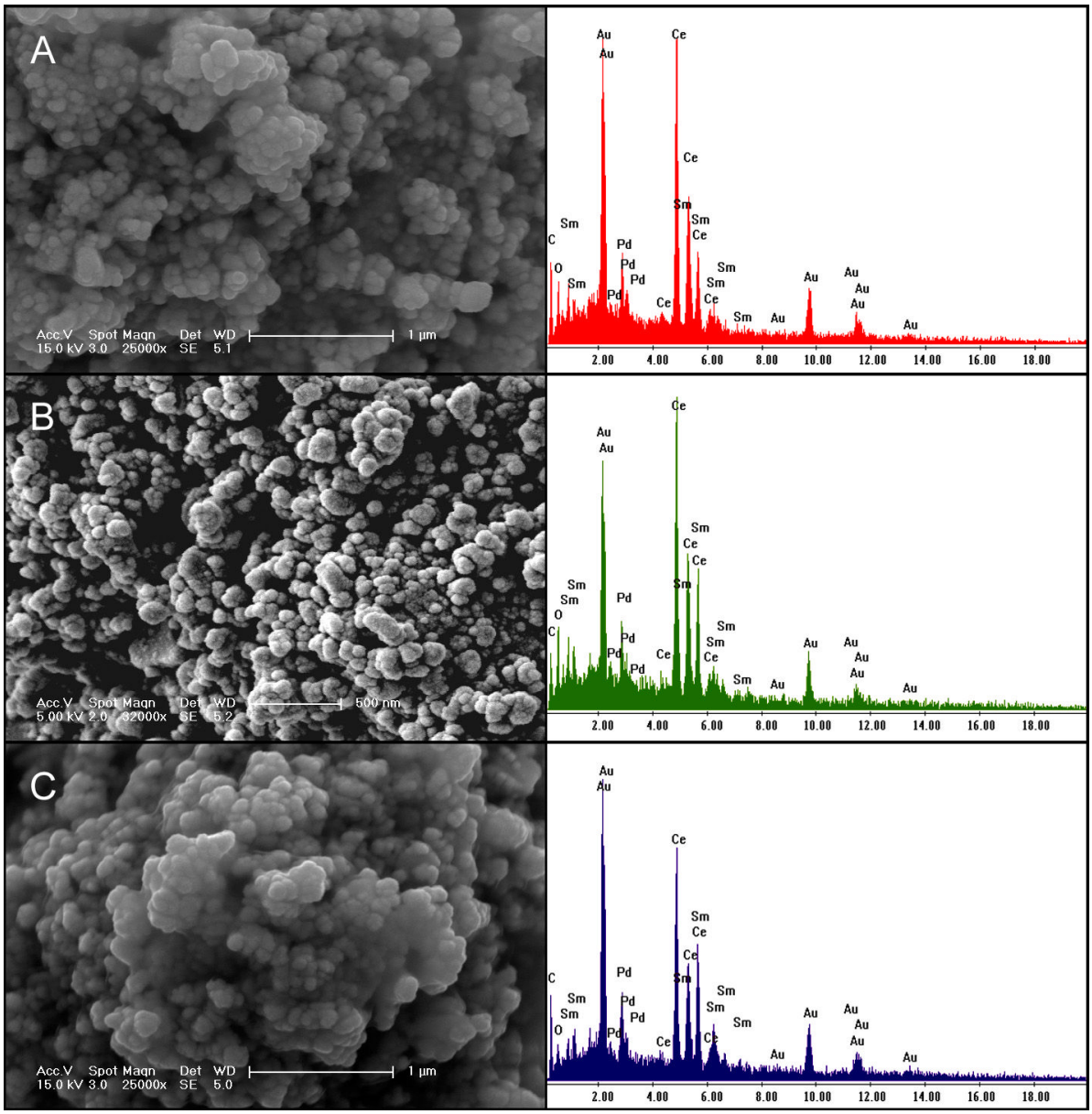

Figure 5.8 SEM images of SDC powders calcined at 500ºC for 2 h and milled at 400 rpm for 1 h, (A) 10SDC, (B) 20SDC and (C) 30SDC with corresponding EDX spectra.

Elemental maps of Sm, Ce and O are shown in Figure 5.9 for a representative 30SDC sample. The individual elements were also found to be evenly distributed in the other two nanoparticulate samples. Therefore no segregation of these elements within any form of agglomerates was observed at this stage of synthesis.

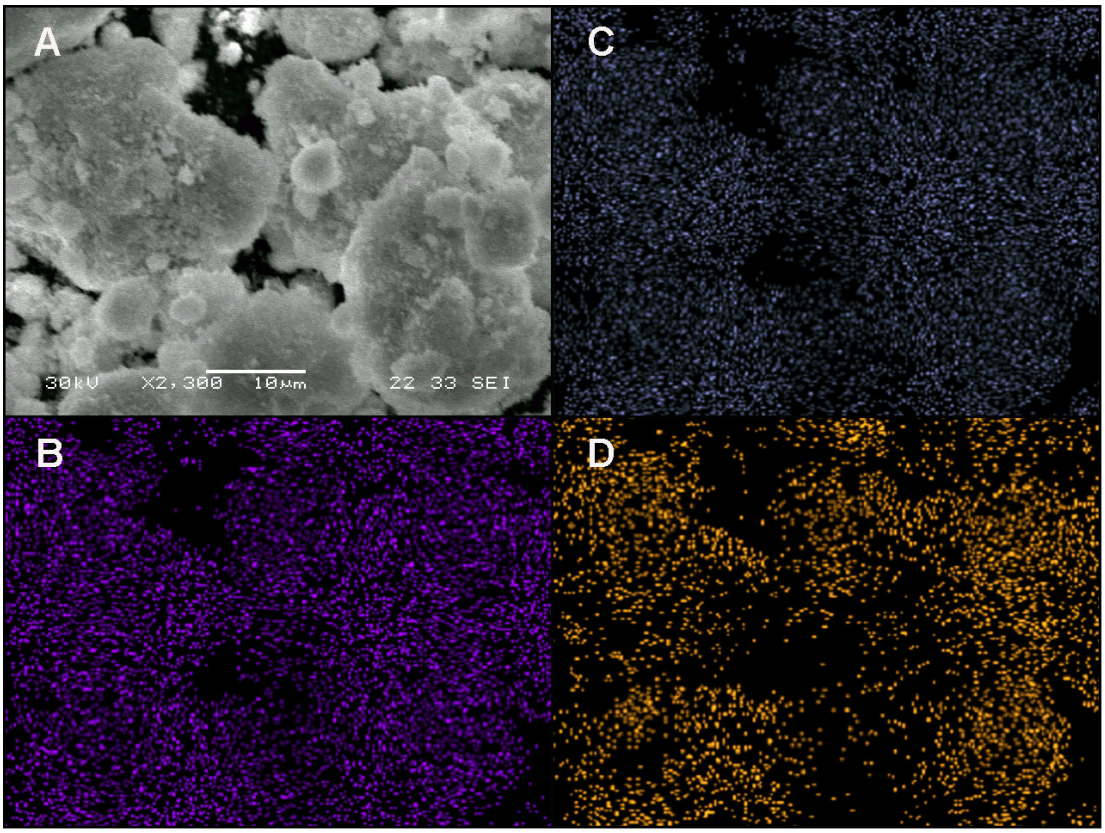

Figure 5.9 EDX map of 30SDC powder calcined at 500ºC for 2 h and milled at 400 rpm for 1 h showing distribution of (B) Sm, (C) Ce and (D) O elements within image (A).

5.3.5.2 Transmission Electron Microscopy

TEM images of all SDC powder samples at low, medium and high magnification are shown in Figure 5.10. All compositions consisted of loosely-agglomerated sheets and clusters, which were composed of individual crystallites of diameter ~10 nm.

The internal crystal structure of individual nanoparticles was observed using high resolution transmission electron microscopy (HR-TEM). These crystallites showed good crystallinity and there was no evidence for widespread defective crystal structures or for crystallites containing several nanodomains. In the absence of these phenomena, therefore, the TEM data confirmed the validity of using the ratio D_{BET}/D_{XRD} as an index of agglomeration. Digital Diffraction Patterns (DDPs) were obtained by processing specific areas of HR-TEM images using a Fast Fourier Transform (FFT) routine. Examples are inset in the corresponding images in Figure 5.10(C), (F) and (I). These represent three different crystallographic orientations and were indexed to the fluorite structure viewed in the [001], [011] and [112] zone axes, respectively. These patterns, and the interplanar spacings measured

from them, were consistent with substituted ceria. EDX analysis was performed in the TEM on several areas of each sample after calcination at 500ºC and confirmed x in $Sm_xCe_{1-x}O_{2-x/2}$ to be 0.094 ± 0.004, 0.202 ± 0.004 and 0.300 ± 0.002 (errors are two standard deviations) for 10SDC, 20SDC and 30SDC, respectively.

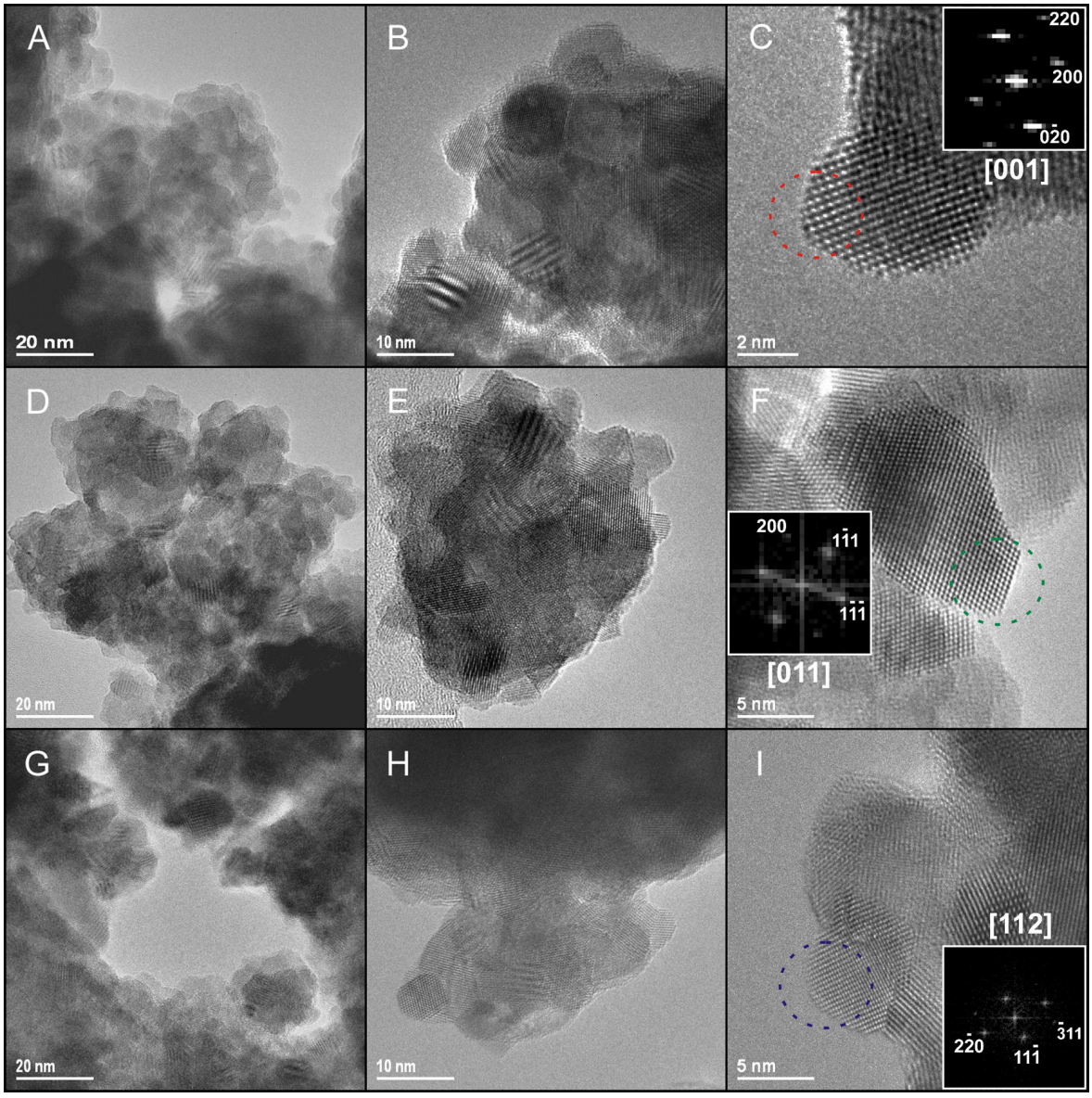

Figure 5.10 Low, medium and high magnification TEM images of nanopowders calcined at 500ºC for 2 h. (A, B, C) 10SDC; (D, E, F) 20SDC; (G, H, I) 30SDC. Digital Diffraction Patterns are inset in the high resolution images.

5.3.6 Inductively Coupled Plasma Mass Spectroscopy

More detailed elemental analysis was performed using the ICP-MS technique in order to find potential impurities, which could have been introduced during processing of synthesised materials, for example, in the milling step (using zirconia balls as grinding media). The ICP-MS results of the impurities detected are presented in Table 5.8 to a precision of two significant figures. These were calculated as an average of 5 measurements obtained from different points in each specimen. Their values were recalculated as wt% standardised with respect to Sm and Ce overall. They all were found to be relatively low, peaking for 20SDC with 0.16 wt% of Si and 0.20 wt% of As. This sample was found to be the most contaminated, because of additional Ca and Gd concentrations of 0.13 and 0.11 wt%, respectively. The highest amount of Gd was found in the 10SDC sample, at 0.15 wt%. Zr was not detected in any samples. Less than 0.05 wt% of Pr was present in all SDC compositions.

It is speculated whether the Gd could have been introduced from other experiments using this element, which were concurrently run in the same research lab. Such cross-contamination effects are difficult to avoid *via* shared equipment, especially high temperature furnaces. It should be noted, however, that because of the position of Gd and Pr in the periodic table, these elements could have been introduced from the starting Sm and Ce nitrates, respectively, even though these were of 99.5% purity. Elements such as Gd and Pr (when co-doped with SDC) were recently reported to have a positive impact on the conductive properties of ceria-based electrolytes.[88] On one hand, a small increase of porosity was reported by Ji *et al* for 5 mol% Sm_2O_3-doped ceria by co-doping of 2 mol% of Pr^{3+}. On the other hand, it resulted in an increase in the total ionic conductivity of the electrolyte.[75] There is no evidence of As usage in the group, so it may also have come from the staring materials. The possibility of some interference among elements introduced into the Ar environment in the ICP-MS instrument may be a source of other unexpected elements. The ^{42}Ca isotope was used to analyse for Ca to avoid the ^{40}Ar peak.

Table 5.8 ICP-MS results for SDC powders calcined at 500ºC for 2 h in wt%.

Sample	*Si*	*Ca*	*As*	*Zr*	*Pr*	*Gd*
10SDC	0.067	0.022	0.056	0	0.047	0.15
20SDC	0.16	0.13	0.20	0	0.045	0.11
30SDC	0	0	0.15	0	0.024	0.065

5.3.7 Dilatometry

The SDC powders calcined at 500°C for 2 h were uniaxially pressed at 200 MPa in a 10 mm diameter die. In order to assess their sintering properties, these SDC green bodies were subjected to a temperature program, which consisted of heating from ambient to 1470ºC at a rate of 2ºC/min followed by an isothermal dwell at 1470ºC for 6 h. Air (50 ml/min) was employed as the purge gas.

Figure 5.11 presents the % change in length, dL/L_o, for each sample and the temperature profile applied. For all three samples, a total dimensional change of 16-18% took place. All three curves had broadly similar shapes. In all cases, the sintering or compaction process started gradually at temperatures as low as 200ºC, but the shrinkage process was relatively slow up to about 500ºC. This is logical since the powders had already been calcined at 500ºC for 2 h during their preparation. From 500 to 600ºC, sample volume decreased rapidly, for 10SDC at an approximately constant rate, but for 20SDC and 30SDC, in what appeared to be a two-stage process, with the higher rates at the higher temperatures. Sintering of the 10SDC was essentially complete by about 1350ºC. However, for the 20SDC and 30SDC, some sintering clearly continued - although at a low rate - after the samples had reached the maximum temperature of 1470ºC. After 6 h at 1470ºC sintering in all samples did appear to be essentially complete since the rate of dimensional change was negligible by this point.

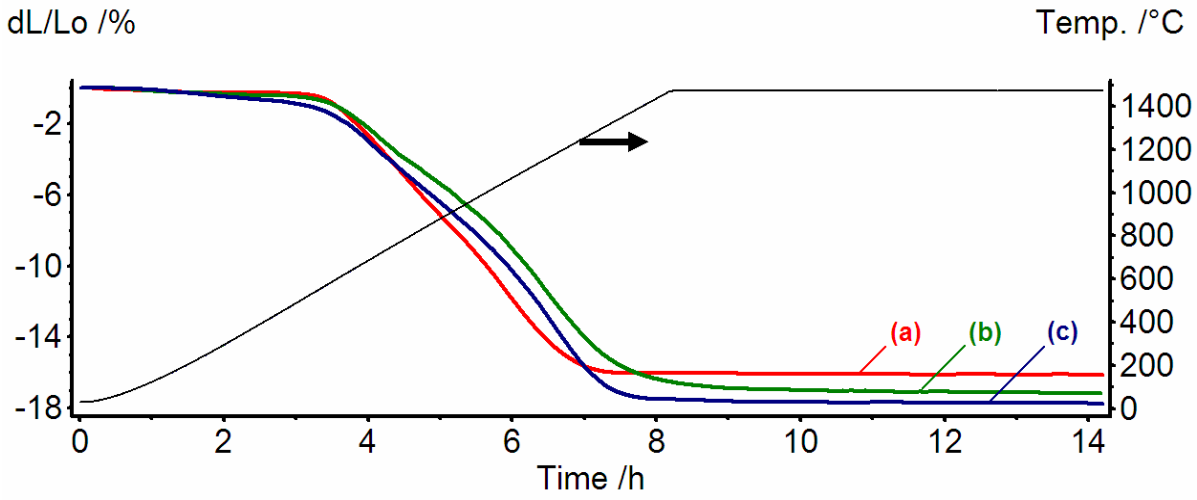

Figure 5.11 Linear dilatometry plots of relative length change against time and temperature for compacted nanopowders: (a) 10SDC, (b) 20SDC and (c) 30SDC.

5.4 Pellet characterisation

Electrolytes were prepared from SDC nanopowders under six different sintering regimes. The grain structure of the resulting SDC ceramics was studied and related to their ionic conductivity as determined by impedance spectroscopy.

The dilatometry results were used to set the conditions of the six sintering regimes to be used in further study of the microstructure and conductivity of the sintered SDC pellets. Three temperatures spanning the range over which sintering finished its rapid phase - 1300ºC, 1400ºC and 1450ºC - and two sintering times - 4 and 6 h - were applied to each of the three SDC compositions. This gave a total of 18 distinct pellet samples.

5.4.1 Density and XRD studies

Dense electrolyte pellets were prepared from the nanopowders calcined at 500ºC for 2 h by uniaxial pressing at 200 MPa in a 13 mm diameter cylindrical die and firing in static air under six different sintering regimes. Heating and cooling rates were 2ºC·min^{-1} and 4ºC·min^{-1}, respectively.

XRD studies on the SDC pellets sintered at 1450ºC for 6 h – the most severe conditions – were consistent with a single phase of fluorite structure. Figure 5.12 shows XRD patterns of the three SDC compositions. These contained no evidence of impurity peaks and since the nanopowders after calcination at 500ºC also appeared to be phase-pure (Figure 5.5), it can reasonably be assumed that the five less severe sintering regimes also gave rise to high purity pellets. The peaks in Figure 5.12 are much sharper than those presented in Figure 5.5 for the nanopowders, because of the significant growth in crystallite size during sintering.

The theoretical densities of the SDC crystal structures were calculated according to Equation 5.2 from the crystallographic information obtained by XRD.[145]

$$\rho_{XRD} = \frac{4 \cdot \left[(1-x) \cdot M_{Ce} + x \cdot M_{Sm} + (2 - \frac{x}{2}) \cdot M_O \right]}{a^3 \cdot N_{Av}} \qquad \textbf{(5.2)}$$

M – the atomic weight (g·mol^{-1}),
x – the dopant mole fraction,
a – the lattice parameter (Å),
N_{Av} – the Avogadro's constant (6.022·10^{23} mol^{-1}),

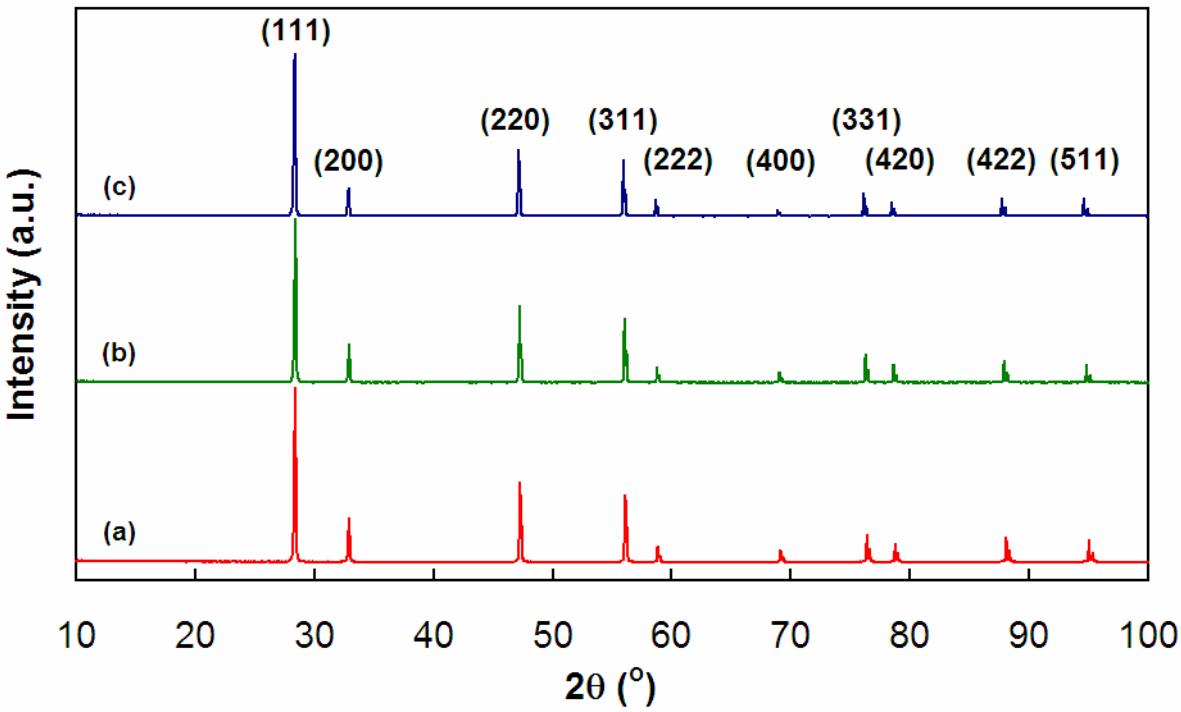

Figure 5.12 XRD patterns of SDC pellets after sintering at 1450ºC for 6 h (a) 10SDC, (b) 20SDC, (c) 30SDC.

The densities of all sintered pellets were obtained from their masses and dimensions. These density values were divided by the corresponding theoretical density to obtain the relative densities (ρ_r) of the fired SDC pellets, which are presented in Table 5.9. The highest relative density - 97% of theoretical - was obtained for 10SDC when the highest sintering temperature and the longest sintering time (1450°C/6 h) were employed. This is consistent with the dilatometry results, which showed that sintering of 10SDC was essentially complete at the lowest temperature of the three compositions.

In all cases, extension of the sintering time from 4 to 6 h gave rise only to a very small improvement in density. For all three compositions, relative densities of more than 95% were achieved at sintering temperatures of both 1400ºC and 1450ºC, and times of either 4 or 6 h. There was also a slight, but general decrease in pellet density with increasing Sm content.

Table 5.9 Sintering temperature (T_s), sintering time (t_s), relative densities (ρ_r) and average grain size (g_a) of SDC pellets.

Sample	T_s / °C	t_s / h	ρ_r / %	g_a / µm
10SDC	1300	4	93.1	0.48
20SDC			92.1	0.52
30SDC			91.3	0.45
10SDC	1400	4	96.0	0.75
20SDC			95.2	0.81
30SDC			95.0	0.73
10SDC	1450	4	96.5	0.99
20SDC			95.6	1.07
30SDC			95.1	0.91
10SDC	1300	6	93.7	0.55
20SDC			93.0	0.54
30SDC			92.5	0.46
10SDC	1400	6	96.7	0.77
20SDC			95.8	0.88
30SDC			95.3	0.75
10SDC	1450	6	97.1	1.06
20SDC			96.7	1.12
30SDC			96.5	0.94

5.4.2 Scanning Electron Microscopy

SDC pellets were polished and thermally etched for examination of their microstructure using SEM. The essential etching process was carried out at a temperature 50°C lower than the corresponding sintering temperature, employing a short dwell time of 1 min but identical ramp rates. Pellets were coated with a 15 nm layer of Au-Pd and SEM images were obtained using a JEOL JSM-5600 instrument. Statistical grain size analyses were carried out for each sample using these images.

Figure 5.13, Figure 5.14 and Figure 5.15 show SEM images of all SDC samples. In order to quantify differences in microstructure caused by the different sintering regimes, many grains were measured from the micrographs of each pellet type using ImageJ software. The resulting data are presented as grain size distribution histograms in corresponding figures. In the SEM images, well-developed, interlocking, roughly hexagonal grains were observed in all samples. Significant porosity was seen in the SDC sample prepared under the mildest sintering regime (1300°C/4 h) and also, to much lesser extent, in the next-mildest (1400°C/4 h).

For 20SDC, the images in Figure 5.14(d) and (e), as well as the relative density values in Table 5.9 indicate that there was a clear reduction in porosity and increase in relative density on sintering at these two temperatures for 2 h longer. The samples sintered at 1400°C for 6 h and at 1450°C for 4 h had excellent microstructure, with very low porosity and large grains. Surprisingly, some pores were observed after sintering at the highest temperature for the longer time (1450°C/6 h, Figure 5.14(f)). This phenomenon is known as an oversintering and has been reported to cause a drop in ionic conductivity in $Ce_{0.8}Sm_{0.1}Nd_{0.1}O_{1.9}$.[90] Grain size distributions for samples sintered at both 4 h and 6 h showed the expected marked increase in mean grain size and broadening of the distribution, which would be expected as sintering temperature increased. However, increasing sintering time at the same temperature from 4 to 6 h had only a small effect on the grain size distributions. Overall, the same trends were seen in the 10SDC and 30SDC samples (Figure 5.13 and Figure 5.15), although porosity was a more marked problem in these two compositions. For example, the 1300°C/6 h samples both showed significant porosity. However, as for 10SDC, the samples prepared at 1400°C for 6 h and at 1450°C for 4 h had very good microstructure. In 10SDC there is some evidence for a bimodal grain size distribution after sintering at 1450°C for 6 h (Figure 5.13). For all compositions, some porosity was observed in the 1450°C/6 h samples. The effect of Sm content on grain size can most easily be seen in Table 5.9. In general, 20SDC had the largest mean grain size and 30SDC the smallest. Indeed, 30SDC was found to be the most difficult to sinter as these pellets often cracked during sintering. The data in Table 5.9 also confirm that changing the sintering time from 4 to 6 h resulted in only small increase in mean grain size.

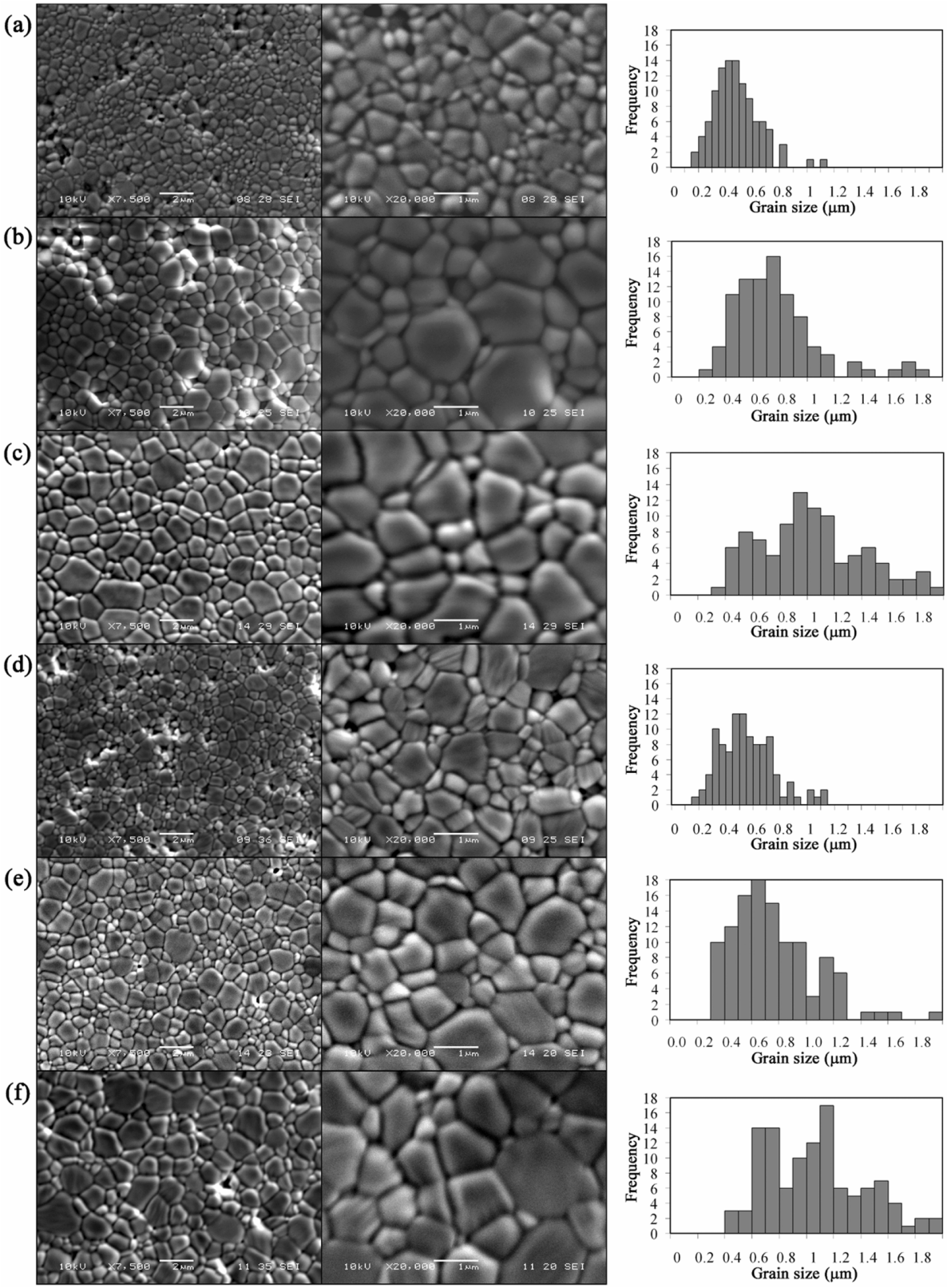

Figure 5.13 Low and high magnification SEM images and associated grain size distribution histograms for 10SDC pellets after sintering as follows: (a) 1300ºC/4h, (b) 1400ºC/4h, (c) 1450ºC/4h, (d) 1300ºC/6h, (e) 1400ºC/6h and (f) 1450ºC/6h.

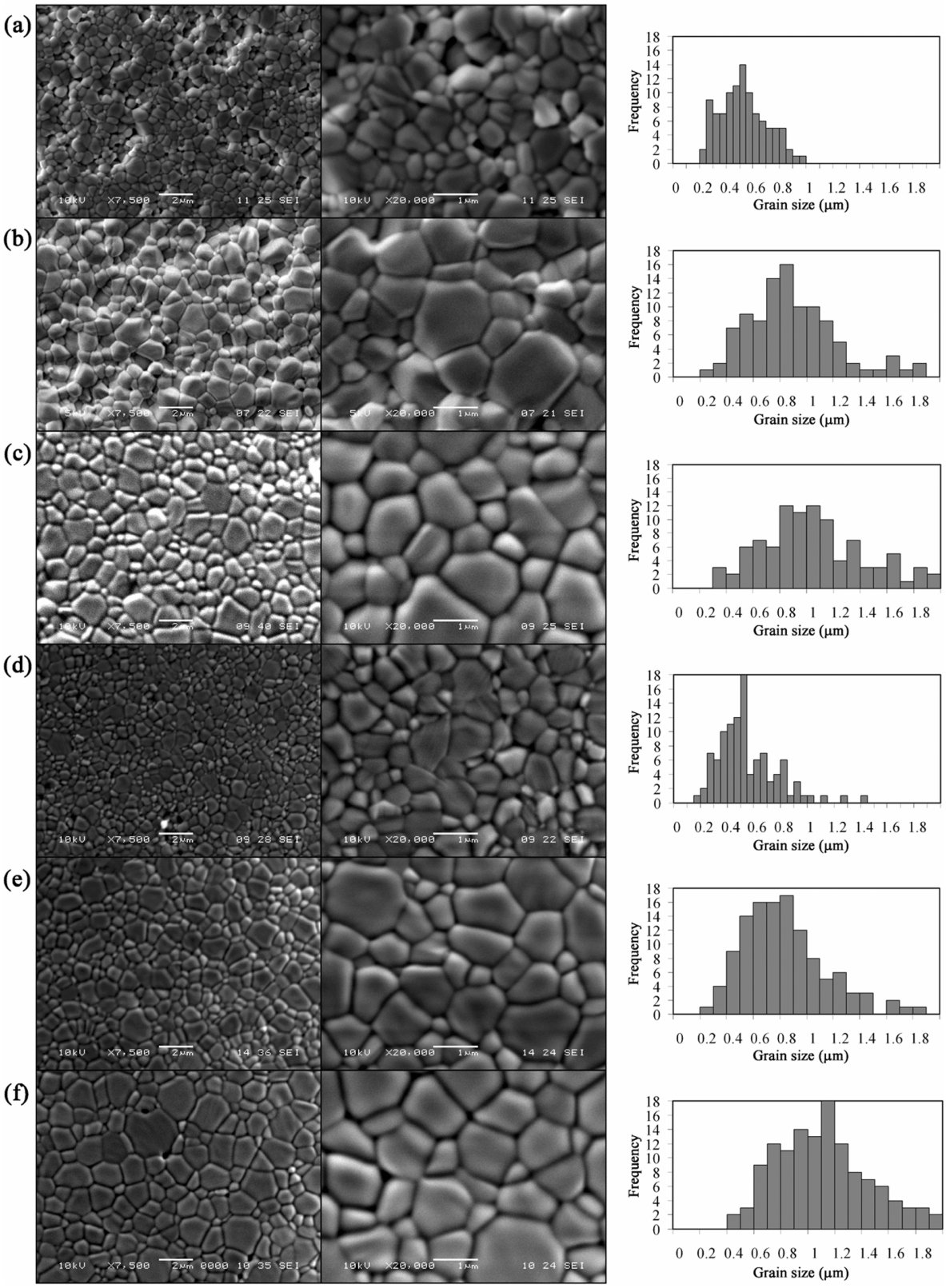

Figure 5.14 Low and high magnification SEM images and associated grain size distribution histograms for 20SDC pellets after sintering as follows: (a) 1300ºC/4h, (b) 1400ºC/4h, (c) 1450ºC/4h, (d) 1300ºC/6h, (e) 1400ºC/6h and (f) 1450ºC/6h.

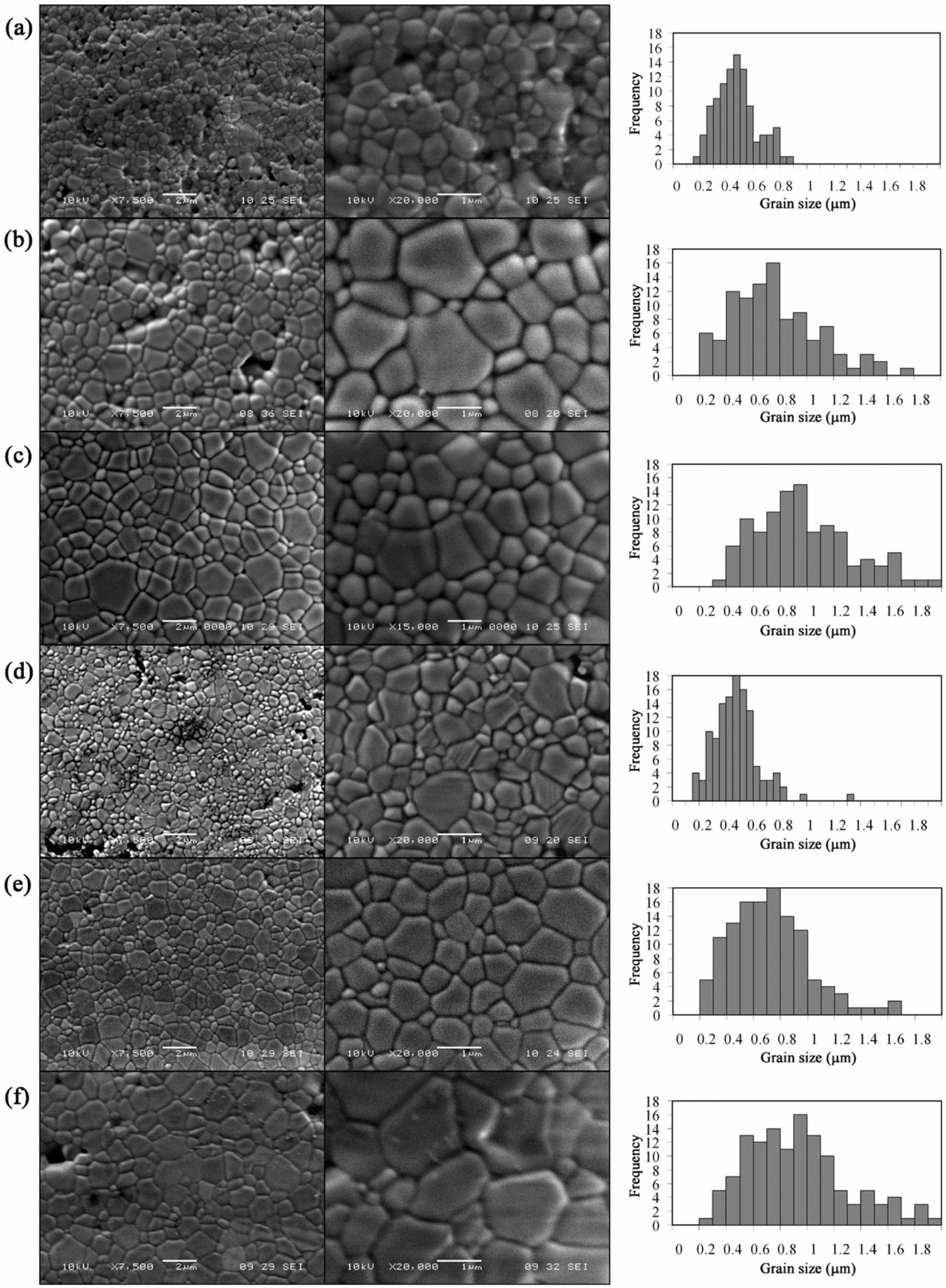

Figure 5.15 Low and high magnification SEM images and associated grain size distribution histograms for 30SDC pellets after sintering as follows: (a) 1300ºC/4h, (b) 1400ºC/4h, (c) 1450ºC/4h, (d) 1300ºC/6h, (e) 1400ºC/6h and (f) 1450ºC/6h.

5.4.3 Impedance Spectroscopy

Twelve samples were chosen for impedance studies in light of density and SEM studies discussed above. Pellets of all three SDC compositions sintered at 1400°C for 4 h and sintered at 1300°C, 1400°C and 1450°C, each for 6 h, were investigated. The SDC nanopowders calcined at 500ºC for 2 h were used to prepare their green bodies. These were pressed uniaxially at 200 MPa in a 25 mm diameter cylindrical, stainless steel die. The sintering process was performed using identical conditions and ramp rates to those applied for the SEM studies. The impact of electronic conductivity was not considered to be a contributor to the overall conductivity value, as for SDC and related doped ceria materials it is reported to be very low under the oxidising conditions employed in these studies.[146, 147] In addition, SDC has ionic transport numbers very close to unity under such conditions, a value that results in good fuel cell efficiency.[148]

Example impedance spectra (Nyquist plots) are presented in Figure 5.16 together with the equivalent electronic circuit, which was used to fit the impedance data. The spectra are all for pellets of 10SDC and vary only in terms of the sintering regime used to prepare them. All spectra contained two arcs, which could be confidently assigned as the bulk and grain boundary responses. Numeric labels indicate the decimal log of the frequency of the applied voltage signal. The bulk arc occurred at the higher frequency. This figure illustrates that changing the sintering regime had very little effect on the bulk arc whereas the grain boundary arc decreased in size (corresponding to a decrease in grain boundary resistance) as the severity of the sintering regime increased from 1300°C/4 h to 1450°C/6 h. This is as expected since the grain boundary arc is dependent on the microstructure of the pellet, particularly on the grain size. It has already been shown above that grain size and grain size distribution changed considerably between the different sintering regimes. The spectra in Figure 5.16 are consistent with a decrease in grain boundary resistance as mean grain size increased.

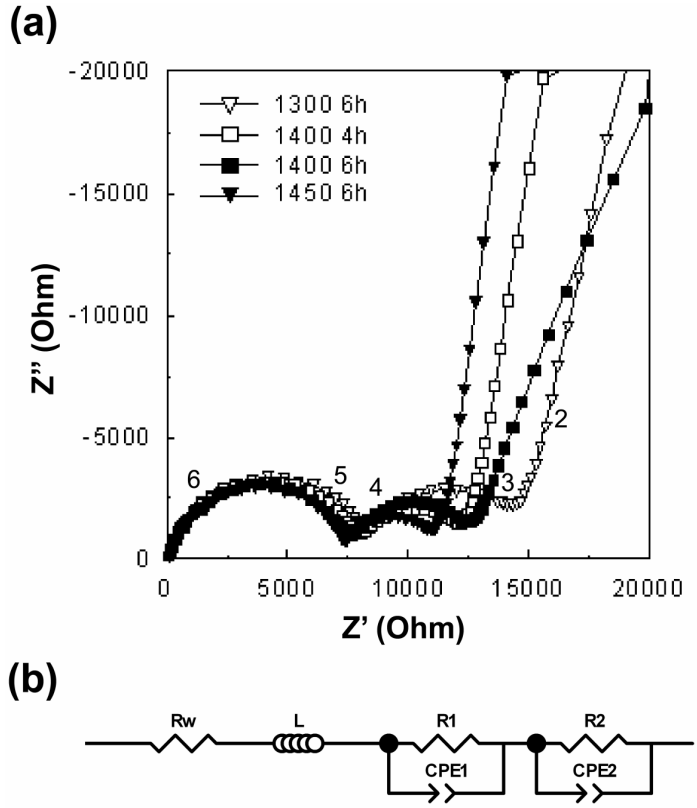

Figure 5.16 (a) Impedance spectra of 10SDC pellets prepared under different sintering regimes, recorded at 200°C. (b) the corresponding equivalent circuit model.

Figure 5.17 illustrates the effect of sample composition on the impedance spectra. In this case, all samples were prepared using the same sintering regime: 1400ºC/6 h. In the impedance spectra recorded at 250°C in Figure 5.17(a) and (b) it can be seen that increasing Sm content caused a marked increase in bulk resistance since the corresponding bulk arc increased in size. Overall electrolyte resistance (bulk plus grain boundary) also increased with increasing Sm content. The grain boundary contribution for 30SDC was very small compared to the corresponding bulk arc. In the spectra obtained at 500ºC in Figure 5.17(c), the arcs were lost because of a large inductive effect in the apparatus. However, the total electrolyte resistance can be obtained from the intercept of the spectra with the Z' axis. The electrolyte resistances of 10SDC and 20SDC were very similar at this temperature but 30SDC still had the highest value.

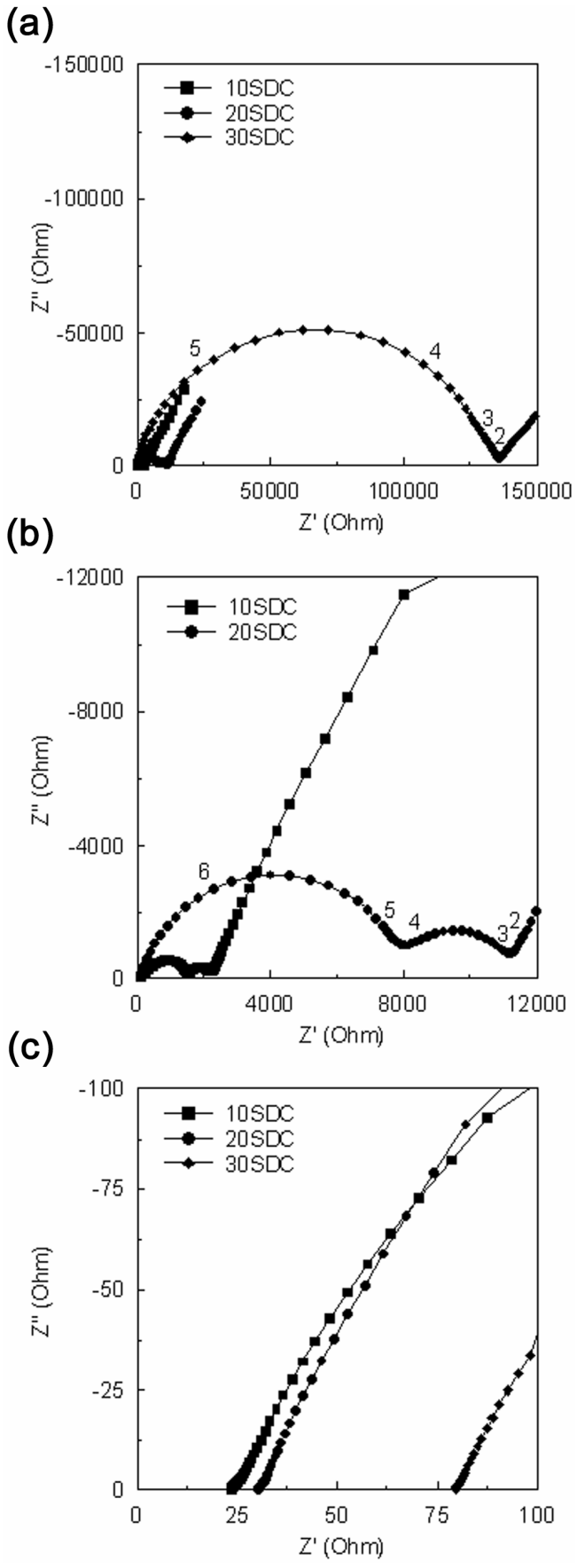

Figure 5.17 Impedance spectra of SDC pellets sintered at 1400ºC for 6 h. (a) recorded at 250ºC; (b) recorded at 250ºC, detail showing spectra for 10SDC and 20SDC; (c) recorded at 500ºC.

Conductivity values for bulk and grain boundary contributions were calculated from the corresponding resistances obtained by fitting the impedance spectra, the thickness of the SDC electrolyte pellets and the geometric area of the Pt electrodes. Arrhenius-type plots of bulk and grain boundary contributions were constructed using these data and are presented in Figure 5.18 for all three SDC compositions and for four sintering regimes.

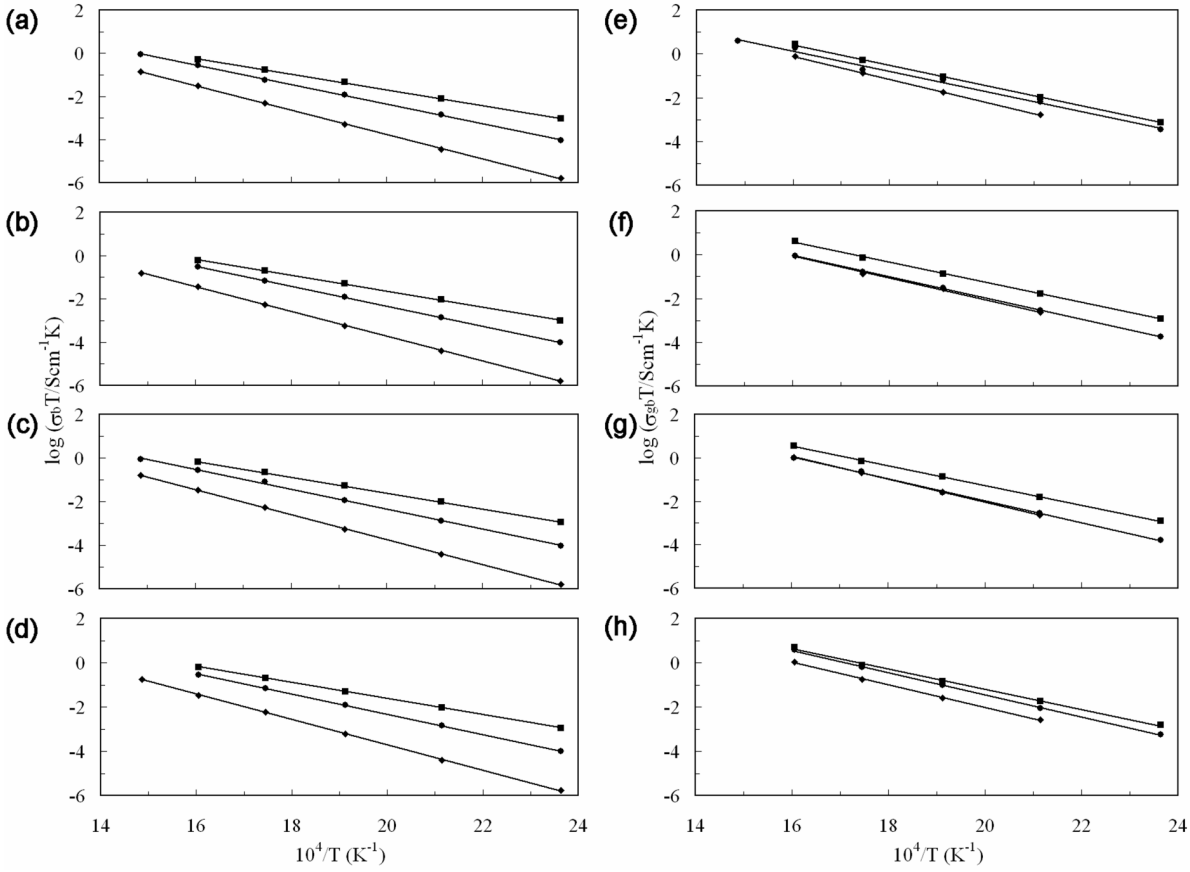

Figure 5.18 Arrhenius–type plots of (a-d) bulk and (e-h) grain boundary conductivity of (■) 10SDC, (●) 20SDC and (♦) 30SDC samples sintered at (a,e) 1300°C/6 h; (b,f) 1400°C/4 h; (c,g) 1400°C/6 h; (d,h) 1450°C/6 h.

Grain boundary conductivity was found to be higher than bulk conductivity for all compositions. In all cases, bulk conductivity increased with decreasing Sm content, in the temperature range presented in the figure, and the bulk conductivity of 30SDC was considerably lower than for the other two compositions. However, the traces tend to converge as measurement temperature increased. The individual sintering regime used to prepare the pellets appeared to have little effect on these bulk conductivity plots. This is confirmed in Figure 5.19(a) where bulk conductivity measured at 300ºC is plotted against Sm content for the four sintering regimes. For each composition, the data points are closely grouped. However, there does seem to be a trend: bulk conductivity increased with the severity of the

sintering regime from 1300ºC/6 h to 1400ºC/4 h and to 1400ºC/6 h, but then dropped on going to 1450ºC/6 h for all three compositions. Turning to the grain boundary plots in Figure 5.19, it is seen that the chemical composition of the electrolyte had much less effect than on bulk conductivity. There is a general, small increase in grain boundary conductivity with decreasing Sm content, a trend which mirrors that seen for the bulk conductivity, although it is much less marked. Indeed, in Figure 5.18(f) and (g), the traces for 20SDC and 30SDC are essentially coincident. Changing sintering regime had a generally more significant effect on grain boundary than on bulk conductivity as is seen in Figure 5.19(b). For each composition, there is a wider spread in the data points than for the bulk data in Figure 5.19(a). With the exception of some close and overlapping points, the general trend is of increasing grain boundary conductivity with increasing severity of sintering regime. Grain boundary conductivities were higher than some of those reported by Zhan *et al*, in studies of similar compositions prepared by conventional ceramic routes.[149] This indicates that the materials obtained in this contribution had low impurity levels.

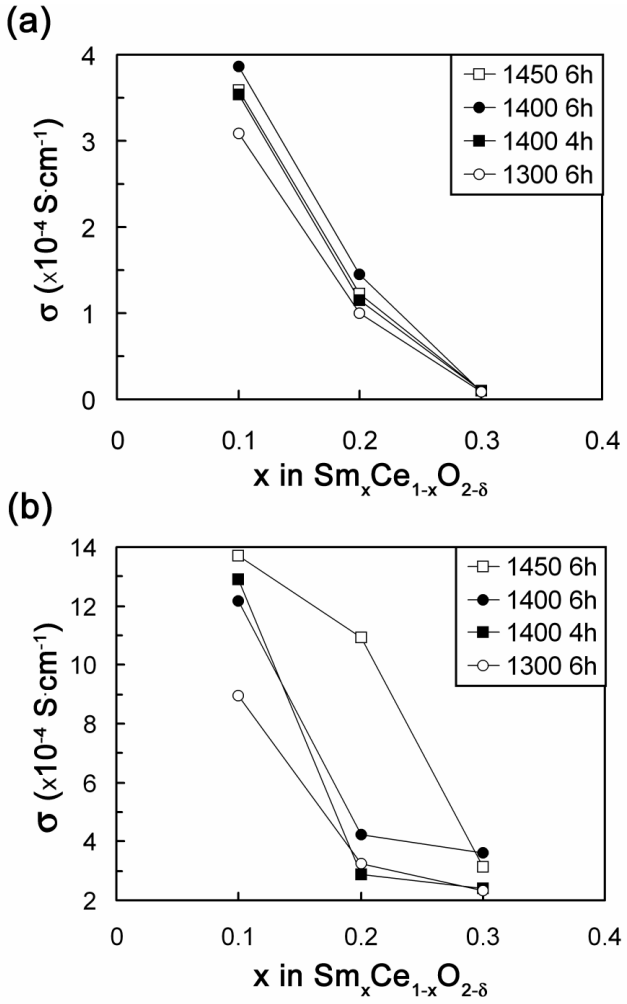

Figure 5.19 (a) bulk and (b) grain boundary conductivity measured at 300ºC for SDC pellets prepared following different sintering treatments as a function of Sm content.

Apparent activation energies were obtained from the slopes of the Arrhenius-type plots in Figure 5.18 and these are presented in Table 5.10. For bulk conductivity, the activation energies were almost exactly the same for each SDC composition, independent of sintering regime. There were quite large differences between compositions, however. Activation energy increased markedly with increasing Sm content. Turning to the activation energies for the grain boundary conductivity, again there was little change between sintering regimes for each individual composition and there was a small general increase in activation energy with increasing Sm content.

Table 5.10 Activation energies (E_a) of bulk and grain boundary conductivity for SDC pellets prepared following different sintering treatments.

Sample	T_s / °C	t_s / h	E_a / eV	
			bulk	*grain boundary*
10SDC	1300	6	0.72	0.92
20SDC			0.90	0.92
30SDC			1.12	1.04
10SDC	1400	4	0.73	0.91
20SDC			0.91	0.97
30SDC			1.13	0.99
10SDC	1400	6	0.72	0.90
20SDC			0.90	1.00
30SDC			1.13	1.04
10SDC	1450	6	0.72	0.91
20SDC			0.91	0.99
30SDC			1.14	1.02

While bulk and grain boundary conductivities give useful insight into the composition-microstructure-conductivity relationship, total electrolyte conductivity is an important parameter for the comparison of electrolyte materials. The total electrolyte conductivity values in this work compared favourably with those quoted in the literature for materials of similar composition.[32, 78] To provide a convenient comparison between all SDC samples, the total conductivity data recorded at 500°C and at 600°C are presented in Figure 5.20.

At 500°C, it is clear that total conductivity increased as Sm content decreased. However, starting at about 600°C, the 20SDC samples begin to overtake 10SDC to attain the highest total conductivity values. This is clear by 700°C. These total conductivity values, including

those at 700°C, as well as the activation energies for total conductivity in low and high measurement temperature regions, are summarized in Table 5.11.

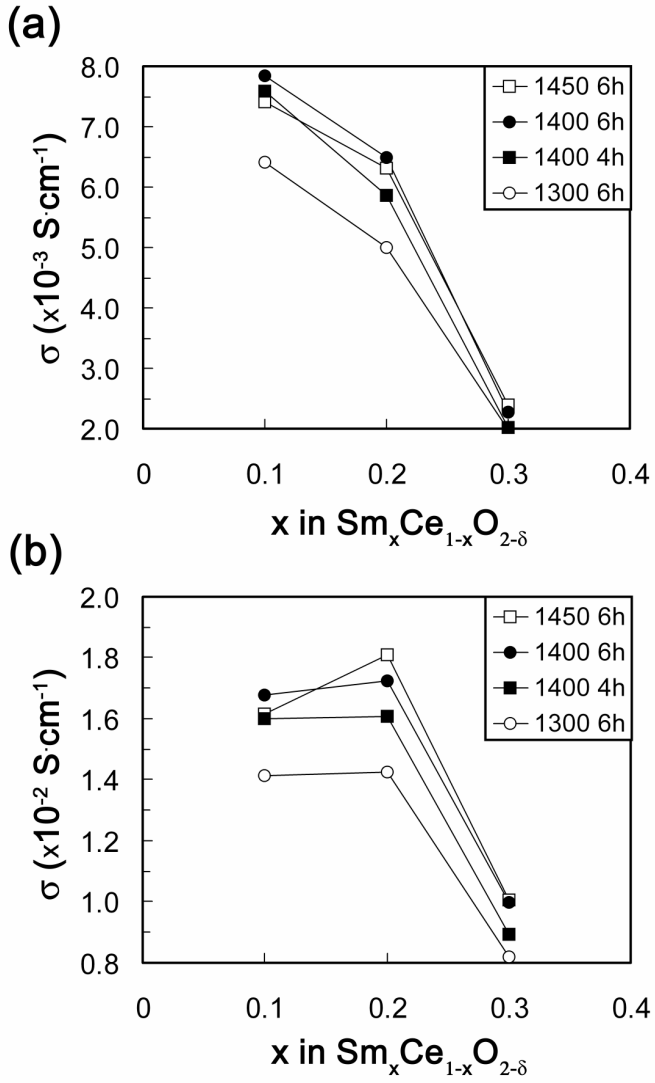

Figure 5.20 Total conductivity of SDC pellets prepared following different sintering treatments as a function of Sm content. Measured at (a) 500°C and (b) 600°C.

There was a clear general increase in total conductivity with increasing sintering time (at the same sintering temperature) and with increasing sintering temperature (for 6 h). This can be attributed to increases in grain boundary conductivity related to an increase in sample density and in grain size as the severity of the sintering regime increased. However, there was an exception to this general trend. Surprisingly, on going from the 1400°C/6 h regime to the 1450°C/6 h regime, most of the total conductivity values for 20SDC and 30SDC stayed about the same and those for 10SDC decreased.

Table 5.11 Total conductivity data (σ), Activation Energies (E_a) and association enthalpies (ΔH_a) for SDC pellets prepared following different sintering treatments.

Sample	T_s/°C	t_s/h	σ /× 10^{-2} S·cm^{-1}			E_a /eV		
			500°C	600°C	700°C	< 500°C	> 500°C	ΔH_a /eV
10SDC	1300	6	0.64	1.41	2.02	0.76	0.38	0.38
20SDC			0.50	1.43	2.20	0.88	0.47	0.41
30SDC			0.20	0.82	1.68	1.12	0.66	0.46
10SDC	1400	4	0.76	1.60	2.56	0.75	0.42	0.33
20SDC			0.59	1.61	2.67	0.91	0.50	0.41
30SDC			0.20	0.89	2.08	1.12	0.73	0.39
10SDC	1400	6	0.78	1.68	2.69	0.75	0.43	0.32
20SDC			0.65	1.73	3.08	0.92	0.49	0.43
30SDC			0.23	0.99	2.27	1.13	0.71	0.42
10SDC	1450	6	0.74	1.61	2.56	0.74	0.42	0.32
20SDC			0.63	1.81	3.07	0.89	0.50	0.39
30SDC			0.24	1.00	2.27	1.13	0.71	0.42

Since mean grain size and density increased on going from the 1400°C/6 h regime to the 1450°C/6 h regime, it seems that these changes in conductivity must be related to some other change in the samples prepared at 1450°C for 6 h. Indeed the evidence from Figure 5.19 is that grain boundary conductivity increased with increasing sintering temperature, while the bulk conductivity showed a drop between 1400°C/6 h and 1450°C/6 h. Although this decrease was relatively small, it appeared to dominate the total conductivity because bulk conductivity was significantly lower than grain boundary conductivity in all cases in these materials. Liu *et al* observed a similar oversintering effect – re-emergence of pore formation and decrease in total ionic conductivity at high sintering temperatures - in Sm- and Nd- co-doped ceria electrolytes sintered at temperatures from 1400°C to 1600°C.[90] Sha *et al* prepared electrolyte pellets of $Ce_{0.8}Sm_{0.1}Y_{0.1}O_{1.9}$ by sintering at temperatures of 1300 to 1600°C.[92] They obtained total, bulk and grain boundary conductivity values at measurement temperatures from 300 to 600°C and observed a decrease in total conductivity with increasing sintering temperature, which also coincided with the emergence of porosity in the samples. Grain boundary conductivity decreased as sintering temperature was increased from 1300 to 1500°C, but then remained approximately constant on going from 1500 to 1600°C. Bulk conductivity, however, showed clear general decreases from 1400 to 1500°C and from 1500 to 1600°C. Therefore, it appears that oversintering caused changes, which had (at least partly) independent effects on grain boundary and on bulk conductivity. The changes in grain

boundary conductivity can be explained by the competing effects of increasing grain size and increasing porosity. The decrease in bulk conductivity would normally be expected to be caused by a chemical or phase change within the bulk material, although no evidence for the latter is seen in the accompanying XRD patterns. In the SDC samples of the current contribution, a similar decrease in bulk conductivity accompanied by emergence of porosity at the highest sintering temperature was observed, most markedly for 10SDC. It is not possible to attribute this effect definitively. The only process which might affect bulk conductivity without affecting the XRD patterns noticeably would be low level diffusion of Sm ions within the individual grains of the material, giving rise to small domains with slightly differing Sm concentrations - and therefore differing conductivities - but retaining the original crystal structure. However, detailed high temperature studies would be required to investigate this possibility further.

The activation energies of total conductivity are presented in Table 5.11 for the temperature regions below 500°C and above 500°C. This is because there was a clear change of gradient at around this temperature. This can be seen for all SDC compositions after the same sintering regime in Figure 5.21 and was found to be a completely general effect across all samples studied.

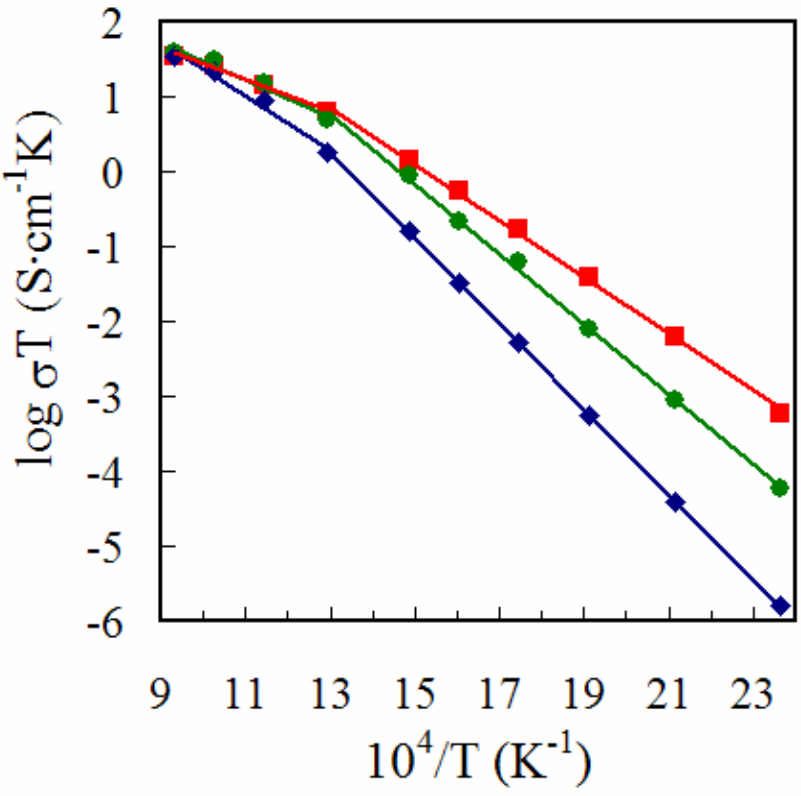

Figure 5.21 Arrhenius–type plots of total electrolyte conductivity of (■) 10SDC, (●) 20SDC and (♦) 30SDC. Samples sintered at 1400°C for 6 h.

In Table 5.11 it is clear that the effect of sintering regime on these values was again minimal: neither the values above nor those below 500°C changed significantly between different sintering regimes for the same SDC composition. However, as was seen for the bulk and grain boundary activation energies, SDC composition had a strong effect on activation energy, which increased with increasing Sm content in all cases. For all SDC compositions and all sintering regimes, the activation energies of total conductivity at measurement temperatures above 500°C were significantly smaller than those pertaining below 500°C. The difference ranged from 0.32 to 0.46 eV and showed a tendency to increase with increasing Sm content, particularly from 10SDC to 20SDC. Qualitatively similar effects have been reported for similar materials. Zhan *et al* observed a curvature in Arrhenius-type conductivity plots for a range of SDC samples prepared by solid state reaction.[149] Arachi *et al* reported similar behaviour for YSZ and scandia-stabilised zirconia systems and explained it as an effect related to the dissociation energy required to separate an oxide ion vacancy from a dopant ion site.[62] Piñol *et al* observed a distinct slope change at 700°C for GDC and suggested that this was caused by increasing interactions between the dopant species and the charge carriers with decreasing temperature.[74] Steele discussed such a change in the activation energy of conductivity in GDC in terms of the migration enthalpy of oxygen ion vacancies (ΔH_m) and the association enthalpy (ΔH_a) between Gd sites and oxygen ion vacancies (Gd'_{Ce}-$V_o^{\bullet\bullet}$), which must be overcome to free vacancies so that they may become involved in conduction.[78] In high purity $Ce_{0.9}Gd_{0.1}O_{1.9}$, Steele obtained values of ΔH_m = 0.64 eV and ΔH_a = 0.13 eV with an inflection in the Arrhenius-type conductivity plot at around 400ºC. In the current contribution, the activation energy of the electrolyte contribution at temperatures above 500ºC can be equated to the migration enthalpy, with average values of ΔH_m = 0.41 eV for 10SDC, 0.49 eV for 20SDC and 0.70 eV for 30SDC. If we assume the difference between the activation energies in the high and low temperature regimes equates to the association enthalpy of Sm'_{Ce}-$V_o^{\bullet\bullet}$ species,[150] we obtain average values of ΔH_a = 0.34 eV for 10SDC, 0.41 eV for 20SDC and 0.42 eV for 30SDC. Clearly, ΔH_m was the more sensitive of these two enthalpies to Sm content and was particularly high for 30SDC.

The activation energies below 500ºC for total electrolyte conductivity (Table 5.11) match very closely with those for bulk conductivity, but not with those for grain boundary conductivity (Table 5.10). This indicates that the bulk contribution was dominant over the grain boundary contribution in these materials. This is in agreement with the data of Figure 5.18, in which bulk conductivity was lower in all cases than grain boundary conductivity. In addition, the activation energies for grain boundary contribution are in the

range 0.90 – 1.04 eV, and so are broadly in the same range as the values for bulk conductivity. Both these factors indicate that the change in gradient in the Arrhenius-type plot (Figure 5.21) is not due to a dominant grain boundary effect in the low temperature region, since grain boundary conductivities would have to be lower and the activation energies for grain boundary conductivity would have to be significantly higher than those for bulk conductivity. This allows some confidence in the values attributed to ΔH_m and ΔH_a.

The work of Faber *et al* is relevant to the increase in ΔH_m observed with increasing Sm content.[151] These authors studied the oxygen ion conductivities of ceria doped with Nd, La, Gd, Y and Yb. They extracted overall activation energies - i.e. $\Delta H_a+\Delta H_m$ - and found a general trend for all dopants: activation energies fell to a minimum at dopant concentrations of around 2-5 mol% and then increased sharply on going to higher dopant concentrations. The authors also cite a value of ΔH_m = 0.49 eV obtained for lightly Y-doped CeO_2 from an earlier ^{17}O NMR study.[152] More specifically, in a recent paper, Omar *et al* obtained activation energy values for bulk ionic conductivity in $Sm_{x/2}Nd_{x/2}O_{2-\delta}$ (x = 0 – 0.18) at temperatures above and below 475ºC.[47] Applying the procedure described above, they obtained values for ΔH_m which showed a minimum at a dopant concentration of about 5 mol%, but then increased with increasing dopant concentration. They obtained ΔH_m = 0.65 eV for x = 0.10 and ΔH_m = 0.80 eV for x = 0.18, the highest value used. A similar increase in ΔH_m with increasing Sm dopant content was observed in the SDC samples described in the present contribution, although the actual values were significantly lower than for the Nd and Sm co-doped materials. This may be related to the different chemical environments – with or without Nd - of the oxygen ions and the oxygen vacancies in these two sets of materials. Turning to the values of ΔH_a, the association enthalpy of Sm'_{Ce}-$V_o^{\bullet\bullet}$ species, Omar et al obtained a very low and approximately constant value of $\Delta H_a \sim 0.05$ eV for $Sm_{x/2}Nd_{x/2}O_{2-\delta}$ in the range, x = 0.08 - 0.18.[47] Kilner reviewed ΔH_a data for CeO_2 doped with trivalent cations, although not Sm^{3+}.[150] However, Gd^{3+} is only slightly smaller (107.8 pm) than Sm^{3+} (109.8 pm) and Kilner did refer to calculated and experimental ΔH_a values of 0.13 eV and 0.17 eV, respectively, for GDC. The former matches the value given by Steele, also for GDC.[78] These values are considerably lower than those obtained for SDC in the present study. However, this review also cited the calculations of Minervini *et al*,[153] who did not consider Sm but gave a value of about 0.38 eV for GDC in which the oxygen vacancy ($V_o^{\bullet\bullet}$) is either a nearest or next nearest neighbour to the Gd'_{Ce} species (ΔH_a falls to 0.21 eV if the $V_o^{\bullet\bullet}$ is a third nearest neighbour). Also, Faber *et al*,[151] obtained ΔH_a values by extrapolating their data to infinite dopant dilution for

a number of dopants, assuming ΔH_m = 0.5 eV (see above). They obtained ΔH_a = 0.23, 0.29, 0.32, 0.40 and 0.67 eV for Nd, La, Gd, Y and Yb dopants, respectively. These last calculated and experimental values for GDC are close to that obtained in the present study, ΔH_a = 0.38 eV, for the sample with the closest dopant concentration, 10SDC.

It is clear that poorly conducting grain boundaries would strongly affect plots of total conductivity and may therefore cause inaccuracies in ΔH_a and ΔH_m values obtained from them. However, this does not seem to apply to the present work since the grain boundary conductivity, unusually, was always higher than that of the bulk. This appears to be a consequence of reducing the incorporation of impurities by using nitrate precursors in the low temperature citrate synthesis route rather than a high temperature ceramic route from the simple oxides, for example.

It is interesting to speculate on the possible effects of preparation route on the mechanisms of ion migration and defect trapping. For example, ideally, the citrate route gives rise to atomic mixing of the dopant (Sm) and host (Ce) cations. The ceramic route relies on inter-diffusion of the starting oxides at high temperature to form the product. Under certain circumstances, this may lead to a product containing nanodomains, too small to detect by XRD, but with differing dopant concentrations. It would be interesting to model such a heterogeneous structure to study how the phenomena of oxygen ion migration, oxygen vacancy trapping and the formation of clusters of more than two defects, and therefore, ΔH_a and ΔH_m, would be affected.

5.5 Summary

A compositional series of high purity, nanoparticulate SDC materials were successfully prepared by a low temperature, inexpensive citrate complexation method.

Crystallization of the SDC product occurred *via* three exothermic processes and the final crystal structure first formed from the gel at a temperature below 300ºC. After calcination at 500ºC, electron microscopy and XRD revealed that the products were foam-like, single-phase materials with high porosity and consisted of primary crystalline particles of about 10 nm diameter present in small clusters. These materials were milled and the resulting nanopowders were used in a detailed study of the effect of chemical composition, sintering temperature and sintering time on their densification, and on the grain structure and ionic conductivity of the resulting dense pellets.

Elemental analysis data, either obtained from EDX or ICP-MS results confirmed the stoichiometric composition of each SDC powder. More accurate ICP-MS data revealed the presence of additional elements such as Si, Ca, As, Pr and Gd. The potential source of this contamination was considered and estimated to have a negligible impact for the further studies of the SDC materials.

Densities of over 95% of theoretical were achieved for all three compositions after sintering at 1400ºC or higher for 4 h or longer and both density and average grain size increased with increasing sintering temperature and sintering time, although the effect of the former was much more marked. Samples sintered at 1400ºC for 6 h or 1450ºC for 4 h showed excellent microstructure for all compositions. However, some porosity was observed after sintering at 1450ºC for 6 h and this oversintering process had a deleterious effect on the overall conductivity, especially of the 10SDC.

Arrhenius-type plots of electrolyte conductivity showed an inflection at around 500ºC and this was interpreted in terms of a defect association enthalpy (ΔH_a) and an oxygen migration enthalpy (ΔH_m), both having been important at low temperatures while the latter became dominant at high temperatures. ΔH_a was less sensitive to Sm content and had values of around 0.4 eV. ΔH_m increased significantly with %Sm and had values of 0.4 – 0.7 eV. At 600ºC, the highest total conductivity was 1.81×10^{-2} S·cm^{-1} for the 20SDC sample sintered at 1450ºC for 6 h.

Results and Discussion

CHAPTER VI – **PALLADIUM SUPPORTED ON SAMARIUM-DOPED CERIA**

6. Palladium supported on samarium-doped ceria

6.1 Introduction

The results presented in Chapter 5 provided an incentive for the preparation of compounds containing palladium supported on samarium-doped ceria powders with a view to their application as catalysts. The citrate complexation method, previously developed in the group was also employed in this project. The aim was to obtain a good dispersion of Pd particles in ceria powders, where the final phases are in nanoparticulate form. To this end, three compositions of previously synthesised SDC nanopowders were used as a support for impregnation of 2 wt% of palladium.

6.2 Synthetic methods

Three synthetic methods were employed and these are denoted with capitals A, B and C as presented in Table 6.1. The first technique was based on direct, one-step preparation of a Pd, Sm and Ce-containing mixed oxide using a modified citrate complexation method (method A). The other two methods were based on a two-step process in which SDC powders synthesised as described in Chapter 5 were impregnated with Pd precursors using the incipient wetness impregnation technique (methods B and C). Table 6.1 contains information of the nine catalysts prepared using these three methods. These were labelled according to their composition and the synthetic method used.

Table 6.1 Compositions of prepared Pd/SDC catalysts.

wt% Pd	***mol% Sm***	***Method A***	***Method B***	***Method C***
		Direct Impregnation	*Incipient Wetness Impregnation*	
2	10	Pd10SDC-A	Pd10SDC-B	Pd10SDC-C
2	20	Pd20SDC-A	Pd20SDC-B	Pd20SDC-C
2	30	Pd30SDC-A	Pd30SDC-B	Pd30SDC-C

6.2.1 Direct technique

Figure 6.1 shows images taken at different points during the direct impregnation technique (Method A). At first, stoichiometric amounts of $Ce(NO_3)_3 \cdot 6H_2O$, $Sm(NO_3)_3 \cdot 6H_2O$ (both Acros Organics, 99.5%) and palladium nitrate dihydrate $Pd(NO_3)_2 \cdot 2H_2O$ (Aldrich,

~40% Pd basis) were dissolved in deionised water separately to make 0.1 M solutions. These were stirred, then combined resulting in a light orange mixture. Anhydrous citric acid (Alfa Aesar, 99.5%) was dissolved in water (0.3 M) and this solution was added to the cation solution in the ratio of four moles citrate per mole of total metal cations. The molar ratio had to be doubled in comparison to SDC synthetic method because attempts at applying a similar procedure were not successful. This was because the gel step was not established due to the low pH. It was found that additional HNO_3 (analytical reagent grade) had to be introduced to dissolve a brown sediment which formed when the ratio of citrate to metal ions was only 2:1. Initially, the mixture of metal nitrates and citric acid in the 4:1 ratio was turbid, but with no precipitate, at room temperature. However, no brown sediment was formed and, therefore, no additional HNO_3 was needed to dissolve it. It was observed that increasing the temperature caused the solution to become transparent with a light orange colour (Figure 6.1A). The temperature was increased to 80ºC and maintained under stirring for 12 h. As water was eliminated and some gases were released, the mixture became non-transparent and bright orange in colour (Figure 6.2B). Further evaporation caused an increase in the viscosity of the mixture. A yellow gel was created which transformed into yellow foam with simultaneous release of brown bubbles. The subsequent calcination and milling procedures were the same as for the preparation of the SDC materials, as described in Section 5.2. These points in the preparation are shown in Figure 6.1 in images E and F, respectively.

The final catalyst powder possessed much darker brown colour than the previously synthesised bare oxides. The residual carbon content was checked for the three final catalysts obtained *via* the direct technique. These were found to be higher than the values for the SDC powders given in Table 5.5, probably because of the increase in the amount of citric acid used. However, they were still relatively low at 0.39 wt% for Pd10SDC-A, 0.63 wt% for Pd20SDC-A and 0.70 wt% for Pd30SDC-A.

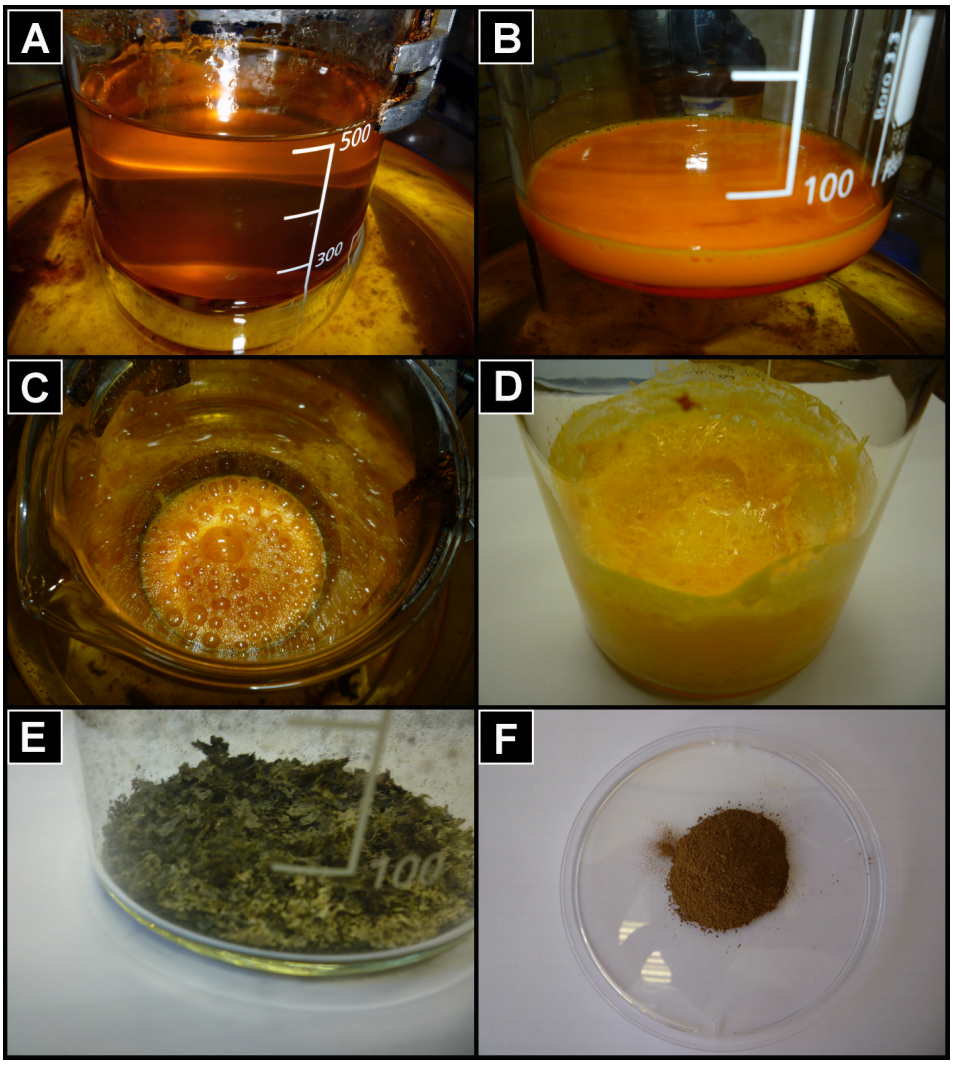

Figure 6.1 Images depicting the sample after each stage of the direct method for preparation of Pd/SDC powders: (A) mixing, (B) evaporation, (C,D) gelation, (E) calcination at 250ºC and (F) milling after final calcination at 500ºC.

6.2.2 Incipient wetness impregnation technique with $Pd(NO_3)_2$

The three compositions of SDC nanopowders, as prepared in Chapter 5, were used as supports for Pd dispersion *via* incipient wetness impregnation (Method B) using $Pd(NO_3)_2 \cdot 2H_2O$ (Aldrich, ~40% Pd basis) as the Pd precursor. An equivalent of 2 wt% of Pd was dissolved in ~3 cm^3 of acetone (Fisher Scientific, laboratory reagent grade) giving a transparent brown solution. This was slowly added from a burette to the SDC powder while the mixture was manually ground in an agate mortar to ensure uniform mixing until the solvent evaporated. Any remaining solution inside the burette was removed by addition of a volume of solvent equivalent to the retention volume of the sample as calculated from BET results (see Table 5.6). Special care was taken in order to fill all spaces between the SDC

nanoparticles with the Pd compound. The powders were manually milled for a further 10-15 min after addition of all of the solution. After the impregnation, the colour of all SDC supports changed from yellow to light brown. Samples were dried for 2 h at 100°C before the final calcination step. This involved heating the sample in a tube furnace at 500°C for 2 h in static air.

6.2.3 Incipient wetness impregnation technique with H_2PdCl_4

This impregnation technique (method C) employed aqueous tetrachloropalladic acid as the Pd medium for dispersion over the SDC supports. H_2PdCl_4 was obtained *in situ* from $PdCl_2$ (Aldrich, 99.9 %) and concentrated HCl (Fisher Scientific, analytical reagent grade). The required amount of $PdCl_2$ was placed in a vial with 1.5 cm^3 of deionised water and stirred on the hot plate. Concentrated HCl was carefully added dropwise to the solution. Some heating was necessary to fully dissolve the $PdCl_2$. The impregnation procedure was similar to that of method B. However, since the aqueous solution evaporated more slowly than the acetone solution of method B, after each addition of solution, each sample was left for 1-2 h to allow penetration of the liquid, and was manually milled until it appeared to be dry. In addition, the samples were dried overnight at room temperature after the impregnation step.

Figure 6.2 is relevant to both incipient wetness impregnation techniques (method B and C) and shows how the Pd solutions were added (image A) as well as the final product (image B) after the calcination step. A much lighter brown colour was observed for the final catalysts obtained *via* both incipient wetness impregnation techniques than in Method A.

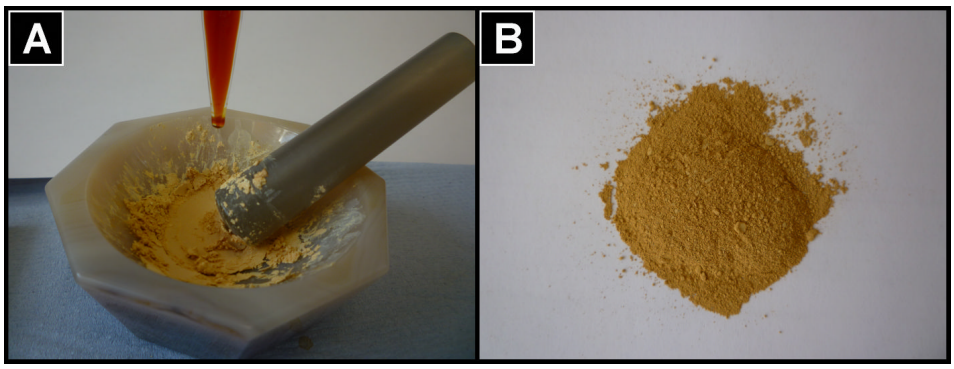

Figure 6.2 Images depicting the incipient wetness technique for Pd impregnation of previously prepared SDC supports in both methods B and C.

6.3 Characterisation of unreduced powders

This section outlines characterisation of the unreduced catalyst samples. It includes thermal analysis results on the catalyst precursor prepared by the direct method (A). In addition, XRD, BET, SEM/EDX and XPS studies were performed.

6.3.1 Thermal analysis

Thermal analysis studies of gel precursors of the Pd/SDC catalysts were performed in the same way as for the precursors of the bare SDC oxides (Section 5.3.1). Three Pd/SDC catalyst precursors were individually investigated using the same instrument and applying similar experimental conditions.

Figure 6.3 shows TG and DTA plots for Pd10SDC-A, Pd20SDC-A and Pd30SDC-A samples run in flowing air (50 ml/min). From all TG curves, it can be seen that the total mass loss occurred gradually in three steps. The total mass change reached almost 79% of the precursor starting mass for each sample and was the highest for Pd20SDC-A. In Table 6.2, the total mass change was divided into three individual mass losses (Δm_n), which corresponded to three steps. The approximate mass ratio of 1:4:2 was assigned to the steps, indicating a dramatic mass change for the second step with a relatively small change for the first step and moderate for the last. The smallest mass loss was observed for the Pd10SDC-A precursor in the first and in the third steps among the three compositions. However, this composition showed the largest mass loss of the three samples during the second step. After each sample reached 500°C, no further mass loss was observed.

Table 6.2 Summary of TG and DTA plots for Pd/SDC gel precursors in air.

Sample	*TG*			*DTA*				
	Δm_1/%	Δm_2/%	Δm_3/%	p_0/°C	p_1/°C	ΔH_1	p_2/°C	ΔH_2
Pd10SDC-A	7.94	48.0	21.3	114	132	-15.53	320	-1405
Pd20SDC-A	10.7	43.8	24.3	111	131	-47.14	316	-1606
Pd30SDC-A	10.6	43.6	24.2	112	133	-35.95	316	-1310

ΔH_n values expressed per mole of final product (kJ·mol^{-1})

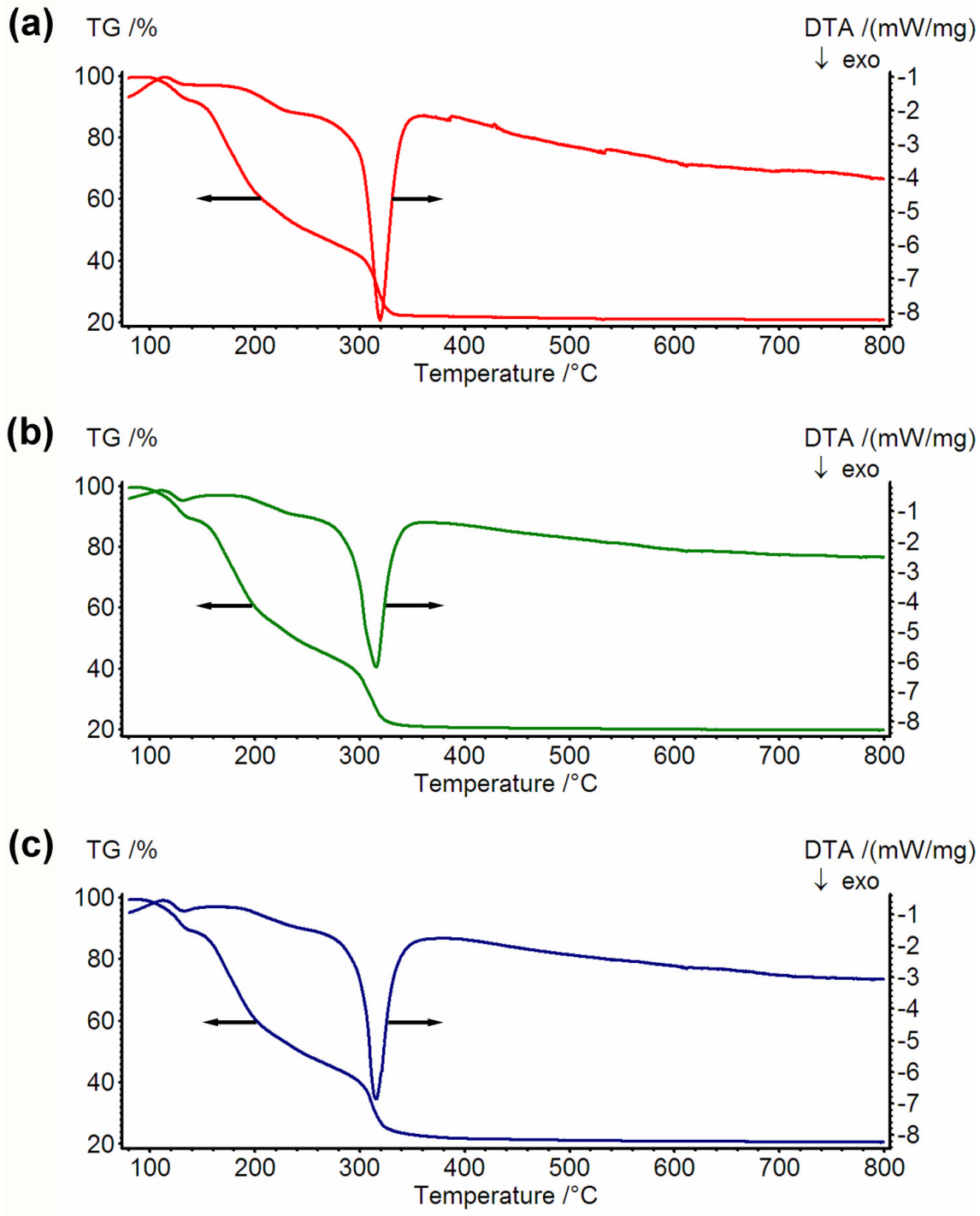

Figure 6.3 Plots of TG and DTA experiments run in air on precursor gels of (a) Pd10SDC-A, (b) Pd20SDC-A and (c) Pd30SDC-A.

Analysis of the DTA peaks showed a certain correlation of enthalpy changes (ΔH_n) to the mass changes in the individual steps. It should be noted that a small endothermic effect occurred at ~110°C in each TG curve. As in the thermal analysis experiments performed on SDC, it occurs a result of the release of physically absorbed water as a consequence of the synthetic route used. The first step in the TG curve corresponded to a very small exothermic effect. Its characteristic peak maximum (p_1) in the DTA curves of all three samples was at around 130°C and was marked with care for Pd10SDC-A. The highest value for the enthalpy change, ΔH_1, was found for Pd20SDC-A. The second step (p_2) appeared as a broad shoulder on each DTA curve and no indicative peak area was identified to allow calculation of the enthalpy change. The last DTA peak (p_3) fell in the range 316 - 320°C and exhibited the strongest exothermic effect. Each DTA plot showed a drift in the heat flow trace during the experiments. In the high temperature region the corresponding first derivative curves (not shown) of TG and DTA were not indicative of any changes and an instrumental artefact was assumed.

Mass spectrometry (MS) data on TG/DTA experiments run in a flow of O_2 were obtained for all precursor catalysts in order to understand the chemical processes occurring during thermal treatment. These are presented in Figure 6.4 as plots of log ion current *versus* temperature, recorded by a quadrupole mass spectrometer (QMS) as mass to charge ratios (m/q) and corresponding to the chemical compounds released. A multi-step decomposition behaviour of the precursor catalysts was observed on each plot. The data show a good agreement with those from the experiments run in air. Only a negligible shift towards lower temperature was noticed in the case of the oxygen environment. Oxygen was employed because of the large concentration of N_2 in air, which could affect the QMS results by masking CO and N_2 released from the gel precursors, which were synthesised from starting nitrates and citric acid. The possibility of using Ar was rejected, because it would result in different chemical processes.

The endothermic liberation of H_2O (m/q = 18) during the first step was confirmed by the presence of a peak with its onset around 100°C. Carbon dioxide (m/q=44) was released as a major product for all catalysts up to 500°C, peaking at about 300°C, as a result of the final burnout of the organic matter. The sharp peak at around 130°C is consistent with the decomposition of the carboxylate groups relating to the mildly exothermic process, p_1. A marked drop in CO_2 concentration was observed at 160°C. In addition, a strong signal from C (m/q=12) and CO (m/q=28) matched the CO_2 traces at this temperature in contrast to the relatively smooth release of NO_2 and NO up to 200°C.

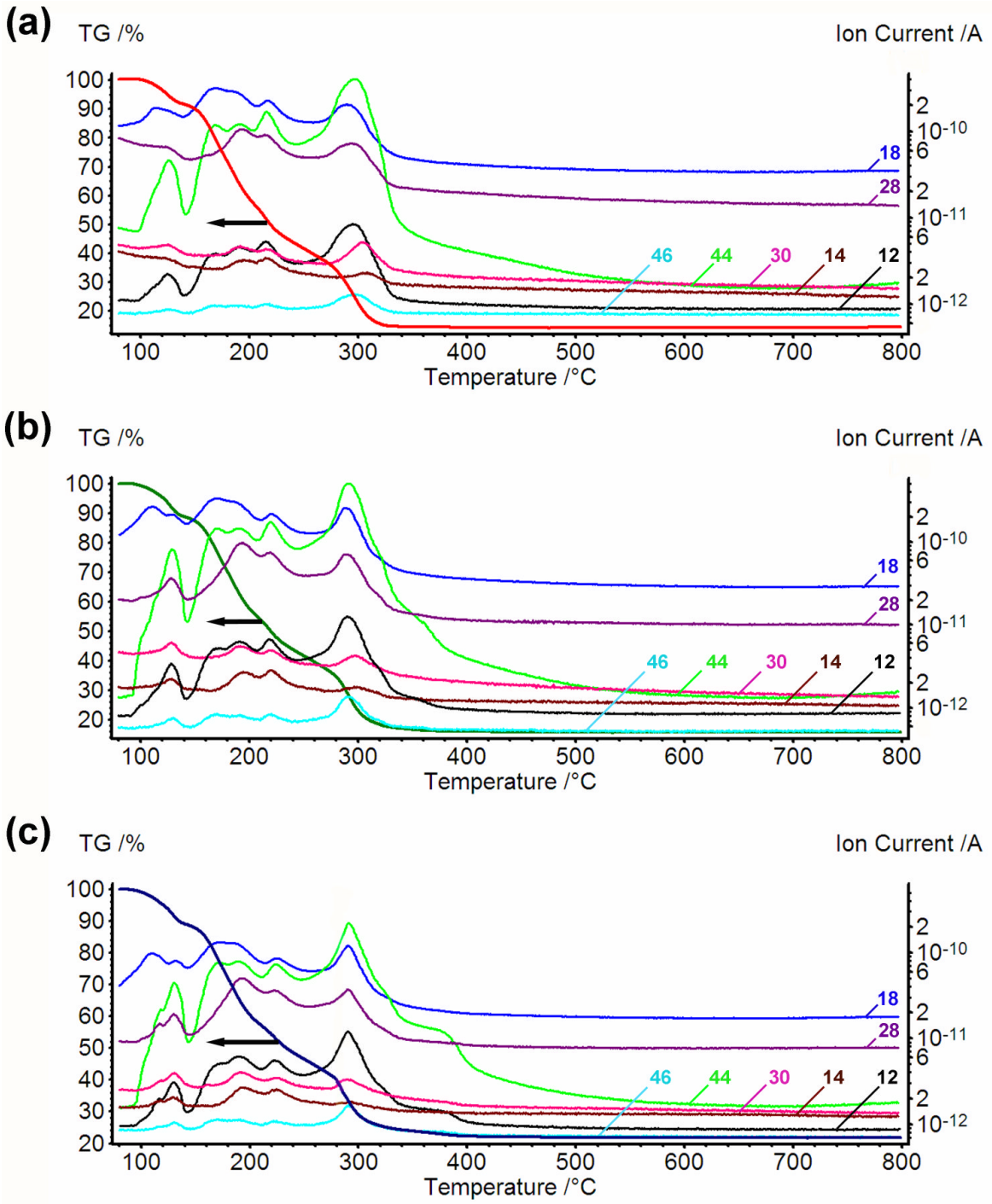

Figure 6.4 TG plots run in O_2 for (a) Pd10SDC-A, (b) Pd20SDC-A and (c) Pd30SDC-A including mass spectrometry data. Mass to charge (m/q) ratios are indicated.

Compared to the analogous experiments carried out on the precursors of the SDC support, the impact of the modified synthetic method as well as addition of 2 wt% of Pd on the synthesis of on the Pd/SDC catalysts were significant. It should be emphasised again that double the amount of the citric acid had to be used in the preparation of the Pd/SDC materials. This modification of the synthetic process resulted in more dramatic changes of heat flow throughout the experiment than in the synthesis of SDC supports.

6.3.2 X-ray Diffraction

The X-ray powder diffraction patterns of the nine Pd/SDC catalysts are presented in Figure 6.5 in three charts, according to the three different synthetic methods used. All investigated Pd/SDC powders were previously calcined at 500°C for 2h. Phase identification was accomplished by comparing peak positions and their intensities with data provided by the ICDD for SDC mixed oxides as well as for PdO and metallic Pd.[142-144, 154, 155]

XRD patterns were characteristic of peaks related to the cubic phase of ceria. A certain shift towards lower values of 2Θ was observed in the patterns with increasing Sm content. This is consistent with the expansion of the unit cell as Sm is introduced. The broadest peaks were noticed in the diffractograms of Method A and the smallest average crystallite sizes were calculated for these catalysts by means of the Scherrer relationship (Eqn. 3.1). These were in the range from 6.7 to 8.3 nm. Crystallite size decreased with increase of Sm content for each preparation method. The results of these calculations are summarised in Table 6.3. Similar results of average crystallite size were found for catalysts produced by method B and C, because both employed the same SDC supports prepared previously. These also matched very well with the particle sizes obtained for the supports (Table 5.3) the values in fact being very slightly smaller for the Pd/SDC samples. If this is a significant effect, it could be a result of the Pd impregnation processes. No Pd containing phases were detected by XRD over the characteristic 2Θ range (35-45°), which might be explained in terms of either the small concentration of Pd introduced or a very small size of the resulting Pd-containing particles, or both effects.

Table 6.3 Lattice parameters (***a***), cell volume (***V***) and average crystallite size (D_{XRD}) for catalysts calcined at 500°C for 2 h.

Sample	***a*** /Å	***V*** /Å^3	D_{XRD}/nm
Pd10SDC-A	5.4237(5)	159.55(5)	8.3
Pd20SDC-A	5.4346(3)	160.51(2)	7.8
Pd30SDC-A	5.4437(2)	161.32(9)	6.7
Pd10SDC-B	5.4223(1)	159.42(6)	10.8
Pd20SDC-B	5.4327(4)	160.34(2)	8.7
Pd30SDC-B	5.4439(2)	161.34(7)	7.4
Pd10SDC-C	5.4231(2)	159.49(7)	10.4
Pd20SDC-C	5.4334(1)	160.40(5)	9.0
Pd30SDC-C	5.4438(3)	161.33(1)	7.6

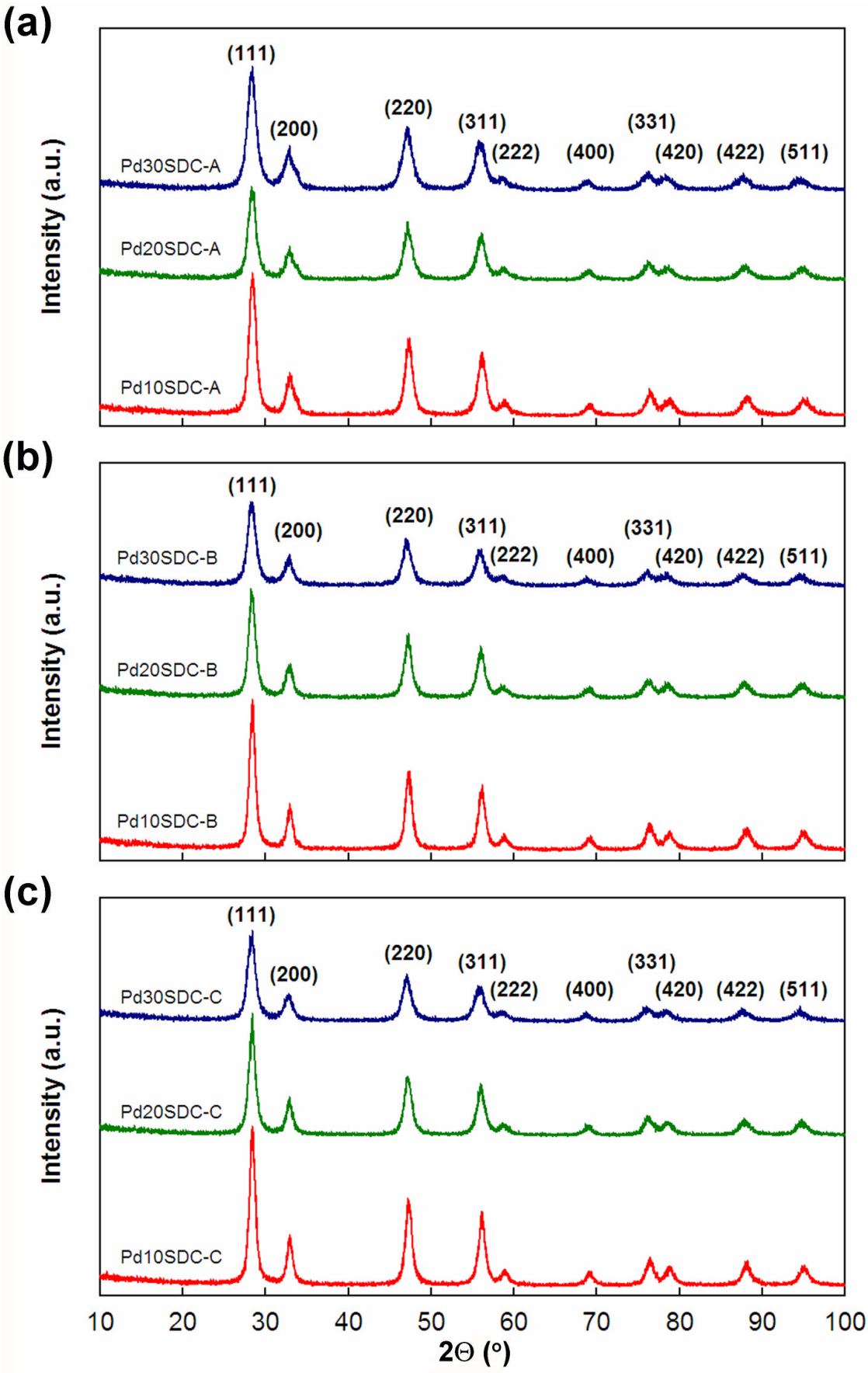

Figure 6.5 XRD patterns of all catalysts prepared using (a) method A, (b) method B and (c) method C.

Figure 6.6 shows the comparison of the main diffraction peak (111) for all catalysts. The data are grouped by composition. It is clear that there was no peak displacement for the catalysts of the same composition obtained with the different methods (each of plots (a), (b) and (c)). However, a (111) peak shift could be confirmed by comparison of catalysts with varying Sm content, as expected.

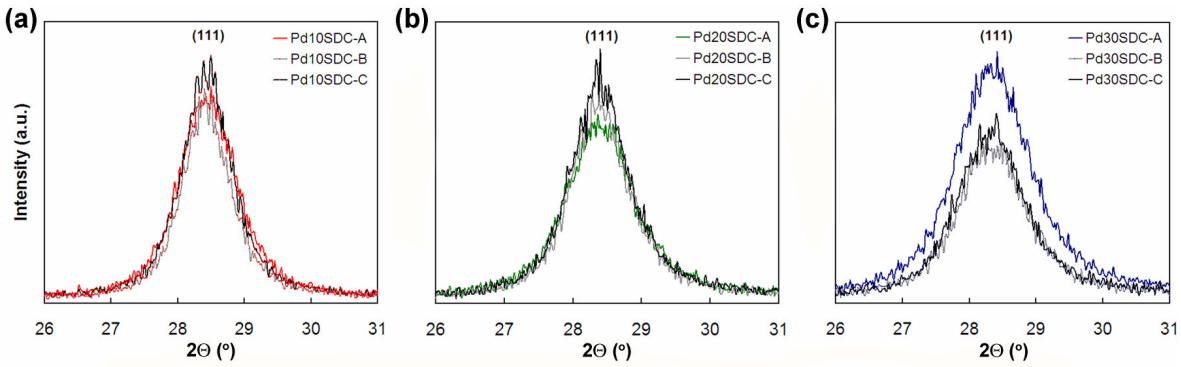

Figure 6.6 Comparison of (111) peak for catalysts obtained by different synthetic methods for (a) Pd10SDC, (b) Pd20SDC and (c) Pd30SDC.

6.3.3 Brunauer-Emmett-Teller method

All powders were prepared with the standard procedure for BET studies, described in Section 3.3. Table 6.4 shows SSA results for the synthesised catalysts calcined at 500°C for 2 h. The SSAs of equivalent SDC supports are also provided here for comparison. A significant increase in SSAs was achieved for catalysts obtained by method A, when the results were compared with those of the bare SDC oxides. These catalysts possessed more than twice the SSAs of the corresponding SDC supports. The highest value was found for the Pd10SDC-A powder. Methods B and C exhibited smaller increases in SSA and the highest values were obtained for Pd10SDC-B and Pd10SDC-C catalysts. The values obtained by these two impregnation methods were comparable. The SSA decreased with increasing Sm content for each impregnation method.

It should be noted that the marked increase in SSA in method A could be the result of smaller particles obtained due to the higher amount of heat released in the final phase of the combustion step, as confirmed in the thermal analysis studies. An alternative, or additional explanation, is that incorporation of the Pd into a Pd-Ce-Sm mixed oxide served to destabilise and break up the nanoparticles.

Table 6.4 Specific surface area (SSA) of all catalysts after their calcination at 500°C for 2 h.

Synthetic method	*Sample*	*SSA* /$m^2 \cdot g^{-1}$
Direct method	Pd10SDC-A	69.4
	Pd20SDC-A	66.5
	Pd30SDC-A	54.1
Incipient wetness $Pd(NO_3)_2$	Pd10SDC-B	42.2
	Pd20SDC-B	35.3
	Pd30SDC-B	26.7
Incipient wetness H_2PdCl_4	Pd10SDC-C	48.3
	Pd20SDC-C	30.6
	Pd30SDC-C	22.4
Citrate method	10SDC	30.2
	20SDC	32.7
	30SDC	21.8

6.3.4 Scanning Electron Microscopy

The microstructure of as-prepared catalysts of method A is presented in Figure 6.7. Egg-shell-like structures (e.g. image F) were observed for all compositions. These were an effect of the preparation method, which is characterised by strong, exothermic release of NO_x, CO_2 and CO gases. A closer examination showed also some branched structures (e.g. image D), similar to those observed in the bare SDC oxides.

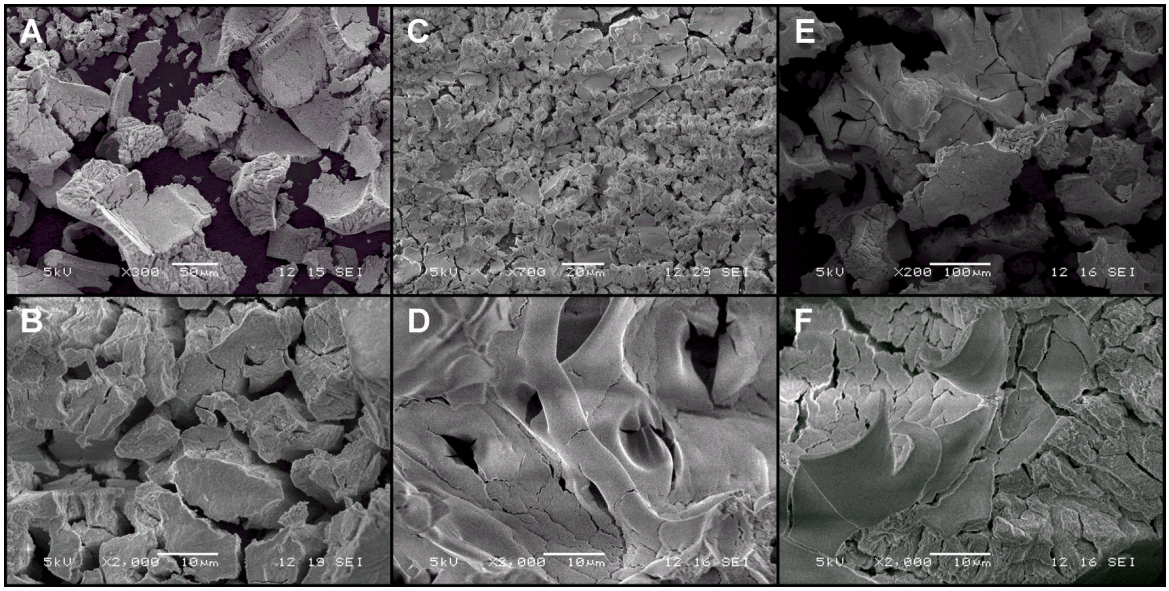

Figure 6.7 Low (A, C, E) and high (B, D, F) magnification micrographs of unmilled Pd/SDC powders calcined at 250ºC for 2 h. (A, B) Pd10SDC-A, (C, D) Pd20SDC-A and (E, F) Pd30SDC-A.

The Pd/SDC-A samples were ground using the standard procedure (400 rpm, 1 h, zirconia balls) in a planetary mill and their microstructure is presented in Figure 6.8 with corresponding EDX spectra. Moreover, an additional milling step was performed on the catalysts obtained by methods B and C, since these catalysts had made use of SDC supports which had been ground in the same way before the Pd impregnation step. The micrographs of these sample groups at the same magnifications are presented in Figures 6.9 and 6.10.

All catalyst samples were examined by EDX in order to investigate their stoichiometry and Pd content. Figure 6.8 shows the microstructure of the ground catalysts obtained by the direct method (A) with their corresponding EDX spectra.

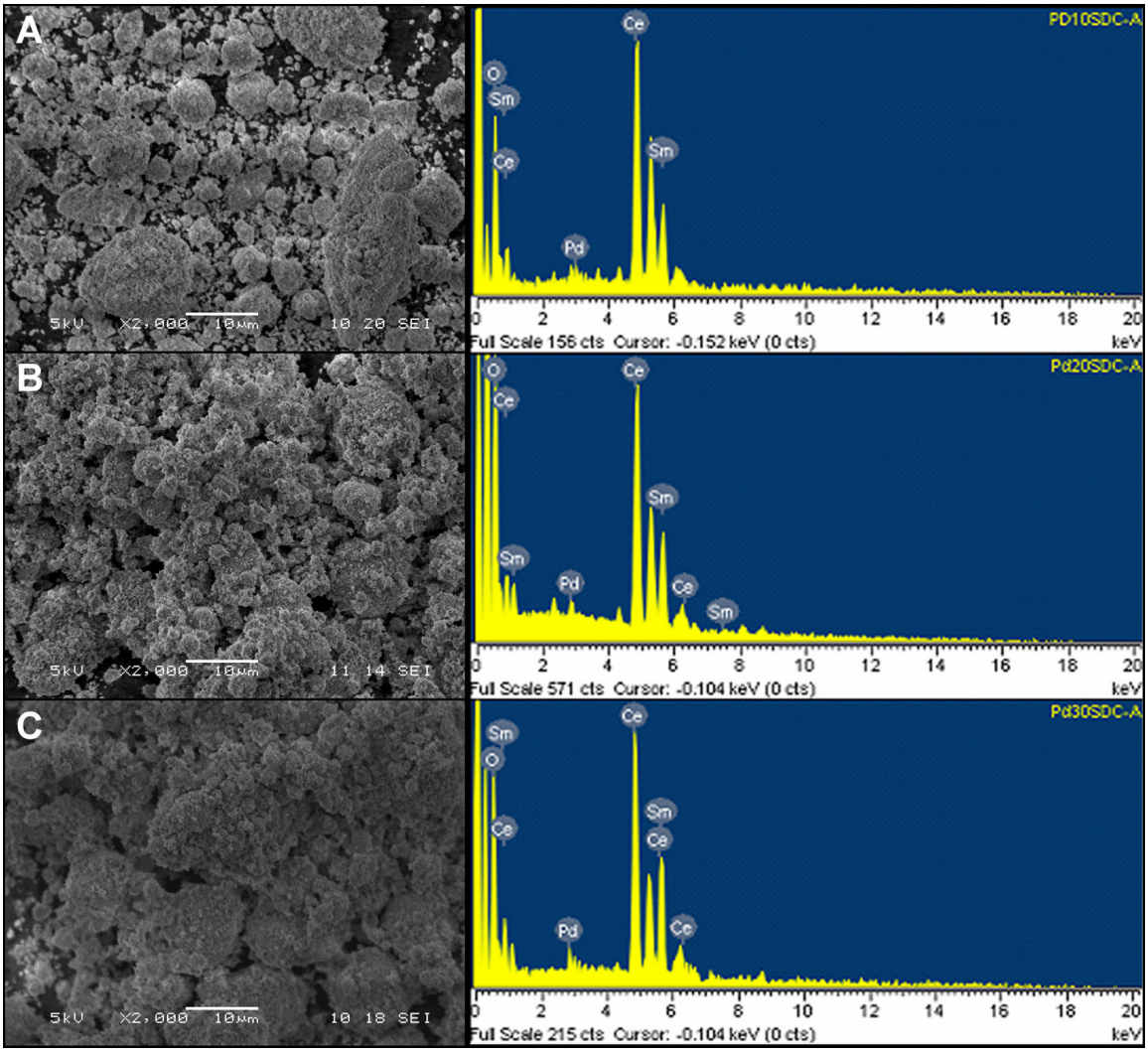

Figure 6.8 SEM images of ground (A) Pd10SDC-A, (B) Pd20SDC-A and (C) Pd30SDC-A powders calcined at 500ºC for 2 h with their corresponding EDX spectra.

EDX spectra obtained for catalysts prepared by method A showed only the expected elements, apart from small peaks for Cu and Zn (not labelled) which come from the SEM

sample holder and should be ignored. Figure 6.9 shows spectra of catalysts prepared by method B. For Pd20SDC-B sample, a Gd content of 1.08 wt% was detected. This is an evident effect of cross-contamination among projects running in the group at the same time. This value was the highest observed.

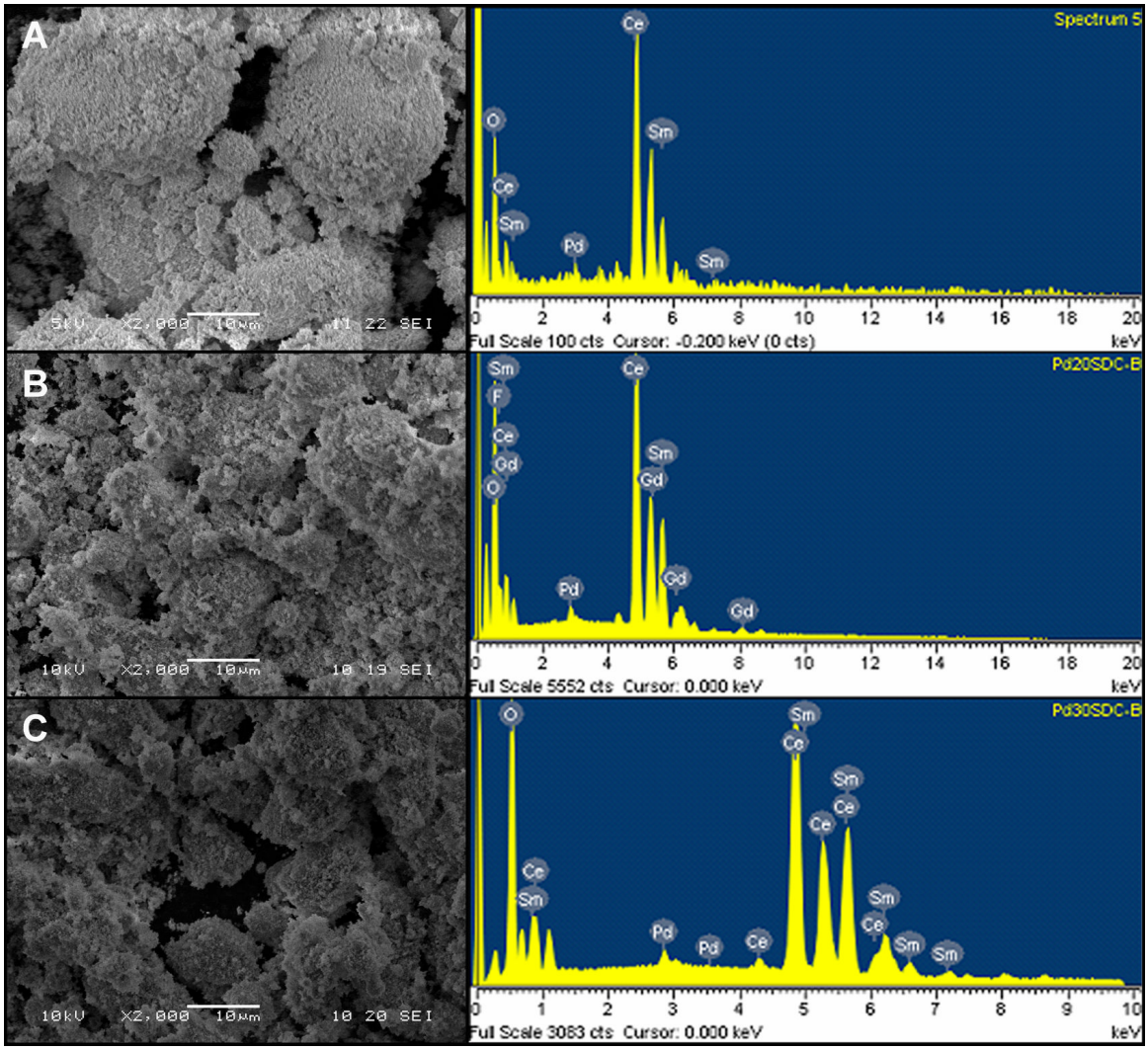

Figure 6.9 SEM images of ground (A) Pd10SDC-B, (B) Pd20SDC-B and (C) Pd30SDC-B powders calcined at 500ºC for 2 h with their corresponding EDX spectra.

Figure 6.10 presents SEM images with corresponding EDX spectra for the catalysts prepared by the incipient wetness technique with H_2PdCl_4 as the palladium dispersion medium. Apart from the expected peaks of C, Ce, Sm, O and Pd, additional peaks for Cl were seen. Clearly, there was some retention of Cl from the H_2PdCl_4, despite the calcination step. 1.42 wt% of chlorine was detected for Pd10SDC-C, while smaller concentrations of Cl were found for Pd20SDC-C and Pd30SDC-C of 0.82 wt% and 0.63 wt%, respectively.

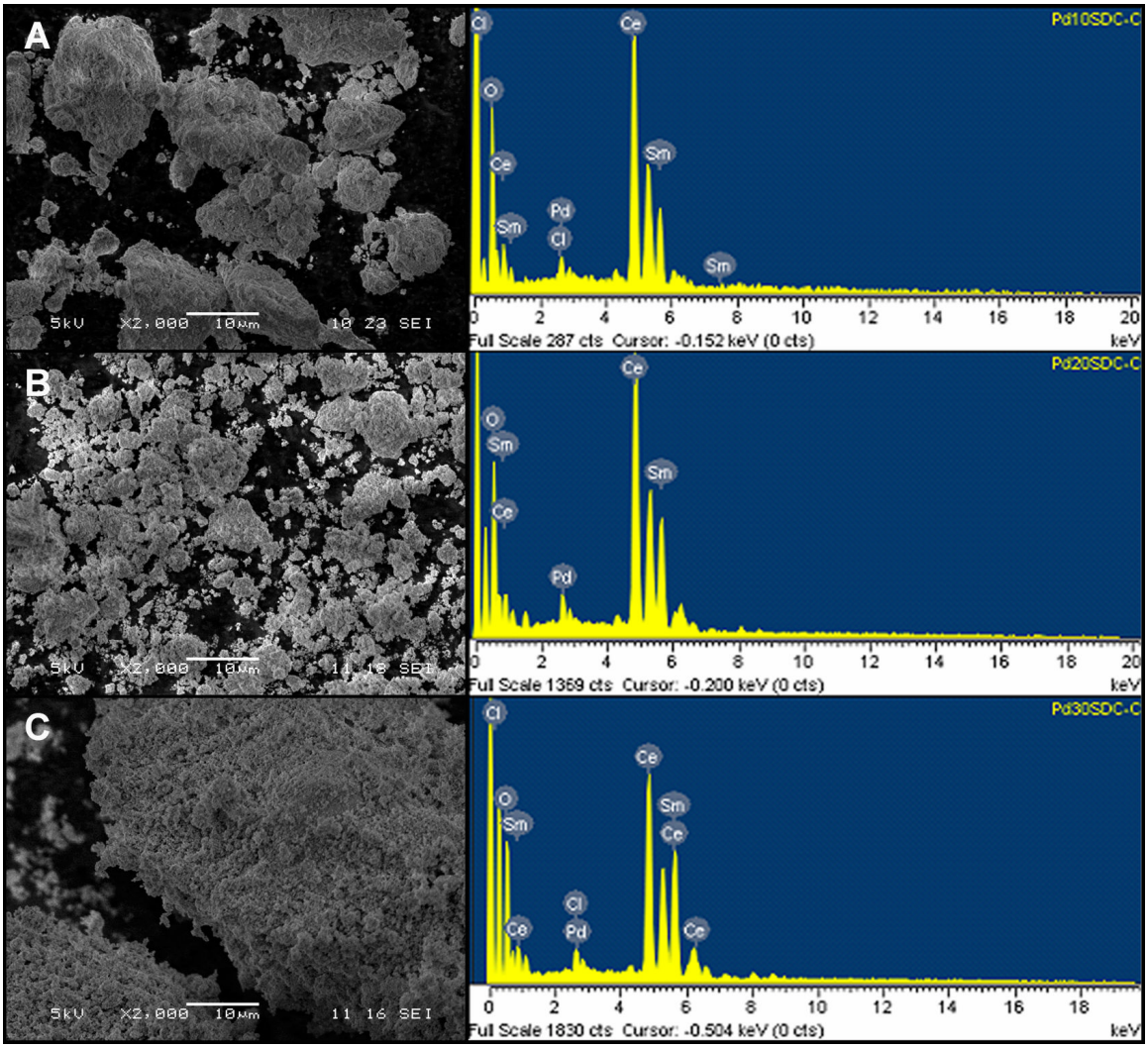

Figure 6.10 SEM images of ground (A) Pd10SDC-C, (B) Pd20SDC-C and (C) Pd30SDC-C powders calcined at 500ºC for 2 h with their corresponding EDX spectra.

Quantitative data from EDX spectra were used to calculate the atomic ratio of Sm/Ce for all catalysts prepared by the three methods. These were found to be close to the expected theoretical values and confirmed the desired stoichiometry of each catalyst. These are displayed in Table 6.5 along with the Pd contents. Although there was slight variation between catalysts, Pd contents were all close to the desired 2 wt% value.

Table 6.5 Sm/Ce atomic ratio and Pd content for all catalysts.

Sample	Sm/Ce (at.)	Pd/(at%)	Pd/(wt%)
Pd10SDC-A	0.117	1.03	2.12
Pd20SDC-A	0.208	0.81	1.67
Pd30SDC-A	0.407	0.94	1.94
Pd10SDC-B	0.114	0.76	1.65
Pd20SDC-B	0.241	0.81	1.77
Pd30SDC-B	0.409	0.93	2.04
Pd10SDC-C	0.116	0.84	1.77
Pd20SDC-C	0.221	1.03	2.35
Pd30SDC-C	0.410	0.88	1.95

6.3.5 X-ray Photoelectron Spectroscopy

The XPS measurements were performed in order to obtain compositional information on all Pd/SDC catalysts. In particular, these studies allowed the determination of the concentrations and oxidation states of the relevant elements at the sample surface, which is of interest in the characterisation of catalytic materials. These quantitative data are summarised in Tables 6.6 and 6.7. Figures 6.11–6.14 contain spectra of Ce, Sm, O and Pd, respectively, for all catalysts. Again, for comparison, XPS spectra of the SDC solid solutions – the bare oxides without Pd – are presented in the last row of Figures 6.11, 6.12 and 6.13. In these figures the colour code assigned to all samples in this thesis is used. All materials were examined by XPS as prepared.

Ce 3d core level XPS spectra of all nine catalysts (plots a-i) and the three SDC supports (plots j-l) are given in Figure 6.11. The first column represents the 10 mol% SDC samples impregnated with 2 wt% Pd (except the last plot for all columns), the second, the 20 mol% SDC samples, and the third, the 30 mol% SDC samples. The top row corresponds to method A, the middle row to method B, the third to method C and the bottom row includes plots (j-l) of the bare SDC oxides. This arrangement is followed in all XPS plots in this section.

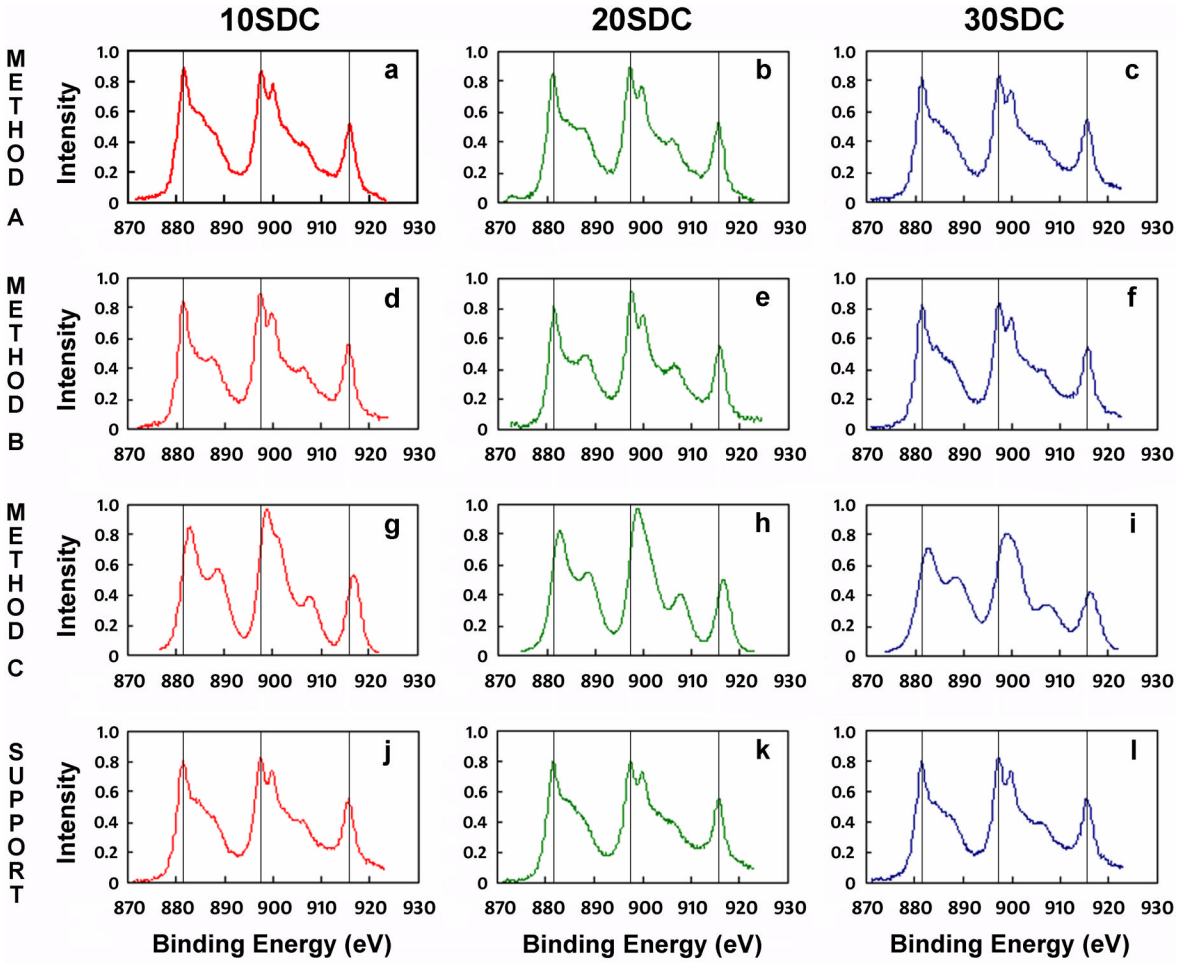

Figure 6.11 Ce 3d core level XPS spectra of all Pd/SDC catalysts (a-i) and SDC supports (j-l).

In general, all Ce 3d core level spectra presented in Figure 6.11 exhibited similar shapes and showed several clear peaks. The three main features at binding energies of around 882, 888 and 897 eV correspond to the Ce $3d_{5/2}$ state of Ce^{4+}, while those peaks at about 900, 907 and 916 eV correspond to the Ce $3d_{3/2}$ state of Ce^{4+}.[156] These peaks indicated that Ce^{4+} is present in each sample. The small features indicated in some spectra at about 885 and 903 eV relate to the $3d_{5/2}$ and $3d_{3/2}$ states, respectively, of Ce^{3+}.[156] The Ce is therefore present mainly in the most oxidised form, with varying but small amounts of Ce^{3+} also indicated. The bare SDC oxide supports and the catalysts made by method A (both one-step citrate preparations) appeared to be more reduced than catalysts made by methods B and C.

The peak positions in the spectra of the SDC supports and samples of Series A and B generally matched closely. However, the spectra of the three catalysts of method C showed a shift (of a few eV) towards higher binding energy, causing overlap of the two peaks at about 900 eV. This could be an effect of the synthetic method used, as the presence of some chlorine was observed by EDX in samples of method C (see Figure 6.10). The presence

of electronegative Cl – remaining from the H_2PdCl_4 precursor – at the catalyst surface would tend to increase Ce and other binding energies.

Samarium XPS spectra are presented in Figure 6.12. These exhibited two main peaks at about 1082 eV and ~1109 eV, which can be assigned to the $3d_{5/2}$ and $3d_{3/2}$ states, respectively, of Sm^{3+}.[157, 158] Some variation in peak areas is seen in Figure 6.12. These were quantified for all elements studied and are presented in Table 6.7. A certain shift to higher values of binding energies (E_b) was again observed in the case of the Series C catalysts, with respect to the other catalysts and the bare oxides, which showed matching peak positions. These shifts could be explained, as for the corresponding behaviour in the Ce peak positions, on the presence of some Cl on the surface of the Series C catalysts.

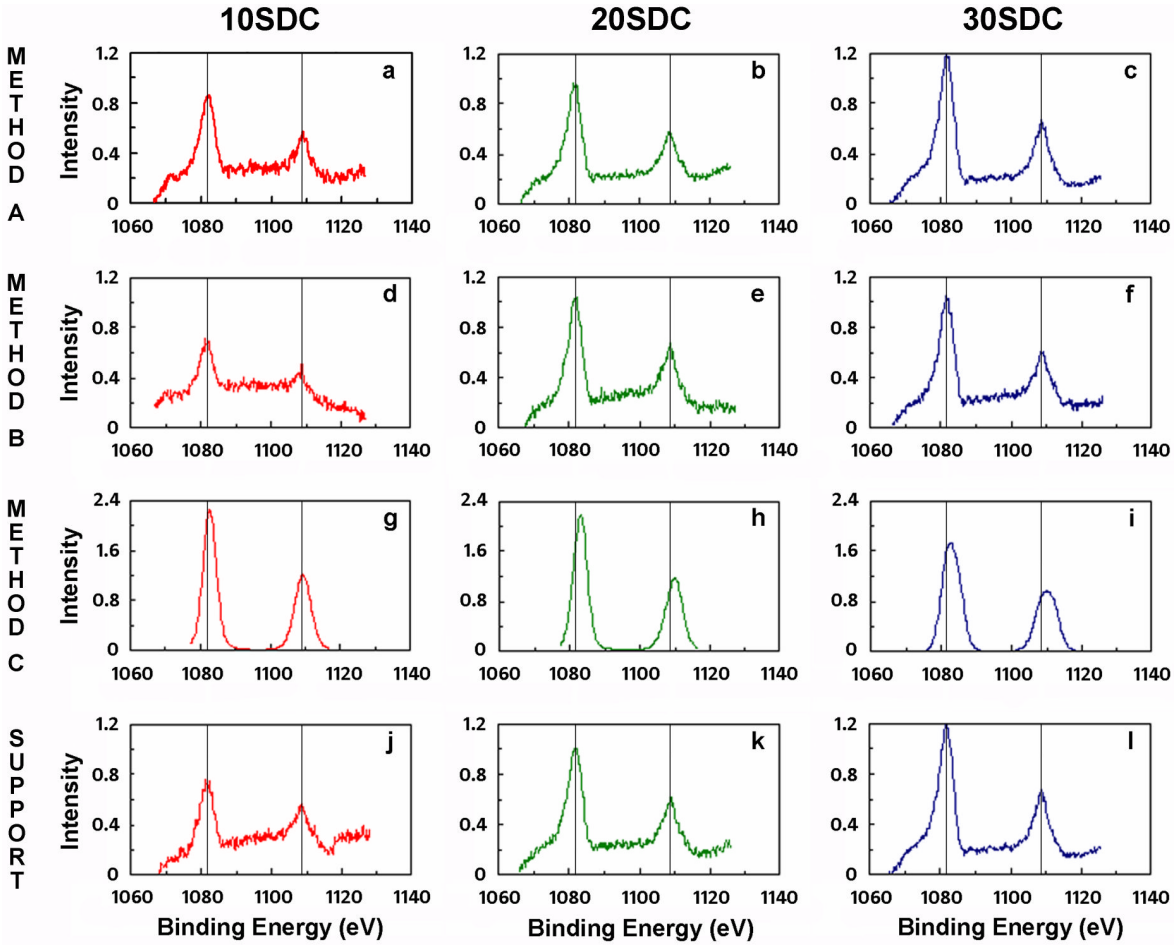

Figure 6.12 Sm 3d core level XPS spectra of catalysts (a-i) and supports (j-l).

The XPS spectra of oxygen 1s core level, are presented in Figure 6.13. As for the other elements, the spectra of the supports and catalysts of Series A and B are very similar and contain two main peaks at consistent binding energies. The peak of lower binding energy (about 528.5 eV) has been reported to represent lattice oxygen, and that of higher E_b to relate

to chemisorbed oxygen or OH species in ceria-based solid solutions.[159] Peak area generally increases with %Sm in the sample. In Series C, the peaks are less intense, the smaller of the two is not distinguishable and the position of the larger peak is shifted to higher binding energy. This peak shift could again be attributed to the presence of electronegative Cl at the surface, as could the lower intensities. The fact that the smaller O 1s peak cannot be seen may be explained either by the lower signal to noise ratio in these spectra or, more tentatively, to the replacement of chemisorbed O and OH species by Cl in the Series C samples.

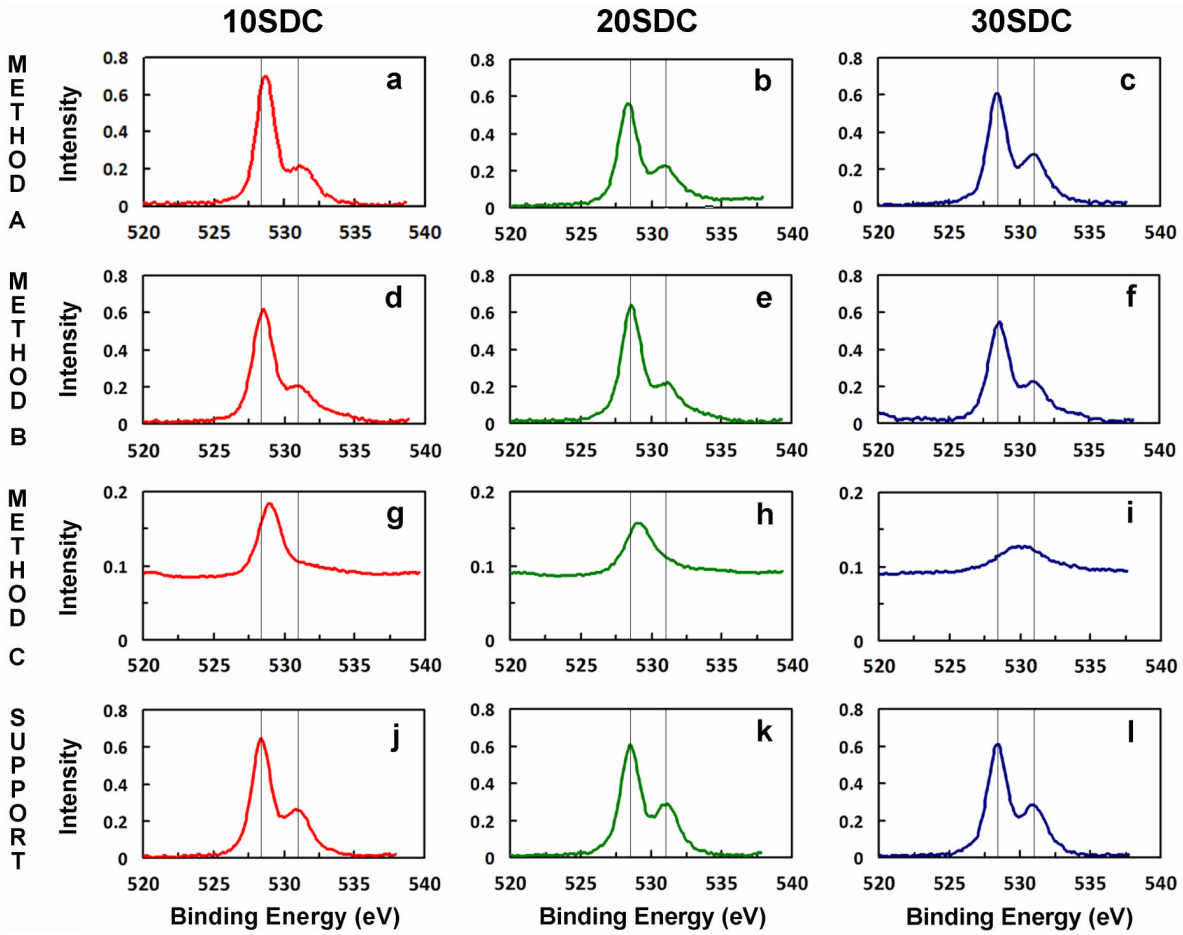

Figure 6.13 O 1s core level XPS spectra of catalysts (a-i) and supports (j-l).

Pd 3d core level XPS spectra are given in Figure 6.14. The two main peaks in each spectrum centred at roughly 337 to 342 eV relate to the $3d_{5/2}$ and $3d_{3/2}$ states of Pd, respectively. However, differences in binding energy as well as other smaller peaks were observed among the catalysts prepared by the three different methods. A peak at 337 eV is characteristic of Pd^{2+} and a peak at around 335 eV is characteristic of (elemental) Pd^{0}. Values between these are assigned to 'electrodeficient' Pd, Pd^{n+}, where $0 < n < +2$.[160-163] On this basis, the Series C catalyst surfaces contained mainly Pd^{2+}, those of the Series B catalysts

contained mainly Pd^{2+} with some Pd^{0} – indicated by the shoulder at 335.5 eV – and the surfaces of the samples of Series A contained Pd^{n+}. These peaks were deconvoluted and their areas measured to quantify the percentage of Pd^{0} (Table 6.6). For all three compositions, the least reduced catalyst surfaces were those of Series A.

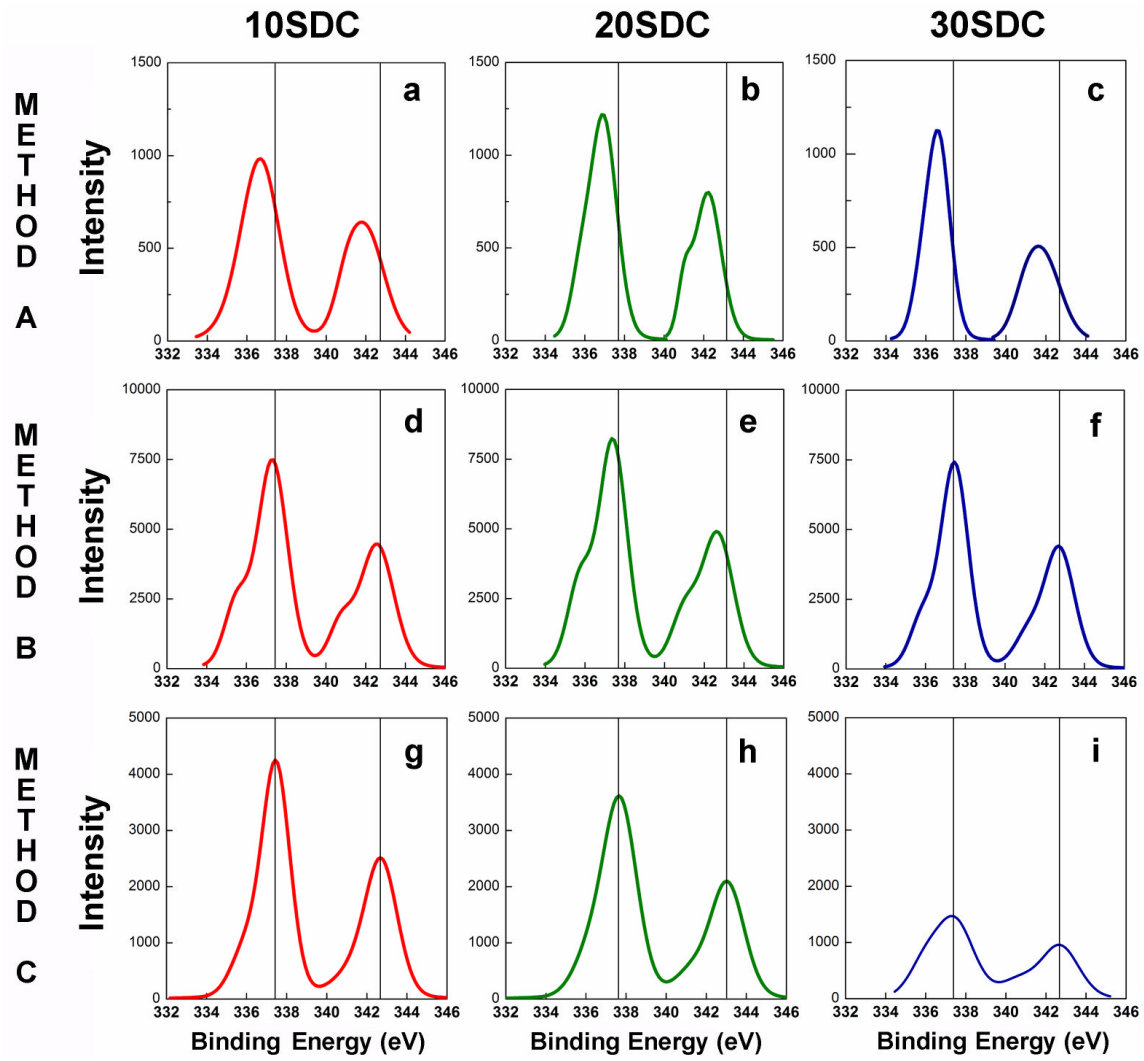

Figure 6.14 Pd 3d core level XPS spectra of catalysts (a-i).

Table 6.6 Concentrations of Pd species for all unreduced catalysts.

Sample	Pd^0 / %	Pd^{2+}+Pd^{n+} / %
Pd10SDC-A	12.8	87.2
Pd20SDC-A	13.4	86.6
Pd30SDC-A	15.6	84.4
Pd10SDC-B	19.3	80.7
Pd20SDC-B	23.7	76.3
Pd30SDC-B	17.1	82.9
Pd10SDC-C	16.1	83.9
Pd20SDC-C	15.1	84.9
Pd30SDC-C	22.9	77.1

Atomic concentrations of the elements of interest in the Pd/SDC catalysts and SDC supports as determined from the XPS spectra are presented in Table 6.7. Surface Sm/Ce ratios are approximately as expected from the bulk concentrations except for Pd10SDC-A and Pd30SDC-A (Sm deficient) and Pd30SDC-C (Sm rich). The large differences in apparent surface Pd concentration - which increased in the order Series A <<< Series C < Series B - are important to understand the catalytic activity of these samples.

Table 6.7 Atomic concentrations for all catalysts samples and SDC supports.

Sample	Total	%O(1s)	%Ce(3d)	%Sm(3d)	%Pd(3d)	Sm/Ce	Pd/Ce	Pd/Sm	Sm/Pd
Pd10SDC-A	75.0	70.6	25.5	3.6	0.29	0.140	0.01	0.0715	14.0
Pd20SDC-A	73.4	72.1	22.0	5.6	0.27	0.256	0.01	0.0390	25.6
Pd30SDC-A	71.4	74.3	18.1	7.5	0.13	0.412	0.01	0.0243	41.2
Pd10SDC-B	69.0	74.1	21.6	1.3	2.97	0.058	0.14	2.4025	0.4
Pd20SDC-B	68.8	73.1	19.4	4.9	2.72	0.252	0.14	0.5562	1.8
Pd30SDC-B	66.4	75.4	16.4	5.6	2.62	0.340	0.16	0.4709	2.1
Pd10SDC-C	76.4	65.6	29.6	3.1	1.73	0.103	0.06	0.5803	1.7
Pd20SDC-C	78.6	64.9	26.3	6.8	1.93	0.260	0.07	0.2689	3.7
Pd30SDC-C	83.0	61.0	22.6	14.9	1.58	0.659	0.07	0.1063	9.4
10SDC	71.1	73.4	22.8	3.7		0.162			
20SDC	68.1	73.7	21.0	5.4		0.257			
30SDC	67.4	73.6	18.3	8.1		0.443			

6.4 Characterisation of reduced powders

All samples were investigated after having been reduced at 500°C in hydrogen for 1 h. These studies were based on XRD, XPS and catalytic activity experiments and are presented in this section.

6.4.1 X-ray Diffraction

Figure 6.15 shows XRD patterns of all nine catalysts after reduction. Qualitative analysis of these diffractograms showed evidence of Pd peaks (marked with reversed triangles) only for samples prepared using method A. These were seen at about $2\Theta = 40°$ in plot (a). This suggests that only the Series A samples contained Pd particles large enough and numerous enough to be detected in XRD. The incipient wetness impregnation techniques (plots (b) and (c)) were therefore found to produce a different kind of Pd dispersion on the SDC supports. Further insight can be gained from XPS of the reduced catalysts.

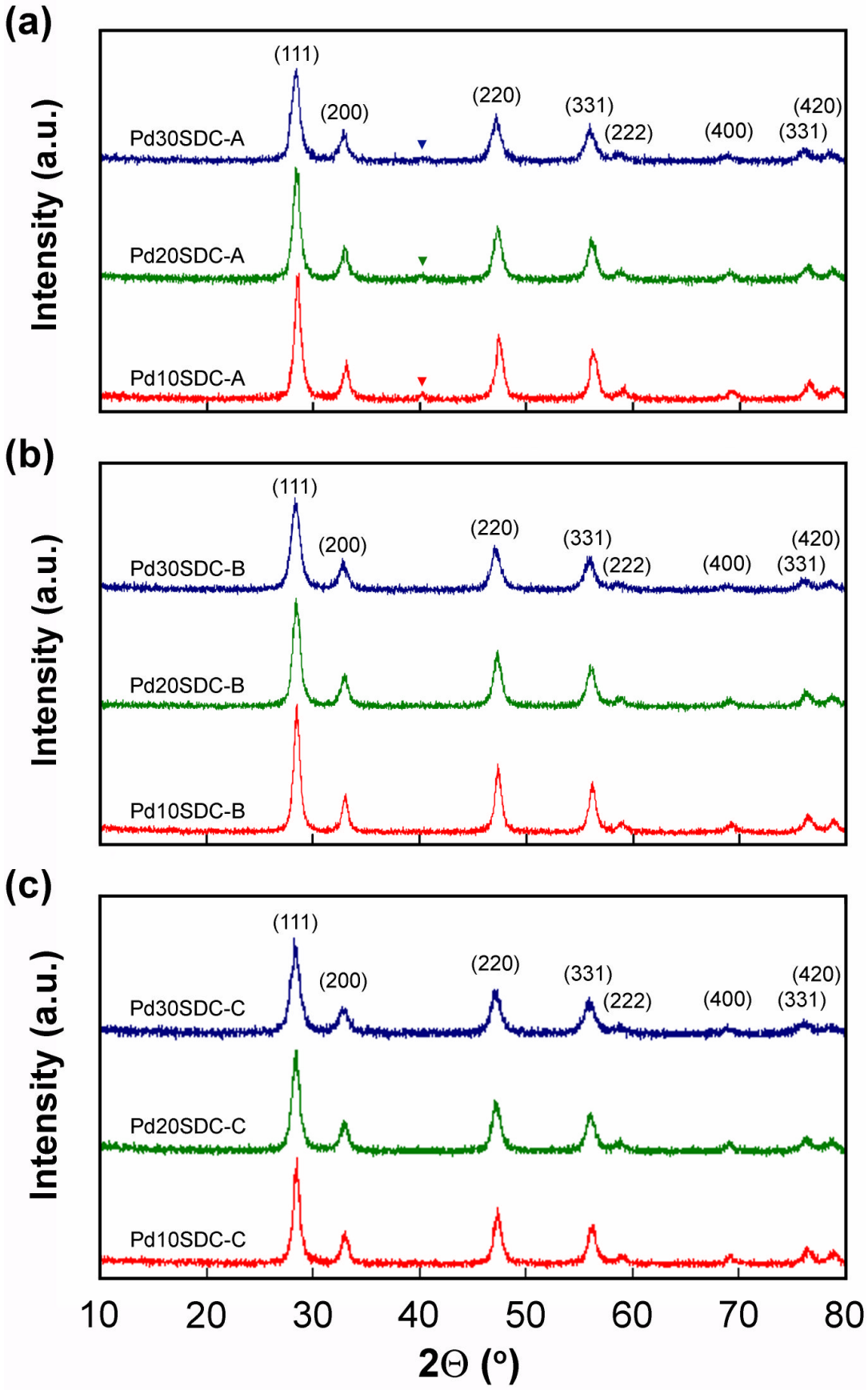

Figure 6.15 XRD patterns of reduced catalysts prepared by (a) method A, (b) method B and (c) method C.

6.4.2 X-ray Photoelectron Spectroscopy

XPS measurements were performed for representative Pd20SDC catalysts prepared by the three impregnation methods, A, B and C. These studies were carried out using samples reduced under similar conditions as for the catalytic activity tests (Section 3.8). The peak positions corresponding to the E_b were compared with spectra of unreduced samples (Figures 6.11–6.14).

Ce 3d core level XPS spectra of the three reduced Pd20SDC catalysts are presented in Figure 6.16. Capitals A, B and C indicate the relevant preparation method. The spectra are surprisingly similar to those of the unreduced samples in Figure 6.11. Ce^{4+} is still clearly the main oxidation state and peaks corresponding to Ce^{3+} (at 886 and 904 eV) are small. As for the as-prepared samples, the spectrum for method C is shifted to higher binding energy, but the shift for the reduced sample is very small. This suggests some loss of Cl from the surface during the reduction process.

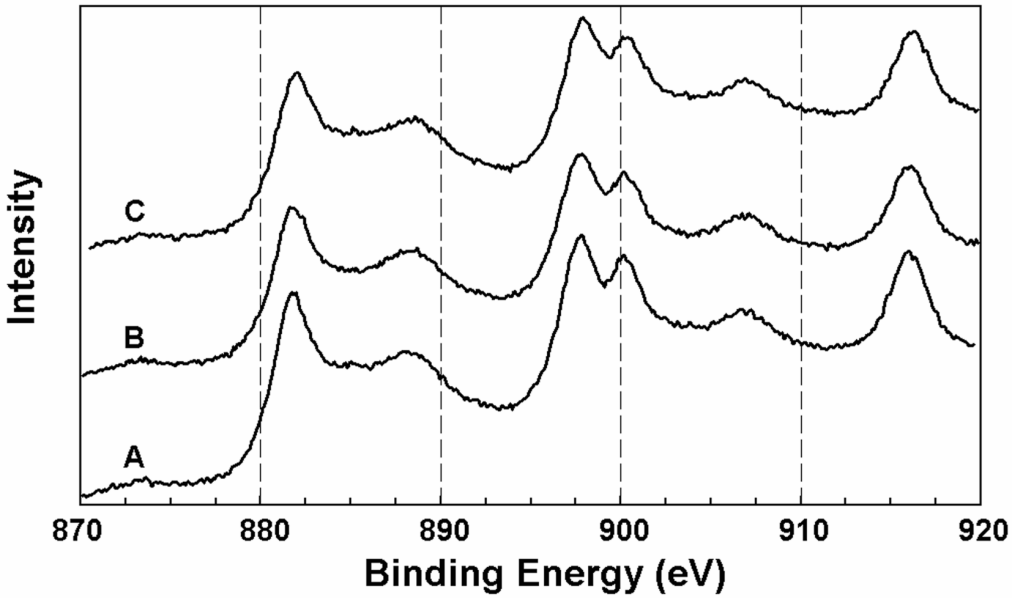

Figure 6.16 Ce 3d core level XPS spectra of reduced Pd20SDC catalysts prepared by method A, B and C.

Figure 6.17 shows Sm 3d core level XPS spectra for the three reduced Pd20SDC catalysts. These spectra are very similar to each other and to those for the as-prepared samples. However, in the reduced samples, there is no visible shift to higher binding energies for the Series C sample. This again suggests Cl was removed from the catalyst surface during reduction.

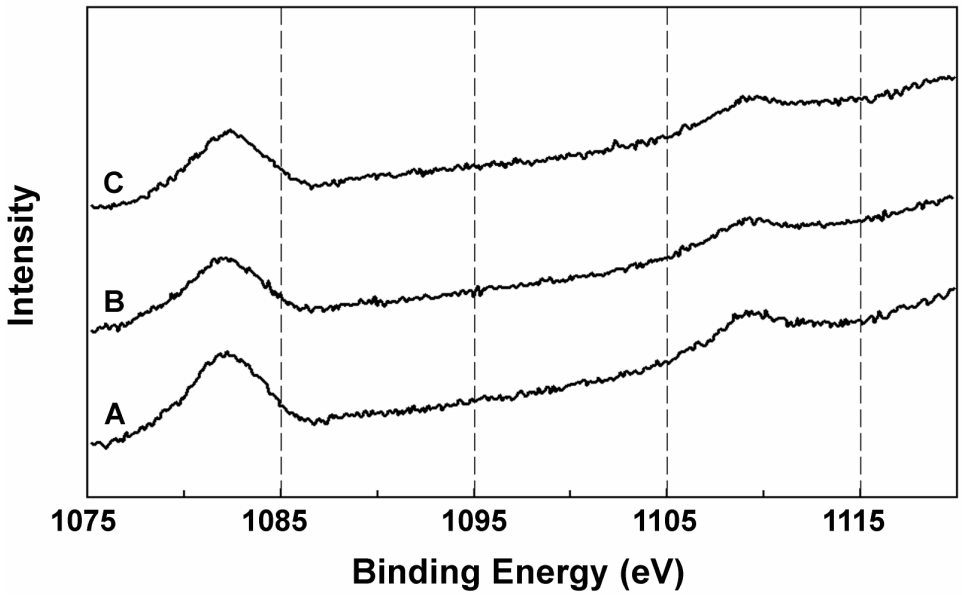

Figure 6.17 Sm 3d core level XPS spectra of reduced Pd20SDC catalysts prepared by method A, B and C.

The oxygen 1s core level XPS spectra are presented in Figure 6.18 for the three reduced catalysts and show two peaks: one at around 528.5 eV which was assigned to lattice oxygen and a smaller feature at 531.5 eV which was assigned as chemisorbed O or OH species.[159] After reduction, the latter are more likely to be OH species. The spectra and peak positions are more similar to each other than before reduction. However, for the Series C catalyst, the main peak is still at slightly higher binding energies than for the other two samples. In addition, the smaller, higher energy feature is much broader for the Series C sample. This indicates a wider range of surface O environments in this sample.

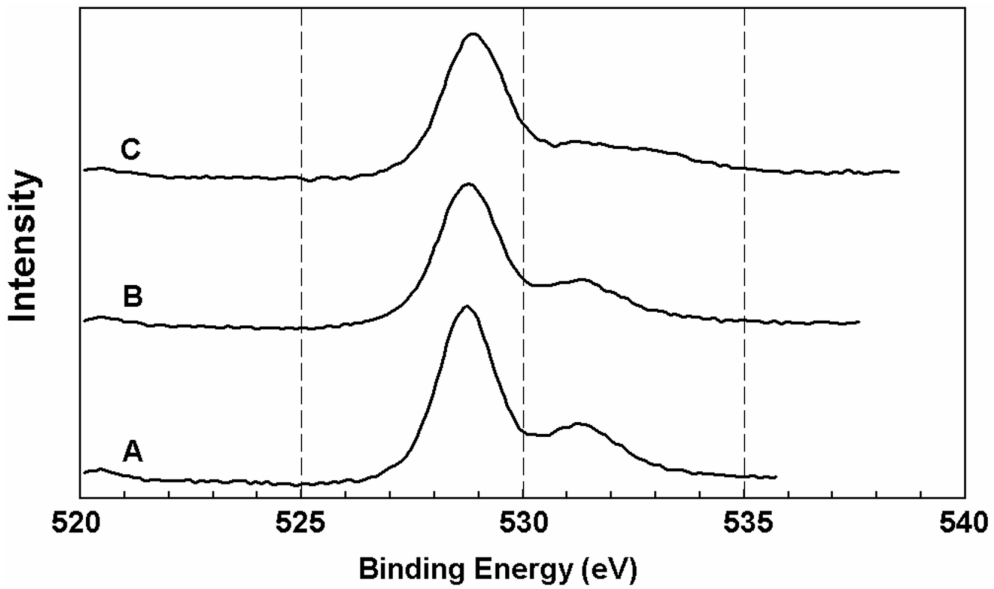

Figure 6.18 O 1s core level XPS spectra of reduced Pd20SDC catalysts prepared by method A, B and C.

Figure 6.19 shows Pd 3d core level XPS spectra for the reduced samples. Concentrating on the region from about 335 eV (corresponding to Pd^0) to about 338 eV (oxidised Pd, Pd^{2+}) it can be seen that there is considerable variation between the spectra. The Series A and B samples appear to have mainly metallic Pd at their surfaces, although the peaks for the former are very low in intensity. The Pd at the surface of the Series C sample was mainly oxidised, with contributions from Pd^{2+} and Pd^{n+} but much less from Pd^o. This difference is likely to be caused by the highly acidic (oxidising) conditions of the impregnation step in method C.

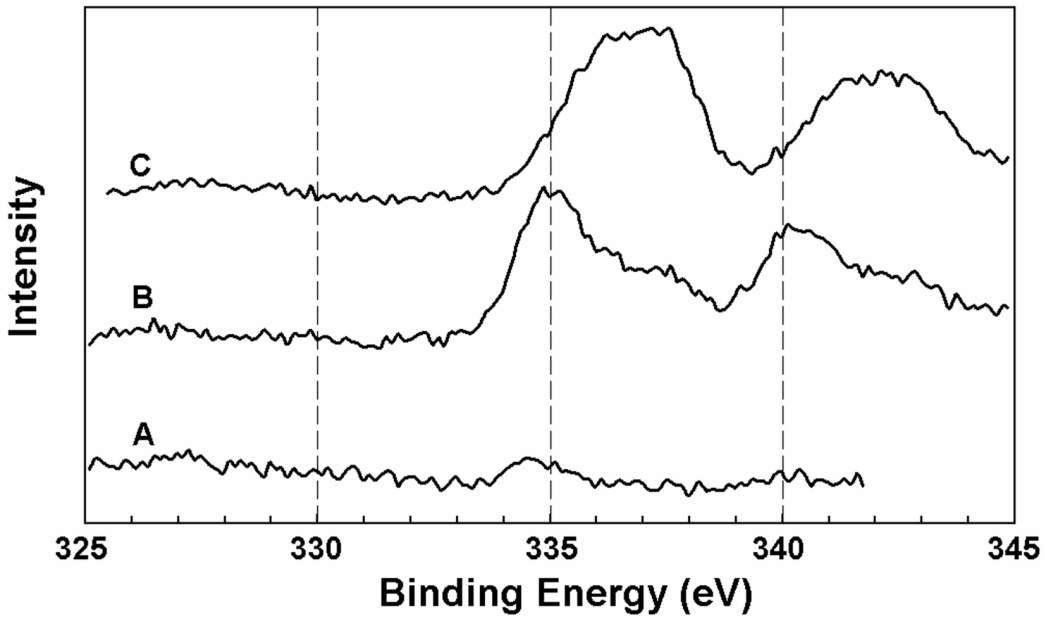

Figure 6.19 Pd 3d core level XPS spectra of reduced Pd20SDC catalysts prepared by method A, B and C.

6.4.3 Catalytic activity

Pd/SDC catalysts and SDC supports were investigated in the light of catalytic activity using various reaction parameters. The methanol conversion and hydrogen yield results are presented in Figure 6.20 and 6.21, respectively. In addition, the selectivities to different products are showed in Table 6.8 and 6.9, after 1 h and 3 h reaction time, respectively.

6.4.3.1. Methanol conversion

As can be seen in Figure 6.20, the materials giving the lowest methanol conversions are the SDC supports, as would be expected since they contain no Pd, the catalytically active phase. For all supports, methanol conversion is below 30 mol%. The fact that the supports show

some conversion may be explained by some non-catalytic reaction and the possible role of the support oxides in the decomposition of methanol and/or water, processes that represent the first steps of the steam reforming of methanol.[164]

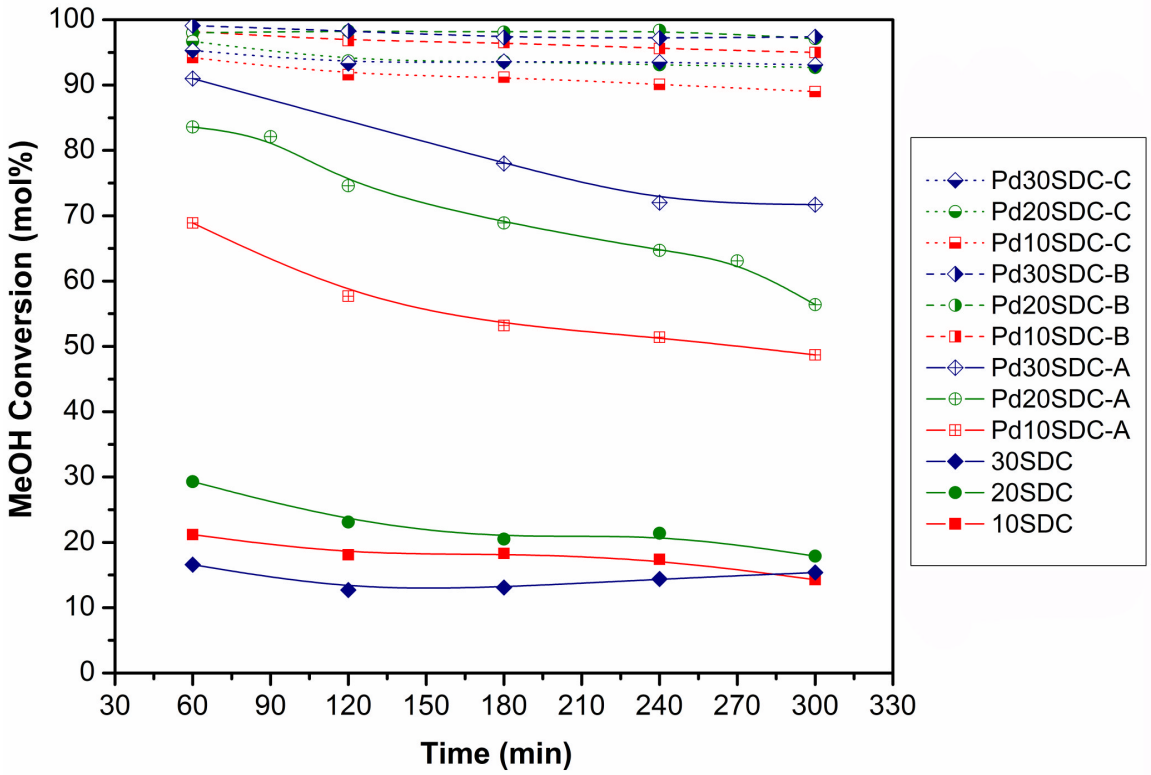

Figure 6.20 Evolution of methanol conversion with time on stream catalysts and supports.

The 20SDC support shows the highest conversion values over the whole of the time on stream. This may be because this sample has the highest SSA among the supports. However, this requires closer study because it has been reported that the decomposition of methanol over CeO_2 is sensitive to the structure.[165] The lowest value of conversion was shown by the 30SDC, again perhaps because of its low SSA.[165] Conversion falls by about 10-30% for the three supports during the catalytic tests and this may be a sign of relatively low thermal stability.

Incorporation of Pd into the samples gives rise to a very marked rise in conversion, which confirms that Pd is a very active metal for the steam reforming of methanol. Considering the three series of Pd/SDC catalysts studied, which were prepared in three different ways, it is clear that the samples of Series B showed the highest conversions, the catalysts of Series A showed the lowest conversions and those of Series C were slightly lower than for Series B. This general trend may be related to the surface compositions obtained by XPS in which catalysts of Series B and C showed much higher surface concentration of Pd than those of

Series A, and values for Series B were slightly higher than for Series C. This trend can be related to the preparation methods. Samples of Series A were prepared in a one-step process, which would lead to the approximately homogeneous incorporation of Pd throughout the bulk of the SDC supports. Series B and C were prepared by impregnation of previously prepared SDC supports with Pd-containing precursor solutions, and so it would be expected that surface concentration of Pd would be high, with no Pd expected in the interior of the SDC support particles. The Series C samples were prepared from a very acidic solution of H_2PdCl_4, unlike those of series B, and there is evidence from previous studies on Pd/CeO_2-Sm_2O_3 that this causes dissolution of the Sm oxide which is then reprecipitated as an amorphous layer containing Sm, O and Pd.[112] During subsequent heat treatment, Pd nanoparticles and samaria crystallites were reprecipitated. This process, if it occurred in these samples, may have resulted in a proportion of the Pd particles being covered by the amorphous layer, reducing the access of the gas-phase reactants to the Pd, so giving rise to the slightly lower conversions seen for Series C as well as to the lower surface concentrations of Pd observed by XPS. In fact, the Sm/Ce ratios calculated from the XPS data are slightly higher for Series C than for the Series B.

The results in Figure 6.20 show that, over the period of the catalytic test, the samples of Series A show a fall in conversion of about 20% while the catalysts of Series B and C exhibit only a much smaller decrease, implying that the latter catalysts are more stable under reaction conditions.

Within each of the three series, there is a tendency for methanol conversion to increase as the Sm content of the support increased. This can be seen most clearly for Series A. This may be explained by the idea that Sm_2O_3 is able to provide basic active sites in the vicinity of the Pd particles which in turn facilitates the adsorption of the reactant species and favours the surface diffusion of the reaction intermediates.[112] It is reasonable to expect this effect to occur also in mixed oxides of Sm and Ce and to increase in importance the higher the concentration of Sm. In each of the Series B and C, the conversions for the 20SDC and 30SDC samples are very similar, but those for 10SDC are clearly lowest in each case. Several changes occur concurrently in the Pd/SDC catalysts as %Sm is increased in these samples: SSA decreases and surface concentration in Pd tends to decrease but the concentration in active basic sites is expected to increase sharply. The conversion results obtained can be considered as the consequence of the sum of these overlapping effects.

6.4.3.2. Hydrogen yield

As for the methanol conversion results, it is clear from Figure 6.21 that the lowest hydrogen yields - below 100% - are given by the bare SDC supports, 20SDC giving the highest values and 30SDC the lowest. This trend can be explained by the increase in SSA in the order 30SDC < 10SDC < 20SDC. It may be relevant that as SSA increases, the accessibility of the surface of CeO_2-based supports for storage (and release) of oxygen, which may promote the WGS reaction, would also increase.

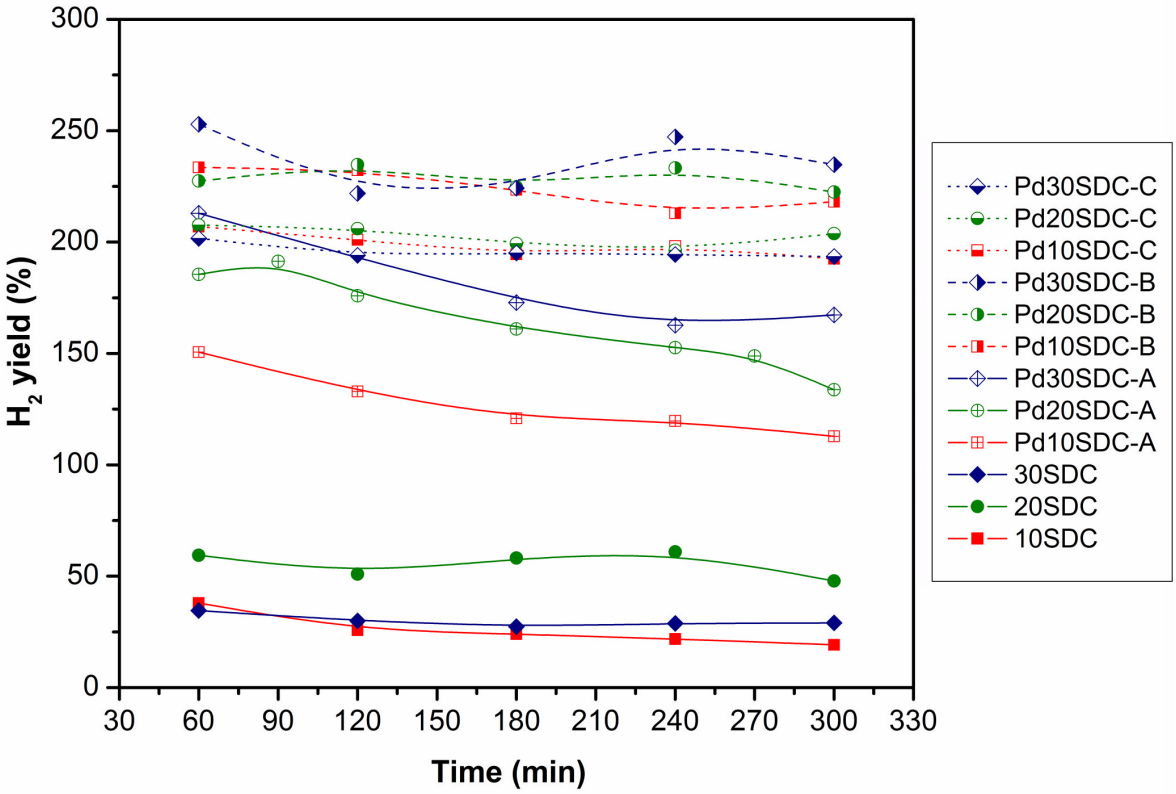

Figure 6.21 Evolution of hydrogen yield with time on stream for Pd/SDC catalysts and bare SDC supports.

The addition of Pd to the catalysts causes a very significant increase in hydrogen yield and in all cases selectivities to H_2 approaching 100% (hydrogen basis) are obtained for all samples. The only other hydrogen-containing product is CH_4, selectivities to which are almost always below 0.5% and never rise above 1.1%. Given the very high selectivities to H_2, the trends observed in H_2 yield are very similar to those already observed for methanol conversion. That is, H_2 yield increases in the order: Series A < C < B. The Series A catalysts suffer a more

marked fall in H_2 yield over the course of the time on stream than the other two series, in which only small falls in yield are seen.

As in the methanol conversion results, as Sm content in the support increased, H_2 yield clearly increases in Series A. For Series B and C, as Sm content increased, the decrease in SSA and the tendency of surface concentration of Pd to decrease, together with the expected increase in the availability of active basic sites appear to cause H_2 yield to be very close for all three compositions in Series C and to show a tendency to increase with increasing Sm content in Series B.

It is interesting to consider the selectivities to carbon-containing compounds and to relate these to the three expected processes, which include the steam reforming in principal reaction (Eqn. 6.1), the decomposition of methanol (Eqn. 6.2) and the WGS reaction (Eqn. 6.3).

$$CH_3OH + H_2O = 3H_2 + CO_2 \quad \textbf{(6.1)}$$

$$CH_3OH = 2H_2 + CO \quad \textbf{(6.2)}$$

$$CO + H_2O = CO_2 + H_2 \quad \textbf{(6.3)}$$

High methanol conversion and high selectivity to H_2 (hydrogen basis) contribute to a high overall yield of H_2. However, there is a further factor which has a multiplicative effect. This is related to the reaction pathway followed from methanol to H_2 and is indicated by the ratio of the selectivity to CO_2 to that of CO (carbon basis). Production of CO_2 implies, on the basis of the above chemical reactions, the conversion of the same number of moles of methanol to CO_2 either by steam reforming or by methanol decomposition followed by WGS, converting CO to CO_2. In both cases, 3 moles of H_2 are produced per mole of methanol (300% yield in notation). On the contrary, production of one mole of CO implies decomposition of one mole of methanol, yielding only 2 moles of H_2 (only 200% yield). Examining the selectivities to CO to CO_2 with this in mind, it is seen that in general, Series C presented the lowest values of S_{CO2}/S_{CO}. This means that the maximum possible yield of H_2 is displaced away from 300% and towards 200%, and gives rise to the lowest experimental values of the three series of catalysts. Thus, relatively low conversions are exacerbated by high S_{CO} to give even lower overall yields of H_2. The highest selectivity to CO_2 is observed for Series B, which also gave the highest methanol conversions. These two beneficial factors multiply to give even higher yields of H_2. Therefore, the superiority of Series B over Series C in Figure 6.21 is more marked than in Figure 6.20. Series B catalysts are best at promoting the complete oxidation of the carbon from methanol, rather than the decomposition reaction leading to CO.

Applying the same considerations to the bare supports shows that S_{CO2}/S_{CO} increases in the order: 30SDC > 10SDC > 20SDC. The latter exhibits both the highest methanol conversion values and the highest yields of H_2 – by a clearer margin – among the supports. The values of S_{CH4} are all very low, but the highest values are observed for the bare supports. This indicates that unwanted side reactions – such as the production of methane by fragmentation of methanol and the hydrogenation of CO and CO_2 – occur more when the active Pd phase is absent.

Table 6.8 Catalytic activity, reaction time 60 min.

Sample	X (%)	S_{CO2} (%)	S_{CO} (%)	S_{CH4} (%)	S_{H2} (%)	H_2 yield /%
Pd10SDC-A	68.9	21.9	77.3	0.82	99.2	150.6
Pd20SDC-A	83.6	23.9	75.6	0.48	99.5	185.5
Pd30SDC-A	91.0	34.9	64.8	0.25	99.7	212.9
Pd10SDC-B	98.2	47.4	50.2	2.48	97.5	233.2
Pd20SDC-B	98.0	36.6	62.4	1.05	98.9	227.7
Pd30SDC-B	99.1	55.3	44.7	0.00	100	253.0
Pd10SDC-C	94.2	21.3	78.2	0.48	99.5	206.7
Pd20SDC-C	96.7	14.7	85.3	0.00	100	207.6
Pd30SDC-C	95.3	12.4	87.4	0.24	99.8	201.5

Table 6.9 Catalytic activity, reaction time 180 min.

Sample	X (%)	S_{CO2} (%)	S_{CO} (%)	S_{CH4} (%)	S_{H2} (%)	H_2 yield /%
Pd10SDC-A	53.2	28.8	70.9	0.37	99.6	120.9
Pd20SDC-A	68.9	34.0	66.0	0.08	99.9	175.9
Pd30SDC-A	78.0	22.2	77.7	0.16	99.8	172.8
Pd10SDC-B	96.5	32.2	67.6	0.27	99.7	223.0
Pd20SDC-B	98.1	29.8	70.2	0.00	100.0	225.4
Pd30SDC-B	97.3	31.3	68.5	0.25	99.8	224.1
Pd10SDC-C	91.2	14.6	85.1	0.24	99.8	194.9
Pd20SDC-C	93.6	13.8	86.0	0.26	99.7	199.1
Pd30SDC-C	93.6	9.1	90.6	0.25	99.7	194.8

6.5 Summary

Three methods were established to incorporate 2 wt% of Pd on nanoparticulate SDC supports with three Sm contents in order to obtain nine Pd/SDC catalysts. These were prepared and tested as methanol reforming catalysts. Characterisation experiments were performed on unreduced and reduced Pd/SDC samples, and on the bare (Pd-free) SDC supports for comparison.

A direct impregnation technique (method A) was established, which employed individual metal nitrates and citric acid as a complexing agent. It was found that incorporation of Pd by this method was only possible if the molar ratio of citric acid to total metal oxide (CA:TO) was doubled to 4:1 from 2:1, the value used in the SDC preparation method (Section 5.2). Thermal analysis experiments were carried out on Pd/SDC gel precursors and more dramatic changes in the heat flow were observed than in the synthesis of the SDC solid solutions. The higher values of enthalpy changes were explained by the presence of double the amount of citrate ions. The two other methods of Pd incorporation (methods B and C) were based on the incipient wetness impregnation technique. These employed the previously synthesised SDC nanopowders (Chapter 5) as supports and solutions of Pd precursors: either $Pd(NO_3)_2 \cdot 2H_2O$ (method B) or H_2PdCl_4 (method C).

All peaks in the XRD patterns of the unreduced Pd/SDC catalysts were assigned to the cubic phase of ceria. Qualitative studies of diffractograms showed no additional Pd-containing phases. Average crystallite sizes, estimated from the XRD patterns using the Scherrer equation, were the smallest for catalysts of Series A and decreased with Sm content. After reduction of the catalysts in a stream of hydrogen at 500°C for 1 h, peaks characteristic of Pd were observed by XRD but only for samples prepared by method A.

SEM micrographs of unground powders obtained by method A showed structures similar to those seen in the SDC supports, which are closely related to the preparation technique. SEM images of ground catalysts of Series A provided further insight into their microstructure. Loosely-agglomerated particles were observed.

EDX spectra were obtained for all Pd/SDC catalysts. These confirmed the oxide support stoichiometry as well as giving Pd contents of about 2 wt%. The presence of Gd, possibly as a cross-contamination effect, was detected in Series B catalysts, while significant concentrations of Cl was found in Series C samples, as a result of preparation method.

The incorporation of 2 wt% of Pd on the SDC supports gave a significant increase in the SSAs of Series A catalysts. These possessed more than twice the SSAs of the corresponding SDC supports. The highest value among all the catalysts - of 69.4 $m^2 \cdot g^{-1}$ - was found for the Pd10SDC-A sample. The SSA value decreased with increasing Sm content for catalysts prepared by this method. Both incipient wetness techniques (method B and C) gave only slightly higher SSAs results in comparison to the bare SDC samples, in the case of catalysts containing 20 and 30 mol% of Sm. Both Pd10SDC-B and Pd10SDC-C possessed markedly higher SSAs of 42.2 and 48.3 $m^2 \cdot g^{-1}$, respectively.

All nine unreduced Pd/SDC samples and the three SDC supports were examined by XPS. The surface concentrations and oxidation states of the relevant elements were determined. Cerium was found to be mainly in the most oxidised form (Ce^{4+}). However, small amounts of Ce^{3+} were also indicated. All Sm 3d core level XPS spectra exhibited two peaks corresponding to Sm^{3+}. In the case of Series C samples, a shift towards higher E_b was observed due to the some Cl introduced within the preparation method. Oxygen 1s core level XPS spectra of SDC supports and catalysts of Series A and B were characteristic of two peaks at similar E_b. In Series C samples, only one, less intense peak, which was shifted towards higher E_b was distinguished. It was interpreted as an effect of the synthetic route applied, where chemisorbed O or OH species were replaced by Cl. Two main peaks were also observed in Pd 3d core level XPS spectra of these unreduced samples. These showed variations in both peak intensity and position between samples prepared by the three different methods. Series A catalysts were characterised by the highest proportion of surface Pd being present as electrodeficient Pd (Pd^{n+}). Series B showed mainly Pd^{2+} with some elemental Pd (Pd^0), while Series C appeared to contain mainly Pd^{2+}at its surface.

XPS studies were also performed on reduced Pd20SDC catalysts prepared by the three different impregnation techniques (methods A, B and C). Ce, Sm and O spectra showed consistency with the results for the unreduced samples. Pd 3d core level XPS spectra indicated differences in oxidation state and in surface concentration of Pd between these three samples. The highest surface concentration of Pd was measured for the Pd20SDC-B catalyst, Pd20SDC-C coming next and the lowest concentration was for the Pd20SDC-A sample. In XPS spectra of Pd20SDC-A and Pd20SDC-B, the peaks at E_b corresponding to the Pd^0 were indicated, with the highest intensity of Series B catalyst. Palladium at the surface of Pd20SDC-C, apart from Pd^0, appeared also with Pd^{2+} and Pd^{n+} contributions as an effect of strong oxidising conditions used in impregnation step of method C.

All samples were found to be catalytically active as methanol reforming catalysts. The activity of Pd in the Pd/SDC catalysts is very high, as can be seen by comparing their performance with that of the bare supports. Catalysts with the highest surface concentrations of Pd, measured by XPS, showed the best performance, giving orders of both increasing methanol conversion and increasing H_2 yield of Series A < C < B. This ranking was more marked for yield of H_2 than for methanol conversion because of the effect of an increased bias towards complete conversion of methanol to CO_2 and H_2. This was identified by considering the selectivities to CO and CO_2.

Changing the Sm content of the support was expected to increase catalytic activity by providing more active basic sites on the support surface for reactant adsorption and surface diffusion. However, it also led to a general decrease in SSA in the Pd/SDC catalysts and was accompanied by some variation in the surface concentration of Pd. Series A, the least active catalysts with by far the lowest surface Pd concentrations, clearly showed increasing methanol conversion and H_2 yield with increasing Sm content, in line with the argument relating to active sites on the support. For both Series B and C, however, the corresponding trends were Pd10SDC < Pd20SDC~Pd30SDC. Here, it was proposed that changes in SSA and in surface Pd concentration had a stronger effect than in Series A.

The best catalytic activity results were obtained for Pd30SDC-B, which gave methanol conversion and H_2 yield values of 97.4% and 236.2 %, respectively, after 5 h on stream.

CHAPTER VII – **CONCLUSIONS**

7. Conclusions

This chapter is divided in three sections, which cover the two SOFC electrolyte materials (YSZ and SDC) and the methanol reforming catalysts (Pd/SDC) – all investigated using the experimental techniques described in Chapter 2.

7.1 Yttria-stabilised zirconia

- The effect of Y content and starting powder particle size on phase and microstructure was thoroughly investigated for both pure ZrO_2 and yttria-stabilised zirconia samples with 3, 5, 8 and 10 mol% of Y_2O_3. In addition, the effect of these parameters on ionic conductivity was studied for the YSZ materials. All powder samples were supplied by the industrial partner, MEL Chemicals Ltd, in two different powder forms, named here as nanopowders and micropowders.
- XRD studies on all compositions derived from the micro- and nanopowders were completed and the patterns were in agreement with data available from ICSD for peaks associated with the monoclinic, tetragonal and cubic phases of the corresponding YSZ sample. More detailed examination of each diffraction pattern in the range of $2\Theta = 70 – 79°$ was performed in order to determine if the tetragonal phase was present. Unstabilised zirconia micropowder exhibited the characteristic monoclinic phase, while for the corresponding nanopowder, the tetragonal phase was observed to be dominant. In the case of the nanopowder set of samples, as mol% of Y_2O_3 increased, the phase of the electrolyte material changed from a mixture of the monoclinic and tetragonal phases to tetragonal and finally cubic phases, at the higher dopant concentrations. It was determined that the tetragonal phase was favoured with respect to the monoclinic phase by the small particle size of the nanopowder samples at low Y contents. XRD patterns of the nanopowders exhibited a significant peak broadening effect caused by the small particles of the starting material. Identical experiments were carried out on sintered YSZ pellets, which gave much sharper and more intense peaks. Therefore, the mixture of characteristic phases could be assessed with more precision. No impurity phases were detected in any of the XRD patterns.
- Electron microscopy results confirmed that the two sets of powders had been prepared with quite different morphologies. HR-TEM data indicated some hard

agglomerates for both nanopowders and micropowders. Individual particles appeared in a variety of shapes and sizes. These were quite rounded at low Y content and slightly more angular for more heavily doped zirconia samples of the nanopowder set. Morphologies of micropowder samples appeared mainly as roughly ovoid (m0YSZ), spherical (m3YSZ) and sharp-edged hexagonal particles (other compositions). Particle size distribution histograms were prepared and an increase of the mean particle size for micropowders (from 81 to 251 nm), and a decrease for nanopowders (from 7.8 to 5.2 nm), was observed with increasing Y content (from 0 to 10 mol% of Y_2O_3).

- High resolution TEM allowed information on the crystallography of individual nanopowders to be obtained. These were found to be consistent with the XRD results.
- EDX results obtained in the TEM instrument showed Y/Zr molar ratios to be in close agreement with the expected nominal values for all samples.
- In dilatometry studies the nanopowders were more active during sintering as they underwent a lower temperature initial shrinkage than the micropowders. Characteristic cracking during the cooling step was confirmed for pure zirconia samples as the result of the tetragonal to monoclinic phase transformation. Two sets of powders were pressed using isostatic and uniaxial techniques. Slightly better sintering characteristics were obtained for the isostatically pressed pellets, which exhibited lower shrinkage. The sintering rates for the nanopowders were more self-consistent than for the micropowders. Thermal expansion coefficients of all samples were calculated and were in good agreement with reported data.
- All of the sintered YSZ bodies appeared in SEM micrographs to have typical well-developed grains. Average grain size increased with increasing Y content. However, some porosity was observed for 10 mol% YSZ, in both the micro- and nanopellets. The identical sintering conditions, which were applied to all pellets, resulted in similar average grain sizes for the 3 and 5 mol% YSZ samples. However, the 8 and 10 mol% YSZ nanopellets had smaller mean grain sizes than the corresponding micropellets.
- IS measurements on 3, 5, 8 and 10 mol% YSZ micro- and nanopellets were completed. Data was presented in Nyquist and Arrhenius plots and showed a small improvement in ionic conductivity values for nanopellets over micropellets. The grain boundary conductivity was found to be higher than the bulk conductivity in all YSZ samples studied. The IS results were in good agreement with literature data and the highest values of overall conductivity were obtained for the 8 mol% YSZ

compositions. The values of capacitance related to the bulk contribution showed no significant change with increasing yttria content. However, they were found to be slightly higher for the micropellets. The capacitance of the grain boundary contribution increased with increasing yttria content in both sets of pellets because of the effect of the corresponding increase in average grain size.

- ICP-MS measurements were performed on dense YSZ pellets of both sample sets. The chemical composition of the supplied YSZ materials was confirmed. However, small but significant amounts of Al, Si, and Hf were detected in the micropellets. Al and Si were found at slightly higher concentrations in the nanopellets. However, Hf was not detected in the nanopellets. The presence of Hf was reported to improve the ionic conductivity of YSZ systems and this may have been a factor in the case of the micropellets, which possessed more than 2 wt% of this element. On the other hand, the higher concentration of Si in the nanopellets may have been responsible for a slight drop in their conductivity.
- The interpretation of the results of the comparative studies of YSZ electrolyte materials presented in this thesis was complicated somewhat by the fact that the starting materials were prepared by two different synthetic techniques, and therefore contained different levels of impurities. However, it is necessary to use different synthetic methods to obtain materials with such different particle sizes.
- Application of nanopowders obtained by a solution method was confirmed to be an interesting approach for the preparation of SOFC electrolytes. It is possible that a reduction in the sintering time and/or temperature can be successfully applied, because such starting materials are more active during initial stages of their densification process. Further work is necessary to determine the precise sintering conditions where nanoparticular starting powders would be most advantageous.
- The processing of YSZ materials must take careful account of the risks of introducing any impurities which, although introduced in small amounts, may significantly affect the materials properties.

7.2 Samarium-doped ceria

- Three compositions of high purity, nanoparticulate SDC materials, $Sm_xCe_{1-x}O_{2-\delta}$ (x = 0.1, 0.2 or 0.3), were successfully prepared by a low temperature, inexpensive citrate complexation technique.

- Thermal analysis results showed that decomposition and crystallisation of all of the SDC gel precursors occurred *via* one endothermic and three exothermic processes. These were assigned by energetic considerations and mass spectrometry analysis of off-gases, respectively, to the loss of adsorbed water at around 100°C, the polymerisation reaction during completion of gel formation at around 125°C, the decomposition of the carboxylate groups of the citrate ions at around 200°C and complete burnout of organic matter at around 300°C. Increasing Sm content in the SDC solid solutions caused the displacement of these processes to higher temperature, but this effect was relatively weak.
- The final crystal structure of the SDC materials was found to form at a temperature below 300ºC by recording diffractograms of precursor samples calcined at different temperatures. XRD studies on powders calcined at 500°C for 2 h revealed that all compositions were single-phase fluorite structured nanocrystals. Mean primary crystallite sizes were determined from main peak broadening using the Scherrer relationship. These values decreased with Sm content and varied from 7.8 to 11.3 nm.
- The specific surface area (SSA) values of ground SDC samples were determined by nitrogen physisorption and exhibited the expected decrease with increase in calcination temperature. After calcination at 500°C, 20SDC showed the highest SSA value of any sample, 32.7 $m^2 \cdot g^{-1}$. In addition, based on BET results, it can be concluded that SDC nanopowders underwent significant agglomeration.
- SEM images showed that as-calcined products were foam-like, branched structures with high porosity. These features were characteristic of the synthetic route applied. The as-prepared samples were milled in order to release the nanoparticles and increase the SSA of all samples.
- EDX results confirmed the expected oxide stoichiometry a uniform distribution of individual elements throughout the mass of the samples and an absence of significant impurities in all the SDC nanopowders.
- TEM images showed loosely-agglomerated clusters, which consisted of individual crystallites of diameter about 10 nm. Therefore, the agreement with XRD results was very good. HRTEM studies were performed in order to investigate the internal crystal structure of individual nanoparticles. These crystallites showed good crystallinity and there was no evidence for widespread defective crystal structures for crystallites containing multiple nanodomains.

- ICP-MS results confirmed the stoichiometric composition of each SDC sample and showed evidence of Si, Ca, As, Pr and Gd in SDC powders calcined at 500°C for 2 h. The most contaminated 20SDC sample possessed 0.16 wt% of Si, 0.13 wt% of Ca and 0.20 wt% of As. Such concentrations were estimated to have a negligible impact on the IS results. On the other hand, the presence of Pr and Gd in small amounts was reported to improve conductive properties of SDC electrolytes. The potential sources of contamination were discussed and in some cases could not be eliminated.
- Sintering behaviour of the SDC nanopowders was examined using dilatometry and shrinkage of 16-18 % was observed for uniaxially compacted powders. All samples were found to start the sintering process with low rates in the low temperature region, to show higher rates after 600°C and to continue up to maximum temperature of the dilatometry experiment. This information was used to help choose the sintering regimes to be used for studies of the properties of dense SDC electrolytes. Sintering temperatures of 1300, 1400 and 1450°C were applied, each for either 4 or 6 h all with the same heating and cooling rates, resulting in a total of 18 pellets to be investigated.
- The microstructure of SDC pellets was investigated using SEM. These studies showed that Sm-doped ceria green bodies require at least 1400°C to result in good densification (95 - 97% of theoretical density). Samples sintered at 1400°C for 6 h or 1450°C for 4 h exhibited excellent microstructure. The oversintering effect was noticed for the 10SDC sample sintered at 1450°C for 6 h, which has reported to be responsible for the decrease in ionic conductivity in ceria electrolytes. The calculated average grain size increased with longer sintering times and higher sintering temperature.
- XRD patterns of sintered SDC pellets were obtained and showed much sharper peaks because of the growth in particle size during thermal treatment. There was no evidence for additional phases and all peaks were assigned to the cubic fluorite phase typical of ceria compounds.
- IS measurements were completed for a representative group of 12 samples. Nyquist plots clearly showed bulk and grain boundary contributions to the conduction process at measurement temperatures below 500°C. Grain boundary conductivity was found to be higher than bulk conductivity for all compositions. The calculated activation energies for bulk and grain boundary contributions showed a generally increasing trend with increasing Sm content for samples of the same sintering regime. Activation energies were calculated from two temperature regions in Arrhenius plots of total

electrolyte conductivity and for all SDC compositions. That is, gradients were calculated above and below characteristic inflection at 500°C. In this way, values of defect association enthalpy (ΔH_a) and oxygen migration enthalpy (ΔH_m), were calculated for these materials. ΔH_a was less sensitive to Sm content and ranged from 0.32 – 0.46 eV among the samples. ΔH_m had values of 0.41 – 0.70 eV and increased with mol% of Sm_2O_3, being particularly high for 30SDC. At 600°C, the highest total conductivity was 1.81×10^{-2} S·cm^{-1} for the 20SDC sample sintered at 1450°C for 6 h.

7.3 Palladium supported on samarium-doped ceria

- Three different impregnation methods were successfully employed to prepare nine candidate methanol reforming catalysts with 2 wt% of palladium supported on each of the three SDC nanopowder compositions.
- Aqueous solutions of individual metal nitrates (Sm, Ce and Pd) and citric acid as a complexing agent were used in the direct impregnation technique (method A). It was found that molar ratio of citric acid to total metal oxide (CA:TO) had to be increased to 4:1 from 2:1 (used in the SDC preparation method) to allow the incorporation of Pd *via* this route. The two other methods (B and C) used the previously synthesised SDC nanopowders as supports for Pd particles. Pd precursors, either $Pd(NO_3)_2{\cdot}2H_2O$ (method B) or H_2PdCl_4 (method C) were employed in these incipient wetness impregnation techniques.
- Thermal analysis studies were performed on gel precursors prepared using the direct impregnation technique (method A). Data were compared with the results of the closely related method used in the preparation of the SDC solid solutions. Due to the doubly increased molar ratio of CA to the TO concentration in the case of Pd/SDC catalysts (only method A), the observed mass loss as well as the enthalpy changes were significantly larger than for the SDC preparation. More exothermic effects were recorded in TG/DTA experiments and more vigorous release of off-gases was recorded using the MS.
- XRD patterns of the unreduced Pd/SDC catalysts were typical of the cubic phase of partly-substituted ceria. No additional Pd containing phases were detected in these samples. The smallest average crystallite sizes were found for catalysts of Series A and decreased with Sm content within the same preparation method. Diffractograms of reduced samples, showed peaks characteristic of the Pd phase only for catalyst

powders prepared by method A. This could be attributed to the presence of larger Pd particles throughout the material of the Series A catalysts, rather than Pd nanoparticles dispersed well across the surface of the SDC, as would be expected in the catalysts prepared by methods B and C.

- XPS studies were performed on the Pd/SDC samples and on the three SDC supports for comparison. The surface concentrations of Ce, Sm, O and Pd and their oxidation states were determined. Cerium was mainly present as Ce^{4+}, although small amounts of Ce^{3+} were also indicated for by XPS for each sample. All Sm 3d core level XPS spectra exhibited two peaks corresponding to Sm^{3+}. Unreduced Series C samples exhibited a shift towards higher E_b in both Ce and Sm peaks. It is suggested that this was caused by the presence of some surface Cl introduced during preparation method C. Oxygen 1s core level XPS spectra of the SDC supports and catalysts of Series A and B showed two peaks at similar E_b which were assigned to lattice oxygen and oxygen chemisorbed on the surface or present as OH species. Only the lattice oxygen peak, shifted towards higher E_b was seen in the Series C samples and was interpreted as an effect of the applied synthetic route. Pd 3d core level XPS spectra of the unreduced samples gave information on the concentration and oxidation state of Pd in samples prepared by the methods A, B and C. Series A catalysts showed the highest proportion of electrodeficient Pd (Pd^{n+}). Series B showed Pd^{2+} with some elemental Pd (Pd^0), while Series C mainly contained Pd^{2+}.
- XPS core level spectra of Ce, Sm and O for three reduced Pd20SDC catalysts (prepared by methods A, B and C) showed consistency with the results of the unreduced samples. In the case of Pd 3d core level XPS spectra, the differences in oxidation state and in surface concentration of Pd between these three samples were significant. The highest surface concentration of Pd was measured for Series B representative catalyst, while the lowest for the Pd20SDC-A. The peaks in XPS spectra of Pd20SDC-A and Pd20SDC-B, were characteristic of the Pd^0, with the highest intensity observed for Series B catalyst. Pd20SDC-C sample, apart from Pd^0, appeared with Pd^{2+} and Pd^{n+} contributions, which could be an effect of strong acidic conditions applied in this impregnation step of Pd.
- Higher values of SSA were noticed for all catalysts than for the bare SDC oxides. This could be attributed either to the dispersion of Pd on the SDC supports or to some restructuring of the support particles in the Pd precursor solutions. In addition, method A resulted in the highest value of SSA for the Pd10SDC-A sample

($69.4\ m^2 \cdot g^{-1}$), and this may be because of the more exothermically favourable direct preparation technique. It was expected that due to the high SSAs of the series A catalysts, significant improvement in catalytic performance would be achieved. However, XPS studies indicated that Pd particles were not concentrated on the surface of the SDC supports.

- SEM images of the unground Pd/SDC powders made using method A showed similar microstructure to the SDC nanopowders. Micrographs of these catalysts after grinding revealed loosely-agglomerated nanoparticles. EDX spectra were obtained for all Pd/SDC catalysts and confirmed the expected oxide support stoichiometry as well as the Pd content to be about the desired value of 2 wt%. Some Gd was detected in Series B catalysts, possibly as a cross-contamination effect, while significant Cl concentration was found in Series C samples, as a result of the preparation method.
- Catalytic activity tests were carried out on reduced samples and all of them were found to be active catalysts for methanol reforming. The activities of the Pd/SDC catalysts were much higher than for the bare supports. According to the XPS results, the catalysts with the highest surface concentrations of Pd showed the best activity. The order of series A < C < B was observed in terms of both increasing CH_3OH conversion and increasing H_2 yield. The increase in the Sm content of the support was expected to increase catalytic activity. However, it also led to a general decrease in SSA in the Pd/SDC catalysts.
- Series A catalysts possessed the lowest surface Pd concentrations and clearly showed increasing CH_3OH conversion and H_2 yield with increasing Sm content. However, the trend for Series B and C was Pd10SDC < Pd20SDC ~ Pd30SDC. It was proposed that changes in SSA and in surface Pd concentration had a stronger effect in the case of catalysts prepared by both incipient wetness impregnation techniques than those in Series A.
- The best catalytic activity results were obtained for Pd30SDC-B, which gave methanol conversion, and H_2 yield values of 97.4% and 236.2 %, respectively, after 5 h on stream.
- Efficient generation of pure hydrogen from the methanol was achieved at high efficiencies. Hydrogen production is likely to play an important role for future power generation systems.

CHAPTER VIII – **FUTURE WORK**

8. Future work

8.1 Yttria-stabilised zirconia

Comparative studies by Neutron Diffraction would be of interest in obtaining more information on the crystallographic structure of YSZ micro- and nanopowders and sintered materials derived from them. Total Neutron Scattering experiments may reveal in more detail the local, structural properties and information on the defects in these YSZ materials. Total Scattering is considered as the sum of elastic scattering (in relation to the structure) and inelastic scattering, which depends on the dynamics of the system under study. In Total Scattering the complete two-dimensional scattering pattern is typically recorded and this can be converted by Fourier Transform in Pair Distribution Function (PDF) analysis to make use of all scattering data, rather than only the positions of Bragg peaks in a one dimensional diffraction pattern. This method has been found to be especially useful for nanoparticles and defective and low-crystallinity materials. The application of the Total Scattering method and atomic PDF analysis may allow for more accurate and local determination of the atomic-scale structure in the YSZ nanomaterials.

Modification of the sintering conditions of the YSZ green bodies to include two or more sintering steps was reported to improve the microstructure and density of YSZ electrolytes. High-speed sintering processes, sometimes including a microwave heating step, would also seem to be a promising approach. The application of the set of analysis techniques used in this thesis to such materials would be of interest.

The study of the sintering behaviour of mixtures of micro and nanopowders would also be an interesting line of research. An increase in the density of such materials would be expected by the filling of pores between the microparticles with nanoparticles, but also through the presence of the large, dense microparticles initially.

8.2 Samarium-doped ceria

The introduction of additional rare-earth elements as co-dopants into the SDC crystal structure seems to be a reasonable option for increasing the ionic conductivity of these electrolyte materials. Recent publications indicate that co-doping with Sm and Nd, Sm and Gd and Nd and Gd may allow ionic conductivities to be further increased above those of SDC.[166-168]

Studies on the improvement of the microstructure should also be performed subsequently, for example, by addition of novel sintering aids. Addition of small amounts of Sr has very recently been found to decrease sintering temperature significantly in CeO_2-based electrolyte materials.[169] A number of recent studies have recently reported slightly better property-performance characteristics.[37, 47, 75, 170-173] However, a compromise between complexity and cost of production, which increases with addition of expensive elements, must be achieved.

8.3 Palladium supported on samarium-doped ceria

Temperature Programmed (TP) methods, which are typically performed on catalysts, may provide more interesting information on catalytic properties of the Pd/SDC compounds. Techniques which could be usefully applied include Temperature Programmed Desorption (TPD), Temperature Programmed Reaction (TPR), Temperature Programmed Surface Reaction (TPSR), Temperature Programmed Reduction (TPRd) and Temperature Programmed Oxidation (TPO).

Application of these catalysts to other reactions, for example, steam reforming of ethanol to give hydrogen, would be an interesting line of research. Ethanol has potential as an alternative starting material and can be obtained from fermentation of biological crops and organic waste. In particular, it has the advantage that it is less toxic than methanol but still easy to transport and store in liquid form.

TEM studies with high resolution EDX mapping would provide valuable information on the distribution of the elements, and especially in the assessment of the size and distribution of the catalytically-active Pd particles. EDX is essential in these samples, because the Pd particles may have a similar particle size and contrast in the TEM to the SDC support. Even EDX mapping is non-trivial, however, because the Pd particles are likely, at least in some of the Pd/SDC materials, to be smaller than the effective size of the electron beam.

Additional information about the oxidation state of Pd and of O might be usefully investigated using XANES studies to complement the studies presented here using XPS.

REFERENCES

1. Stambouli, A. B.; Traversa, E., Fuel cells, an alternative to standard sources of energy. *Renewable and Sustainable Energy Reviews* **2002,** 6, (3), 295-304.

2. International Energy Outlook. *U.S. Energy Information Administration, U.S. Department of Energy* **2010**.

3. Meeting the Energy Challenge, A White Paper on Energy. *Department of Trade and Industry* **2007**.

4. Stambouli, A. B.; Traversa, E., Solid oxide fuel cells (SOFCs): a review of an environmentally clean and efficient source of energy. *Renewable and Sustainable Energy Reviews* **2002,** 6, (5), 433-455.

5. Yamamoto, O., Solid oxide fuel cells: fundamental aspects and prospects. *Electrochimica Acta* **2000,** 45, (15-16), 2423-2435.

6. Varcoe, J. R.; Slade, R. C. T., Prospects for Alkaline Anion-Exchange Membranes in Low Temperature Fuel Cells. *Fuel Cells* **2005,** 5, (2), 187-200.

7. Dicks, A. L., Molten carbonate fuel cells. *Current Opinion in Solid State and Materials Science* **2004,** 8, (5), 379-383.

8. de Bruijn, F., The current status of fuel cell technology for mobile and stationary applications. *Green Chemistry* **2005,** 7, (3), 132-150.

9. Sammes, N.; Bove, R.; Stahl, K., Phosphoric acid fuel cells: Fundamentals and applications. *Current Opinion in Solid State and Materials Science* **2004,** 8, (5), 372-378.

10. Lin, H.-L.; Yu, T. L.; Huang, L.-N.; Chen, L.-C.; Shen, K.-S.; Jung, G.-B., Nafion/PTFE composite membranes for direct methanol fuel cell applications. *Journal of Power Sources* **2005,** 150, 11-19.

11. Smitha, B.; Sridhar, S.; Khan, A. A., Solid polymer electrolyte membranes for fuel cell applications--a review. *Journal of Membrane Science* **2005,** 259, (1-2), 10-26.

12. Tang, H.; Wang, S.; Pan, M.; Jiang, S. P.; Ruan, Y., Performance of direct methanol fuel cells prepared by hot-pressed MEA and catalyst-coated membrane (CCM). *Electrochimica Acta* **2007,** 52, (11), 3714-3718.

13. Yin, Y.; Zhu, W.; Xia, C.; Gao, C.; Meng, G., Low-temperature SOFCs using biomass-produced gases as fuels. *Journal of Applied Electrochemistry* **2004,** 34, (12), 1287-1291.

14. Huijsmans, J. P. P., Ceramics in solid oxide fuel cells. *Current Opinion in Solid State and Materials Science* **2001,** 5, (4), 317-323.

15. Irvine, J. T. S.; Jones, F. G. E.; Connor, P. A., University Court of the University of St Andrews. “Fuel Cell”. British Patent Applied for 0125276.6. **2001**, (20 October).

16. Haile, S. M., Fuel cell materials and components. *Acta Materialia* **2003,** 51, (19), 5981-6000.

17. Singhal, S. C., Advances in solid oxide fuel cell technology. *Solid State Ionics* **2000,** 135, (1-4), 305-313.

18. Badwal, S. P. S., Stability of solid oxide fuel cell components. *Solid State Ionics* **2001,** 143, (1), 39-46.

19. Kharton, V. V.; Tsipis, E. V.; Marozau, I. P.; Viskup, A. P.; Frade, J. R.; Irvine, J. T. S., Mixed conductivity and electrochemical behavior of $(La_{0.75}Sr_{0.25})_{0.95}Cr_{0.5}Mn_{0.5}O_{3-\delta}$. *Solid State Ionics* **2007,** 178, (1-2), 101-113.

20. He, H.; Hill, J. M., Carbon deposition on Ni/YSZ composites exposed to humidified methane. *Applied Catalysis A: General* **2007,** 317, (2), 284-292.

21. Chen, M.; Kim, B. H.; Xu, Q.; Nam, O. J.; Ko, J. H., Synthesis and performances of Ni-SDC cermets for IT-SOFC anode. *Journal of the European Ceramic Society* **2008,** 28, (15), 2947-2953.

22. Wang, Z.; Weng, W.; Cheng, K.; Du, P.; Shen, G.; Han, G., Catalytic modification of Ni-Sm-doped ceria anodes with copper for direct utilization of dry methane in low-temperature solid oxide fuel cells. *Journal of Power Sources* **2008,** 179, (2), 541-546.

23. Bebelis, S.; Kotsionopoulos, N.; Mai, A.; Tietz, F., Electrochemical characterization of perovskite-based SOFC cathodes. *Journal of Applied Electrochemistry* **2007,** 37, (1), 15-20.

24. Yokokawa, H.; Horita, T.; Sakai, N.; Dokiya, M.; Kawada, T., Thermodynamic representation of nonstoichiometric lanthanum manganite. *Solid State Ionics* **1996,** 86-88, (Part 2), 1161-1165.

25. van Roosmalen, J. A. M.; Cordfunke, E. H. P., Chemical reactivity and interdiffusion of (La, Sr)MnO_3 and (Zr, Y)O_2, solid oxide fuel cell cathode and electrolyte materials. *Solid State Ionics* **1992,** 52, (4), 303-312.

26. Seo, E. S. M.; Yoshito, W. K.; Ussui, V.; Lazar, D. R. R., Influence of the starting materials on performance of high temperature oxide fuel cells devices. *Materials Research* **2004,** 1, 215-220.

27. Inaba, H.; Tagawa, H., Ceria-based solid electrolytes. *Solid State Ionics* **1996,** 83, (1-2), 1-16.

28. Bellino, M. G.; Lamas, D. G.; Walsöe de Reca, N. E., Enhanced Ionic Conductivity in Nanostructured, Heavily Doped Ceria Ceramics. *Advanced Functional Materials* **2006,** 16, (1), 107-113.

29. Kharton, V. V.; Figueiredo, F. M.; Navarro, L.; Naumovich, E. N.; Kovalevsky, A. V.; Yaremchenko, A. A.; Viskup, A. P.; Carneiro, A.; Marques, F. M. B.; Frade, J. R., Ceria-based materials for solid oxide fuel cells. *Journal of Materials Science* **2001,** 36, (5), 1105-1117.

30. Haile, S. M., Materials for fuel cells. *Materials Today* **2003,** 6, (3), 24-29.

31. Guo, W.; Liu, J.; Zhang, Y., Electrical and stability performance of anode-supported solid oxide fuel cells with strontium- and magnesium-doped lanthanum gallate thin electrolyte. *Electrochimica Acta* **2008,** 53, (13), 4420-4427.

32. Kharton, V. V.; Marques, F. M. B.; Atkinson, A., Transport properties of solid oxide electrolyte ceramics: a brief review. *Solid State Ionics* **2004,** 174, (1-4), 135-149.

33. Kilner, J. A., Fast anion transport in solids. *Solid State Ionics* **1983,** 8, (3), 201-207.

34. Fuentes, R. O.; Baker, R. T., Synthesis and properties of Gadolinium-doped ceria solid solutions for IT-SOFC electrolytes. *International Journal of Hydrogen Energy* **2008,** 33, (13), 3480-3484.

35. Zhang, X.; Decès-Petit, C.; Yick, S.; Robertson, M.; Kesler, O.; Maric, R.; Ghosh, D., A study on sintering aids for $Sm_{0.2}Ce_{0.8}O_{1.9}$ electrolyte. *Journal of Power Sources* **2006,** 162, (1), 480-485.

36. Yoshida, H.; Miura, K.; Fukui, T.; Ohara, S.; Inagaki, T., Sintering behavior of Ln-doped ceria compounds containing gallia. *Journal of Power Sources* **2002,** 106, (1-2), 136-141.

37. Yoshida, H.; Inagaki, T., Effects of additives on the sintering properties of samaria-doped ceria. *Journal of Alloys and Compounds* **2006,** 408-412, 632-636.

38. Tianshu, Z.; Hing, P.; Huang, H.; Kilner, J., The effect of Fe doping on the sintering behavior of commercial CeO_2 powder. *Journal of Materials Processing Technology* **2001,** 113, (1-3), 463-468.

39. Yan, R.; Chu, F.; Ma, Q.; Liu, X.; Meng, G., Sintering kinetics of samarium doped ceria with addition of cobalt oxide. *Materials Letters* **2006,** 60, (29-30), 3605-3609.

40. Tok, A. I. Y.; Du, S. W.; Boey, F. Y. C.; Chong, W. K., Hydrothermal synthesis and characterization of rare earth doped ceria nanoparticles. *Materials Science and Engineering: A* **2007,** 466, (1-2), 223-229.

41. Li, S.-P.; Lu, J.-Q.; Fang, P.; Luo, M.-F., Effect of powder thermal treatment on the microstructure and electrical properties of doped ceria ceramics. *Materials Letters* **2009,** 63, (20), 1689-1692.

42. Zhang, T. S.; Ma, J.; Chen, Y. Z.; Luo, L. H.; Kong, L. B.; Chan, S. H., Different conduction behaviors of grain boundaries in SiO_2-containing 8YSZ and CGO20 electrolytes. *Solid State Ionics* **2006,** 177, (13-14), 1227-1235.

43. Zhang, T. S.; Ma, J.; Kong, L. B.; Chan, S. H., Effect of SiO_2 content on the ionic conductivity of $Ce_{0.8}Gd_{0.2}O_{2-\delta}$ ceramics. *Journal of Materials Science* **2004,** 39, (20), 6371-6373.

44. Zhang, T. S.; Ma, J.; Chan, S. H.; Hing, P.; Kilner, J. A., Intermediate-temperature ionic conductivity of ceria-based solid solutions as a function of gadolinia and silica contents. *Solid State Sciences* **2004,** 6, (6), 565-572.

45. Badwal, S. P. S.; Rajendran, S., Effect of micro- and nano-structures on the properties of ionic conductors. *Solid State Ionics* **1994,** 70-71, (Part 1), 83-95.

46. Hos, J. P.; McCormick, P. G., Mechanochemical synthesis and characterisation of nanoparticulate samarium-doped cerium oxide. *Scripta Materialia* **2003,** 48, (1), 85-90.

47. Omar, S.; Wachsman, E. D.; Nino, J. C., Higher conductivity Sm^{3+} and Nd^{3+} co-doped ceria-based electrolyte materials. *Solid State Ionics* **2008,** 178, (37-38), 1890-1897.

48. Lee, D.; Lee, I.; Jeon, Y.; Song, R., Characterization of scandia stabilized zirconia prepared by glycine nitrate process and its performance as the electrolyte for IT-SOFC. *Solid State Ionics* **2005,** 176, (11-12), 1021-1025.

49. Wang, Z.; Hui, R.; Bogdanovic, N.; Tang, Z.; Yick, S.; Xie, Y.; Yaroslavski, I.; Burgess, A.; Maric, R.; Ghosh, D., Plasma spray synthesis of ultra-fine YSZ powder. *Journal of Power Sources* **2007,** 170, (1), 145-149.

50. Huang, W.; Shuk, P.; Greenblatt, M., Properties of sol-gel prepared $Ce_{1-x}Sm_xO_{2-x/2}$ solid electrolytes. *Solid State Ionics* **1997,** 100, (1-2), 23-27.

51. Wang, Y.; Mori, T.; Li, J.-G.; Yajima, Y.; Drennan, J., Synthesis, characterization and sinterablity of 10 mol% Sm_2O_3-doped CeO_2 nanopowders via carbonate precipitation. *Journal of the European Ceramic Society* **2006,** 26, (4-5), 417-422.

52. Purohit, R. D.; Saha, S.; Tyagi, A. K., Powder characteristics and sinterability of ceria powders prepared through different routes. *Ceramics International* **2006,** 32, (2), 143-146.

53. Muccillo, E. N. S.; Rocha, R. A.; Muccillo, R., Preparation of Gd_2O_3-doped ZrO_2 by polymeric precursor techniques. *Materials Letters* **2002,** 53, (4-5), 353-358.

54. Yuan, F. L.; Chen, C. H.; Kelder, E. M.; Schoonman, J., Preparation of zirconia and yttria-stabilized zirconia (YSZ) fine powders by flame-assisted ultrasonic spray pyrolysis (FAUSP). *Solid State Ionics* **1998,** 109, (1-2), 119-123.

55. Lu, C.; An, S.; Worrell, W. L.; Vohs, J. M.; Gorte, R. J., Development of intermediate-temperature solid oxide fuel cells for direct utilization of hydrocarbon fuels. *Solid State Ionics* **2004,** 175, (1-4), 47-50.

56. Steele, B. C. H.; Heinzel, A., Materials for fuel-cell technologies. *Nature* **2001,** 414, (6861), 345.

57. Zhao, L.; Huang, X.; Zhu, R.; Lu, Z.; Sun, W.; Zhang, Y.; Ge, X.; Liu, Z.; Su, W., Optimization on technical parameters for fabrication of SDC film by screen-printing used as electrolyte in IT-SOFC. *Journal of Physics and Chemistry of Solids* **2008,** 69, (8), 2019-2024.

58. La O, G. J.; Hertz, J.; Tuller, H.; Shao-Horn, Y., Microstructural Features of RF-sputtered SOFC Anode and Electrolyte Materials. *Journal of Electroceramics* **2004,** 13, (1), 691-695.

59. Atkinson, A.; Barnett, S.; Gorte, R. J.; Irvine, J. T. S.; McEvoy, A. J.; Mogensen, M.; Singhal, S. C.; Vohs, J., Advanced anodes for high-temperature fuel cells. *Nat Mater* **2004,** 3, (1), 17-27.

60. Hilpert, K.; Steinbrech, R. W.; Boroomand, F.; Wessel, E.; Meschke, F.; Zuev, A.; Teller, O.; Nickel, H.; Singheiser, L., Defect formation and mechanical stability of perovskites based on LaCrO3 for solid oxide fuel cells (SOFC). *Journal of the European Ceramic Society* **2003,** 23, (16), 3009-3020.

61. Föger, K.; Love, J. G., Fifteen years of SOFC development in Australia. *Solid State Ionics* **2004,** 174, (1-4), 119-126.

62. Arachi, Y.; Sakai, H.; Yamamoto, O.; Takeda, Y.; Imanishai, N., Electrical conductivity of the ZrO_2-Ln_2O_3 (Ln=lanthanides) system. *Solid State Ionics* **1999,** 121, (1-4), 133-139.

63. Navrotsky, A., Thermochemical insights into refractory ceramic materials based on oxides with large tetravalent cations. *J. Mater. Chem.* **2005,** 15, 1883 - 1890.

64. Fevre, M.; Finel, A.; Caudron, R., Local order and thermal conductivity in yttria-stabilized zirconia. I. Microstructural investigations using neutron diffuse scattering and atomic-scale simulations. *Physical Review B (Condensed Matter and Materials Physics)* **2005,** 72, (10), 104117-13.

65. Weber, A.; Ivers-Tiffée, E., Materials and concepts for solid oxide fuel cells (SOFCs) in stationary and mobile applications. *Journal of Power Sources* **2004,** 127, (1-2), 273-283.

66. Yamamoto, O.; Arati, Y.; Takeda, Y.; Imanishi, N.; Mizutani, Y.; Kawai, M.; Nakamura, Y., Electrical conductivity of stabilized zirconia with ytterbia and scandia. *Solid State Ionics* **1995,** 79, 137-142.

67. Lv, Z. G.; Yao, P.; Guo, R. S.; Dai, F. Y., Study on zirconia solid electrolytes doped by complex additives. *Materials Science and Engineering: A* **2007,** 458, (1-2), 355-360.

68. Guo, X.; Vasco, E.; Mi, S.; Szot, K.; Wachsman, E.; Waser, R., Ionic conduction in zirconia films of nanometer thickness. *Acta Materialia* **2005,** 53, (19), 5161-5166.

69. Chen, X. J.; Khor, K. A.; Chan, S. H.; Yu, L. G., Influence of microstructure on the ionic conductivity of yttria-stabilized zirconia electrolyte. *Materials Science and Engineering A* **2002,** 335, (1-2), 246-252.

70. Yashima, M.; Kakihana, M.; Yoshimura, M., Metastable-stable phase diagrams in the zirconia-containing systems utilized in solid-oxide fuel cell application. *Solid State Ionics* **1996,** 86-88, (Part 2), 1131-1149.

71. Mayo, M. J.; Suresh, A.; Porter, W. D., Thermodynamics for nanosystems: grain and particle-size dependent phase diagrams. *Reviews on Advanced Materials Science* **2003,** 5, (2), 100-1009.

72. Zha, S.; Xia, C.; Meng, G., Effect of Gd (Sm) doping on properties of ceria electrolyte for solid oxide fuel cells. *Journal of Power Sources* **2003,** 115, (1), 44-48.

73. Mogensen, M.; Lybye, D.; Bonanos, N.; Hendriksen, P. V.; Poulsen, F. W., Factors controlling the oxide ion conductivity of fluorite and perovskite structured oxides. *Solid State Ionics* **2004,** 174, (1-4), 279-286.

74. Piñol, S.; Najib, M.; Bastidas, D. M.; Calleja, A.; Capdevila, X. G.; Segarra, M.; Espiell, F.; Ruiz-Morales, J. C.; Marrero-López, D.; Nuñez, P., Microstructure–conductivity relationship in Gd- and Sm-doped ceria-based electrolytes prepared by the acrylamide sol–gel-related method. *Journal of Solid State Electrochemistry* **2004,** 8, (9), 650-654.

75. Ji, Y.; Liu, J.; He, T.; Wang, J.; Su, W., The effect of Pr co-dopant on the performance of solid oxide fuel cells with Sm-doped ceria electrolyte. *Journal of Alloys and Compounds* **2005,** 389, (1-2), 317-322.

76. Kuharuangrong, S., Ionic conductivity of Sm, Gd, Dy and Er-doped ceria. *Journal of Power Sources* **2007,** 171, (2), 506-510.

77. Balazs, G. B.; Glass, R. S., ac impedance studies of rare earth oxide doped ceria. *Solid State Ionics* **1995,** 76, (1-2), 155-162.

78. Steele, B. C. H., Appraisal of $Ce_{1-y}Gd_yO_{2-y/2}$ electrolytes for IT-SOFC operation at 500°C. *Solid State Ionics* **2000,** 129, (1-4), 95-110.

79. Eguchi, K.; Setoguchi, T.; Inoue, T.; Arai, H., Electrical properties of ceria-based oxides and their application to solid oxide fuel cells. *Solid State Ionics* **1992,** 52, (1-3), 165-172.

80. Shemilt, J. E.; Williams, H. M., Effects of composition and processing method on the low temperature conductivity of samaria-doped ceria electrolytes. *Journal of Materials Science Letters* **1999,** 18, (21), 1735-1737.

81. Jung, G. B.; Huang, T. J.; Huang, M. H.; Chang, C. L., Preparation of samaria-doped ceria for solid-oxide fuel cell electrolyte by a modified sol-gel method. *Journal of Materials Science* **2001,** 36, (24), 5839-5844.

82. Jung, G.-B.; Huang, T.-J.; Chang, C.-L., Effect of temperature and dopant concentration on the conductivity of samaria-doped ceria electrolyte. *Journal of Solid State Electrochemistry* **2002,** 6, (4), 225-230.

83. Peng, R.; Xia, C.; Fu, Q.; Meng, G.; Peng, D., Sintering and electrical properties of $(CeO_2)_{0.8}(Sm_2O_3)_{0.1}$ powders prepared by glycine-nitrate process. *Materials Letters* **2002,** 56, (6), 1043-1047.

84. Alifanti, M.; Baps, B.; Blangenois, N.; Naud, J.; Grange, P.; Delmon, B., Characterization of CeO_2-ZrO_2 Mixed Oxides. Comparison of the Citrate and Sol-Gel Preparation Methods. *Chemistry of Materials* **2002,** 15, (2), 395-403.

85. Fuentes, R. O.; Baker, R. T., Synthesis of Nanocrystalline CeO_2-ZrO_2 Solid Solutions by a Citrate Complexation Route: A Thermochemical and Structural Study. *The Journal of Physical Chemistry C* **2009,** 113, (3), 914-924.

86. Fuentes, R. O.; Baker, R. T., Structural, morphological and electrical properties of $Gd_{0.1}Ce_{0.9}O_{1.95}$ prepared by a citrate complexation method. *Journal of Power Sources* **2009,** 186, (2), 268-277.

87. Kaspar, J.; Fornasiero, P.; Balducci, G.; Di Monte, R.; Hickey, N.; Sergo, V., Effect of ZrO_2 content on textural and structural properties of CeO_2-ZrO_2 solid solutions made by citrate complexation route. *Inorganica Chimica Acta* **2003,** 349, 217-226.

88. Wang, F.-Y.; Wan, B.-Z.; Cheng, S., Study on Gd^{3+} and Sm^{3+} co-doped ceria-based electrolytes. *Journal of Solid State Electrochemistry* **2005,** 9, (3), 168-173.

89. Lapa, C. M.; Souza, D. P. F. d.; Figueiredo, F. M. L.; Marques, F. M. B., Electrical and microstructural characterization of two-step sintered ceria-based electrolytes. *Journal of Power Sources* **2009,** 187, (1), 204-208.

90. Liu, Y.; Li, B.; Wei, X.; Pan, W., Nitrate Combustion Synthesis and Electrical Conductivity of the Sm^{3+} and Nd^{3+} Co-Doped Ceria Electrolyte. *Journal of the American Ceramic Society* **2008,** 91, (12), 3926-3930.

91. Sha, X.; Lü, Z.; Huang, X.; Miao, J.; Jia, L.; Xin, X.; Su, W., Preparation and properties of rare earth co-doped $Ce_{0.8}Sm_{0.2-x}Y_xO_{1.9}$ electrolyte materials for SOFC. *Journal of Alloys and Compounds* **2007,** 424, (1-2), 315-321.

92. Sha, X.; Lu, Z.; Huang, X.; Miao, J.; Liu, Z.; Xin, X.; Zhang, Y.; Su, W., Influence of sintering temperature on electrical property of the $Ce_{0.8}Sm_{0.1}Y_{0.1}O_{1.9}$ electrolyte. *Journal of Alloys and Compounds* **2007,** 433, 274-278.

93. Laosiripojana, N.; Assabumrungrat, S., The effect of specific surface area on the activity of nano-scale ceria catalysts for methanol decomposition with and without steam at SOFC operating temperatures. *Chemical Engineering Science* **2006,** 61, (8), 2540-2549.

94. Goguet, A.; Meunier, F.; Breen, J. P.; Burch, R.; Petch, M. I.; Faur Ghenciu, A., Study of the origin of the deactivation of a Pt/CeO_2 catalyst during reverse water gas shift (RWGS) reaction. *Journal of Catalysis* **2004,** 226, (2), 382-392.

95. Terribile, D.; Trovarelli, A.; de Leitenburg, C.; Dolcetti, G.; Llorca, J., Unusual Oxygen Storage/Redox Behavior of High-Surface-Area Ceria Prepared by a Surfactant-Assisted Route. *Chemistry of Materials* **1997,** 9, (12), 2676-2678.

96. Saeki, M. J.; Uchida, H.; Watanabe, M., Noble metal catalysts highly-dispersed on Sm-doped ceria for the application to internal reforming solid oxide fuel cells operated at medium temperature. *Catalysis Letters* **1994,** 26, (1), 149-157.

97. Bakhmutsky, K.; Zhou, G.; Timothy, S.; Gorte, R., The Water–Gas-Shift Reaction on Pd/Ceria–Praseodymia: The Effect of Redox Thermodynamics. *Catalysis Letters* **2009,** 129, (1), 61-65.

98. Gatica, J. M.; Baker, R. T.; Fornasiero, P.; Bernal, S.; Kaspar, J., Characterization of the Metal Phase in NM/$Ce_{0.68}Zr_{0.32}O_2$ (NM: Pt and Pd) Catalysts by Hydrogen Chemisorption and HRTEM Microscopy: A Comparative Study. *The Journal of Physical Chemistry B* **2001,** 105, (6), 1191-1199.

99. Gatica, J. M.; Baker, R. T.; Fornasiero, P.; Bernal, S.; Blanco, G.; Kaspar, J., Rhodium Dispersion in a Rh/$Ce_{0.68}Zr_{0.32}O_2$ Catalyst Investigated by HRTEM and H_2 Chemisorption. *The Journal of Physical Chemistry B* **2000,** 104, (19), 4667-4672.

100. González-Velasco, J. R.; Gutiérrez-Ortiz, M. A.; Marc, J.-L.; Botas, J. A.; González-Marcos, M. P.; Blanchard, G., Contribution of cerium/zirconium mixed oxides to the activity of a new generation of TWC. *Applied Catalysis B: Environmental* **1999,** 22, (3), 167-178.

101. Priolkar, K. R.; Bera, P.; Sarode, P. R.; Hegde, M. S.; Emura, S.; Kumashiro, R.; Lalla, N. P., Formation of $Ce_{1-x}Pd_xO_{2-\delta}$ Solid Solution in Combustion-Synthesized Pd/CeO_2 Catalyst: XRD, XPS, and EXAFS Investigation. *Chemistry of Materials* **2002,** 14, (5), 2120-2128.

102. Bera, P.; Priolkar, K. R.; Gayen, A.; Sarode, P. R.; Hegde, M. S.; Emura, S.; Kumashiro, R.; Jayaram, V.; Subbanna, G. N., Ionic Dispersion of Pt over CeO_2 by the Combustion Method: Structural Investigation by XRD, TEM, XPS, and EXAFS. *Chemistry of Materials* **2003,** 15, (10), 2049-2060.

103. Zhao, M.; Shen, M.; Wang, J., Effect of surface area and bulk structure on oxygen storage capacity of $Ce_{0.67}Zr_{0.33}O_2$. *Journal of Catalysis* **2007,** 248, (2), 258-267.

104. Acuna, L. M.; Munoz, F. F.; Cabezas, M. D.; Lamas, D. G.; Leyva, A. G.; Fantini, M. C. A.; Baker, R. T.; Fuentes, R. O., Improvement in the Reduction Behavior of Novel ZrO_2-CeO_2 Solid Solutions with a Tubular Nanostructure by Incorporation of Pd. *The Journal of Physical Chemistry C* **2010,** 114, (46), 19687-19696.

105. Ilieva, L.; Pantaleo, G.; Ivanov, I.; Venezia, A. M.; Andreeva, D., Gold catalysts supported on CeO_2 and CeO_2-Al_2O_3 for NO_x reduction by CO. *Applied Catalysis B: Environmental* **2006,** 65, (1-2), 101-109.

106. Wang, J. B.; Shih, W.-H.; Huang, T.-J., Study of Sm_2O_3-doped CeO_2/Al_2O_3-supported copper catalyst for CO oxidation. *Applied Catalysis A: General* **2000,** 203, (2), 191-199.

107. Dicks, A. L., Hydrogen generation from natural gas for the fuel cell systems of tomorrow. *Journal of Power Sources* **1996,** 61, (1-2), 113-124.

108. Wang, X.; Gorte, R. J., The effect of Fe and other promoters on the activity of Pd/ceria for the water-gas shift reaction. *Applied Catalysis A: General* **2003,** 247, (1), 157-162.

109. Li, Y.; Fu, Q.; Flytzani-Stephanopoulos, M., Low-temperature water-gas shift reaction over Cu- and Ni-loaded cerium oxide catalysts. *Applied Catalysis B: Environmental* **2000,** 27, (3), 179-191.

110. Andreeva, D.; Ivanov, I.; Ilieva, L.; Abrashev, M. V.; Zanella, R.; Sobczak, J. W.; Lisowski, W.; Kantcheva, M.; Avdeev, G.; Petrov, K., Gold catalysts supported on ceria doped by rare earth metals for water gas shift reaction: Influence of the preparation method. *Applied Catalysis A: General* **2009,** 357, (2), 159-169.

111. Olah, G. A., Beyond Oil and Gas: The Methanol Economy. *Angewandte Chemie International Edition* **2005,** 44, (18), 2636-2639.

112. Gómez-Sainero, L. M.; Baker, R. T.; Metcalfe, I. S.; Sahibzada, M.; Concepción, P.; López-Nieto, J. M., Investigation of Sm_2O_3-CeO_2-supported palladium catalysts for the reforming of methanol: The role of the support. *Applied Catalysis A: General* **2005,** 294, (2), 177-187.

113. Baker, R. T.; Gomez-Sainero, L. M.; Metcalfe, I. S., Pretreatment-Induced Nanostructural Evolution in CeO_2-, Sm_2O_3-, and CeO_2/Sm_2O_3-supported Pd Catalysts for Intermediate-Temperature Methanol Fuel Cells. *The Journal of Physical Chemistry C* **2009,** 113, (28), 12465-12475.

114. http://www.icdd.com/profile/overview.htm, International Centre for Diffraction Data. *access date:* **2011,** June.

115. Skoog, D. A.; Holler, F. J.; Nieman, T. A., *Principles of Instrumental Analysis*. 5th ed.; Brooks/Cole: 1997.

116. http://en.wikipedia.org/wiki/File:Scheme_TEM_en.svg#globalusage, TEM schematic. *access date:* **2011,** June.

117. Rodriguez-Carvajal, J. *Version 0.2. Laboratoire Leon Brillouin (CEA-CNRS)* Sacley, France, 1998.

118. http://www.netzsch-thermal-analysis.com/en/products, STA 449 C Jupiter - product brochure. *access date:* **2011,** April.

119. http://www.netzsch-thermal-analysis.com/en/products/detail/pidt6.html, DIL 402 C - product brochure. *access date:* **2011,** June.

120. Chen, Z.; Trice, R.; Wang, H.; Porter, W.; Howe, J.; Besser, M.; Sordelet, D., Co-Doping of Air Plasma-Sprayed Yttria- and Ceria-Stabilized Zirconia for Thermal Barrier Applications. *Journal of the American Ceramic Society* **2005,** 88, (6), 1584-1590.

121. Lamas, D. G.; Walsöe De Reca, N. E., X-ray diffraction study of compositionally homogeneous, nanocrystalline yttria-doped zirconia powders. *Journal of Materials Science* **2000,** 35, (22), 5563-5567.

122. Weller, M. T., *Inorganic materials chemistry*. Oxford University Press: 1994.

123. Lamas, D. G.; Rosso, A. M.; Anzorena, M. S.; Fernández, A.; Bellino, M. G.; Cabezas, M. D.; Walsöe de Reca, N. E.; Craievich, A. F., Crystal structure of pure ZrO_2 nanopowders. *Scripta Materialia* **2006,** 55, (6), 553-556.

124. Inorganic Crystal Structure Database, FIZ, Karlsruhe, Germany.

125. Stadelmann, P. A., EMS - a software package for electron diffraction analysis and HREM image simulation in materials science. *Ultramicroscopy* **1987,** 21, (2), 131-145.

126. Zhu, Q.; Fan, B., Low temperature sintering of 8YSZ electrolyte film for intermediate temperature solid oxide fuel cells. *Solid State Ionics* **2005,** 176, (9-10), 889-894.

127. Han, M.; Tang, X.; Yin, H.; Peng, S., Fabrication, microstructure and properties of a YSZ electrolyte for SOFCs. *Journal of Power Sources* **2007,** 165, (2), 757-763.

128. Pratihar, S. K.; Sharma, A. D.; Basu, R. N.; Maiti, H. S., Preparation of nickel coated YSZ powder for application as an anode for solid oxide fuel cells. *Journal of Power Sources* **2004,** 129, (2), 138-142.

129. Hayashi, H.; Saitou, T.; Maruyama, N.; Inaba, H.; Kawamura, K.; Mori, M., Thermal expansion coefficient of yttria stabilized zirconia for various yttria contents. *Solid State Ionics* **2005,** 176, (5-6), 613-619.

130. Badwal, S. P. S., Zirconia-based solid electrolytes: microstructure, stability and ionic conductivity. *Solid State Ionics* **1992,** 52, (1-3), 23-32.

131. Gibson, I. R.; Dransfield, G. P.; Irvine, J. T. S., Influence of yttria concentration upon electrical properties and susceptibility to ageing of yttria-stabilised zirconias. *Journal of the European Ceramic Society* **1998,** 18, (6), 661-667.

132. Haering, C.; Roosen, A.; Schichl, H.; Schnoller, M., Degradation of the electrical conductivity in stabilised zirconia system: Part II: Scandia-stabilised zirconia. *Solid State Ionics* **2005,** 176, (3-4), 261-268.

133. Choi, K.-H.; Choi, Y.-G.; Park, M.-W.; Kodash, V. Y.; Groza, J. R.; Lee, J.-S., Effects of alumina additions on sintering behavior of $Ce_{0.8}Sm_{0.2}O_{1.9}$ ceramics synthesized by Pechini method. *Journal of Alloys and Compounds* **2008,** 463, (1-2), 484-487.

134. Lee, J.-S.; Choi, K.-H.; Ryu, B.-K.; Shin, B.-C.; Kim, I.-S., Effects of alumina additions on sintering behavior of gadolinia-doped ceria. *Ceramics International* **2004,** 30, (5), 807-812.

135. Colomer, M. T.; Traqueia, L. S. M.; Jurado, J. R.; Marques, F. M. B., Role of grain boundaries on the electrical properties of titania doped yttria stabilized zirconia. *Materials Research Bulletin* **1995,** 30, (4), 515-522.

136. Zhuiykov, S., An investigation of conductivity, microstructure and stability of HfO_2-ZrO_2-Y_2O_3-Al_2O_3 electrolyte compositions for high-temperature oxygen measurement. *Journal of the European Ceramic Society* **2000,** 20, (7), 967-976.

137. Khollam, Y. B.; Deshpande, A. S.; Patil, A. J.; Potdar, H. S.; Deshpande, S. B.; Date, S. K., Synthesis of yttria stabilized cubic zirconia (YSZ) powders by microwave-hydrothermal route. *Materials Chemistry and Physics* **2001,** 71, (3), 235-241.

138. Kosinski, M. R.; Baker, R. T., Preparation and property-performance relationships in samarium-doped ceria nanopowders for solid oxide fuel cell electrolytes. *Journal of Power Sources* **2011,** 196, (5), 2498-2512.

139. Earnest, C. M., Modern thermogravimetry. *Analytical Chemistry* **1984,** 56, (13), 1471A-1486A.

140. Barbooti, M. M.; Al-Sammerrai, D. A., Thermal decomposition of citric acid. *Thermochimica Acta* **1986,** 98, 119-126.

141. Chung, D. Y.; Lee, E. H., Microwave-induced combustion synthesis of $Ce_{1-x}Sm_xO_{2-x/2}$ powder and its characterization. *Journal of Alloys and Compounds* **2004,** 374, (1-2), 69-73.

142. PDF, (Powder Diffraction File) 01-075-0157. $Sm_{0.1}Ce_{0.9}O_{1.95}$. ICDD, (2009).

143. PDF, (Powder Diffraction File) 01-075-0158. $Sm_{0.2}Ce_{0.8}O_{1.9}$. ICDD, (2009).

144. PDF, (Powder Diffraction File) 01-075-0159. $Sm_{0.3}Ce_{0.7}O_{1.85}$. ICDD, (2009).

145. Li, J.-G.; Ikegami, T.; Mori, T., Low temperature processing of dense samarium-doped CeO2 ceramics: sintering and grain growth behaviors. *Acta Materialia* **2004,** 52, (8), 2221-2228.

146. Abrantes, J. C. C.; Pérez-Coll, D.; Núñez, P.; Frade, J. R., Electronic transport in $Ce_{0.8}Sm_{0.2}O_{1.9-\delta}$ ceramics under reducing conditions. *Electrochimica Acta* **2003,** 48, (19), 2761-2766.

147. Shimonosono, T.; Hirata, Y.; Ehira, Y.; Sameshima, S.; Horita, T.; Yokokawa, H., Electronic conductivity measurement of Sm- and La-doped ceria ceramics by Hebb-Wagner method. *Solid State Ionics* **2004,** 174, (1-4), 27-33.

148. Milliken, C.; Guruswamy, S.; Khandkar, A., Properties and Performance of Cation-Doped Ceria Electrolyte Materials in Solid Oxide Fuel Cell Applications. *Journal of the American Ceramic Society* **2002,** 85, (10), 2479-2486.

149. Zhongliang, Z.; Ting-Lian, W.; Hengyong, T.; Zhi-Yi, L., AC Impedance Investigation of Samarium-Doped Ceria. *Journal of The Electrochemical Society* **2001,** 148, (5), A427-A432.

150. Kilner, J. A., Fast oxygen transport in acceptor doped oxides. *Solid State Ionics* **2000,** 129, (1-4), 13-23.

151. Faber, J.; Geoffroy, C.; Roux, A.; Sylvestre, A.; Abelard, P., A systematic investigation of the dc electrical conductivity in rare-earth doped ceria. *Applied Physics A* **1989,** 49, 225-232.

152. Fuda, K.; Kishio, K.; Yamauchi, S.; Fueki, K.; Onoda, Y., ^{17}O NMR study of Y_2O_3-doped CeO_2. *J. Phys. Chem. Solids* **1984,** 45, (11), 1253-1257.

153. Minervini, L.; Zacate, M. O.; Grimes, R. W., Defect cluster formation in M_2O_3-doped CeO_2. *Solid State Ionics* **1999,** 116, 339-349.

154. PDF, (Powder Diffraction File) 00-006-0515. *PdO*. ICDD, (2010).

155. PDF, (Powder Diffraction File) 00-001-1201. *Pd*. ICDD, (2010).

156. Ingo, G. M.; Paparazzo, E.; Bagnarelli, O.; Zacchetti, N., XPS studies on cerium, zirconium and yttrium valence states in plasma-sprayed coatings. *Surface and Interface Analysis* **1990,** 16, (1-12), 515-519.

157. Uwamino, Y.; Ishizuka, T.; Yamatera, H., X-ray photoelectron spectroscopy of rare-earth compounds. *Journal of Electron Spectroscopy and Related Phenomena* **1984,** 34, (1), 67-78.

158. Gómez-Sainero, L. M.; Baker, R. T.; Vizcaino, A. J.; Francis, S. M.; Calles, J. A.; Metcalfe, I. S.; Rodriguez, J. J., Steam Reforming of Methanol with Sm_2O_3-CeO_2-Supported Palladium Catalysts: Influence of the Thermal Treatments of Catalyst and Support. *Industrial & Engineering Chemistry Research* **2009,** 48, (18), 8364-8372.

159. Orliukas, A. F.; Salkus, T.; Kezionis, A.; Venckute, V.; Kazlauskiene, V.; Miskinis, J.; Laukaitis, G.; Dudonis, J., XPS and impedance spectroscopy of some oxygen vacancy conducting solid electrolyte ceramics. *Solid State Ionics* **2011,** 188, (1), 36-40.

160. Gómez-Sainero, L. M.; Seoane, X. L.; Fierro, J. L. G.; Arcoya, A., Liquid-Phase Hydrodechlorination of CCl_4 to $CHCl_3$ on Pd/Carbon Catalysts: Nature and Role of Pd Active Species. *Journal of Catalysis* **2002,** 209, (2), 279-288.

161. Figoli, N. S.; Largentiere, P. C.; Arcoya, A.; Seoane, X. L., Modification of the Properties and Sulfur Resistance of a Pd/SiO_2 Catalyst by La Addition. *Journal of Catalysis* **1995,** 155, (1), 95-105.

162. Álvarez-Montero, M. A.; Gómez-Sainero, L. M.; Martin-Martinez, M.; Heras, F.; Rodriguez, J. J., Hydrodechlorination of chloromethanes with Pd on activated carbon catalysts for the treatment of residual gas streams. *Applied Catalysis B: Environmental* **2010,** 96, (1-2), 148-156.

163. Ordoñez, S.; Díaz, E.; Bueres, R. F.; Asedegbega-Nieto, E.; Sastre, H., Carbon nanofibre-supported palladium catalysts as model hydrodechlorination catalysts. *Journal of Catalysis* **2010,** 272, (1), 158-168.

164. Smith, G. K.; Lin, S.; Lai, W.; Datye, A.; Xie, D.; Guo, H., Initial steps in methanol steam reforming on PdZn and ZnO surfaces: Density functional theory studies. *Surface Science* **2011,** 605, (7-8), 750-759.

165. Yi, N.; Si, R.; Saltsburg, H.; Flytzani-Stephanopoulos, M., Steam reforming of methanol over ceria and gold-ceria nanoshapes. *Applied Catalysis B: Environmental* **2010,** 95, (1-2), 87-92.

166. Ahn, J. S.; Omar, S.; Yoon, H.; Nino, J. C.; Wachsman, E. D., Performance of anode-supported solid oxide fuel cell using novel ceria electrolyte. *Journal of Power Sources* **2010,** 195, (8), 2131-2135.

167. Li, B.; Wei, X.; Pan, W., Improved electrical conductivity of $Ce_{0.9}Gd_{0.1}O_{1.95}$ and $Ce_{0.9}Sm_{0.1}O_{1.95}$ by co-doping. *International Journal of Hydrogen Energy* **2010,** 35, (7), 3018-3022.

168. Dikmen, S.; Aslanbay, H.; Dikmen, E.; Sahin, O., Hydrothermal preparation and electrochemical properties of Gd^{3+} and Bi^{3+}, Sm^{3+}, La^{3+} and Nd^{3+} codoped ceria-based electrolytes for intermediate temperature-solid oxide fuel cell. *Journal of Power Sources* **2010,** 195, (9), 2488-2495.

169. Zheng, Y.; He, S.; Ge, L.; Zhou, M.; Chen, H.; Guo, L., Effect of Sr on Sm-doped ceria electrolyte. *International Journal of Hydrogen Energy* **2011,** 36, (8), 5128-5135.

170. Raza, R.; Abbas, G.; Wang, X.; Ma, Y.; Zhu, B., Electrochemical study of the composite electrolyte based on samaria-doped ceria and containing yttria as a second phase. *Solid State Ionics* **2011,** 188, (1), 58-63.

171. Dudek, M., Ceramic oxide electrolytes based on CeO_2 - Preparation, properties and possibility of application to electrochemical devices. *Journal of the European Ceramic Society* **2008,** 28, (5), 965-971.

172. Pikalova, E. Y.; Maragou, V. I.; Demina, A. N.; Demin, A. K.; Tsiakaras, P. E., The effect of co-dopant addition on the properties of $Ln_{0.2}Ce_{0.8}O_{2-\delta}$ (Ln = Gd, Sm, La) solid-state electrolyte. *Journal of Power Sources* **2008,** 181, (2), 199-206.

173. Kang, Y. J.; Park, H. J.; Choi, G. M., The effect of grain size on the low-temperature electrical conductivity of doped CeO_2. *Solid State Ionics* **2008,** 179, (27-32), 1602-1605.